SPECTRAL REGULATION OF LIQUID-FILLED WINDOWS USING NOVEL SPECTRALLY SELECTIVE MATERIALS AND MECHANICAL STRUCTURES

PU JIHONG

PhD

The Hong Kong Polytechnic University

This program is jointly offered by The Hong Kong Polytechnic University and Harbin Institute of Technology

2026

The Hong Kong Polytechnic University

Department of Building Environment and Energy Engineering

Harbin Institute of Technology

Civil Engineering

Spectral Regulation of Liquid-Filled Windows Using Novel Spectrally Selective Materials and Mechanical Structures

PU Jihong

A thesis submitted in partial fulfilment of the requirements for the Degree of Doctor of Philosophy

Jun 2025

CERTIFICATE OF ORIGINALITY

I hereby declare that this thesis is my own work and that, to the best of my knowledge and belief, it reproduces no material previously published or written, nor material that has been accepted for the award of any other degree or diploma, except where due acknowledgement has been made in the text.

_____________________ (Signed)

PU JIHONG (Name of student)

Abstract

Windows are the weakest links of building energy saving. Heat loss and gain through windows account over 30% of the total HVAC energy consumption in buildings. Among the various heat transfer mechanisms, radiative exchange plays a dominate role, contributing to over 50% of the total energy exchange through windows. Passive solar radiative heat gain through windows can exceed 600 W/m^2. Developing novel window technologies that combine superior optical performance and solar radiation management capabilities is crucial for enhancing building energy efficiency. Solar spectrum coupled visible (VIS) and near-infrared (NIR) components, where VIS provides daylight while NIR contributes to indoor solar heat gain. To achieve on-demand regulation of VIS and NIR through windows, this study focuses on two core scientific problems: (1) the VIS/NIR decoupling of solar spectrum and (2) on-demand modulation of windows' optical properties, and series of spectrally selective window technologies was proposed and validated.

First, a novel spectrally selective material was developed to achieve effective solar VIS/NIR decoupling. Specifically, a water-based fluid was prepared using biomass dye, i.e. sodium copper chlorophyllin (SCC) and $CuSO_4$, capable of selectively absorbing NIR while transmitting VIS. This material demonstrated a high visible transmittance over 56%, and significantly reduced solar heat gain below 25%, achieving a maximum figure of merit ($\boldsymbol{FOM=T_{lum}/T_{sol}}$) of 3.06, superior to all reported counterparts, including cesium tungsten bronze and transparent conductive oxide nanomaterials. Remarkably, the optical properties remained fairly stable over a 9-month weathering cycle and 48 hours UV exposure (300 W), confirming excellent long-term stability and high light/heat decoupling performance.

Subsequently, a triple-layered spectrally selective liquid filled window (LFW) was designed. A mathematical model was developed to analyze the window's optical and thermal properties and the model was validated through experiments. The model was then used to assess the energy-saving performance of the triple-layered spectrally selective LFW under Hong Kong's climatic conditions. With varying solar incidence angles and varying solar spectral power distribution throughout the year, the average monthly visible transmittance of the triple layered LFW exceeded 40%, while the

solar heat gain coefficient (SHGC) remained below 0.26, effectively balancing daylighting and solar heat insulation. Compared to conventional triple glazing, the triple layered LFW reduced solar heat gain by approximately 65%, with an annual reduction of about 1717.8 MJ/m^2 in solar energy input under typical Hong Kong weather conditions, demonstrating significant energy-saving potential.

Furthermore, leveraging the fluidic nature of the working medium, a passive ammonia-pressure-powered thermos-responsive smart window (APPs) was developed. This window automatically adapts its transmittance in response to temperature change, exhibiting high visible transmittance (84% in bleached state, >50% in colored state) and up to 70% solar modulation ability. The switching temperature can be flexibly tuned between 20 to 80°C, by adjusting the ammonia concentration, enabling compatibility with diverse building environments. Field tests showed that under sunny conditions, APPs windows reduced indoor air temperatures by approximately 4.3°C compared to traditional double glazing, while performing comparably under cloudy conditions. Energy simulations conducted in different cities confirmed that APPs windows offer strong energy-saving potential across different climate zones. Compared to conventional low-e double glazing, the APPs window reduced HVAC energy consumption by 15 to 40 MJ/m^2, in both hot-humid and cold climates.

Additionally, an actively switchable rotatochromic bi-static (RB) window was proposed and fabricated for actively regulating indoor solar heat gain. Utilizing liquid paraffin (LP) and an SCC/$CuSO_4$-based solution as working fluids, the window employs gravity-induced fluid flipping to reversibly switch between two optical modes. Optical testing revealed excellent performance of the RB window: solar modulation exceeding 60%, visible transmittance of up to 90% in the bleached state and 56% in the colored state, haze below 1%, and a color rendering index (CRI) above 80. Outdoor tests during summer showed that this window reduced indoor floor temperatures by up to 11°C, and alleviated indoor glare. Energy simulations in four cities across different climate zones demonstrated that the window effectively reduced heating and cooling energy consumption by 30% to 40%.

Finally, to address the windows' secondary thermal radiation from spectrally selective glazing to indoors, and to enhance sky radiative cooling in summer, a Janus bi-static

(JB) window was developed. In summer, the window exhibits excellent shading (T_{sol} < 30%) and high radiative cooling potential (IR emissivity > 0.9); in winter, it provides high solar transmittance (T_{sol} > 70%) and thermal insulation (IR emissivity < 0.3), achieving broadband modulation of solar and thermal radiation. Detailed optical characterization confirmed its superior solar heat gain control, IR emissivity modulation, and visible light transmission compared to state-of-the-art smart window technologies. Field tests in Hong Kong under hot-humid conditions showed a peak indoor temperature reduction of over 10 °C. Energy simulations conducted across 1929 global sites demonstrated that it exhibits superior energy-saving performance compared to traditional low-e glazing in nearly all regions worldwide with latitudes below 60°.

This work begins with the design of spectrally selective materials and systematically builds an integrated multi-functional smart window system capable of dynamic regulation across visible, near-infrared, and mid-infrared bands. Through modeling and field testing, the energy-saving performance of these windows was thoroughly evaluated across various climate zones. The findings may provide some technical support for advancing green and sustainable development of buildings.

Keywords: Building Energy, Spectral regulation, Liquid filled window, Sodium Copper Chlorophyllin, Optical transmission model, Janus structure

Publications during Ph.D. study

Journal papers arising from the thesis:

[1] **Pu Jihong**, Han Miao, Shen Chao*, Wang Julian, Lu Lin*. Constructing a New Biomass-Based Bistatic Window for Solar Regulation. *Advanced Science*, 2024, 2401991.

[2] **Pu Jihong**, Shen Chao*, Wang Julian, Zhang Yingbo, Zhang Chunxiao, Soteris Kalogirou. Near-infrared absorbing glazing for energy-efficient windows: A critical review and performance assessments from the building requirements. *Nano Energy*, 110 (2023) 108334.

[3] **Pu Jihong**, Shen Chao*, Lu Lin, Long Yi, Zhang Chunxiao, Shuai Yong, Soteris. A. Kalogirou. Ammonia powered thermal-responsive smart window with spectral regulation of Cu^{2+} and sodium copper chlorophyllin. *Energy Conversion and Management*, 299 (2024) 117815.

[4] **Pu Jihong**, Han Miao, Lu Lin*, Shen Chao*, Wang Fang. Spectrally selective design and energy-saving demonstration of a novel liquid-filled window in hot and humid region. ***Energy***, 297 (2024) 131090.

[5] **Pu Jihong**, Shen Chao*, Lin Lu. Investigating the annual energy-saving and energy-output behaviors of a novel liquid-flow window with spectral regulation of ATO nanofluids. *Energy*, 283 (2023) 129111.

[6] **Pu Jihong**, Shen Chao*, Yang Shaoxin, Zhang Chunxiao, Dorota Chwieduk, Soteris Kalogirou. Feasibility investigation on using silver nanorods in energy saving windows for light/heat decoupling. *Energy*, 245 (2022) 123289.

[7] **Pu Jihong**, Yingxiao Li, Dan Xu, Chao Shen*, Lu Lin*. A Quantitative Investigation on the Cooling Benefits of Retrofitting Building Skylights with Broadband-Spectrum Selectivity in China. *Applied Energy.* 381 (2025) 125101.

[8] **Pu Jihong**, Shen Chao*, Lin Lu*. Hourglass-Inspired Janus Window for

VIS-NIR-MIR Broadband Spectral Regulation (**submitted**)

Other journal papers during Ph.D. study:

[1] **Pu Jihong**, Dan Xu, Chao Shen, Lu Lin*. Broadband spectrum-regulation of building integrated photovoltaic skylights via functional polymeric film. *Energy Conversion and Management*, 326 (2025) 119453.

[2] **Pu Jihong**, Shen Chao*, Zhang Chunxiao, Liu Xingjiang. A semi-experimental method for evaluating frosting performance of air source heat pumps. *Renewable Energy*, 173 (2021) 913-925.

[3] **Pu Jihong**, Shen Chao*, Zhang Chunxiao, Yan Xu. A semi-experimental investigation on the anti-frosting potential of homogenizing the uneven frosting for air source heat pumps. *Energy & Buildings*, 260 (2022) 111939.

[4] Yu Jiangsheng, **Pu Jihong**, Xie Dongsheng, Ai Zhenhai, Lang Yongwen, Cao Menghua, Duan Chunhui*, Lu Lin*, Gang Li*. Semitransparent organic photovoltaics with wide geographical adaptability as sustainable smart windows. *Nature Communications*, to appear.

[5] Han Miao, **Pu Jihong**, Liu Yongdong, Liu Xingjiang, Mei Hongyuan, Shen Chao*. Near-infrared blocking window based on ATO-CWO/PVB nano-lamination. *Renewable Energy*, 219 (2023) 119382.

Acknowledgements

This dissertation not only represents my academic and research efforts over the past few years, but more importantly, it embodies the support, guidance, and encouragement my supervisors, colleagues, friends, and family. I would like to extend my heartfelt gratitude to all those who have accompanied me along this journey.

First and foremost, I would like to sincerely thank my supervisor, Professor LU Lin, for her humility, rigor, and unwavering dedication to students' development. Her meticulous academic attitude, tireless professionalism, and optimistic approach to life have deeply inspired me and will remain a lifelong influence. I wish Professor LU good health and continued success in all her endeavors.

I am also deeply grateful to my supervisor, Professor Shen Chao, for his invaluable guidance and encouragement throughout the past seven years. From the initial topic selection to the final drafting of this thesis, Professor Shen has provided consistent support both academically and personally. His rigorous scholarship and pragmatic spirit have greatly shaped my academic path and will continue to guide me in the future.

I would like to thank Professors Lin Borong, Lan Dongchen and Mak Cheuk Ming for their insightful comments and constructive suggestions during my oral examination. Their feedback greatly improved the quality of my work.

Special thanks go to Xu Dan, Gao Yu, Lai Cong, Yang Haotian, Han Miao, and many others (just to name a few). I will always treasure the unforgettable hiking days we shared in Hong Kong, those moments have become some of my most cherished memories.

Special thanks to Xu Dan, Gao Yu, Lai Cong, Yang Haotian, and Han Miao, etc (just to name a few). I will always cherish the unforgettable hiking days in Hong Kong with you.

My heartfelt thanks also go to my parents and my girlfriend, Bu Subei, for their unwavering support and encouragement. Amid the pressures and fatigue of research, a simple phone call or a family reunion has always been a source of comfort and renewed energy. Their understanding, love, and constant presence have been my greatest strength throughout this journey.

Finally, I would like to sincerely acknowledge The Hong Kong Polytechnic University (PolyU) and Harbin Institute of Technology (HIT) for their comprehensive support during my academic years. From research funding to living and learning resources, both institutions have provided an excellent environment that nurtured my personal and academic growth.

With this dissertation, I extend my deepest gratitude to everyone who has supported, guided, and accompanied me along the way.

Pu Jihong

December 2025

TABLE OF CONTENT

List of Figures

List of Tables

Nomenclature

Symbols

$\boldsymbol{A_{sol}}$	Solar absorbance, dimensionless
$\boldsymbol{A_z}$	Solar azimuth angle, rad
$\boldsymbol{c}$	Specific heat capacity, J/kg·K
$\boldsymbol{CT_{o-t}}$	Critical transition temperature from colored to bleached state, ℃
$\boldsymbol{CT_{t-o}}$	Critical transition temperature from bleached to colored state, ℃
$\boldsymbol{d}$	Thickness, m
$\boldsymbol{H}$	Hour angle, rad
$\boldsymbol{h_{c,in}}$	Convective heat transfer coefficient between glazing and indoor air, $W/m^2·K$
$\boldsymbol{h_{c,out}}$	Convective heat transfer coefficient between glazing and outdoor air, $W/m^2·K$
$\boldsymbol{h_{r,in}}$	Radiative heat transfer coefficient between glazing and indoor environment, $W/m^2·KW/m^2·K$
$\boldsymbol{h_{r,out}}$	Radiative heat transfer coefficient between glazing and outdoor environment, $W/m^2·KW/m^2·K$
$\boldsymbol{h_s}$	Solar altitude angle, rad
$\boldsymbol{K_{abs}}$	Absorbing coefficient, dimensionless
$\boldsymbol{l_{local}}$	Local longitude, °

$l_{standard}$	Standard meridian of the time zone, °
m	Mass, kg
$mp(\lambda)$	Macular pigment transmittance, dimensionless
n	Refractive index, dimensionless
$Q_{r,out}$	Radiative heat transfer between window and outdoor environment, W/m^2
R_A	Thermal resistance of the air gap, $m^2 \cdot K/W$
R_{in}	Thermal resistance of heat transfer from glazing to indoor environment, $m^2 \cdot K/W$
R_{out}	Thermal resistance of heat transfer from glazing to outdoor environment, $m^2 \cdot K/W$
S	Optical path lenght, m
$S_{rods}(\lambda)$	Spectral response of rod cells, lum/W
$S_{cone}(\lambda)$	Spectral response of cone cells, lum/W
t	Time, s
T	Temperature, °C
$T(\lambda)$	Transmittance, dimensionless
T_A	Atmospheric transmittance after aerosol extinction, dimensionless
T_{local}	Local time
T_{lum}	Photopic luminous (visible) transmittance, dimensionless

T_{mel}	Mealnopic transmittance, dimensionless
T_N	Atmospheric transmittance after N_2 absorption, dimensionless
T_O	Atmospheric transmittance after O_2 absorption, dimensionless
T_R	Atmospheric transmittance after Rayleigh scattering, dimensionless
T_{sky}	Sky temperature, ℃
T_{sol}	Solar transmittance, dimensionless
T_W	Atmospheric transmittance after water vapor absorption, dimensionless
$V(\lambda)$	Photopic luminous efficiency function, lum/W
X	Red stimulus value, dimensionless
Y	Yellow stimulus value, dimensionless
Z	Blue stimulus value, dimensionless

Greek Symbols

v_a	Air velocity, m/s
ε	Emissivity, dimensionless
δ	Stefan–Boltzmann constant, 5.67×10^{-8} (W/m^2K^{-4})
δ	Solar declination angle, °
ρ	Density, kg/m^3
ρ	Interfacial reflectance, dimensionless

θ Incident angle, °

θ' Angle of refraction, °

σ Thickness, m

ϕ Latitude, °

$\Phi(\lambda)$ Ground-level solar radiation, $W/(m^2 \cdot nm)$

$\Phi_{out}(\lambda)$ Extraterrestrial solar radiation, $W/(m^2 \cdot nm)$

λ_g Thermal conductivity of glazing, W/(m K)

λ Wavelength, μm

Subscript

a Air

f Fluid

g Glazing

in Indoor

out Outdoor

Dimensionless Number

Re Reynolds Number

Nu Nusselt Number

Ra Rayleigh Number

Pr Prandtl Number

Gr Grashof Number

Abbreviation

APPs Ammonia Pressure Powered

ATO Antimony Tin Oxide

CCT Color Temperature

CIE International Commission on Illumination

CLA Circadian Lighting

CRI Color Rendering Index

CS Circadian Stimulus

CWO Cesium Tungsten Oxide

ipRGCs Intrinsically Photosensitive Retinal Ganglion Cells

ITO Indium Tin Oxide

LFW Liquid Filled Window

LP Liquid Paraffin

LSG Light-to-solar-gain

LSPR Localized Surface Plasmon Resonance

NIR Nera-infrared

PDLC	Polymer Dispersed Liquid Crystal
SCC	Sodium Copper Chlorophyllin
SHGC	Solar heat gain coefficient
SPD	Suspended Particle Device
SSF	Spectrally selective fluids
SV	Blue-Yellow Opponent Signal
TCO	Transparent Conductive Oxide
TMY	Typical Meteorological Year
UDI	Useful Daylight Illuminance
UV	Ultraviolet
U	Overall Heat Transfer Coefficient
VIS	Visible Light
VOF	Volume of Fluid

Chapter 1 Introduction

1.1 Research background

After World War II, energy depletion and global warming gradually became the focus of global issues. Excessive use of primary energy continually increased the global greenhouse gas concentration. As recorded by the Mauna Loa Observatory, the CO_2 concentration in Hawaii increased from 316 ppm to 414 ppm [1], which results in a global mean temperature anomaly maintaining a stable growth from about 0.2 to 1.2 °C (**Figure 1.1**), from 1970 to 2020. Global warming has become the most devastated environmental problem facing humankind, especially with the recent Australia bushfire burning, black rain in Hong Kong, and others ecological and natural habitat destruction. To combat these effects, there has been a global pact to maintain the global average temperature average temperature rise below 2 °C above industrial level and limit the rise below 1.5 °C following Paris Agreement [2]. To address global environmental issues and achieve sustainable development, the 28th annual United Nations (UN) climate meeting (**COP28**) calls on countries to accelerate low- and zero-emission technologies [3]. Energy conservation and emission reduction became an urgent mission of all area, and buildings are of significant relevance.

According to World Green Building Council (**WBGC**), building accounts for 39% of global carbon emission presence in the atmosphere; 28% of it is allocated to building energy related usage such as space heating, cooling, ventilation and electric appliances [4]. Windows are the weakest part of building energy loss, accounting for 30% of the building energy consumption. Moreover, contemporary architectural design embraces the trend of high window-to-wall ratios to meet aesthetic demands. It is foreseeable that the proportion of energy consumption attributed to windows in buildings will continue to increase in the future. Consequently, improving the energy efficiency of windows has become a vital strategy in achieving sustainable building performance and meeting carbon neutrality goals.

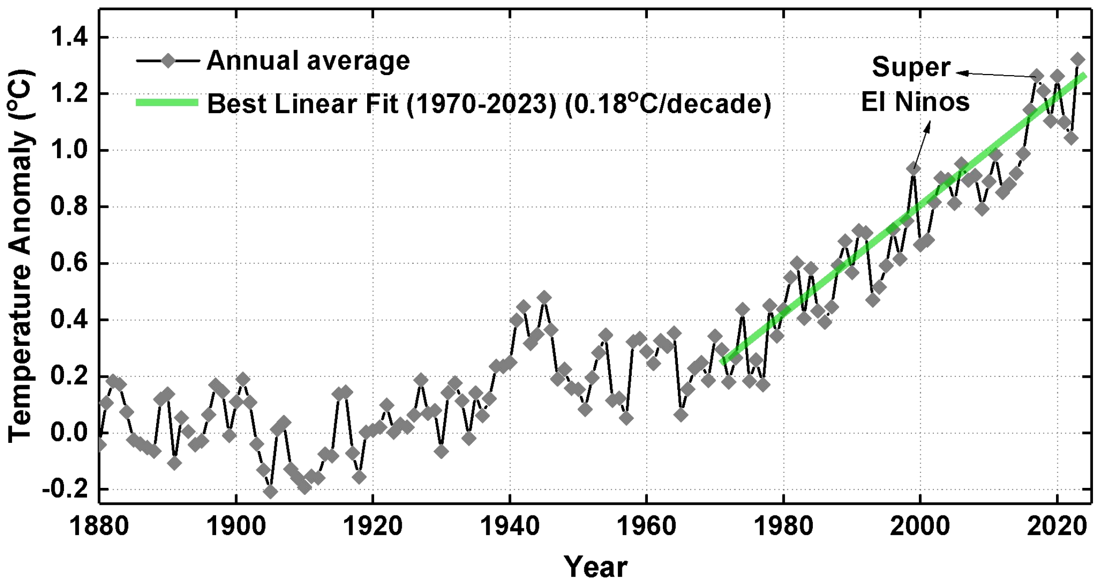

Figure 1.1 The Global Surface Temperature Relative to 1880–2023 Mean

1.2 Approaches for energy efficient windows

Windows contribute to buildings' energy loss mainly through two pathways: thermal conductive heat transfer and radiant heat transfer. Physically, the conductive heat transfer of single-layered windows is no more than 100 W/m^2, and can be further decreased below 20 W/m^2 by thermal insulation improvements. On the other hand, solar radiation transmitting windows can exceed 600 W/m^2, and its modulation in different seasons may also significantly affect the building energy use.

Corresponding to the two primary energy loss pathways of windows, energy-saving improvements are typically targeted at either reducing the overall heat transfer coefficient (**U-value**) or controlling the solar heat gain coefficient (***SHGC***).

1.2.1 Thermal insulation technologies to decrease the U value

The U-value is a comprehensive metrics of the overall heat transfer performance of window frames and glazing, it can be calculated by **Equation (1-1)**:

$$U = \frac{\sum A_g U_g + \sum A_f U_f}{A_w} \tag{1-1}$$

where A_g is the area of glazing (m^2), U_g is the heat transfer coefficient of the window's glazings (W/m^2·K), A_g is the area of frame (m^2), and U_f is the heat transfer coefficient of the window frame (W/m^2·K).

The heat transfer coefficient of glazing system or frame is determined by three aspects, namely, the convective heat transfer, the heat conduction, and thermal radiation (**Figure 1.2**). The U value of glazing system or frame can be calculated by **Equation (1-2)**:

$$U_{g(f)} = \frac{1}{\sum_{i=1}^{n} \frac{d_i}{\lambda_i} + \frac{1}{h_{in}} + \frac{1}{h_{out}} + \frac{1}{h_{r,in}} + \frac{1}{h_{r,out}}} \tag{1-2}$$

Where d_i denotes the thickness of the i^{th} layer of glazing or frame, λ_i is the thermal conductivity, and h_{in} and h_{out} are the convection heat transfer coefficient of the inner and outer glazing pane, $h_{r,in}$ and $h_{r,out}$ are the radiation heat transfer coefficient of the windows to indoor and outdoor environments.

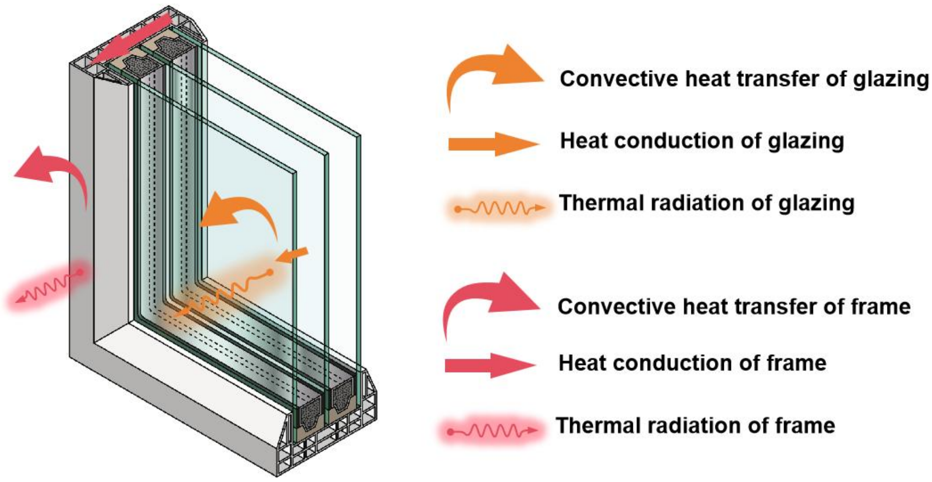

Figure 1.2 Schematic diagram of the multi-pane hollow window

Therefore, the design principles for a low U-value is to enhance the thermal insulation of window frames and glazing materials by insulate the heat convection/conduction and radiation.

1.2.2 Spectrally selective technologies to regulation the SHGC

Sunlight consists of a multi-frequency composite spectrum, which includes ultraviolet, visible light, and near-infrared radiation. When sunlight passes through a window, it introduces coupled light and heat into the indoor environment. Buildings require daylighting throughout the year, but their heating needs vary between winter and summer seasons. Spectrally selective technologies are effective solutions for blocking thermal radiation heat transfer whilst enabling daylighting. From the building application perspective, both visible transmittance and **SHGC** should be considered in the design and application process of windows, for reasonable daylighting and energy-saving. Therefore, the design principles for a spectrally selective window aim to achieve a high visible transmittance whilst blocking the solar NIR.

In the past decades, both static and dynamic windows have been developed to regulate indoor solar heat. Static windows have fixed optical performance; they can passively reject the NIR whilst enabling a high level of luminous transmittance, which is highly promising for hot regions. Dynamic windows, featuring tunable optical properties, can adapt to both hot and cold conditions. In the following content, both static and dynamic windows will be introduced.

1.3 Current development of energy efficient windows

In the early stages, windows were primarily designed to fulfill the lighting and ventilation needs of residents. However, the inherent materials used in windows contribute significantly to energy loss, which ultimately undermines the overall energy efficiency of buildings [5]. Recognizing this issue, there has been a rapid advancement in construction techniques and a growing awareness of the energy crisis, leading to the demand for specific requirements regarding window size, structural design, and thermal insulation performance. As a response to these challenges, energy-saving technologies such as double-glazed windows, vacuum glazing, and low-emissivity (low-e) glazing have emerged, and these technologies greatly enhanced the thermal insulation performances of windows.

In the 21st century, glazing facades with a large window-to-wall ratio became popular as a fashionable trend in architectural design. However, this aesthetic choice presented challenges in controlling solar heat gain, leading to extensive developments in shading technologies. Consequently, spectrally selective windows, including both static glazings and dynamic glazings, were developed to effectively regulate indoor solar heat gain. This represents a significant shift towards ultra-low energy consumption windows, addressing the demand for energy-efficient solutions in buildings.

Overviewing the developments in the past century, it can be concluded that energy-efficient window technologies have experienced three distinct stages from thermal insulation to solar spectral regulation.

(1) Thermal insulation

A low U-value is always desirable for buildings in all seasons, to reduce both the space cooling and heating load. Thermal insulation improvements, including vacuum windows [6], aerogel [7, 8] and liquid filled windows [9-11], can effectively decrease the U value of window to 1 W/(m^2K). Further integrating the low-emissivity features in multi-layered windows to insulate the long-wave thermal radiation heat transfer would further decrease the U-value to be lower than 0.5 W/(m^2K). Due to the superior thermal insulation performance and mature production processes, the multi-layered thermal insulation windows with low-e coatings have already been commercially available, and they are widely sort after for cold regions with extremely low outdoor temperature, to reduce the building space heating load [12].

(2) Solar regulation

For hot regions, since the main challenge is maintaining lower indoor temperatures, the reduction on windows' **SHGC** is generally given higher priority than decreasing the U-value. For a south-facing window, the solar radiation transmitting windows can easily exceed 600 W/m^2, and its modulation in different seasons will significantly affect the building energy use.

Spectrally selective glazing represents a key technological advancement for the next-generation buildings as it allows for the regulation of the **SHGC** value while maintaining the interior visual quality. Thus, related research works, including both static and dynamic spectrally selective windows, have been reported extensively.

Static window achieves solar regulating through the inherent near-infrared (NIR) reflecting or NIR absorbing properties (**Figure 1.3**) **[13]** of optical materials. Commercially available low-e coating is a typical NIR reflecting technology that can achieve high luminous transmittance and low SHGC simultaneously. The low-e glazing made from *Pilkington/Nippon Sheet Glass Co., Ltd.* can ensure a lower SHGC than 0.3 whilst maintaining a luminous transmittance above 0.5. However, it has been found that the NIR-reflecting design has induced unexpected side-effects, such as light pollution and high condensation risks **[14]**. NIR absorbing materials, including transition metallic ions and nanoparticles, can overcome the shortcomings of low-e coatings. Ion-based glazing and nanoparticle-based glazing represent two representative NIR absorbing material, and they have been demonstrated to have lower solar transmittance than most of the low-e glazing. However, since the NIR absorbing windows would passively reject solar energy in the whole year round, that may negatively affect indoor thermal comfort in cold seasons.

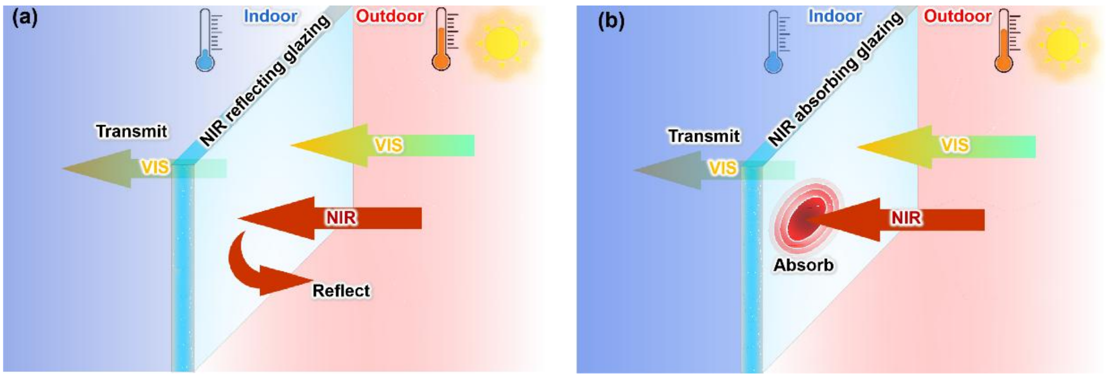

Figure 1.3 Schematic diagrams of the (a) NIR reflecting glazing, (b) NIR absorbing glazing [13].

Dynamic windows, including thermochromic **[15]**, electrochromic **[16]**, photochromic **[17]**, and mechanochromic **[18]** glazings, can intelligently regulate indoor solar irradiation via modulating windows' optical properties, and the related smart window technologies have been remarkably improved in the past decades, but there still exist serious challenges that are related to the irreversible reactions, high cost, high haze rates and narrow color gamut of the dynamic window devices. In addition, different dynamic windows are subject to the inherent defects of chromic materials. To be specific, VO_2-based smart windows exhibit poor color rendering performance and photo-biological effects in both hot and cold states [19]. Hydrogel-based windows show undesired high haze rate and low luminous transmittance in hot state [20]. Chromic material-based electrochromic devices, such as the WO_3- and V_2O_5- based products are unable to provide full control of the visible band, resulting in a narrow color gamut [21] and poor solar modulation ability. Currently, although great progress has been achieved in smart windows, neither thermochromic nor electrochromic smart windows are ready to be put into large-scale residential use in this stage.

1.4 Organization of the thesis

To improve the energy efficiency of building windows, this thesis addresses two core scientific challenges: (1) decoupling light and heat in solar radiation, and (2) achieving on-demand modulation of the windows' optical properties. The thesis consists of eight chapters dedicated to the research and development of spectral regulation strategies in liquid-filled windows, aiming to advance window technologies that combine high optical performance with effective solar radiation management.

Chapter 2 will provide a comprehensive review of the state-of-the-art developments in spectrally selective window technologies, including NIR-reflecting, NIR-absorbing, and optically tunable dynamic window systems. Following the literature review, the research gaps, objectives, and methodology will be outlined in this chapter.

Chapter 3 will introduce a set of metrics for spectrally selective windows. Based on these metrics, it will conduct an analysis of relevant data reported in the existing literature to compare the light-heat decoupling characteristics of current spectrally selective materials. To achieve precise solar spectral regulation, the chapter will further explore novel, stable, and high-performance materials beyond current systems. It will discuss the design principles and strategies for optimizing their optical properties, laying the foundation for the development of energy-efficient windows with precise spectral regulation, as detailed in the following chapters.

Chapter 4 will design a static spectrally selective window based on the spectrally selective material developed in Chapter 3. A mathematical model will be established to analyze the window's optical and thermal properties, and its accuracy will be validated through experimental testing. The model will subsequently be used to evaluate the energy-saving performance of the triple-layered LFW under Hong Kong's climatic conditions.

Chapter 5 will further develop a thermal-responsive dynamic window based on the thermodynamics of ammonia solution and the spectral regulation of the material developed in Chapter 3. A cyclic test and durability demonstration will be conducted to evaluate the feasibility of the new device. An outdoor experimental demonstration of the new window will be performed using two hot chambers. Meanwhile, the energy-saving potential of the new dynamic window will be assessed using building simulation tools (EnergyPlus), and the results will demonstrate that the window will be highly promising for building applications in both hot and cold regions.

Chapter 6 will introduce a novel actively switchable window for solar regulation in buildings. Optical switching will be achieved through gravity-induced flow behavior of the two immiscible liquids. The optical properties of the smart window will be thoroughly characterized in this chapter. Outdoor validation experiments will be to confirm its practical energy-saving potential. Additionally, energy consumption simulations using meteorological data from various climate zones and cities will be conducted to demonstrate the energy-saving performance of the bi-static window under different climatic conditions.

Chapter 7 will further enhance the bi-static window developed in Chapter 6 by incorporating a Janus structure, aiming to address the issue of secondary thermal radiation from windows to indoor spaces and to improve sky radiative cooling performance during summer. Material simulations and characterization will be conducted for both the PDMS and AgNW layers. The optical performance of the Janus bi-static window will be comprehensively analyzed, and key parameters will be used to demonstrate its superior performance compared to state-of-the-art smart window technologies. Experimental testing of the novel Janus bi-static window will be carried out in Hong Kong to validate its real-world feasibility.

Finally, **Chapter 8** will present the conclusions on the main findings and contributions of this research. It will also outline the prospects and recommendations for future work.

This work begins with the design of spectrally selective materials and systematically builds an integrated multi-functional smart window system capable of dynamic regulation across visible, near infrared, and mid-infrared bands. Through modeling and field testing, the energy-saving performance of these windows will be thoroughly evaluated across various climate zones. The findings may provide some technical support for advancing green and sustainable development of buildings.

Chapter 2 Literature Review

Spectral regulation offers a promising pathway for enhancing windows' energy-saving performance. This study focuses on the investigation of the spectral regulation of spectrally selective windows. Before defining the specific research scope of this work, a comprehensive literature review need to be conducted to analyze the current state of relevant technologies, identify existing research gaps, and clarify the objectives of this study. The structure of this chapter is organized as follows: Section 2.1 presents a comprehensive review of current spectral regulation technologies for windows, with a detailed examination of spectrally selective reflecting technologies, spectrally selective absorbing technologies, and dynamic smart window technologies. Section 2.2 provides a critical analysis of the existing literature, to identify key research gaps. Based on these findings, Section 2.3 outlines the specific research objectives and scope of this study. Finally, Section 2.4 outlines the technical roadmap underpinning the research conducted in this study.

2.1 Development of spectral regulation technologies

In the past decades, spectrally selective windows, such as NIR reflecting windows, NIR absorbing windows, and various dynamic smart windows, have been widely studied, developed, and applied in different climatic conditions for building energy-saving purposes. One major pathway of spectrally selective glazings to achieve energy savings is through solar radiation control, either by NIR reflection or absorption. This chapter provides a categorized review and analysis of spectral regulation technologies based on their functional classifications. The discussion is divided into three main sections: static spectrally selective reflection technologies (section 2.1.1), static spectrally selective absorption technologies (section 2.1.2), and dynamic spectral regulation technologies (section 2.1.3). Each section offers a comprehensive review, covering the optical regulation mechanisms, spectral selectivity performance, and current application status.

2.1.1 NIR reflecting glazings

Low-e glazing is a typical NIR reflecting technology for energy-efficient windows.

Low-e coating is a fairly mature technique that has a history of more than 40 years [12, 22]. According to the production process, low-e coatings can be classified into two categories: hard coatings and soft coatings.

2.1.1.1 Categories of low-e glazings

(1) Hard coating

The first engineering demonstration of low-e glazing was conducted in 1978, in America by the Interqane. After that, the low-e coating technologies then occupied the energy saving glasses market, and currently have commanded a market share of more than 50%. Early stage (around 1980s) low-e glazings were predominantly based on hard coatings, also known as pyrolytic or on-line coatings. These coatings involve applying doped metal oxides, such as indium doped tin oxide (ITO) and fluorine doped tin oxide (FTO) [23, 24], to the glazing surface, typically through a chemical vapor deposition (CVD) process. Hard coatings offer good resistance to chemical and mechanical wear compared to other types of materials. However, their performance in terms of reflecting solar NIR energy and long-wave radiation is relatively inferior.

(2) Soft coating

Soft coatings, also known as metal-based multilayer coatings, are applied to hardened glass surfaces. Typically, this involves high-rate magnetron sputtering, depositing layers of at least one conductive metal with a thickness of approximately 10 nm. Silver is the most commonly used metal due to its excellent optical properties, particularly its high transmittance in the visible (VIS) spectrum. Copper and gold [25] are also potential candidates, but they exhibit undesirable absorption of short-wavelength light below 0.5 μm, which limits their effectiveness. In actual application of the soft low-e coating, due to the poor weathering assessment of metal layer, they are sandwiched between optically transparent dielectric layers, which can be made of various metal oxides such as zinc, tin, bismuth, or titanium.

2.1.1.2 Application of low-e windows

Currently, the majority of commercial low-e glazing products are silver-based, with over 90% of low-e glass on the market utilizing silver coatings. And the technical reports have demonstrated that the triple-layered silver coating can decrease the ***SHGC*** to 0.3 whilst maintaining a good luminous transmittance **[12, 26]**.

However, silver possesses a high complex refractive index in the VIS spectrum, leading to significant visible reflectance. To address this issue, additional high-refractive-index buffer layers are typically deposited above the silver layer to reduce visible reflectivity **[28]**, which substantially increases manufacturing costs. Furthermore, due to the high chemical reactivity of elemental silver, it is susceptible to oxidation and degradation, thereby requiring protective layers to prevent corrosion and enhance durability **[27]**. Additionally, the coated layers often exhibit insufficient mechanical strength and poor scratch resistance, limiting their application primarily to the cavity-facing surfaces of multi-pane glazing systems. In addition, it should be noted that most low-e coatings may have a strong solar NIR reflection (about 50%), which is not beneficial to winter situations **[29]**. It has been also found that the reflected solar heat may contribute to urban heat island effects **[30, 31]** and the reflective heat-induced degradation of surrounding building structures **[32]**. Additionally, the low-e windows have been also associated with relatively higher condensation risks, especially in the single-pane sector **[14]**.

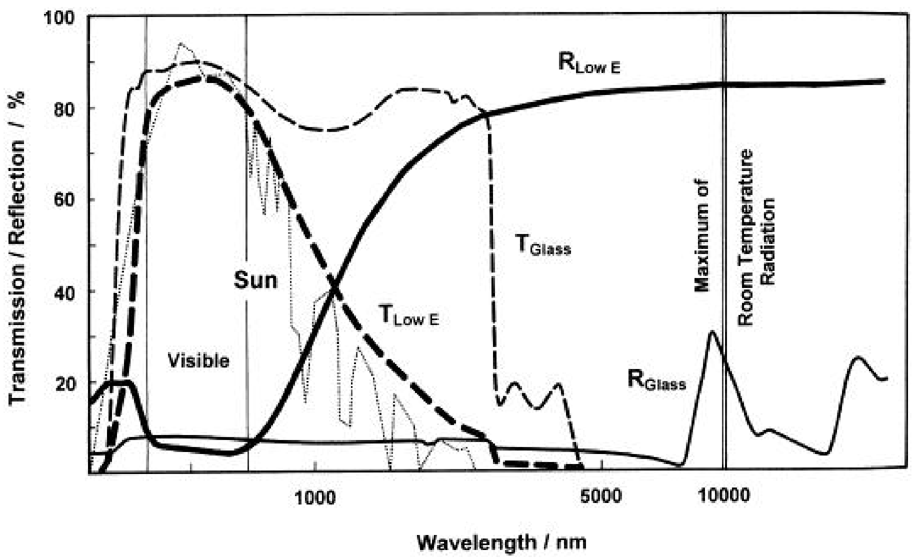

Figure 2.1 Optical properties of a silver-based low emissivity glazing **[27]**

2.1.2 NIR absorbing glazings

NIR absorbing glazings selectively absorb the NIR through photo-thermal conversion of optical materials, such as the transition metallic ions [33], and nanoparticles/composites [34-37], can overcome some shortcomings of low-e glazings (i.e. condensation risks and VIS reflection). Well-designed multi-pane structures combined with low-e coatings may manage the thermal emission flowing directions of the absorbed free solar energy, depending on seasons [38]. Thus, there is a high incentive to design the next generation of buildings with advanced NIR absorbing glazings and innovative window structures, to rationally utilize the free source of solar thermal energy. In the past decades, ***NIR*** absorbing glazing technologies have experienced extreme growth, both in the development of new theoretical models and the application of new techniques

2.1.2.1 Ion-based NIR absorbing glazings

Among the NIR absorbing glazings, ion-based NIR absorbing glazing is a technique that has been manufactured on an industrialized scale. The spectrally selective feature of ion-based glazing is built upon transition metallic ions and VIA (representing S, Se, and Te) ions [13]. **Figure 2.2** clarifies the commonly used elements. Among them, the transition metallic ions are most extensively employed because their spectrum absorption matches the solar power of VIS and NIR bands.

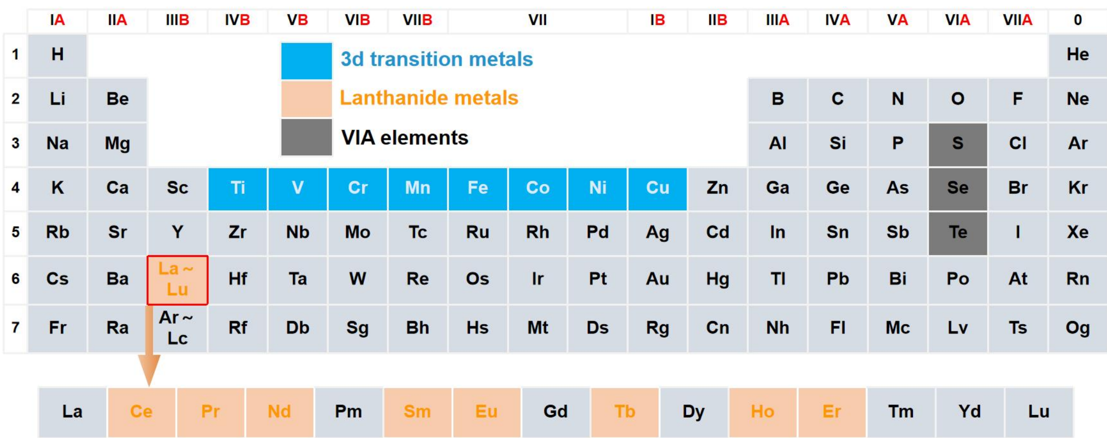

Figure 2.2 Typical glazing dopants in the periodic table

(1) Fundamental physics of spectral regulation

The light absorption of ion-based spectrally selective glazing is caused by the ***d-d*** electrons transition of transition metallic ions, and the fundamental physics was explained by Bates [39] and Kumar [40] in 1959, using the Ligand Field Theory. For transition metallic ions, the light absorption is caused by the ***d-d*** electrons transition of transition metallic ions. There are five degenerate ***d*** orbitals, three lie in-between the axes, and are denoted as d_{xy}, d_{xz}, d_{yz}, the other two lies in the axes and are denoted as d_{z2} and $d_{x2\text{-}y2}$, as illustrated in Figure 2.3 (a). In glazing medium, the transition metallic ions exist as octahedral complexes or tetrahedral complexes. When the ions exist in the octahedral complexes, six O^{2-} occupied the vertex of the ***x***, ***y***, and ***z*** axes, destabilizing the d_{z2} and $d_{x2\text{-}y2}$ more than the d_{xy}, d_{xz}, d_{yz} orbitals. Then the energy level of d_{z2} and $d_{x2\text{-}y2}$ would be higher than d_{xy}, d_{xz}, d_{yz} orbitals, and the energy difference is denoted as Δ_o, as depicted in Figure 2.3 (b). While if the metallic ions form tetrahedral complexes, the charge force of O^{2-} destabilizes the d_{xy}, d_{xz}, d_{yz} orbitals more than the d_{z2} and $d_{x2\text{-}y2}$ orbitals, cause splitting energy of Δ_t.

(2) Optical regulation strategies

Overviewing the fundamental research conducted on the optical properties of ions, it can be concluded that the optical regulations are achieved from three aspects: materials, ions' valence state, and the structure of the ligands.

Ions' materials: Theoretically, the splitting energy of the metallic ions increases going from 3***d*** to 4***d*** to 5***d*** transition metallic elements. The transition metal ions in the third period of the periodic table have the lowest Δ_o that matches the typical solar power in the VIS and NIR band, thus they drew the most attention in energy-saving glazing [13]. The lanthanide metals have the splitting energy responsible for UV and blue light but are incompetent in NIR absorbing, thus they are rarely used in buildings. Figure 2.3 (c) to (h) depict absorption performances of six kinds of representative transition metallic ions. Contrastively, iron ions are most promising for energy-saving applications, for their expanded and broadened absorption in the NIR band, but with few influences on VIS.

Valence states: A higher valence state of ions would result in higher splitting energy and thus shift absorption towards the UV band [41-43]. The valence states of metallic ions can be controlled by modifying the oxidizing or reducing atmosphere during the glass formation process. Introducing an oxidizing atmosphere in the formation of float glazing would convert Fe^{2+} to Fe^{3+}, thus shifting the absorption from the NIR to the UV band, resulting in less NIR absorbing performance and exhibiting yellow or green color. The Ti^{3+} exhibits absorption in the blue light band, while Ti^{4+} is in the UV band. Introducing the reducing atmosphere into a titanium-doped glass would increase the proportion of Ti^{3+}, converting the clear glass into yellow color.

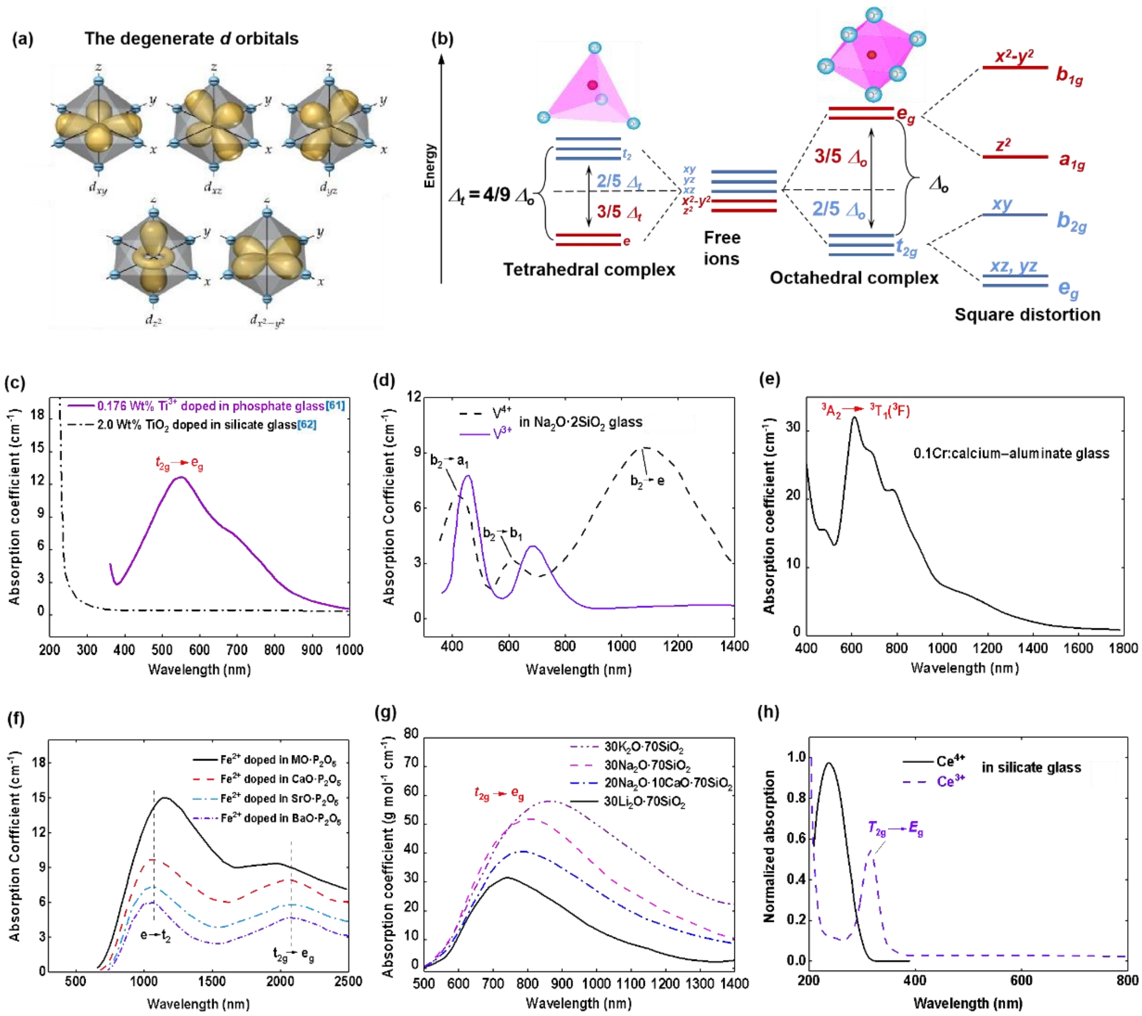

Figure 2.3 Scheme illustration of **(a)** the five 3d orbitals, **(b)** the splitting of 3***d*** orbitals in octahedral complex and tetrahedral complex; **(c)-(h)** Spectral absorption of Titanium ions [47, 48], Vanadium ions [46], Chromium ions [49], iron ions [13], copper ions [50], Cerium ions doped glass.

Structure of ligands: The splitting energy of different structured ligands is different. As predicted by the point of charge model, in the tetrahedral complex, the splitting energy equals 4/9 of that in the octahedral complex. Controlling the component of the glass medium can regulate the structure of ligands. For example, using phosphate glass as a host medium, the tetrahedral complexes of Co^{2+} would partly be converted into octahedral complexes, thus causing the blue shift of the absorption peak **[44]**. In addition, it should be noted that in some special glass mediums, the tetrahedral or octahedral complexes may be distorted by asymmetrical electronic power and then will further be split into several energy levels **[45]**. For example, in silicate glazing, square distortion of the octahedral complexes of [VO_6], leads to three absorption peaks corresponding to $\boldsymbol{b_2}$ to $\boldsymbol{a_1}$, $\boldsymbol{b_2}$ to $\boldsymbol{b_1}$, and $\boldsymbol{b_2}$ to $\boldsymbol{e}$ transition, as shown in **Figure 2.3 (d) [46]**.

(3) Categories and performance assessment

Overviewing the literatureS and patents published in the past decades **[51-54]**, ion-based glazing, according to whether it contains iron, can be divided into two categories: (1) iron ions-based glass and (2) other ions-based glass. Iron ions have historically been employed as dopants in the energy-saving window because of their outstanding UV and NIR absorption. Other ions-based nonferrous glazing is generally used for aesthetic decoration, as they don't have much response to solar NIR.

Iron ions doped glazing: Fe^{3+} has strong absorption in the ***UV*** band, and partly absorbs the blue light, showing the glazings with blue or yellow color. Fe^{2+} has smaller $\boldsymbol{\Delta_o}$ and $\boldsymbol{\Delta_t}$ than Fe^{3+}, which corresponds to ～1000 nm and ～2000 nm respectively. Improving the Fe^{2+} to Fe^{3+} ratio can significantly improve the NIR absorption of ferrous glass. To improve the Fe^{2+} to Fe^{3+} ratio, Fu et al **[54]** introduced the reductive silicon powder, with a 1:3 molar ratio of Si/Fe^{3+} into the iron-doped fluorophosphates glass. **Figure 2.4 (a)** depicts the spectral transmittance of their tested samples. As listed in **Table 1**, the iron-doped glass fabricated by Fu et al **[54]** can reject over 50% of the solar NIR while maintaining a luminous transmittance above 70%. In this regard, the iron ion doped glass is highly promising to be used in hot zones for light/heat decoupling. Besides Fe^{x+}, other transition metallic ions, such as titanium, cesium, chromium, tin, and iron co-doped glazings can further broaden the absorption in the UV and NIR band. Figure 2.4 (b) shows the spectral transmittance of the best-recorded cases of the Fe^{x+} and other ions co-doped glazings. As seen, the spectral transmission bands are further narrowed to the VIS band, demonstrating that the Fe^{x+} and other ions co-doped glazings have better light/heat decoupling ability.

The doping of VIA *ions*, such as selenium ions, will absorb the VIS, thus darkening the glazing. Selenium mainly exists as Se_x^-, SeO_3^{2-} and SeO_4^{2-} in the glass. SeO_3^{2-} and SeO_4^{2-} are high transparency, while Se_x^- can cause three absorption peaks. The first one located in the UV band, is caused by the Se_2 dimer, and the second one at ～500 nm, is assigned to the Se^{2-} dimer, and the last one is in the red light and NIR band and is attributed to the Se^{3-} trimer [55]. The iron and selenium co-doping can significantly reduce the VIS transmittance, and change the color of glazing [56]. To enrich the color of the Se-doped glazings, selenium is usually co-doped with the cobalt ions in actual products. Cobalt, normally existing as Co^{2+} in glass, has a strong VIS absorption at about 650 nm, owing to the $^4A_2$ to $^4T_1$ electron transition in the tetrahedral crystal field [57]. Thus, the Se, Co^{2+}, and co-doped glass can exhibit blue, gray, amber, and bronze colors.

Other ions-based glass: Figure 2.4 (d) shows the spectral transmittance of the nonferrous glazings. The typical dopants for aesthetic decoration include copper, chromium, cobalt, selenium, neodymium, etc. The Cu^{2+} doped glazing adopted by Central Glass, Inc. in Japan [51] shows extraordinary NIR response between 800 to 1100 nm, owing to the ***d-d*** electron transitions of Cu^{2+}. The spectral transmittance of the products is shown in Figure 2.4 (d). However, Cu^{2+} doped glazings are not efficient in light/heat decoupling, since they cannot effectively absorb the NIR with a larger wavelength than 1100 nm [50, 58]. In addition, Cu is unsuitable to co-doped with irons, because Cu^{2+} is usually doped in an oxidizing atmosphere to convert Cu^+ into Cu^{2+}, while the Fe^{2+} glazing is usually formed in a reducing atmosphere.

Other transition metallic ions doped glazings also exhibit strong absorption in the VIS band. For example, the ZnO, Sb_2O_3, and Nd_2O_3 co-doped glass shows multi-absorption peaks in the VIS band [51] and exhibits blue or blue-violet color. Despite the colorful outlooks, however, the nonferrous glazings have little response to the UV or NIR band and are incompetent in light/heat decoupling.

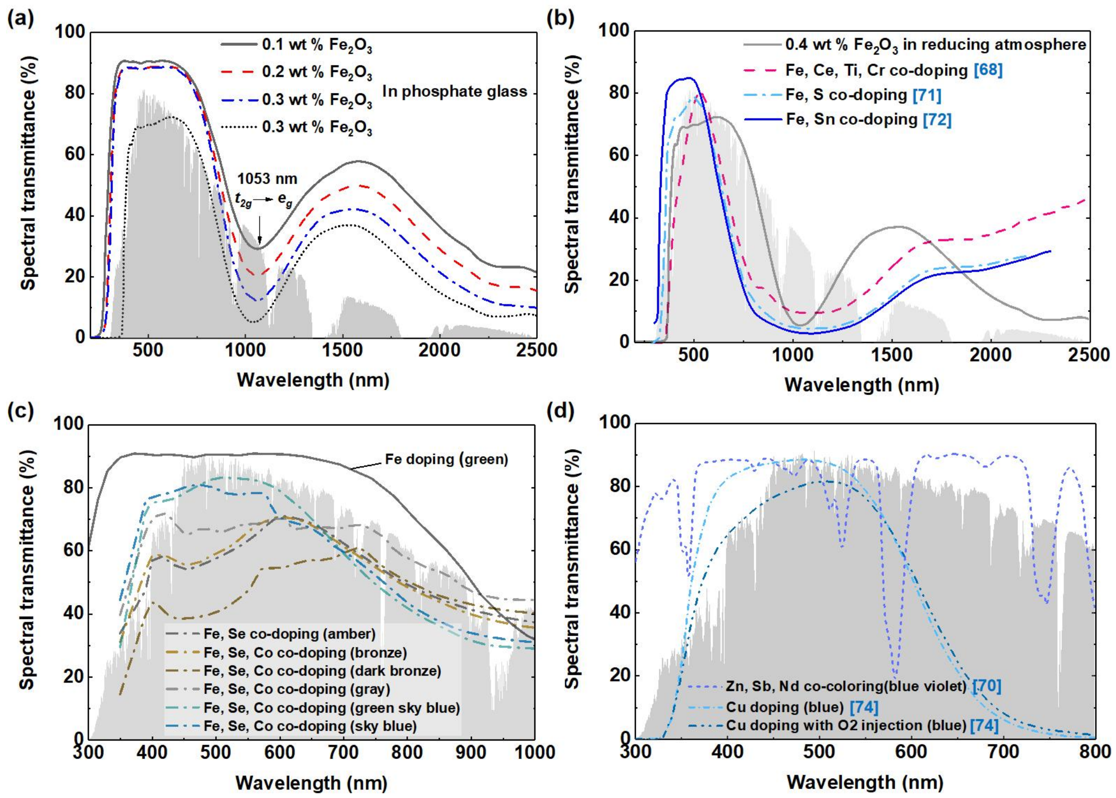

Figure 2.4 Spectral transmittance of **(a)** Fe^{2+} doped fluorophosphates glazings **[54]**; **(b)** Iron ions and other ions co-doped glazings **[53, 59, 60]**; **(c)** Iron ions and Se co-doped glazings **[56]**; **(d)** Other ions-based tinted glazings **[51]**.

2.1.2.2 Nanoparticle-based spectrally selective glazings

(1) Fundamental physics of spectral regulation

Nanostructures possess flexibly regulated optical performance, offering an opportunity for energy-saving windows to selectively absorb NIR and transmit VIS **[29]**. From the fundamental perspective, localized surface plasmon resonance (LSPR) is deemed as the major contributor to enhanced light absorption of nano-particles.

The LSPR of nanoparticles is essentially the energy propagation process between incident light and plasmons. The incident light with similar frequencies to the surface plasmons (SPs) will excite the nanoparticles' SPs **[61-63]**. The excited SPs absorb the photon energy from incident light through Landau damping, and then convert the photon energy into thermal energy within 1 ns [64-67], as illustrated in Figure 2.5 (c).

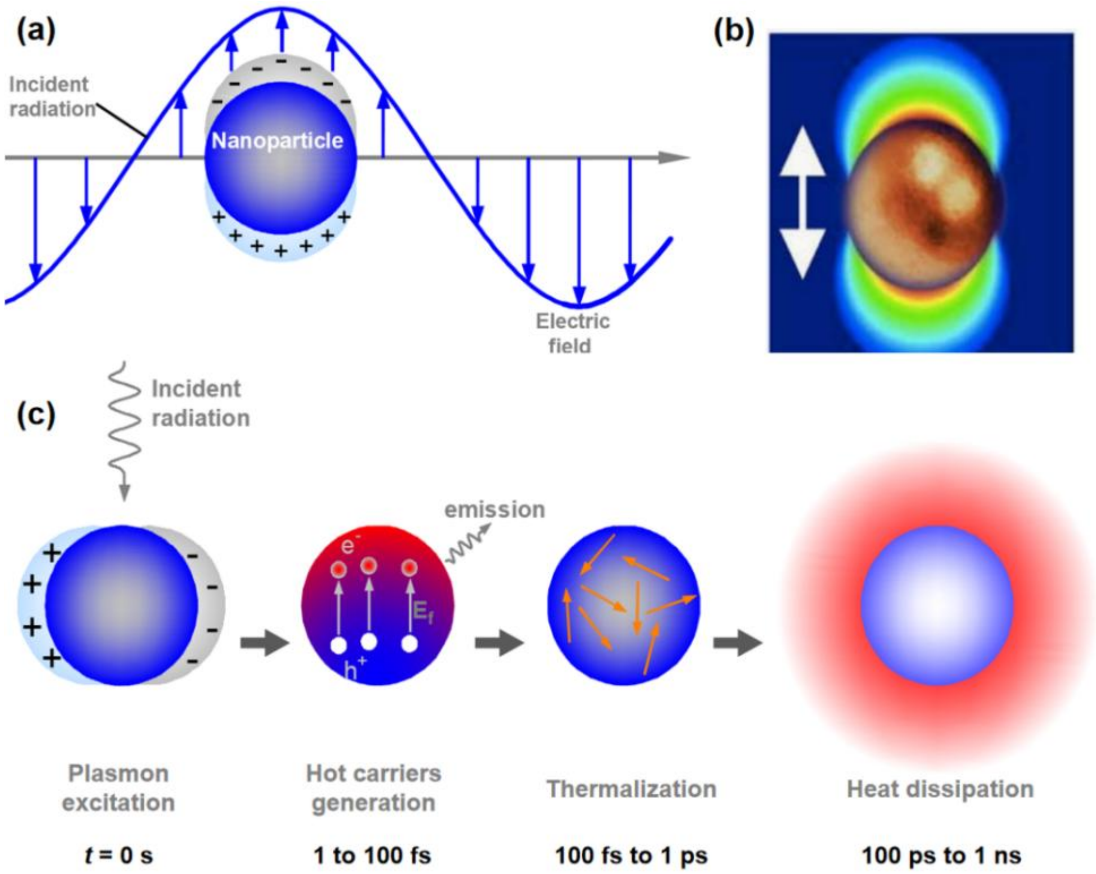

Figure 2.5 (a) schematic illustration of the LSPR, (b) Electric field distributions around an excited nanoparticle, and (c) schematic illustration of the photon energy thermalization process.

(2) Categories

The frequencies of LSPR determine the optical properties of nanoparticles. When used for energy-efficient glazings, nanoparticles with LSPR frequency matching the typical solar power in the VIS and NIR band are competent. The nanomaterials used in windows glazings include four categories:

1) Metallic nanocomposites;
2) iron-oxide nanoparticle-based films;
3) transparent conductive metallic oxide (TCO) nanoparticle-based films;

4) alkali-doped tungsten oxide (M_xWO_3) nanoparticle-based films.

(3) Optical regulation strategies

1) Metallic nanocomposites

The optical properties of noble metal-glazing nanocomposites can be regulated four main aspects: Particle size, Particle geometry, Particle arrangement, and Host medium.

Particle size: As shown in **Figure 2.6 (a)** and **(b)**, for the metallic nanoparticles with sufficiently small size (e.g. smaller than 8.5 nm), the absorption peaks decrease with the decrease of particle size **[68, 69]** owing to the smaller particle size than the mean free path length of the electrons. However, for the metallic particles with a larger diameter (e.g. more than 20 nm), Zhang et al. **[70]** reported that the increased particle size would result in smaller absorption peaks and a red shift of the absorption band (as shown in **Figure 2.6c**), which is considered to be caused by the larger specific surface area of particles and the lower oscillation frequency of SPs **[71, 72]**. For spherical nanoparticles with different sizes, the absorption peaks are tunable at 380 to 480 nm for Ag nanocomposites **[69, 70]**, at 500 to 550 nm for Au nanocomposites **[68]**, and at 550 nm to 590 nm for Cu nanocomposites **[73]**. The particle size regulation may enhance the VIS absorption, but cannot gift the spherical metallic nanoparticles-based glazings with NIR absorption ability **[74]**.

Host medium: Zhang et al. **[70]** concluded that the absorption peaks of Ag-based nanocomposites increased linearly with the increase of the refractive index of the host medium. For example, with the refractive index of the host medium increasing from 1 to 2, the absorption peaks of Ag nanoparticles moved from 360 nm to 510 nm, as shown in **Figure 2.6d**. A similar conclusion has also been supported by Lee et al. **[71]**. However, for the transparent solid host medium, the refractive indexes are generally fixed at about 1.5. The change of host medium is not a viable option for regulating the optical performance of glazings.

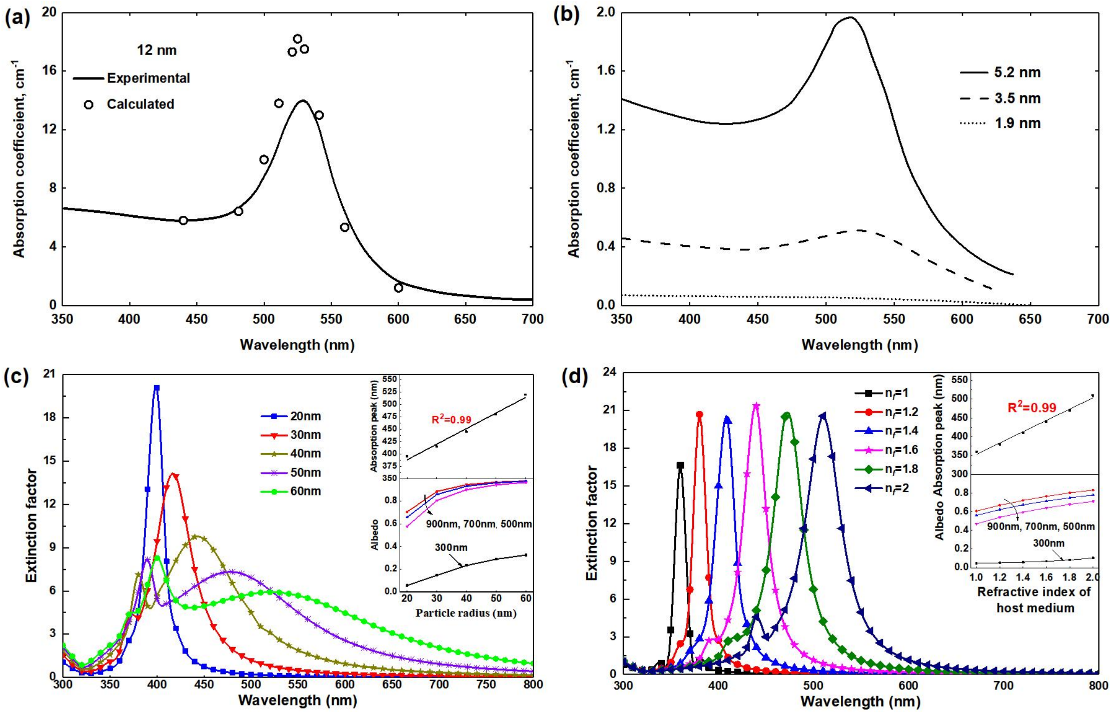

Figure 2.6 (a) Absorption spectrum of Au nanoparticles with a diameter of 12 nm in silicate glazing [68]; **(b)** Absorption spectrum of Au nanoparticles of different diameters [68]; **(c)** Extinction factors of Ag nanoparticles of different diameters [70]; **(d)** Extinction factors of Ag nanoparticles in different host medium [70].

Particle arrangement: If the nanoparticles are closely connected, their surface EM fields are spatially coupled, and this was demonstrated to enhance the surface plasmon resonances [75-78], and thus change the optical properties. A rational designation of arrangement may enhance and broaden the absorption of nanoparticles. Guo et al. [78] designed films with worm-like assemblies of noble metallic nanoparticles and can expand the absorption band to 500 to 900 nm, as shown in Figure 2.7. However, it should be noted that the reported cases with designed arrangements of metallic nanoparticles have little NIR absorption, thus they are incompetent to replace the traditional Low-E glass or ion-based glazings for energy-saving use.

Particle geometry: Non-spherical nanoparticles usually have multiple absorption peaks, owing to different resonance frequencies of plasma on different surfaces caused by the asymmetry of geometric structure. Among the non-spherical nanostructures, nanorods and nanoellipsoids are demonstrated to be highly promising to be used in light/heat decoupling [79]. The nanorods or nanoellipsoids have two absorption peaks, where one is caused by the transverse plasmon resonances, located in the short wavelength range, and another one is induced by the longitudinal plasmon resonances, locates in the long wavelength range [80], and can be linearly adjusted by changing the aspect ratio [81]. Silver nanorods (AgNRs) [79] with a smaller diameter than 30 nm and an aspect ratio between 3 to 10 are highly promising for making energy-saving windows. With a thickness of 10 mm and mass concentration of 5 ppm, the blended AgNR/PMMA nanocomposites were demonstrated to have a higher luminous transmittance than 50%, whilst blocking the solar radiation by about 80%. However, the fabrication of AgNRs remains an issue. The reported methods are difficult to precisely control the particle size below 30 nm, and the length of the AgNRs below 10. Long silver nanorods, known as silver nanowires (AgNWs), are more widely used than short nanorods [83-85]. Although the LSPR of AgNWs arose little NIR absorption, the densely interleaved AgNWs can scatter the NIR by light interference [86]. Lin et al. [87] developed the AgNWs/polyvinyl butyral (AgNWs/PVB) glass coatings to isolate infrared radiation heat transfer. Figure 2.8 exhibits the optical performance of the AgNWs-coated glass. As shown, the AgNWs lowered the MIR emissivity by 30% than the clear glass, whilst maintaining the luminous transmittance above 80%. In addition, AgNWs-based coatings can be fabricated through the spray method, making them flexible to upgrade the existing clear glazings.

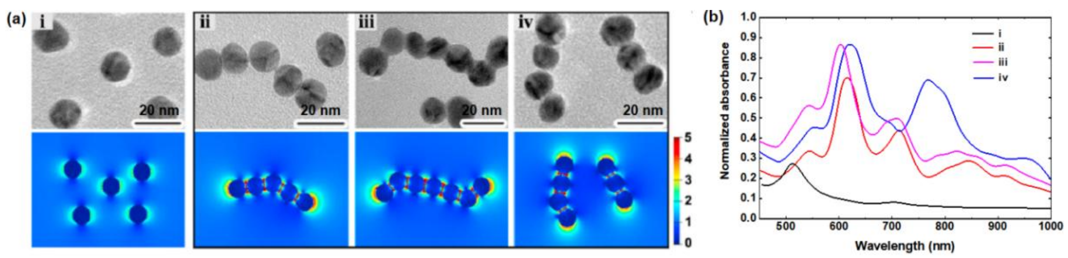

Figure 2.7 (a) ***TEM*** images and the corresponding electric field distributions of four kinds of worm-like assemblies of metal nanoparticles [78]; **(b)** Normalized absorbance of these four samples [78].

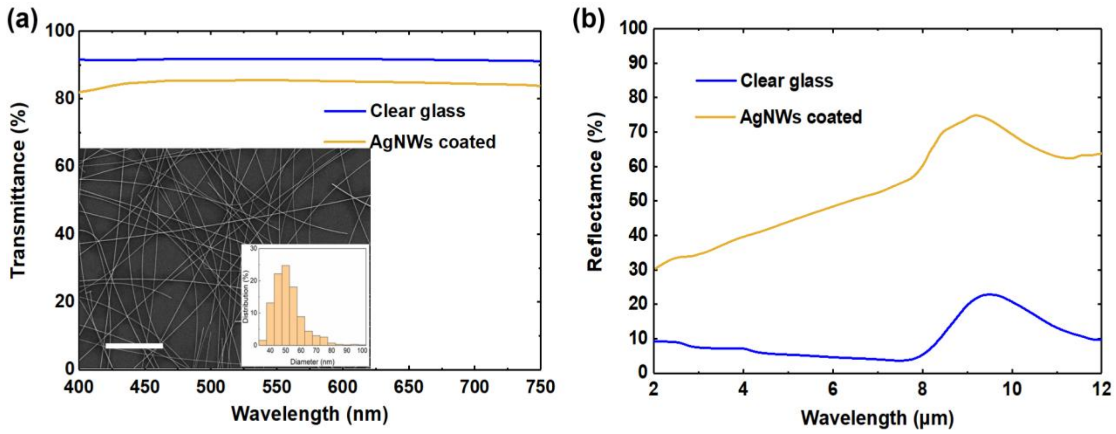

Figure 2.8 **(a)** spectral transmittance in the visible band; **(b)** spectral reflectance of the Mid-infrared band **[87]**.

Orientation of particles: The oriented nanorods (nanoellipsoids) can be formed by stretching glass nanocomposites, mainly through two approaches: force stretching **[88]** and high temperature stretching **[89, 90]**. These two techniques can precisely control the aspect ratio of the nanorods or nanoellipsoids, gifting the glazings with controllable optical polarization properties. The glazings made of oriented nanorods (nanoellipsoids) nanocomposites have been widely used in the field of optics. However, they have yet to be used for architectural windows, a major reason is their unstable color appearance changes with the incident light angles.

2) Iron-oxide nanocomposites

Fe_3O_4 is a typical magnetic material, and Fe_3O_4 nanoparticles display paramagnetic properties. To match the solar radiation of the VIS and NIR band, the optical absorption of Fe_3O_4-based nanocomposite is primarily adjusted by two approaches:

Magnetic field to control the particle orientation: The external magnetic field forces the disordered Fe_3O_4 nanoparticles into an ordered configuration, allowing them to be used in the dynamic modulation of solar radiation **[91, 92]**. Li et al. **[92]** reported the 1D Fe_3O_4@SiO_2 nanochains and demonstrated that the light transmittance could be dynamically changed from 20% to 80% by a magnetic field of 50-100 Oe, as seen in **Figure 2.9**. The modulation ability of the Fe_3O_4@SiO_2 nanochains makes them appealing for smart windows. However, because the

$Fe_3O_4@SiO_2$ nanochains have low blue light transmittance and appear yellow or red color, they cannot provide effective color rendering performance for residential buildings.

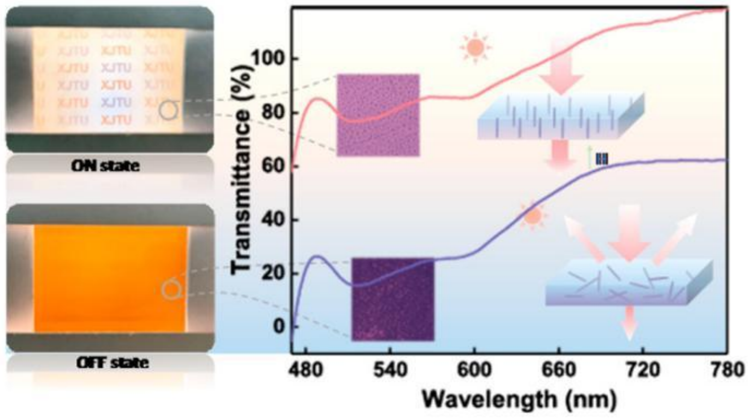

Figure 2.9 Spectral transmittance of the $Fe_3O_4@SiO_2$ nanochains [92].

As seen in **Figure 2.10 (a)**, Fe_3O_4 nanoparticles can absorb some VIS, but exhibit no NIR absorption [29]. The core-shell structure of $Fe_3O_4@Cu_{2-x}S$ can extend the LSPR to the NIR band, enabling the NIR absorption with a wavelength greater than 800 nm. Wang et al. [36, 38] designed and tested the optical transmittance of $Fe_3O_4@Cu_{2-x}S$ coated glass, as shown in **Figure 2.10b** and **c**. Their findings indicated that $Fe_3O_4@Cu_{2-x}S$ coatings have a moderate ability of light/heat decoupling and provide good color rendering capability.

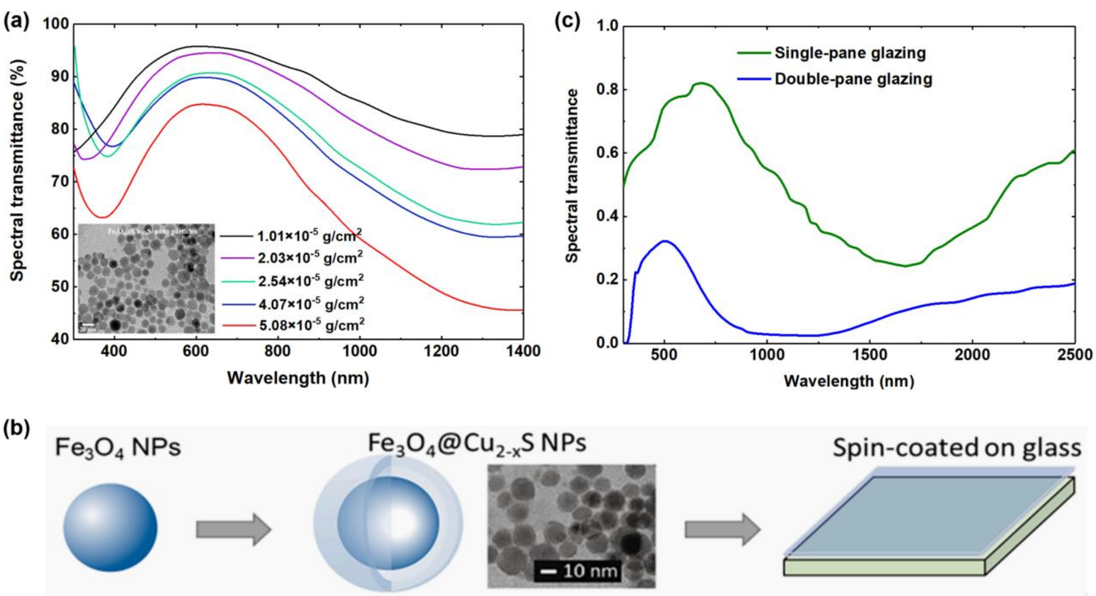

Figure 2.10 (a) Spectral absorption of the Fe_3O_4@$Cu_{2-x}S$ nanocomposite films **[29]**, (b) schematic of the Fe_3O_4@$Cu_{2-x}S$ coated glass, (c) spectral absorption of Fe_3O_4@$Cu_{2-x}S$ coated glazings **[36, 38]**.

3) Transparent Conductive Oxide (TCO) nanocomposites

The LSPR of TCO nanoparticles matches the solar spectrum between 1500 and 2500 nm and thus can potentially be used for energy-efficient glazings. The mainstream TCO materials include In_2O_3, ZnO, and SnO_2, as well as their alloy mixtures **[93]**. Among these TCO nanomaterials, ATO is the most promising in energy-saving use, due to its outstanding NIR absorbing performance and its low fabrication cost.

The optical properties of ATO nanoparticles can be regulated from two aspects: (I) to enhance the NIR absorption caused by LSPR, and (II) to avoid the VIS absorption caused by the electronic transition in the band gap **[94, 95]**. The detailed optical properties of ATO nanoparticles may be affected by:

Doping level of Sb: Pure SnO_2 lacks free carriers and shows poor NIR absorbing performance. They would partly absorb the VIS due to the electronic transition in the band gap **[96]**. When doping Sb elements into the SnO_2, on the one hand, the Sb^{5+} replaces the Sn^{4+} in the lattice, forming donor energy level, and contributing a free carrier (electron) to the conduction band, and the LSPR of the free carriers gifts the ATO nanoparticles with the NIR absorption. On the other hand, Sb^{5+} doping would widen the band gap, shifting the absorption from VIS to the UV band. However, it should be noted that the excessive doping of Sb would introduce Sb^{3+}, which would replace the Sn^{4+} to form the acceptor levels, canceling the function of Sb^{5+}. Therefore, there is a critical doping level of Sb that maximizes the function of ATO. Rahal et al. **[94]** reported a critical doping level of 0.8wt%, as shown in **Figure 2.11a**. While, in an oxidizing atmosphere, the Sb^{3+} would partly be converted into Sb^{5+}, then there would be a higher critical doping level of Sb **[97-99]**. For example, Gürakar et al **[99]** reported a critical doping level of Sb of ～4wt%, as shown in **Figure 2.11b**. Generally, for Sb exposed to air, the Sb doping level of 7% to 13% is demonstrated to be the most feasible **[100, 101]**.

Annealing: The increase in annealing temperature is beneficial for Sb^{5+} to replace Sn^{4+} **[95, 102]**. Leem et al **[95]** studied the optical performance of ATO films after 30 minutes of annealing, at the temperature of 300°C to 700°C, and demonstrated that the increased annealing temperature improved the VIS transmittance, as shown in **Figure 2.11 (d)**. Such a phenomenon was attributed to the broadened bandgap caused by Sb^{5+}. However, when the annealing temperature exceeds 1000°C, Shen et al. **[96]** reported that the increase in annealing temperature will reduce the content of Sb^{5+}, and decrease the NIR absorbing ability of ATO nanoparticles. The color of ATO particles at the annealing temperatures of 600°C, 800°C, 1000°C, and 1100°C are shown in **Figure 2.11 (c)**.

Co-doping: Sole ATO-based composite films absorb the NIR between 1500 nm to 2500 nm **[103-106]**. Co-doped other NIR absorbing materials, such as ITO and YTO **[107-111]**, can broaden the NIR absorption band, increasing the light/heat decoupling ability.

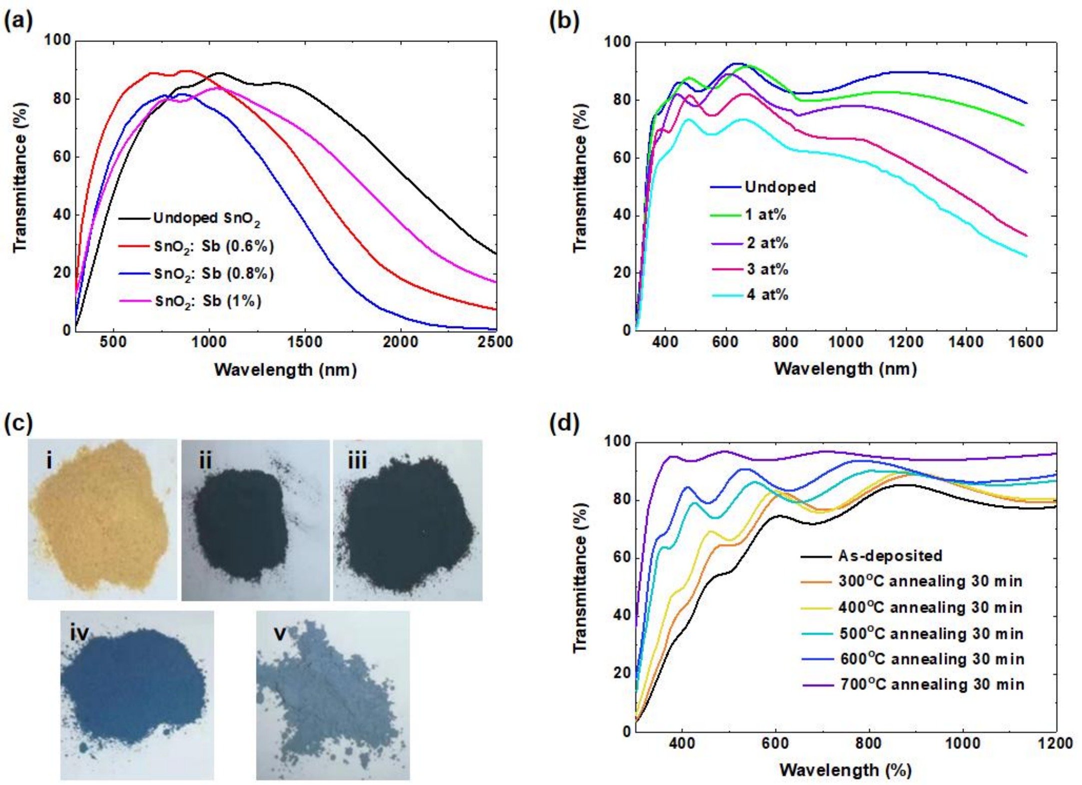

Figure 2.11 (a) Spectral transmittance of Sb (0–1 wt.%) doped SnO_2 films **[94]**; **(b)** Spectral transmittance plot of Sb (0–4 wt.%) doped SnO_2 films **[99]**; (c) The color of

ATO powder annealed at different temperature (i: before annealing, ii: 600°C, iii: 800°C, iv: 1000°C, v: 1100°C) [96]; (d) Spectral transmittance of ATO films after annealing 30 min at different temperatures [95].

4) M_xWO_3 nanocomposites

WO_3 has little response to VIS or NIR. Doping alkali metal ions, such as Li^+, Na^+, K^+, and Cs^+, provides the WO_3 with NIR absorbing ability from two approaches: (I) generating free carriers for LSPR to enable the absorption between 1100 to 2500 nm [112-115] (**Figure 2.12 a**); and (II) reducing W^{6+} to W^{5+} for the small polarons hopping to enable the absorption between 700 nm to 1100 nm [112, 114, 115] (**Figure 2.12 b**);

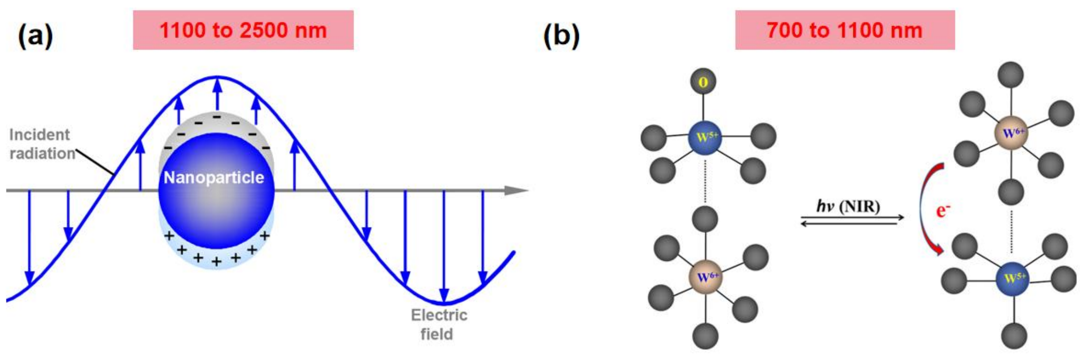

Figure 2.12 Schematic illustration of **(a)** LSPR of the free carriers, **(b)** small polarons hopping between the W^{6+} and W^{5+} [112].

The optical properties of the M_xWO_3 are determined by the LSPR and the small polarons hopping between the W^{6+} and W^{5+} and can be affected by the materials of alkali dopants and co-doping of other materials.

Material of alkali dopants: Yang et al [116, 117] fabricated the M_xWO_3-silicate glass nanocomposites by a melt-quenching method. **Figure 2.13 (a)** exhibits their optical performance. As seen, KxWO3-silicate glass does not show NIR absorbing ability. Li_xWO_3-silicate glass has the strongest NIR absorption but sacrifices too much ***VIS*** transmittance. Na_xWO_3-silicate glass is the most pragmatic, as it enabled luminous transmittance of 63.8% and only a transmittance of 7% at 1500 nm. Guo et al. [118] synthesized the $(NH_4)_xWO_3$ nanorods and made the NIR absorbing composites films based on the $(NH_4)_xWO_3$ nanorods. As seen in **Figure 2.13 (b)**, NH^{4+} doping ensured more luminous transmittance and absorbed more NIR than Na^+ or Li^+. Yao et al. [119] fabricated hexagonal Cs_xWO_3 nanoparticles with different Cs doping levels, and reported their optical performance, as shown in **Figure 2.13 (c)**. Comparing **Figure 2.13 (a)**, **(b),** and **(c)**, it could be concluded that the $Cs_{0.33}WO_3$ nanoparticles are the most promising among the M_xWO_3.

Co-doping: Co-doping other materials can increase the free carrier concentration of ***LSPR***, or affect the small polaron hopping between the W^{6+} and W^{5+}. Shen et al. [115] doped fluorine into Cs_xWO_3 nanoparticles to increase the free carrier concentration, and enhanced the absorption of NIR within the range from 1500 nm to 2500 nm, as shown in **Figure 2.13 (d)**. Zhang et al. [112] prepared Li, Cs co-doped tungsten bronze, and demonstrated that Li, Cs co-doping can increase W^{5+} content and the free carriers' concentration, thus improving the NIR absorbing ability. Liu et al. [120] doped Pt in Cs_xWO_3 to promote oxygen vacancies and W^{5+} generation, and demonstrated a higher NIR absorbing ability, as shown in **Figure 2.13 (f)**.

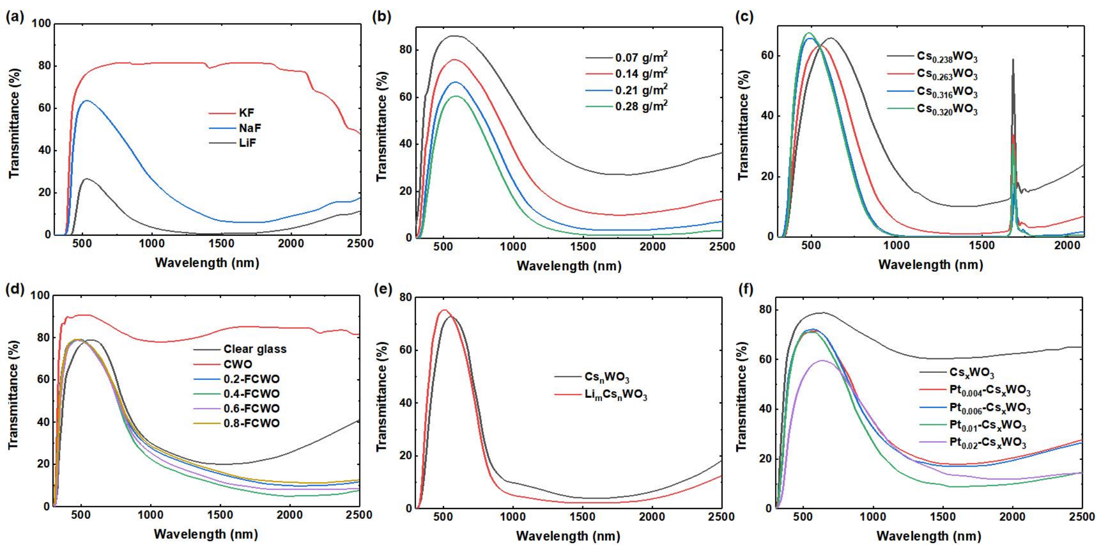

Figure 2.13 Spectral transmittance of **(a)** alkali metal tungsten bronze-doped silicate glazings [116, 117]; **(b)** films containing different densities of $(NH_4)_xWO_3$ nanorods [118]; **(c)** toluene dispersions of Cs_xWO_3 nanoparticles with different Cs doping levels [119]; **(d)** films containing F-doped Cs_xWO_3 nanoparticles with different F/W molar ratios (0.2, 0.4, 0.6 and 0.8) [115]; **(e)** films containing Li doped Cs_xWO_3

nanoparticles [112]; **(f)** films containing Pt doped Cs_xWO_3 with different Pt/W molar ratio (0.004, 0.006, 0.01, 0.02) [120].

(4) Application assessment

1) Metallic nanocomposites

Spherical metallic nanocomposites exhibit enhanced photon absorption in the visible (VIS) band; however, such glass composites are ineffective in absorbing near-infrared (NIR) radiation. In contrast, metallic nanorods or nanoellipsoids with optimized aspect ratios can efficiently absorb NIR while maintaining high luminous transmittance, making them highly promising candidates for energy-efficient glazing applications. Nevertheless, achieving low-cost and high-precision fabrication with precise geometric control over nanoparticle morphology remains a significant challenge [13].

2) Iron-oxide nanocomposites

Fe_3O_4 nanocomposites show rich magnetic and optical behaviors, making them popular in photothermal therapy [121, 122], solar energy harvesting [123, 124], and optical switchable smart windows [91, 92]. On the other hand, the Fe_3O_4–based nanocomposite films were demonstrated to have unique phenomena of heat dissipation, as revealed by Wang et al. [36] (**Figure 2.14**). Such semi-directional heat dissipation of the Fe_3O_4–based nanocomposite film can be desirable for buildings, as it can be used to strengthen the solar heat gain controls in different seasons [36, 38].

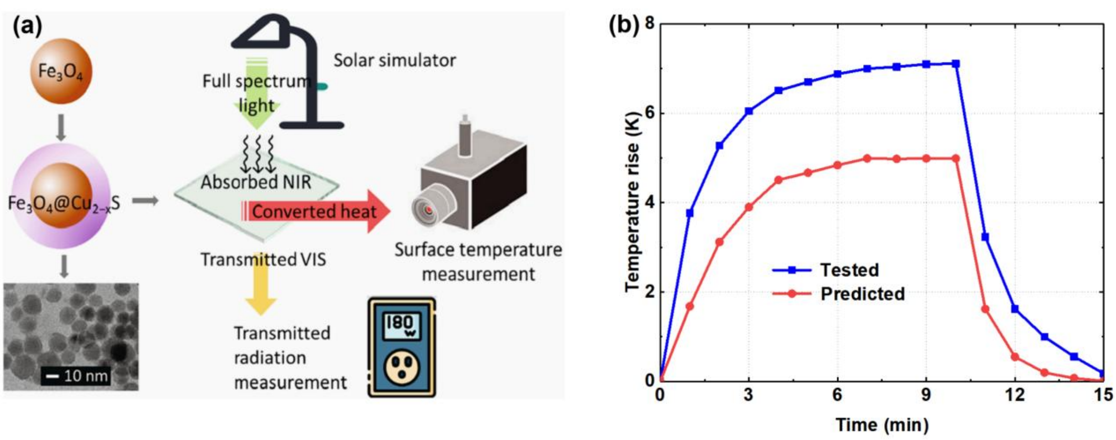

Figure 2.14 (a) Schematic of the platform to test the photothermal effects of $Fe_3O_4@Cu_{2-x}S$–coated glass; (b) tested and predicted temperature rises of the $Fe_3O_4@Cu_{2-x}S$–coated glass [36].

3) Transparent Conductive Oxide (TCO) nanoparticle-based films

ATO has a low-manufacturing cost and is expedient to form films by adding the ATO particles or ATO nanoslurry into aqueous resin to form nanocomposites [96, 103]. Besides, an obvious advantage of ATO-based nanocomposites is that ATO nanoparticles can withstand long-lasting weathering evaluation in an oxidation and humid environment [103].

4) M_xWO_3 nanoparticle-based films

M_xWO_3 combines LSPR and small polarons hopping mechanisms for NIR absorption, thereby exhibiting strong light/heat decoupling capabilities. However, its commercial application remains limited due to poor weathering resistance [114, 125, 126], as the oxidizing atmosphere easily converts the W^{5+} to W^{6+}.

2.1.3 Dynamic spectrally selective windows

Well-regulated solar radiation heat transfer could lower the buildings space cooling in summer and space heating loads in winter. In this regard, chromic-based materials, including electrochromic, thermochromic, photochromic, and mechanochromic materials, have been applied in windows. According to whether need external energy input or not, dynamic smart windows can be categorized into passive smart windows and active smart windows.

2.1.3.1 Passive smart windows

Passive smart window, include the photochromic [128], humidity-responsive smart windows [129], thermochromic (TC) [129-131], are desired in a variety of applications because they can be self-powered to trigger the color change, however, their performance are limited by the spectrally selective features of the dynamic materials. Among the passive smart window technologies, TC is the most desirable transparency switching trigger way, because it can change the optical properties in response to temperature change. VO_2 was considered to be the most promising material for the phase-change TC smart window, which can selectively regulate the NIR transmittance at a critical transition temperature of 68℃ **[15, 132]**. VO_2 exhibits a distinct thermochromic behavior due to a reversible metal-insulator transition that occurs at approximately 68℃ (341 K) **[133, 134]**. Below this critical temperature, VO_2 is in a monoclinic (M1) crystal structure and behaves as a semiconductor, characterized by low electrical conductivity and high transmittance in the infrared (IR) region. In this phase, vanadium atoms form paired chains (V-V dimers), which open an electronic bandgap and limit the movement of charge carriers. As the temperature increases beyond the transition point, VO_2 undergoes a structural transformation to a tetragonal rutile-type metallic phase. In this high-temperature phase, the V-V dimers break, the crystal lattice becomes more symmetric, and electrons become delocalized, resulting in a sharp increase in electrical conductivity and a significant reduction in IR transmittance due to free-carrier absorption **[135]**. This abrupt and reversible change in both optical and electronic properties is the underlying mechanism of VO_2's thermochromism. Such properties make VO_2 highly attractive for applications in smart windows. However, three inherent limitations are inevitable for VO_2-based smart windows, which hinders them from their commercial application: **(1)** A metal-to-insulator transition temperature at 68℃ is not suitable for building applications, otherwise, auxiliary heating agents or modifying dopants are required to trigger the NIR shielding property **[136, 137]**; **(2)** the visible transmittance and solar regulation capacity are inferior. Single layered VO_2 films generally have lower than 20% solar modulation ability (ΔT_{sol}) **[138, 139]**, and the improved ΔT_{sol} always comes with a penalty on the luminous transmittance (T_{lum}). Although some improvements in ΔT_{sol} and T_{lum} has been achieved by elements doping **[139-145]**, multi-layered **[146]**, and nanoporous structural design **[147-149]**. It is still challenging for VO_2 based smart windows to have a ΔT_{sol} above 25% whilst maintaining a T_{lum} at 50%; and **(3)** the VO_2 films almost filtered the blue light with wavelength smaller than 500 nm (**Figure 2.15**), both in cold and hot state, which means it would have a poor color rendering performance **[19]**, and improper photo-biological effects **[150]**. In a healthy lighting environment, enough exposure to blue light around 480 nm (which is also called the melanopic light) in the early parts of the day is desired, which is closely associated with the suppression of melatonin secretion [148, 151]. In this regard, the application of VO_2 based smart windows may disturb the circadian rhythm and affect people's mood, creating unhealthy photo-biological effects.

Another type of thermochromic window: hydrogel smart window, can overcome the above three shortcomings [152-154]. However, due to the high haze and low luminous transmittance in hot state, hydrogel smart window could be undesirable for some building applications. Thus, it is still a challenge to further enhance the solar modulation ability, luminous transmittance and reduce the haze rate on TC windows.

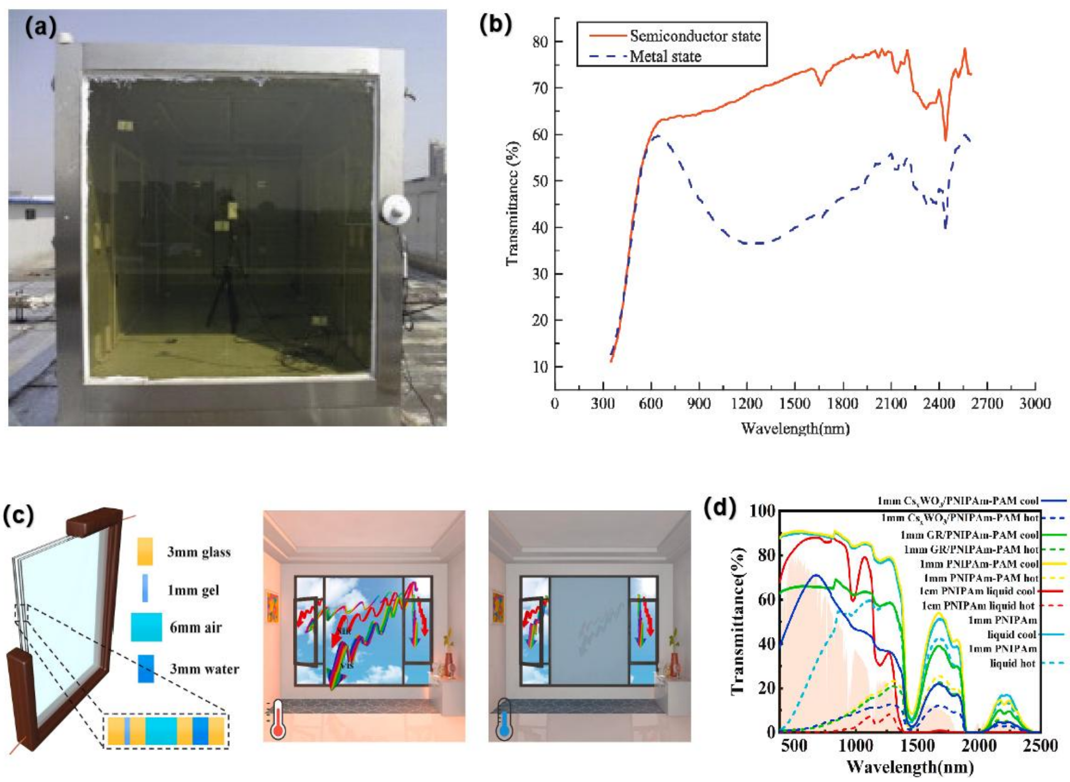

Figure 2.15 (a) A sample of VO_2-based window [134], (b) spectral transmittance of VO2 film in the semiconductor state and metal state [134]; (c) schematic representation of hydrogel-based smart window [154], (d) spectral transmittances of the hydrogel-based smart window [154].

2.1.3.2 Active smart windows

Active smart window, include magnetochromic and mechanochromic [155], electrochromic (EC) [156], liquid crystals [157] and suspended particle devices [158] achieve optical regulation by external stimulus, they are more controllable and more commercially available. Chromic material-based EC devices, especially the WO_3- and V_2O_5- [159] based products, are reliable and flexible techniques that have been commercialized. However, EC devices are primarily developed to regulate visible light; their solar NIR tenability is usually inferior. In addition, the EC windows are unable to provide full control of the visible band, resulting in a narrow color gamut [21].

2.1.3.3 Application and performance assessments

Table 2-1 and Figure 2.16 summarized the performance of typical smart window technologies. These smart window technologies either suffer from inferior solar modulation ability or showcase high scattering behaviors that are undesirable for building applications. Currently, although great progress has been achieved in smart windows, neither TC nor EC smart windows are ready to be put into large-scale residential use in this stage. For the large-scale real-life application, it is essential to develop a new type of smart windows to settle the irreversible switching, high cost, narrow color gamut, poor luminous level and low solar modulation ability.

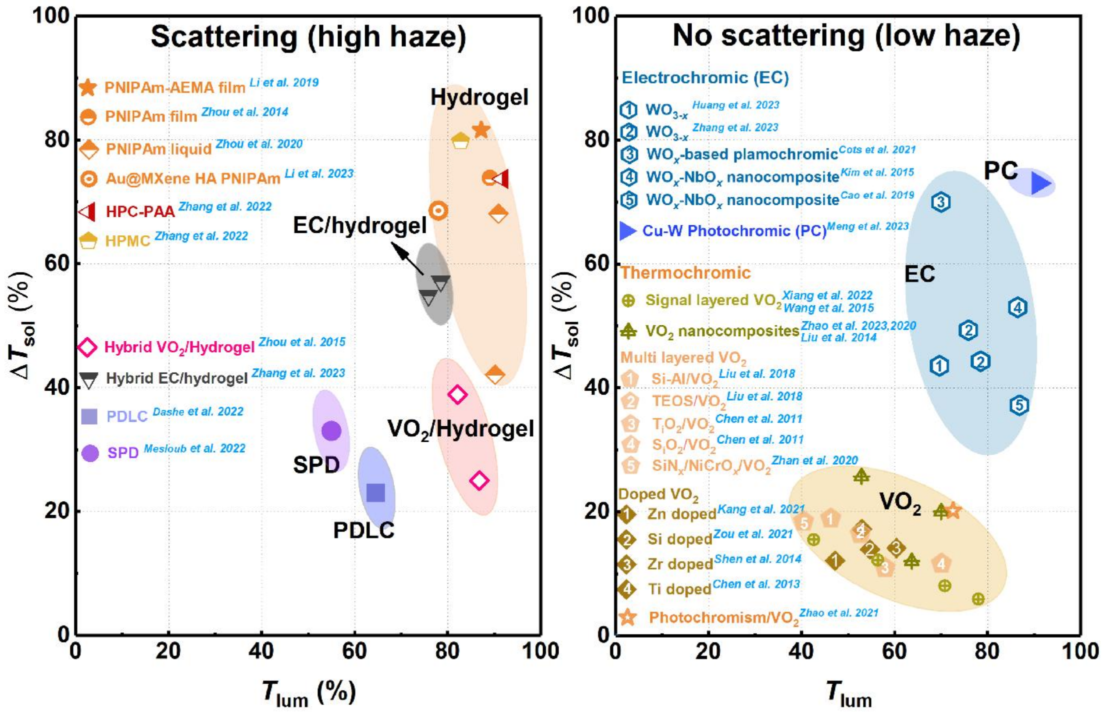

Figure 2.16 Performance comparison of the state-of-the-art dynamic windows

Table 2-1 Categories, materials, luminous transmittance and solar modulation ability of the thermochromic (TC) and electrochromic (EC) smart windows

Categories	*TC* materials (*EC* materials)		T_{lum} (%)		ΔT_{sol} (%)	Ref
			Bleached	Opaque		
VO_2-based TC windows	Signal layer VO_2		78	77	5.9	Wang *et al.* 2015
			42.6	39.7	15.5	Xiang *et al.* 2022
			56.4	55.6	12.2	
	Multi-layered VO_2	Si-Al/VO_2	46.3	41.4	18.9	Liu *et al.* 2018
		TEOS/VO_2	52.7	48.7	16.4	
		VO_2(55nm)/TiO_2(140nm)	50.6	52.1	7.2	Chen *et al.* 2011
		VO_2(55nm)/TiO_2(420nm)	58	53.9	10.9	
		VO_2(90nm)/SiO_2(85nm)	70.1	66.2	11.6	Liu *et al.* 2020
	Zn doped VO_2		47.2	51.92	12.1	Kang *et al.* 2021
	Si doped VO_2		54.7		13.9	Zou *et al.* 2021
	Zr doped VO_2		60.4		14	Shen *et al.* 2014
	Ti doped VO_2		53		17.2	Chen *et al.* 2013
	VO_2-based nanocomposites		52.9	37.3	25.7	Zhao *et al.* 2023
			63.7	54.4	12	Liu *et al.* 2014
			43.3	39.9	14.1	
			～50	～50	17	Zhao *et al.* 2020
			～70	～60	20	Zhao *et al.* 2020
Hydrogel-based TC window			89.1	0.6	73.9	Zhou *et al.* 2013
			91.8	73.7	73.7	Zhang *et al.* 2022
			87.2	0.5	81.6	Li *et al.* 2019
			90.2	39	42.1	Zhou *et al.* 2020
			90.9	1.26	68.1	
VO_2/hydrogel hybrid products			86.8	61.8	25	Zhou *et al.* 2015
			82.1	43.2	38.9	
EC window	WO_{3-x} nanoflowers		69.7	41.7	43.6	Huang *et al.* 2023
	WO_x-based plasmochromic		79		70	Cots *et al.* 2021
	Ta-doped TiO_2 nanocrystals		93.4	4.3	80	Cao *et al.* 2019
	WO_{3-x}-NbO_x nanocomposite		93	22	78	Kin *et al.* 2015
EC/TC dual-responsive windows	H^+ doped hydrogel-WO_3	thermochromic	78.5	22.3	42.4	Zhang *et al.* 2023
		electrochromic	78.5	16.3	49.3	
		thermo-/electro-dual-chromic	78.5	4	57.2	
	Li^+ doped hydrogel-WO_3	thermochromic	75.9	12	46.5	
		electrochromic	75.9	22.1	44.3	
		thermo-/electro-dual-chromic	75.9	4.1	54.9	
PC	Cu-W-PC		91	18	73	Meng *et al.* 2023

2.2 Research gaps

Spectrally selective windows offer an intelligent solution for achieving high visible transmittance and desirable levels of solar heat gain coefficient (SHGC). Over the past decades, significant progress has been achieved in the development of spectrally selective windows, including both static and dynamic windows. Despite these advancements, achieving precise solar spectral regulation and creating comfortable, healthy indoor lighting environments remain ongoing challenges. Extensive research efforts have focused on various aspects of this field, including the design of high-performance spectrally selective materials, improvements in glazing technologies, and the integration of these innovations into building applications. Nevertheless, several critical research gaps persist, including the following:

(1) Current spectrally selective materials for solar regulation typically rely on transition metal ions or plasmonic nanoparticles. However, transition metal ion-based materials often exhibit narrow and weak absorption bands, while plasmonic nanoparticles, whether applied as surface coatings or nanofluids between glazing layers, face significant stability issues. Thin-film coatings suffer from poor weather resistance and may degrade over time, while nanofluids are prone to particle agglomeration. Moreover, both material types generally fail to achieve a light-to-solar gain ratio (LSG) above 2.0. Therefore, the development of new spectrally selective materials with enhanced weather resistance, structural stability, and precise spectral control is crucial.

(2) For static windows, various computational models have been developed to analyze light and heat transfer. However, most existing models do not differentiate between direct and diffuse solar radiation when simulating annual energy performance. They also fail to consider the effects of solar incidence angle on reflectivity, as well as changes in the solar spectral power distribution under different atmospheric conditions and solar altitudes. As a result, these models lack the precision required for accurate performance prediction. Therefore, it is essential to develop a more accurate light and heat transfer model, particularly for spectrally selective windows, to better assess their energy-saving potential.

(3) For passive dynamic windows, thermochromism is considered one of the most promising approaches for transparency switching. However, current VO_2-based thermochromic windows face several critical limitations. Firstly, VO_2 exhibits low transmittance in the short-wavelength visible region, resulting in a narrow color gamut and potential visual discomfort. Secondly, it remains challenging to simultaneously achieve high photopic luminous transmittance ($\boldsymbol{T_{lum}}$) and effective solar modulation ($\boldsymbol{\Delta T_{sol}}$). Alternatively, hydrogel-based thermo-responsive windows offer high transparency in the cold state and excellent solar modulation, with $\boldsymbol{\Delta T_{sol}}$ values exceeding 70%. Nevertheless, their switching mechanism relies on light scattering, which leads to high haze and poor luminous transmittance in the opaque state. Therefore, to enable the practical adoption of thermochromic windows in buildings, key issues such as limited modulation capability and high haze must be addressed.

(4) For active dynamic windows, functionality relies on external stimuli such as electric fields, magnetic fields, or mechanical forces. However, several critical limitations persist. Electrochromic technologies are primarily effective in modulating visible light but offer limited tunability in the NIR region, which is crucial for thermal regulation. Other active systems, such as PDLC and SPD, also face challenges including irreversible switching, high haze, and limited luminous transmittance. Consequently, despite their controllability, current active dynamic windows still fall short in achieving the comprehensive performance required for scalable residential deployment. Key challenges include enhancing solar modulation capability, broadening spectral tunability, improving visual transparency, and ensuring long-term stability.

(5) For next-generation smart windows, the ability to regulate emissivity in the MIR region is essential for achieving seasonally adaptive thermal control and enhancing building energy efficiency. However, current technologies struggle to achieve simultaneous and effective modulation across a broad spectral range, particularly in the NIR and MIR regions. Many existing systems compromise visible transmittance and exhibit limited modulation performance. Therefore, there is a critical need to develop smart window technologies that can maintain high visible transmittance while offering strong and tunable control across both the NIR and MIR band.

2.3 Research objectives and methodology

Based on the identified research gaps, this PhD thesis aims to address the following objectives, with a particular focus on the integration of spectrally selective materials into window systems.

(1) To fabricate optical materials with precise solar spectrum transmittance that enable low SHGC, high luminous transmittance, and healthy photo-biological effects.

(2) To develop, validate, and implement an accurate model for the optical and thermal transmission behavior of spectrally selective windows.

(3) To develop and validate a new thermo-responsive dynamic window with high solar modulation ability, high luminous transmittance, rational color rendering index (CRI), and feasible transparency switching temperature.

(4) To develop and validate an actively switchable window with high solar modulation ability, high luminous transmittance, and rational color rendering index (CRI).

(5) To develop and validate a solar-thermal dual regulation strategy to enable window to achieve high luminous transmittance, effective solar modulation, and strong emissivity tunability.

The flow chart of the research methodology to realize the above objectives is shown in **Figure 2.17**.

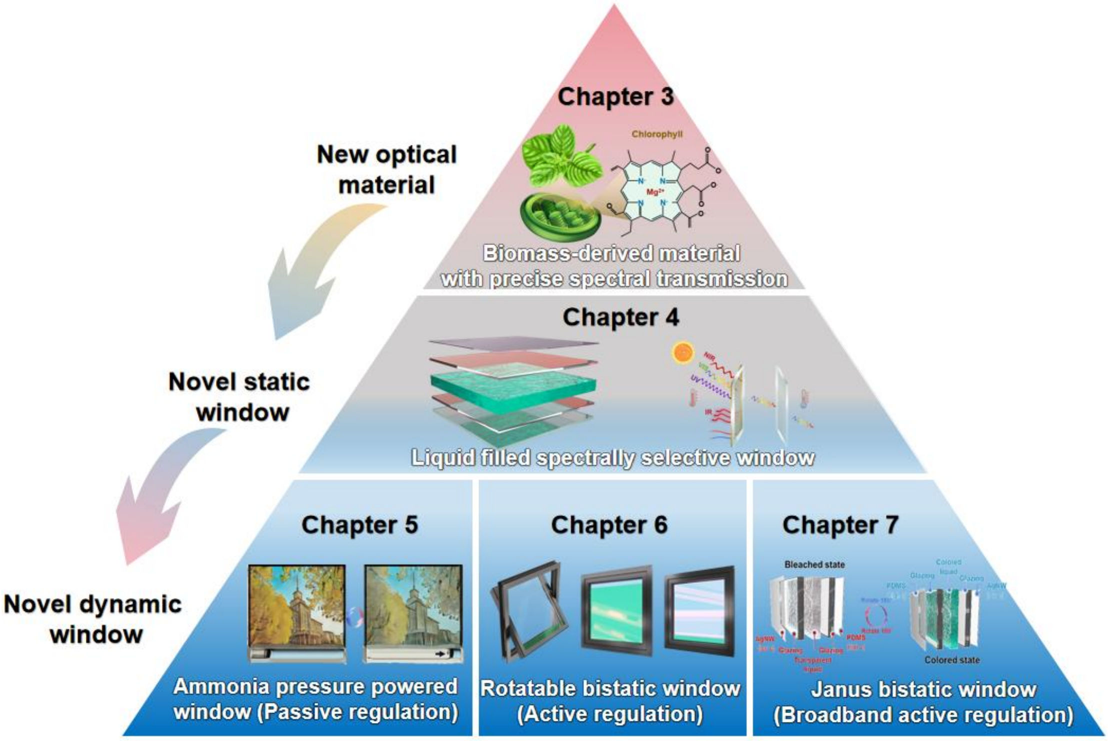

Figure 2.17 Flow chart of the research methodology

Chapter 3 Development of a new biomassed spectrally selective material

The solar spectrum is a composite spectrum (**Figure 3.1**), in VIS and NIR are inherently coupled. As sunlight passes through windows into indoor spaces, it delivers both light and heat simultaneously. In hot climate regions, windows are expected to transmit VIS light to meet daylighting needs while blocking NIR radiation to reduce cooling loads. Against this backdrop, the development of spectrally selective strategies that selectively block NIR while allowing VIS transmission has emerged as a key approach for creating a comfortable indoor optical and thermal environment. This study aims to regulate the optical transmittance of windows through the use of spectrally selective materials. To explore and develop new optical materials with precise solar spectral selectivity, this chapter first defines key metrics for quantifying the performance of spectrally selective materials and window systems. It then presents an in-depth analysis of the VIS/NIR decoupling performance of existing materials. To further enhance this decoupling capability, the chapter investigates novel, stable, and high-performance alternatives beyond current material systems. The design principles and optical optimization strategies of these new materials are discussed in detail, laying the foundation for the development of energy-efficient windows with precise spectral regulation in the subsequent chapters.

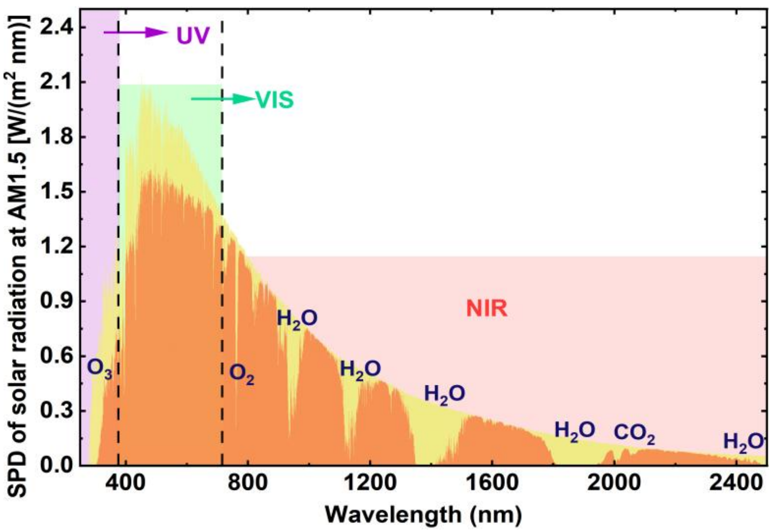

Figure 3.1 Spectral power distribution (SPD) of solar radiation at air mass 1.5

3.1. Evaluation metrics for spectrally selective windows

From the building window application perspective, both thermal and optical behaviors need to be taken into account because the window thermal performance may greatly affect the overall heating and cooling energy use, and the window optical performance may have impacts on the indoor visual comfort, electrical lighting use, and even user health. Some studies have reported the related issues of spectrally selective windows, including the visual discomfort and circadian luminous deficiency caused by the incomplete solar spectral distribution of daylight **[160-162]**. Thus, when considering the energy-saving application of spectrally selective windows, the rationality of the spectral distribution of daylighting should be evaluated. To determine whether the spectrally selective windows can ensure a rational spectral distribution for both thermal and optical application purposes, we collected the representative data reported in published studies, by the software package "Getdata", and computed two key metrics based on the spectral data to assess their energy-saving potential and visual quality. The data reduction processes are detailed as follows.

(1) Solar transmittance of windows

The solar transmittance of the spectrally selective windows can be calculated by:

$$T_{sol} = \frac{\int_{300}^{2500} T(\lambda)\Phi_{solar}(\lambda)d\lambda}{\int_{300}^{2500} \Phi_{solar}(\lambda)d\lambda} \tag{3-1}$$

where T_{sol} (dimensionless) is the solar radiation transmittance;

$T(\lambda)$ (dimensionless) is the radiation transmittance;

$\Phi_{solar}(\lambda)$ ($W \cdot m^{-2} \cdot nm^{-1}$) is the spectral power distribution of solar radiation.

(2) Visible transmittance of windows

The visible light transmittance, also called luminous transmittance, is determined by the spectral sensitivity of human visual cells, the spectral power distribution of solar radiation, and the spectral transmittance of the window, it can be calculated by calculated by:

$$T_{lum} = \frac{\int_{380}^{780} T(\lambda)\ V(\lambda)\ \Phi_{solar}(\lambda)\ d\lambda}{\int_{380}^{780} V(\lambda)\ \Phi_{solar}(\lambda)\ d\lambda} \tag{3-2}$$

where **T_{lum} (λ)** (dimensionless) is the photopic light transmittance of glazing;

Φ_{solar} (λ) ($W \cdot m^{-2} \cdot nm^{-1}$) is the incident SPDs (AM1.5).

$V(\lambda)$ (dimensionless) is the luminous efficiency function (**Figure 3.2**) **[163]**.

(3) Solar heat gain coefficient (SHGC)

The SHGC is defined as the ratio of solar heat that enters a building's interior to the total solar radiation incident on the window or glazing system, it compromises of two parts: (1) the directly transmitted portion of solar radiation, and (2) the fraction of absorbed solar energy that is subsequently transferred into building interior. It can be calculated by:

$$SHGC = T_{sol} + \left(A_{STPV} - PCE\right)\frac{\frac{1}{R_{in}}}{\frac{1}{R_{in}} + \frac{1}{R_{out}}} \tag{3-3}$$

where **T_{sol}** (dimensionless) is the solar transmittance of the STPV window;

A_{STPV} is the (dimensionless) is the solar absorptivity of the STPV window;

R_{in} (m^2K/W) is the thermal resistance of heat transfer from PV glazing to the building interior, which include the thermal resistance of the air gap and the second glazing pane;

R_{out} (m^2K/W) is the thermal resistance of heat transfer from PV glazing to outdoor environment.

Since glazing has a good thermal conductivity of 1.3 W/(m·K), its conductive thermal resistance can be neglected. In buildings, to avoid secondary heat gain caused by heat transfer from the glass to the interior, spectrally selective glass is typically placed on the exterior side.

(4) Light/heat decoupling ability

The LSG is a metric commonly used by the National Fenestration Rating Council

(NFRC) and the U.S. Department of Energy, to evaluate the VIS/NIR decoupling ability of windows. It is defined as:

$$LSG = \frac{T_{\text{lum}}}{SHGC} \tag{3-4}$$

It should be noted that SHGC is an uncertain variable, as its value depends on both the structural parameters of the window and the outdoor environmental conditions. Since LSG is determined by SHGC, its specific value cannot be precisely defined. Therefore, the Figure of Merit (FOM) [164], as defined in literature related to spectrally selective glazing, is used here instead of LSG to evaluate the VIS/NIR decoupling ability of spectrally selective materials. For single-pane window structures, since the absorbed solar heat is easily dissipated, the value of FOM is approximately equal to the LSG. When it comes to multi-pane window structures, the placement of the absorbing layer and the combination with low-e coatings may complicate the heat dissipation direction. FOM is defined and expressed as follows:

$$FOM = \frac{T_L}{T_s} \tag{3-5}$$

(5) Color rendering capacity

When sunlight transmits through the windows, it is supposed to cover the entire color gamut. An incomplete VIS spectrum would result in unsaturated reflected light, which would cause color distortion, is easy to cause visual fatigue [165], and may lead to myopia [166, 167]. The Color Rendering Index (CRI) can be used to assess the quality of the gamut relative to natural daylight. The required CRI for different occasions are [168]:

- Above 90 for occasions with high visual requirements, such as galleries, painting studios, healthcare facilities, and museums;
- Above 80 for traditional residential buildings, such as homes, restaurants, schools, hotels, and office buildings.

Detailed calculation of CRI can be divided into four steps [169]:

Step 1: determining the reference illuminant

The correlated color temperature (CCT) can be calculated using McCamy's approximate formula [170], based on the incident spectral distribution:

$$CCT = 437(\frac{X-0.332}{0.1858-Y})^3 + 3601(\frac{X-0.332}{0.1858-Y})^2 - 6861(\frac{X-0.332}{0.1858-Y}) + 5514 \quad (3\text{-}6)$$

$$X = \int_{380}^{780} P(\lambda)\ \bar{x}(\lambda)\ d\lambda \quad (3\text{-}7)$$

$$Y = \int_{380}^{780} P(\lambda)\ \bar{y}(\lambda)\ d\lambda \quad (3\text{-}8)$$

$$Z = \int_{380}^{780} P(\lambda)\ \bar{z}(\lambda)\ d\lambda \quad (3\text{-}9)$$

where $\boldsymbol{X}$, $\boldsymbol{Y}$, and $\boldsymbol{Z}$ are the stimulus values of red, yellow, and blue primary colors.

$\boldsymbol{P(\lambda)}$ represents the spectral intensity of light.

$\bar{\boldsymbol{x}}(\boldsymbol{\lambda})$, $\bar{\boldsymbol{y}}(\boldsymbol{\lambda})$, $\bar{\boldsymbol{z}}(\boldsymbol{\lambda})$ represents the color matching function of red, green, and blue, which were given by the CIE standard [171] (Figure 3.3).

In case the CCT is less than 5000 K, the Planckian radiator with the same CCT as the incident light serves as the reference illuminant. Otherwise, the CIE daylight phase with the same CCT is used as the reference illuminant.

Step 2: calculating the color appearance

The tristimulus values of the tested light source $(X_i, Y_i, Z_i)_T$ and the reference illuminant $(X_i, Y_i, Z_i)_R$ can be calculated by **Equations (3-12)** to **(3-14)**, according to the spectral intensity. The chromaticity coordinates are then clarified as $(\boldsymbol{u_i}, \boldsymbol{v_i})_T$ and $(u_i, v_i)_R$. Given the 14 reference illuminants, $(u_i, v_i)_T$ can be transformed into the coordinates $(u_{i,k}, v_{i,k})_T$. And then the $(u_{i,k}, v_{i,k})_T$ and $(u_i, v_i)_R$ can be converted into the CIE1964 W*, U*, V* color space, which are expressed as $(W^*_i, U^*_i, V^*_i)_T$ and $(W^*_i, U^*_i, V^*_i)_R$.

Step 3: calculating the color difference

The color difference is denoted by ΔE_i, which is defined as the Euclidean distance between $(W^*_i, U^*_i, V^*_i)_T$ and $(W^*_i, U^*_i, V^*_i)_R$.

Step 4: calculating the ***CRI***

The color differences (ΔE_i) are transformed into special CRI-s (Ri) by **Equations (3-15)**. In **Equations (3-15)**, the multiplier, 4.6, was used to ensure a CRI of 50 for the traditional warm white halophosphate fluorescent lamp.

$$Ri = 100 - 4.6\Delta E_i \tag{3-10}$$

The average value of the fourteen non-saturated samples provides the general color rendering index:

$$R_a = \frac{1}{14}\sum_{i=1}^{14} R_i \tag{3-11}$$

In this study, these four processes for calculating the CRI were achieved in the software package, "*ColorCalculator*" **[172]**.

(6) Photo-biological effects

There are three primary types of photoreceptor cells in the human retina: rods, cones, and intrinsically photosensitive retinal ganglion cells (ipRGCs) **[151]**. Unlike rods and cones, which are responsible for image formation, ipRGCs do not contribute to visual perception. Instead, they are highly sensitive to blue light and play a vital role in the non-visual photobiological effects of light **[173-175]**. Through their regulation of the circadian rhythm, biological clock, and melatonin secretion, ipRGCs have a significant impact on sleep, mood, and overall health **[176, 177]**. To evaluate non-visual lighting effects on the human body, several metrics have been developed. Among them are:

Circadian Light (CLA) **[178]**:

$$CLA = \begin{cases} 1548 \times \left\{ \int S_{\text{mel}}(\lambda)\Phi(\lambda)d\lambda + a_{\text{b-y}} \cdot SV - a_{\text{rod}} \left[1 - e^{\frac{-\int S_{\text{rods}}(\lambda)\Phi(\lambda)d\lambda}{RodSat}} \right] \right\}, & if \;\; SV > 0 \\ 1548 \times \int S_{\text{mel}}(\lambda)\Phi(\lambda)d\lambda, \quad if \;\; SV \leq 0 & \end{cases} \quad (3\text{-}12)$$

$$SV = \int \frac{S_{\text{s-cone}}(\lambda)}{mp(\lambda)}\Phi(\lambda) - k\int \frac{V(\lambda)}{mp(\lambda)}\Phi(\lambda) \quad (3\text{-}13)$$

Circadian Stimulus (CS) **[179-181]**:

$$CS = 0.7 - \frac{0.7}{1 + \left(\frac{CLA}{355.7}\right)^{1.1026}} \quad (3\text{-}14)$$

and the Melanopic to Photopic Ratio (M/P) **[182, 183]**:

$$M / P = \frac{\int_{380}^{780} I(\lambda)\ S_{\text{mel}}(\lambda)\ d\lambda}{\int_{380}^{780} I(\lambda)\ V(\lambda)\ d\lambda} \quad (3\text{-}15)$$

$$T_{\text{mel}} = \frac{\int_{380}^{780} T(\lambda)\ S_{mel}(\lambda)\ \Phi_{solar}(\lambda)\ d\lambda}{\int_{380}^{780} S_{mel}(\lambda)\ \Phi_{solar}(\lambda)\ d\lambda} \quad (3\text{-}16)$$

The melanopic transmittance (**T_{mel}**) were calculated by.

$$T_{\text{lum/mel}} = \frac{\int_{380}^{780} T(\lambda)\ S_{\text{lum/mel}}(\lambda)\ \Phi(\lambda)\ d\lambda}{\int_{380}^{780} S_{\text{lum/mel}}(\lambda)\ \Phi(\lambda)\ d\lambda} \quad (3\text{-}17)$$

where **S_{mel} (λ)** (dimensionless) is the action spectra of ipRGC (**Figure 3.2**);

$S_{\text{s-cone}}$ (λ), $S_{\text{lum-dark}}$ (λ) (dimensionless) are the action spectra of photopic; sensitivity of s-cone and rods respectively **[163]**;

mp **(λ)** (dimensionless) represents the macular pigment transmittance;

Constant values: **$a_{\text{b-y}}$** = 0.7000, **a_{rod}** = 3.3000, ***k*** = 0.2616;

RodSat = 6.5 W/m^2;

SV (dimensionless) is the blue-yellow opponent signal.

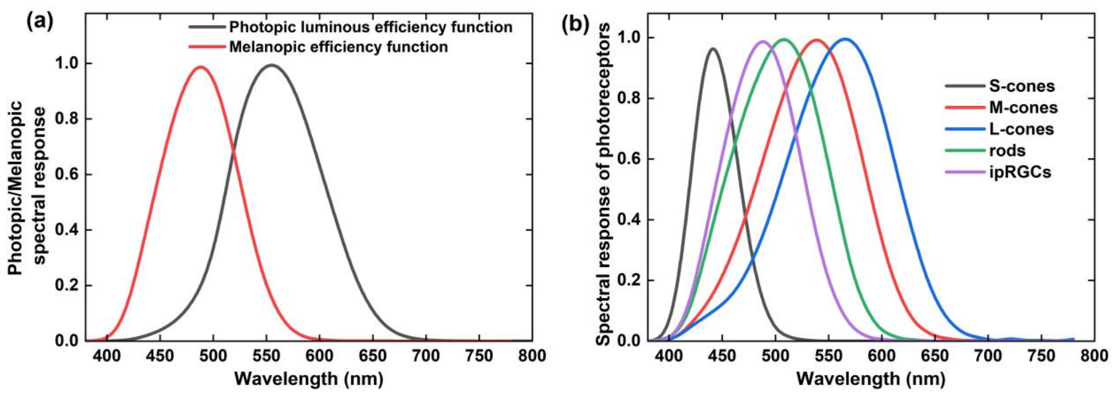

Figure 3.2 (a) Photopic/Melanopic spectral response functions; and (b) spectral response functions of photoreceptor cells in the human eyes.

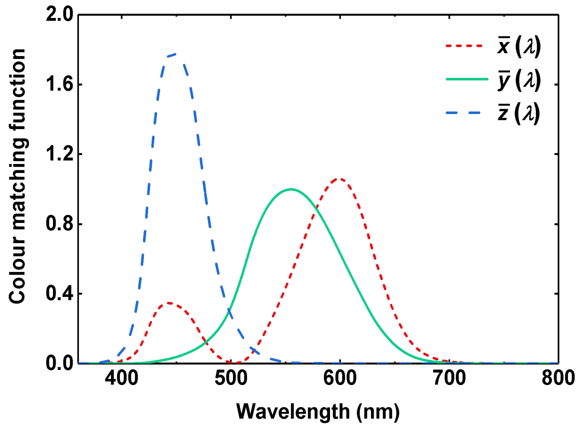

Figure 3.3 Color matching functions

3.2. Performance eveluation of current spectrally selective materials

Strategies for regulating the solar spectrum primarily include NIR reflection and NIR absorption technologies. NIR reflection is typically achieved through coatings of metals or TCOs, and this approach has been extensively developed and widely applied. Therefore, this chapter focuses on a specific subset of NIR-absorbing technologies, using the optical performance of NIR-reflecting glazing as a baseline for comparison.

As described in **Chapter 2**, spectrally selective windows are primarily derived from two major categories of materials: transition metallic ions and plasmonic nanoparticles. Currently, many researches have focused on spectrally selective energy-saving window technologies based on these two material types. However, most of these studies approach the topic from a materials science perspective, emphasizing the intrinsic functional properties of the materials themselves. The reported data typically include material-level performance parameters, while application-level indicators relevant to architectural glazing, as discussed in Section 3.1, are rarely addressed.

To bridge the gap between material properties and architectural applications, this section compiles available optical data on spectrally selective materials from recent literature worldwide. In cases where raw data were not provided, spectral transmittance, absorptance, and reflectance curves were extracted using GetData software. A comprehensive analysis was then performed to evaluate the materials' thermal insulation performance and color rendering characteristics from an architectural perspective.

3.2.1 Performance eveluation of ions-based glazings

Accroding the the NIR absorbing materials listed in Chapter 2.1.2.1, in this section, four types of ion-doped glasses were collected based on the study by Fu et al. **[54]** and several domestic and international patents: (1) glass doped with only iron ions, (2) glass co-doped with iron ions and other transition metal ions, (3) glass co-doped with iron ions and VIA ions, and (4) transition metal ion-doped glass without iron ions. The spectral transmittance data of these glasses were analyzed using the data processing method described in **Chapter 3.1**, and the results are presented in **Tables 3-1** through **3-4**.

According to the data reported by Fu et al. **[54]** (**Table 3-1**), glazing doped solely with iron ions (10 mm thickness) can achieve a NIR transmittance below 50% while maintaining a visible light transmittance above 70% and a CRI exceeding 95, resulting in a FOM close to 1.5.

In addition to iron ions, other transition metal ions also exhibit favorable absorption characteristics in both the VIS and NIR region. The collected data further show that co-doping with iron and zinc ions can increase the FOM to 1.83, while co-doping iron ions with cesium, titanium, and chromium ions can raise the FOM to 1.89. However, since many of these transition metallic ions have absorption within the VIS range, co-doping multiple ions may lead to a significant reduction in the CRI. As shown in **Table 3-2**, when the FOM of ions deped glazings exceeds 1.8, the CRI typically drops below 90. This limits its applicability in buildings where high color rendering is essential, such as art museums and galleries.

In the case of selenium and iron ions co-doped glazing (**Table 3-3**), the visible transmittance drops from 0.9 to 0.5, yet the CRI of the transmitted light remains above 90. For typical residential buildings, where the window-to-wall ratio is generally less than 0.4, national standards often require visible light transmittance above 60%. Therefore, the use of selenium-doped glass is somewhat limited in such applications.

As for transition-metal-doped glazings without iron ions, its effectiveness in NIR shielding is relatively poor. Thus, its solar spectrum control performance is rarely highlighted in literature, and the solar transmittance or FOM values are generally not reported or calculated (**Table 3-4**).

Table 3-1 Detailed information of iron ion-based glazings

Dopants	**Thickness**	**Color**	T_{sol}	T_{lum}	***FOM***	***CRI***	**Refs.**
0.1wt% F_2O_3 doped in reducing atmosphere	10 mm	Green	0.707	0.903	1.279	97	Fu et al. [54]
0.2wt% F_2O_3 doped in reducing atmosphere	10 mm	Green	0.667	0.888	1.331	97	
0.3wt% F_2O_3 doped in reducing atmosphere	10 mm	Green	0.637	0.885	1.391	97	
0.4wt% F_2O_3 doped in reducing atmosphere	10 mm	Green	0.476	0.709	1.491	96	

Table 3-2 Detailed information of iron and other transition metallic ions co-doped glazings

Dopants	**Thickness**	**Color**	T_{sol}	T_{lum}	***FOM***	***CRI***	**Refs.**
0.62wt% Fe_2O_3, 0.12wt% FeO, 0.1wt% TiO_2, 7ppm CoO	5 mm	Green	0.53	0.78	1.479	95	Central Glass, Inc. [13]
0.4wt% Fe_2O_3, 1.1wt% CeO_2, 1.1wt% TiO_2, 17 ppm Cr_2O_3, 0.2wt% FeO	5 mm	Green	0.39	0.74	1.891	87	
0.54wt% Fe_2O_3, 0.13wt%FeO, 0.1wt% TiO_2, 17ppm Cr_2O_3	5 mm	Green Blue	0.54	0.78	1.439	96	
0.38wt% Fe_2O_3, 1wt% CeO_2, 1wt% TiO_2, 0.5wt% SnO, 17ppm Cr_2O_3, 0.17wt% FeO	5 mm	Green Blue	0.43	0.71	1.634	92	
0.05% to 2wt% Fe, 0.1% to 15wt% Sn	0.833 mm	Blue	0.39	0.71	1.828	88	Rao et al. [13]
0.54wt% Fe_2O_3, 0.14wt% FeO, 0.24wt% SO_3	5 mm	Green	0.52	0.78	1.513	94	Pecoraro et al. [60]
0.74wt% Fe_2O_3, 0.2wt% FeO, 0.22wt% SO_3	5 mm	Green Blue	0.41	0.67	1.617	92	
0.80wt% Fe_2O_3, 0.23wt% FeO, 0.03wt% SO_3	5 mm	Green Blue	0.38	0.67	1.779	90	
0.51wt% Fe_2O_3, 0.28wt% FeO, 0.24wt% SO_3	5 mm	Green Blue	0.38	0.70	1.870	89	

Table 3-3 The detailed information of iron and other ions co-doped glazings

Dopants	**Thickness**	**Color**	T_{sol}	T_{lum}	*FOM*	*CRI*	**Refs.**
Fe and Se	——	Amber		0.64		97	Kondrashov et al. [13]
Fe, Se, and Co	——	Bronze		0.66		98	
Fe, Se, and Co	——	Dark bronze		0.49		97	
Fe, Se, and Co	——	Gray		0.68		98	
Fe, Se, and Co	——	Green		0.81		95	
Fe, Se, and Co	——	Sky blue		0.76		96	
0.204wt% Fe_2O_3, 0.0035wt% CoO, 0.00081wt% Se, 0.0014wt% NiO	5 mm	Neutral gray	0.58	0.67	1.14	91	Kato et al. [13]
0.222wt% Fe_2O_3 0.0034wt% CoO 0.00077wt% Se	5 mm	Neutral gray	0.57	0.66	1.17	90	
0.397wt% Fe_2O_3, 0.41wt% CeO_2, 0.31wt% TiO_2, 0.6% CoO, 8.1ppm Se	4 mm	Bronze		0.73		97	Mie et al. [184]
0.203wt% Fe_2O_3, 0.41et% CeO_2, 6.5%wt CoO, 10.2ppm Se	4 mm	Bronze		0.74		97	

Table 3-4 Detailed information of nonferrous tinted glazings

Dopants	**Thickness**	**Color**	T_{lum}	**CRI**	**Refs.**
4wt% ZnO, 0.25wt% Sb_2O_3, 10wt% Nd_2O_3	< 0.5 mm	Blue-violet	0.709	78	Stewart R.L. [13]
7%wt ZnO, 0.25wt% Sb_2O_3, 8wt% Nd_2O_3	< 0.5 mm	Blue-violet	0.747	81	
2.8wt% Cu ions	0.5 mm	Blue	0.656	73	Nobutake Nagano et al. [13]
2.8wt% Cu ions with O_2 injection	0.5 mm	Blue	0.647	75	

Figure 3.4 summarizes and compares the spectral selectivity and color rendering performance of various transition-metal-doped glazings. For comparison, it also includes ordinary clear glazing and NIR absorbing low-e glazing based on literature data. Among them, iron ions-based glazing demonstrate superior FOM compared to conventional low-e glazing, making them promising candidates for hot climate regions. The FOM values of iron doped glasses range from approximately 1.3 to 1.5. With additional co-doping of elements such as titanium, cesium, or chromium, the FOM can be further increased to above 1.8. However, it is important to note that in order to maintain a CRI above 90, the FOM of such materials should generally not exceed 1.8.

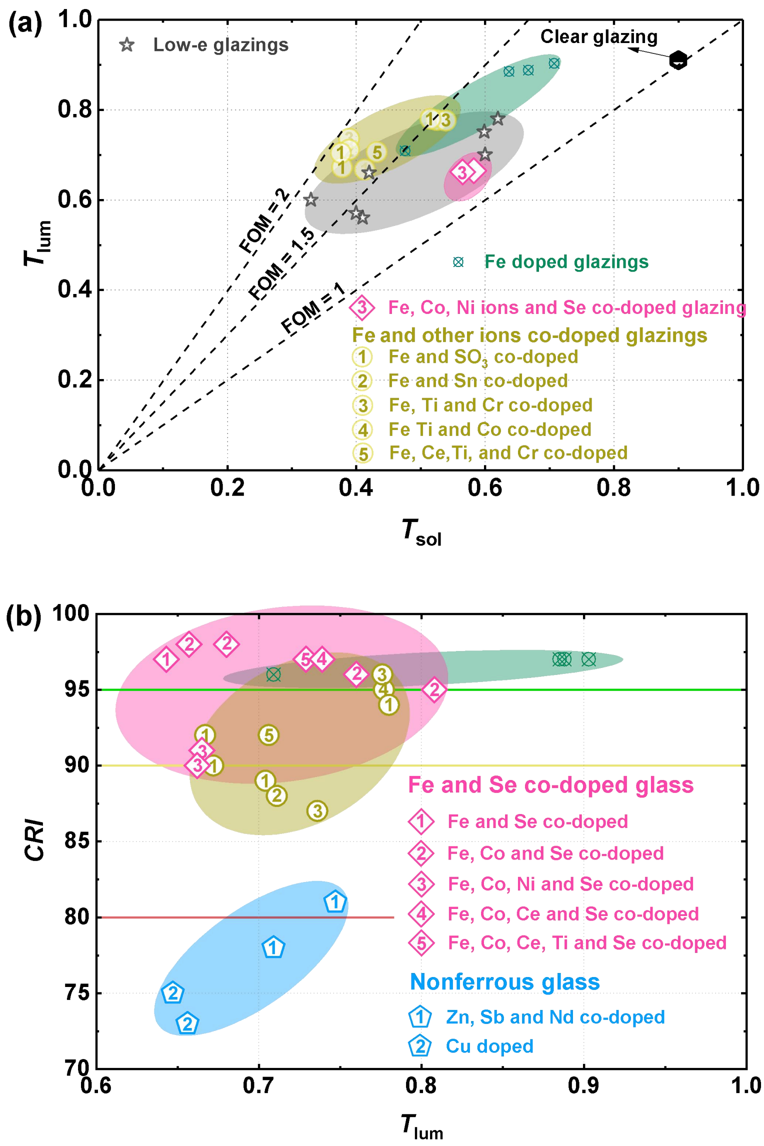

Figure 3.4 Summary of **(a)** the light/heat decoupling ability and **(b)** the color rendering performance of the ion-based glazings (the CRI of 95 is a baseline that commercial low-e glazings can meet [12, 185], 90 represents the baseline of a good color rendering [185] that is crucial for art galleries, museums; 80 represents the baseline for civil buildings [186, 187]).

3.2.2 Performance evaluation of nanoparticle-based glazings

This chapter analyzed three types of plasmonic nanomaterials applied in spectrally selective windows: Fe_3O_4 nanocomposites, ATO nanocomposites, and M_xWO_3 nanocomposites. The corresponding data is summarized in Tables 3-5 to 3-7.

Table 3-5 summarizes the parameters of Fe_3O_4 nanocomposite films. The data indicate that Fe_3O_4 nanoparticles exhibit excellent CRI in glazing applications, achieving CRI values above 90 while maintaining a high FOM above 1.8.

Table 3-6 presents the performance parameters of ATO nanocomposites. With visible transmittance at 70%, ATO-based nanocomposites generally exhibit FOM values below 1.3. However, hybrid nanoparticles doped with other substances can achieve FOM values exceeding 1.6.

Table 3-7 summarizes the performance parameters of M_xWO_3-based light/heat decoupling materials. Certain Cs_xWO_3 films or glazing exhibit FOM values greater than 2.0, demonstrating strong potential for solar heat modulation in energy-saving window applications. However, Cs_xWO_3-related products perform poorly in weathering assessments. In oxidative or humid environments, W^{5+} ions are easily converted to W^{6+}, leading to material degradation. This significantly limits the commercial viability.

Table 3-5 The performance parameters of Fe_3O_4-based nanocomposites

Category	**Content (g/cm^2)**	**Particle size (nm)**	T_{sol}	T_{lum}	***FOM***	***CRI***	**Refs.**
Fe_3O_4 films	4.57×10^{-4}	10	—	0.74	—	98	Lin et al. **[188]**
$Fe_3O_4@Cu_{2-x}S$ films	4.57×10^{-4}	15	—	0.83	—	99	Lin et al. **[188]**
$Fe_3O_4@Cu_{2-x}S$ films	5.08×10^{-5}	15 to 20	—	0.82	—	98	Lyu et al. **[123]**
$Fe_3O_4@Cu_{2-x}S$ films	2.54×10^{-4}	15	0.64	0.77	1.20	99	Wang et al. **[36]**
$Fe_3O_4@Cu_{2-x}S$ films	——	15	0.16	0.29	1.82	92	Wang et al. **[38]**

Table 3-6 The performance parameters of ***ATO***-based nanocomposites

Category	*Thickness*	*Concentration*	*Particle size*	*Doping level: Sb/(Sb+Sn)*	*Annealing*	T_{sol}	T_{lum}	*FOM*	*CRI*	*Refs.*
ATO/PVA films	——	25wt% ATO	27.8 nm	10mol %	1000 °C for 4*h*	0.49	0.71	1.45	98	Shen et al. [96]
ATO/PVA films	——	20wt% ATO	27.8 nm	10mol %	1000 °C for 4*h*	0.66	0.82	1.25	98	
ATO/PVP films	~5 μm	10wt% ATO	7-12 nm	——	——	0.58	0.73	1.26	99	Xu et al. [104]
ATO/PVA films	10 to 15 μm	——	25.9 nm	10mol %	1000 °C for 4*h*	0.62	0.80	1.28	98	Shen et al. [105]
ATO/silicone films	~5 μm	12 wt ATO	< 15 nm	——	——	0.50	0.72	1.44	99	Qu et al. [103]
ATO films	~0.45 μm	12.5wt%	Spray-grown	1%	450°C for 40 min	0.60	0.70	1.18	98	Parra et al. [106]
ATO coated quartz glass	——	——	3.7 nm	11mol%	550 °C for 1*h*	0.80	0.82	1.02	98	Sum et al. [189]
ATO-MWNT/PVP films	~5 μm	10wt% ATO 0.2% MWNTs	7-12 nm ATO; 8 nm MWNT	——	——	0.39	0.59	1.49	98	Xu et al. [104]

ATO-CWO/PVA films	15 to 20 μm	6wt% ATO 6wt% CWO	14.3 nm CWO; 27.8 nm ATO	10% mol	1000 ℃ for 4*h*	0.43	0.70	1.61	98	Shen et al. [107]
ATO-CWO/PVA films	——	——	——	——	——	0.49	0.76	1.56	98	Zhang et al. [108]
ATO-ITO /PGMEA films	——	——	——	——	——	0.33	0.61	1.87	97	Kim et al. [109]
ATO-YTO coated glass	～0.3 μm	——	——	11mol% Sb 9mol% Yb	600 ℃ for 1*h*	0.67	0.81	1.21	98	Li et al. [110]
ATO nanofluids	10 mm	100 ppm	80 nm	——	——	0.74	0.93	1.26	98	Zhang et al. [101, 190]
ATO-WO_3 nanofluids	10 mm	0.01vol%	42.18 nm	——	——	0.40	0.74	1.85	97	Yuan et al. [111]
ATO/Graphite nanofluids	10 mm	0.025% ATO 0.0001% Graphite	—	10mol%	——	0.64	0.89	1.39	98	Shen et al. [191]

Table 3-7 The performance parameters of M_xWO_3-based nanocomposites

Category	*Particle size*	*Doping level*	*Concentration*	T_{sol}	T_{lum}	*FOM*	*CRI*	*Refs.*
Li_xWO_3-silicate glass	exists as ions	x=4.37	26.2mol% Li^+; 6mol% WO_3	0.12	0.25	2.14	81	Yang et al. [116]
Na_xWO_3-silicate glass	exists as ions	x=4.37	26.2mol% Na^+; 6mol% WO_3	0.39	0.62	1.60	94	Yang et al. [116]
K_xWO_3-silicate glass	exists as ions	x=4.37	26.2mol% K^+; 6mol% WO_3	0.74	0.77	1.05	97	Yang et al. [116]
$(NH_4)_xWO_3$ films	—	x=0.29	0.07 g/m^2	0.68	0.86	1.26	99	Guo et al. [118]
$(NH_4)_xWO_3$ films	—	x=0.29	0.28 g/m^2	0.36	0.59	1.66	95	
Cs_xWO_3 films	30 nm	x=0.320	—	0.31	0.61	1.96	93	Long et al. [192]
Cs_xWO_3 films	—	x=0.30	—	0.32	0.37	1.17	97	Shi et al. [193]
Cs_xWO_3 films	0.1-0.5 μm	x=0.3	—	0.44	0.74	1.69	97	Liu et al. [194]
Cs_xWO_3 films	—	—	—	0.60	0.83	1.38	98	Li et al. [195]
Cs_xWO_3/PVA films	219.2±40.1 nm	—	—	0.37	0.71	1.92	95	Zhang et al. [112]
Cs_xWO_3/PVA films	—	x=0.31	—	0.54	0.78	1.46	98	Shen et al. [113]

Cs_xWO_3 composites films	66.81 nm	x=0.263	—	0.32	0.62	1.93	95	Yao et al. [119]
Cs_xWO_3 composites films	39.66 nm	x=0.316	—	0.29	0.60	2.10	93	
Cs_xWO_3 composites films	33.73 nm	x=0.320	—	0.28	0.60	2.12	93	
Cs_xWO_3/PMMA nanocomposites	28 nm	x=0.320	0.3wt%	0.50	0.80	1.60	98	Yao et al. [127]
Pt_n-Cs_xWO_3/PVA films	diameter: 10-30 nm; length: 20-80 nm	n=0.01, $x \approx 0.32$	—	0.47	0.71	1.51	98	Liu et al. [120]
F_n-Cs_xWO_3/PVA films	—	x=0.3, n=0.21	—	0.49	0.76	1.54	98	
Li_n-Cs_xWO_3/PVA films	957.9±313.5 nm	Li/Cs molar ratio of 0.25	—	0.37	0.72	1.96	95	Zhang et al. [112]

Figure 3.5 compares the performance of energy-saving windows based on different types of plasmonic nanoparticles from three key aspects: visible transmittance, FOM, and color CRI. $Fe_3O_4@Cu_{2-x}S$ nanoparticles demonstrate strong absorption in both VIS and NIR regions, making them suitable for reducing cooling loads in buildings. However, their light/heat decoupling capability is relatively weak, with FOM values ranging from approximately 1.2 to 1.8, as shown in **Figure 3.5a**. Nonetheless, $Fe_3O_4@Cu_{2-x}S$-based films can achieve CRI values above 98, indicating excellent color rendering performance and unique potential in customized thermal management designs for window systems.

ATO is one of the most promising nanomaterials currently, due to its low cost, high stability, and mature fabrication processes. With visible transmittance above 70%, ATO-based nanocomposites typically exhibit FOM values between 1.2 and 1.5 (see **Figure 3.5a**). By doping with other materials such as ITO or WO_3, their light/heat decoupling performance can be further enhanced. Studies have shown that doped ATO can achieve FOM values exceeding 1.8, making it highly suitable for energy-efficient windows. Furthermore, ATO-based composites generally have CRI values above 97, fully meeting the color fidelity requirements for various architectural applications. Consequently, ATO nanocomposites exhibit great potential for commercialization.

Cs_xWO_3 composites possess the best VIS/NIR decoupling performance among the studied materials. These nanocomposites can achieve FOM above 2 while maintaining visible transmittance over 60%. Their CRI values also exceed 90, satisfying the basic color rendering requirements of buildings. However, the poor weather resistance of Cs_xWO_3, particularly its susceptibility to degradation due to the oxidation of W^{5+} to W^{6+}, significantly constrain its large-scale commercial application.

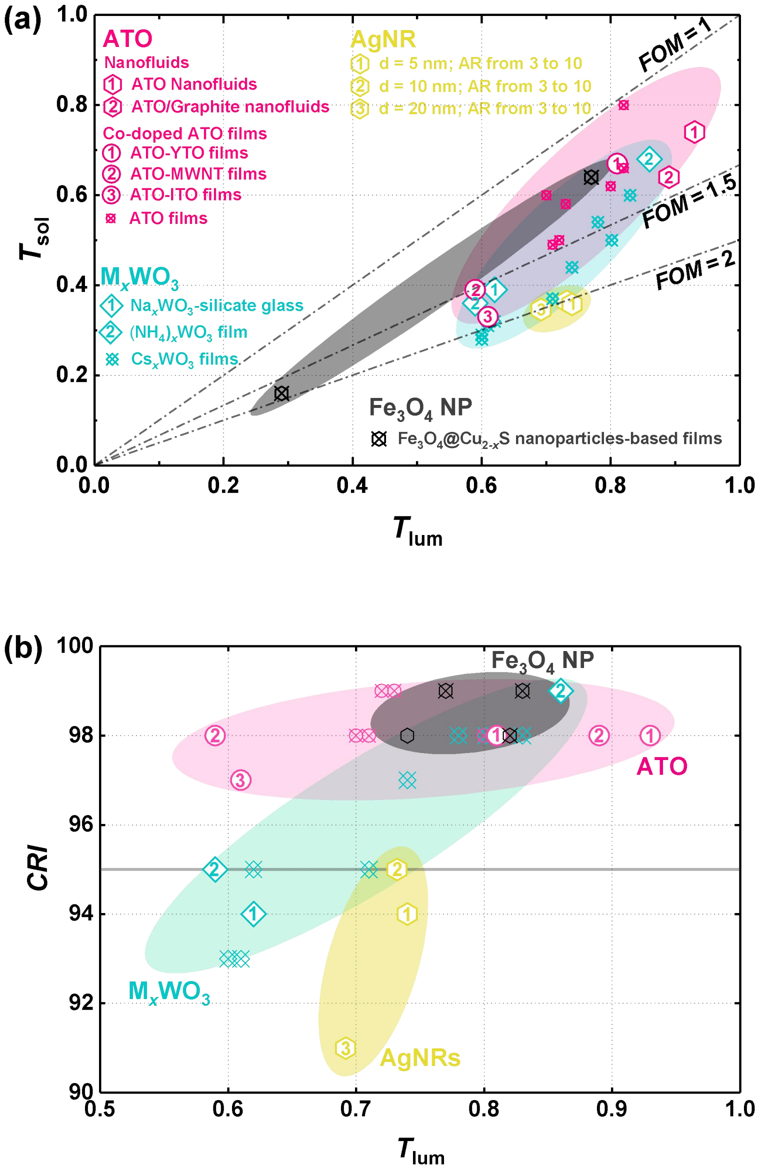

Figure 3.5 Summary of **(a)** the light/heat decoupling performance and **(b)** the color rendering performance of the nanoparticles-based glazings (the CRI of 95 represents the baseline that most of the Low-e glass can meet [12, 185], 90 represents the baseline of a good color rendering that is crucial for art galleries, museums [186, 187]).

3.3 The development of a novel biomass-derived spectrally selective material

Among the two main categories of spectrally selective materials discussed in Section 3.2, both transition metal ions and plasmonic nanoparticles exhibit superior VIS/NIR decoupling performance compared to traditional low-emissivity (low-e) glazing. This chapter explores the development of a water-based spectrally selective material. For nanoparticle-based systems, water-based nanofluids face significant challenges such as nanoparticle agglomeration, which hinders the long-term stability of their optical properties. Given the intrinsic spectral absorption characteristics of water molecules, the spectrally selective material in a water-based system should primarily target the NIR region between 800 nm and 1200 nm. Accordingly, this study aims to develop a durable, stable, and precisely targeted VIS/NIR decoupling material by aligning the spectral absorption profile of the material with that of water molecules,u.

3.3.1 The spectral transmittance of $CuSO_4$ solution

When copper ions form octahedral coordination complexes in aqueous solution, the ***d-d*** transition absorption peak of these complexes occurs around 820 nm, which complements the absorption bands of water molecules, enabling the solution to effectively block nearly all NIR energy in solar spectrum. To evaluate the feasibility of using $CuSO_4$ solution as a spectrally selective fluid, this study prepared solutions of varying concentrations by mixing solid $CuSO_4{\cdot}5H_2O$ with deionized water. The mixtures were stirred for 2 hours in a sealed container using a magnetic stirrer.

Figure 3.6 presents the spectral transmittance of $CuSO_4$ solutions at different mass concentrations and fluid thicknesses. For a 2 mm-thick solution with $CuSO_4{\cdot}5H_2O$ mass concentrations of 5%, 10%, and 20%, the visible transmittances (T_{lum}) were 84%, 81%, and 75%; the solar transmittances (T_{sol}) were 58%, 46%, and 37%; the FOM values were 1.46, 1.75, and 2.05y; the melanopic transmittances (T_{mel}) were 84%, 84%, and 86%; and the *CRI* values were 97, 92, and 83, respectively.

For a 20% mass concentration solution at thicknesses of 1 mm, 5 mm, and 10 mm, the T_{lum} values were 80%, 61%, and 50%; T_{sol} were 46%, 28%, and 25%; FOM values were 1.72, 2.21, and 2.03; and CRI values were 85, 87, and 91, respectively.

These data indicate $CuSO_4$ solution effectively filters NIR solar, achieving FOM values higher than most nanocomposites, while maintaining a CRI above 80. However, it is worth noting that the solubility of copper ions varies with temperature. High-concentration $CuSO_4$ solutions are prone to crystallization under elevated temperatures, making the 20% mass concentration unsuitable for liquid flilled window applications. Additionally, the strong absorption of copper ions in the red VIS region leads to an excess of blue light in the transmitted spectrum, resulting in a high T_{mel} value. This imbalance introduces limitations in terms of color rendering and non-visual lighting performance.

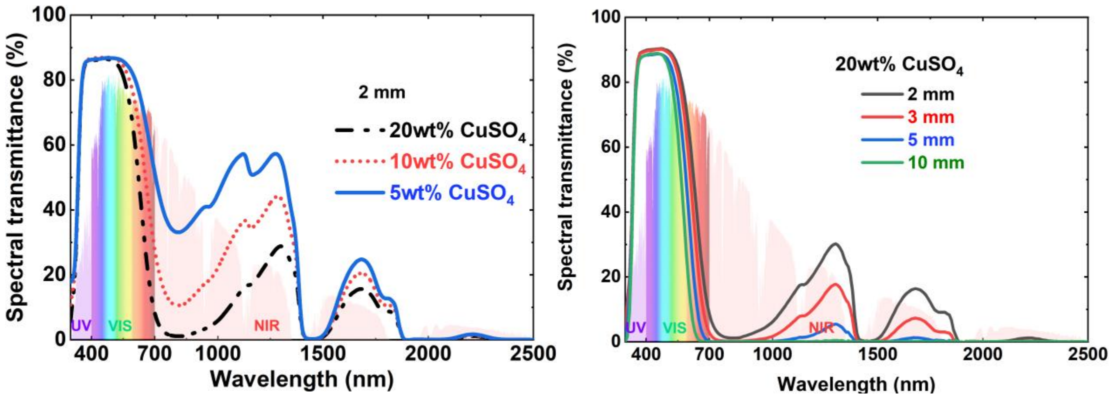

Figure 3.6 Spectral transmittance of $CuSO_4$ aqueous solution with (a) different $CuSO_4{\cdot}5H_2O$ concentration and (b) liquid thickness.

3.3.2 Spectral transmittance of chlorophyll/$CuSO_4$ blended solution

To further enhance the light/heat decoupling capability within the concentration constraints of copper sulfate solution, this study introduces a green plant pigment, i.e., chlorophyll, which can absorb blue light and part of the red-light spectrum. The goal is to refine solar spectrum modulation and achieve precise light/heat decoupling.

Human eyes is most sensitive to green light, as it lies in the middle of the visible spectrum (with a peak sensitivity around 555 nm). This makes green light appear particularly bright and "comfortable". Chlorophyll itself exhibits high transmittance in the green region while effectively absorbing blue light and part of the red-light spectrum (**Figure 3.7**). By balancing the spectral absorption of chlorophyll and copper ions, it is theoretically possible to restore the natural M/P (melanopic-to-photopic) ratio of sunlight, thereby optimizing non-visual effects.

However, as a natural pigment, chlorophyll is prone to photo degradation and oxidation, and it is inherently insoluble in water. To prevent oxidative degradation and to ensure long-term stability, chlorophyll must undergo a copper substitution reaction to form chlorophyll-copper-sodium (SCC), which is water-soluble and exhibits enhanced durability. **Figure 3.7** illustrates the molecular structure of SCC and the corresponding electronic transition characteristics. The electronic transitions from the ground state to excited state 1 and excited state 2 correspond to red and blue light absorption, respectively.

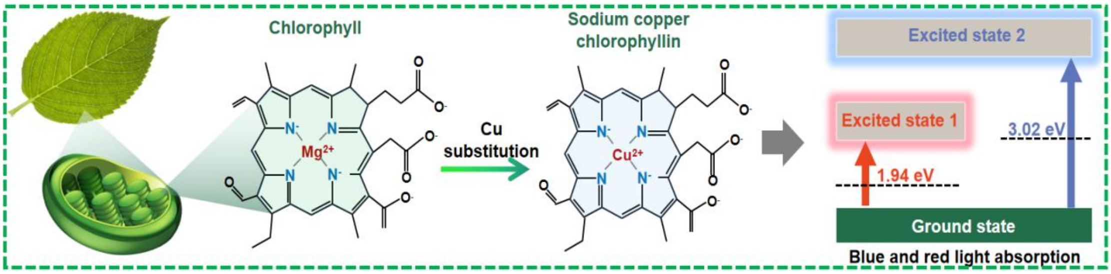

Figure 3.7 Molecular structure of SCC and schematic of its electronic transition

The SCC/$CuSO_4$ aqueous solution combines the absorption features of SCC, Cu^{2+}, and water molecules, enabling broadband absorption across the solar spectrum, including the ultraviolet region, low-visual-sensitivity blue and red light, as well as the NIR range. In the SCC molecule, the porphyrin ring coordinated with copper facilitates electronic transitions that absorb red light (around 640 nm) and blue light (around 410 nm). The [CuO_6] complex formed by Cu^{2+} undergoes *d–d* transitions, absorbing photons with an energy of 1.51 eV, resulting in an absorption peak near 820 nm. Meanwhile, the O–H bonds in water molecules contribute through stretching (v_1), bending (v_2), and asymmetric stretching (v_3) vibrations. Their combination and overtone bands can block a significant portion of infrared radiation with wavelengths greater than 1000 nm. **Figure 3.8** illustrates the spectral absorption characteristics of the SCC and $CuSO_4$ mixed solution.

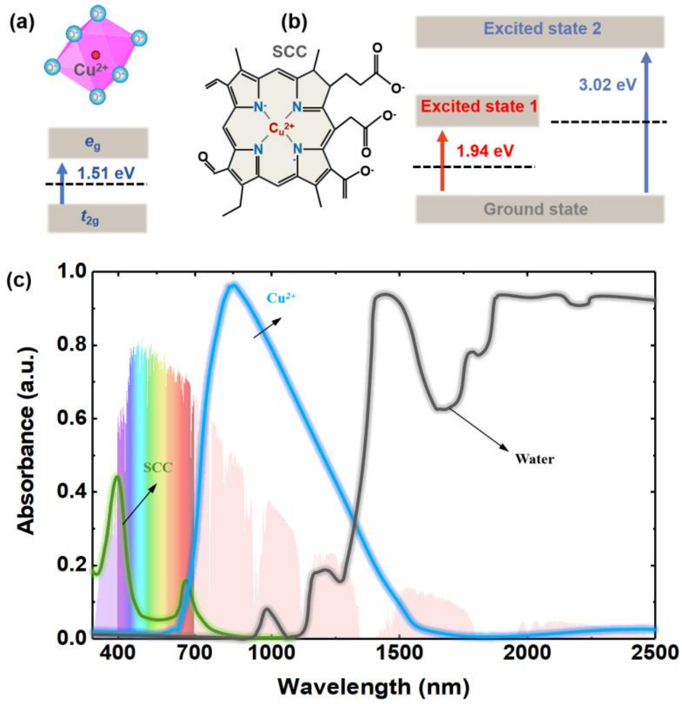

Figure 3.8 (a) Bandgap width of the d-d transition of Cu^{2+}, bandgap widths of SCC and (c) Absorption features of the SCC molecules, Cu^{2+} ions, and water molecules

3.3.3 Preparation of chlorophyll/$CuSO_4$ blended solution

When blending the Cu^{2+} and SCC together, it is important to note that the Cu^{2+} leads to the ionization of water, resulting in a weakly acidic solution. However, the SCC molecules tend to agglomerate into small particles in acidic environments. As illustrated in **Figure 3.9 (a)**, a solution prepared by simply dissolving SCC and Cu^{2+} together in water is unstable and loses absorption in the blue light within 5 months. To ensure long-term optical stability of the blended solution, polysorbate-80 was employed in the preparation process.

The detailed preparing process can be divided into three stages:

(1) **Preparation of highly concentrated (1wt%) SCC emulsion:** 120 g of Polysorbate-80 and 177 ml of deionized (DI) water were mixed in a 75°C-water bath for 1 hour. Then, 3 g of SCC powder was dissolved in the Polysorbate-80/water mixture using a magnetic stirrer for 120 minutes at room temperature.

(2) **Preparation of the $CuSO_4$ solution:** $CuSO_4$ solution was prepared by directly dissolving $CuSO_4 \cdot 5H_2O$ into DI water, with magnetic stirrer for 120 minutes at room temperature.

(3) **Preparation of the SCC/$CuSO_4$ blended solution (SCBS):** The blended solution was prepared by mixing the highly concentrated SCC solution and $CuSO_4$ solution, followed by the addition of water to dilute the solution.

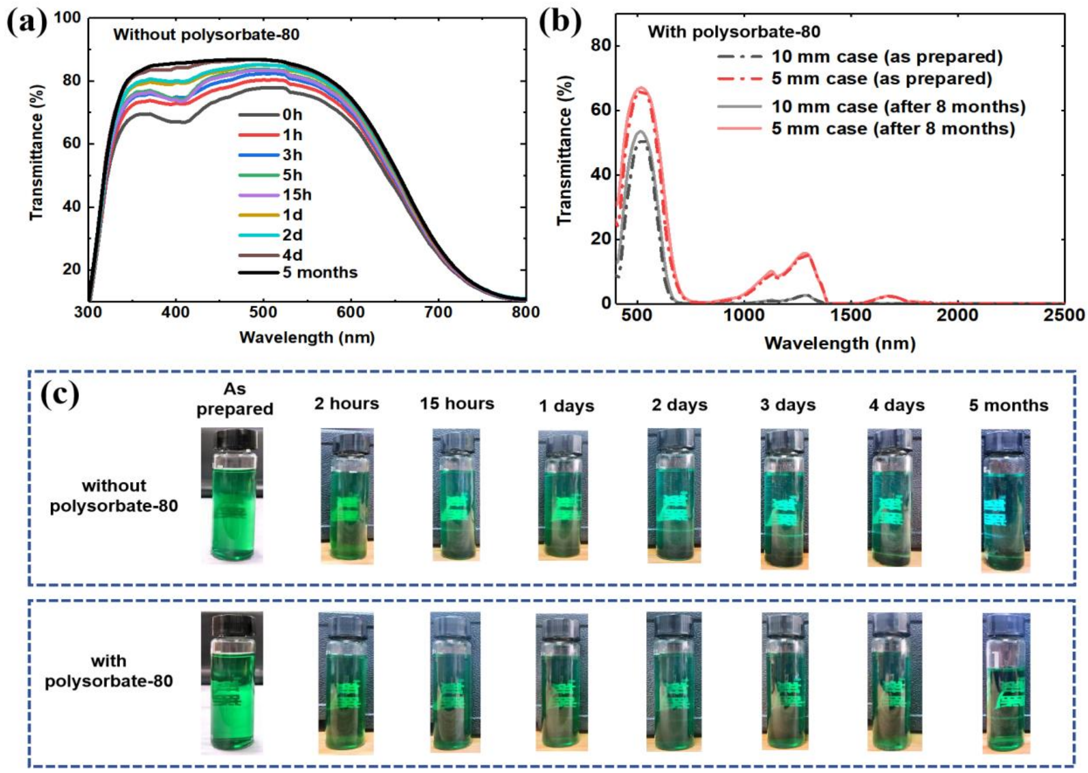

Figure 3.9 (a) Spectral transmittance of the SCBS prepared without polysorbate-80, (b) with polysorbate-80, and (c) the optical photos of the SCBSs.

As depicted in **Figure 3.9 (b)**, the prepared solution with polysorbate-80 exhibited a fairly stable optical transmittance over a period of 8 months. Furthermore, the optical photos in **Figure 3.9 (c)** clearly demonstrate the superior stability of the SCBS prepared with polysorbate-80 compared to the ordinary solution without polysorbate-80, as the solution without polysorbate-80 gradually converted into blue color while the solution with polusorbate-80 always maintain green-blue color.

In addition, due to the presence of UV in the solar spectrum, it is necessary to further evaluate the UV exposure stability of the SCBS. A UV stability test was conducted using a 300 W high-power UV lamp for a 48-hour exposure experiment. As shown in Figure 3.10 (c), the results demonstrate that the proposed mixed solution maintains stable optical performance under intense UV exposure for 48 hours, confirming its excellent ultraviolet stability.

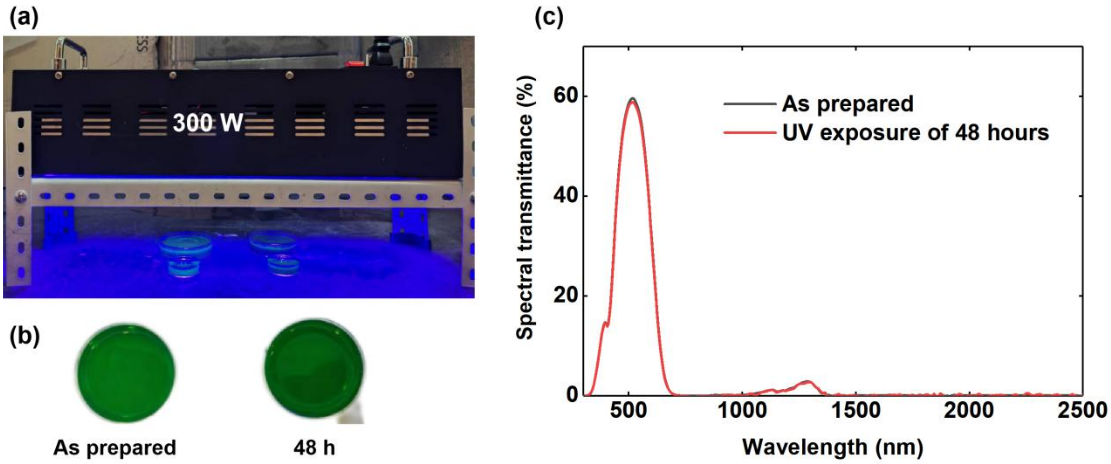

Figure 3.10 (a) experimental rig for UV stability test, (b) optical photos of the 0.05%SC and 10%CuSO4 solutions; (c) results of the UV stability test.

3.3.4 Optical performance of the chlorophyll/$CuSO_4$ blended solution

Figure 3.11 illustrates the spectral transmittances of the SCBSs with different SCC and $CuSO_4$ contents. All the transmittance tests were carried out on the Lambda-950 UV-VIS-NIR spectrophotometer. Since the solutions were intended for use as interlayers in windows, the cuvettes made of glasses were employed as carriers for the solutions, and pure air was used as the background in the transmittance tests. As depicted in Figure 3.11 (a), the $CuSO_4$ solution effectively blocks solar NIR radiation due to the *d-d* transition of Cu^{2+}, which absorbs NIR in the range of 700 to 1400 nm. Additionally, water efficiently filters out NIR with a greater wavelength than 1400 nm. However, it is important to mention that high mass fractions of $CuSO_4$ solution are prone to crystallization and may lead to excessive UV and blue light intensity in the daylight. To address this, SCC, which absorbs short-wave radiation to achieve electronic transitions between excited and ground states, was incorporated to cut down the UV and blue light transmittance. As shown in **Figure 3.11 (b)**, while the SCC solution does not filter solar NIR radiation, it effectively blocks UV and reduces blue light content. Furthermore, blending the $CuSO_4$ and SCC together, as shown in **Figure 3.11 (c)** and **(d)**, enables the blocking of solar NIR, UV, and some blue light. The transmitted spectrum aligns with the photopic luminous efficiency function, ensuring an extremely low SHGC while maintaining a considerable level of visible transmittance.

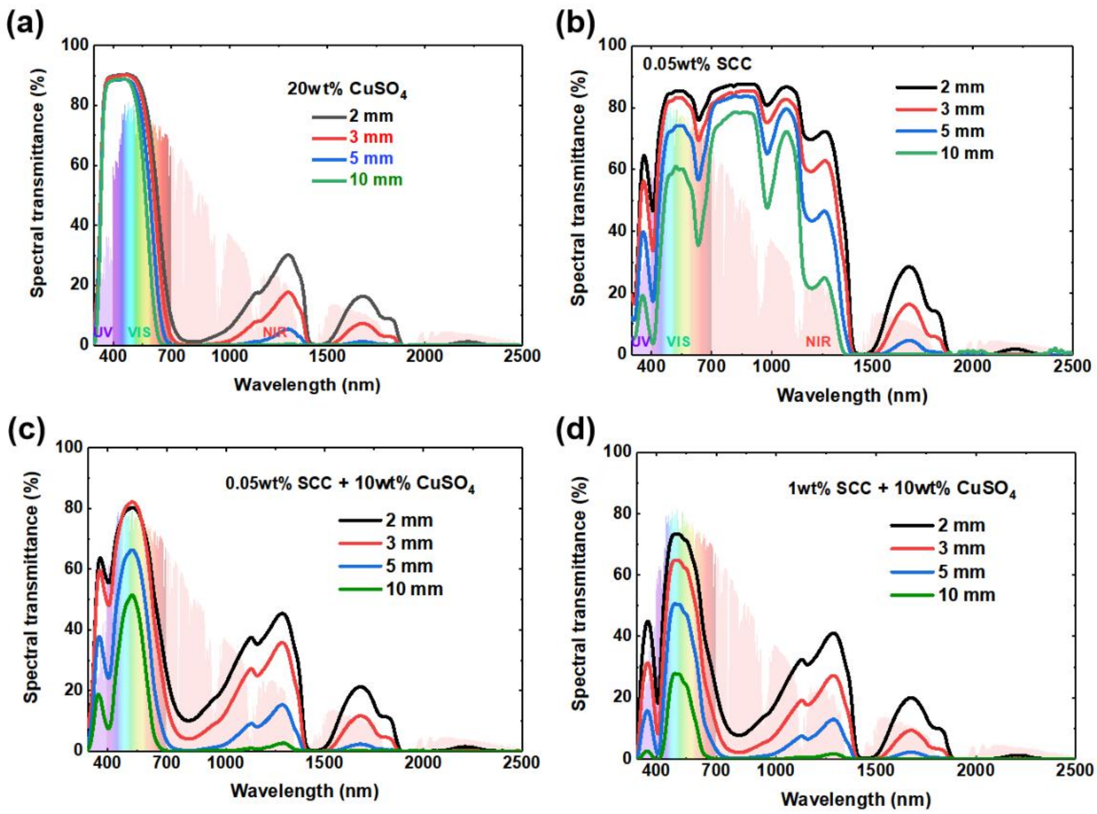

Figure 3.11 Spectral transmittance of different spectrally selective fluids: (a) 20% $CuSO_4$ solution, (b) 0.05% SCC solution, (c) 0.05%SCC/10%$CuSO_4$ solution, (d) 0.1%SCC/10%$CuSO_4$ solution.

Figure 3-12 presents a comparison of the spectral transmittance between the 5 mm-thick 0.05% SCC/10% $CuSO_4$ blended solutions and other typical solar control materials such as ion-based glazing, ITO glazing, ATO-based glazing, and Cs_xWO_3-based glazings. The spectral transmittance data recorded in references **[54, 96, 127, 191]** were collected and partially fitted. Among the curves depicted in **Figure 3-12**, ITO or ATO nanocomposites are ineffective in blocking NIR of 800-1400 nm, although their LSPR efficiently filters out the NIR with wavelengths larger than 1500 nm. Cs_xWO_3-based glazings are excellent in shielding NIR from 800 to 1300 nm, but the poor weathering assessment and expensive cost of Cs_xWO_3 nanoparticles cast a shadow on its large-scale application. In contrast, the SCBS shows a broader absorption range compared to any other counterparts listed in **Figure 3-12**. Although SCBS attenuates some blue and red light, it maintains high transmittance in the green light band, which is highly sensitive to the eyes for providing strong photopic visual effects. Consequently, SCBS holds great promise for energy-efficient windows in hot regions.

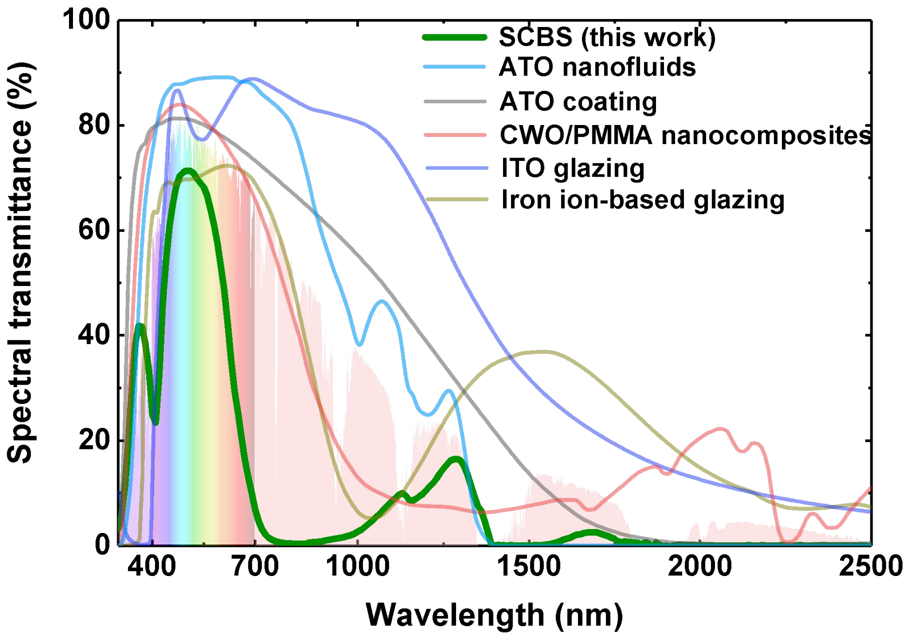

Figure 3.12 Spectral transmittance of windows or glazings with SCBS solution, ATO nanofluids, ATO coating, CWO/PMMA nanocomposites, ITO coating and ion-based glazing.

In this chapter, the FOM is used to evaluate the light/heat decoupling of windows. **Figure 3.13** compares the FOM of the SCBS and other counterparts, including the M_xWO_3, ATO, and transition metallic ion-based glazings. As shown, ATO nanoparticle-based nanofluids or films fail to achieve a higher LSG than 1.60, because the LSPR of ATO nanoparticles is not effective in absorbing NIR between 800 nm and 1400 nm. Metallic ion-based glazings effectively block the *NIR* around 1000 nm, resulting in high LSG values of approximately 1.8. M_xWO_3 nanoparticle-based glazings combine the absorption properties of small polaron transition and LSPR, allowing them to absorb nearly the entire NIR band. However, reported state-of-the-art *LSG* for M_xWO_3-based products, i.e., the Cs_xWO_3 (CWO) glazings, have not exceeded 2.0. Compared with the above counterparts, SCBS could not only filter the NIR, but also block the UV, and shield some blue and red light. It can effectively convert the sun light into a "cold light source", leading to high FOM around 3.0 (**Table 3-8**). This data quantitatively demonstrate that the SCBS offers energy-related advantages over the reported spectrally selective glazings.

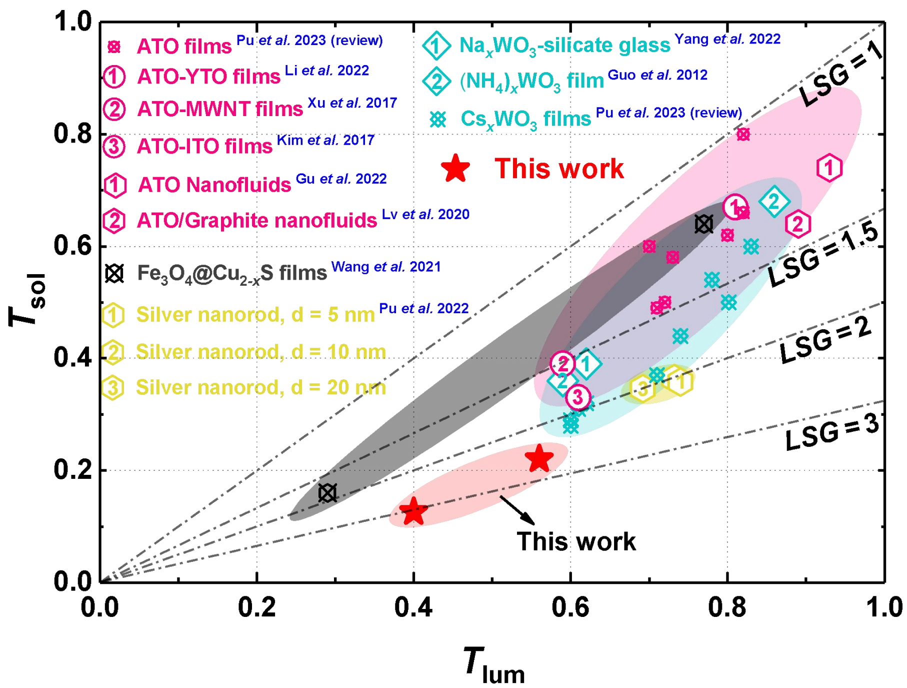

Figure 3.13 Comparison of the performance for the SCBS and other counterparts.

Table 3-8 Detailed optical properties of the spectral splitting fluids with different thickness and different concentration

Thickness	Mass concentration	T_{lum} (%)	T_{sol} (%)	T_{mel} (%)	*FOM*	*M/P*	*CRI*	Color coordinates	
								x	*y*
2 mm	20% $CuSO_4$	74.6	36.5	85.5	2.04	0.96	83	0.29	0.34
	10% $CuSO_4$	80.7	46.2	86.7	1.75	0.90	92	0.31	0.34
	5% $CuSO_4$	84.0	57.7	86.8	1.46	0.87	97	0.32	0.34
	0.15% SCC	64.6	60.2	61.5	1.07	0.80	91	0.34	0.38
	0.10% SCC	70.7	63.1	69.1	1.12	0.82	92	0.33	0.37
	0.05% SCC	79.9	69.2	78.5	1.15	0.83	96	0.33	0.36
	10% $CuSO_4$	84	45.9	90.1	1.83	0.90	91	0.31	0.34
	0.05% SCC/10% $CuSO_4$	74.5	41.1	74.3	1.81	0.84	89	0.32	0.36
	0.1% SCC/10% $CuSO_4$	66.4	34.5	63.4	1.92	0.80	85	0.31	0.37
3 mm	10% $CuSO_4$	81	39.3	90.4	2.06	0.94	88	0.3	0.34
	0.05% SCC/10% $CuSO_4$	74.1	35.6	73.6	2.08	0.83	84	0.31	0.37
	0.1% SCC/10% $CuSO_4$	56.2	24.7	54.1	2.28	0.81	80	0.31	0.38
5 mm	10% $CuSO_4$	78.4	33.7	89.4	2.33	0.96	81	0.28	0.34
	0.05% SCC/10% $CuSO_4$	55.9	21.9	55	2.55	0.83	72	0.30	0.38
	0.1% SCC/10% $CuSO_4$	41	15.1	39.3	2.72	0.81	68	0.29	0.40
10 mm	10% $CuSO_4$	65.1	29.5	88.8	2.21	1.15	68	0.25	0.33
	0.05% SCC/10% $CuSO_4$	38.6	12.6	37.2	3.06	0.81	56	0.27	0.41
	0.1% SCC/10% $CuSO_4$	19.4	6.0	19	3.23	0.82	49	0.26	0.43

3.4 Summary

This chapter focuses on the decoupling of VIS and NIR in the solar spectrum, systematically exploring material design strategies and performance evaluation methods for achieving VIS/NIR decoupling in energy-efficient windows. First, key performance indicators for spectrally selective materials and windows are defined, including solar transmittance, visible light transmittance, SHGC, LSG, FOM, non-visual lighting impact metrics (such as the M/P ratio), and color rendering index (CRI). Next, the VIS/NIR decoupling performance of transition metallic ions and plasmonic nanocomposites is comprehensively compared, revealing the potential limitations of current VIS/NIR decoupling materials. To better meet the decoupling requirements of liquid filled windows, a novel composite material composed of a biomassed dye, i.e., SCC and $CuSO_4$ in aqueous solution is proposed. The study demonstrates that this hybrid solution achieves broadband spectral selectivity for solar energy rejection. By adjusting the concentration and thickness, the SCC/$CuSO_4$ mixed solution can significantly reduce solar heat gain while maintaining high visible light transmittance. The FOM reaches a maximum of 3.06. Furthermore, the mixed solution exhibits excellent stability under ultraviolet exposure and long-term weathering conditions, while maintaining outstanding color rendering and non-visual lighting characteristics, highlighting its strong potential for building applications.

Chapter 4 Liquid-filled static window with spectral regulation of the biomass-derived materials

The spectrally selective fluid proposed in **Chapter 3** of this study can help buildings block NIR radiation, thereby reducing building space cooling energy consumption. However, it is important to note that the fluid achieves energy savings by absorbing NIR, which is then converted into heat. A portion of this heat may be transferred indoors through convection and thermal radiation, leading to secondary solar heat gain. To mitigate this issue, this chapter proposes a liquid-filled window (LFW) with the SCC/$CuSO_4$ blended solution proposed in Chapter 3, to reduce the direct solar heat gain, and then proposes a triple-layered structure to reduce the secondary solar heat gain. To validate the feasibility of this triple-layered LFW, a transient model was developed, considering the dynamic SPDs of solar radiation as well as the impact of varying incident angles on the window's reflective properties. This chapter experimentally validated the model and finally used it to demonstrate the energy-saving performance of the proposed triple-pane LFW in hot climate regions.

4.1 Structural design of a triple-layered liquid filled window (LFW)

This chapter proposes a triple-layered design for spectrally selective LFW. The structure adopts a layered configuration consisting of "glazing-SCC/$CuSO_4$ blended solution (SCBS)-glazing-air-low-e glazing", aiming to effectively reject solar heat, thereby enhancing the thermal management performance of building envelopes.

As illustrated in **Figure 4.1a**, the structure, from exterior to interior, includes: standard clear glazing, a 5 mm-thick layer of 0.05 wt% SCC/10 wt% $CuSO_4$ blended solution, a second layer of clear glazing, an air gap, and a low-e glazing layer.

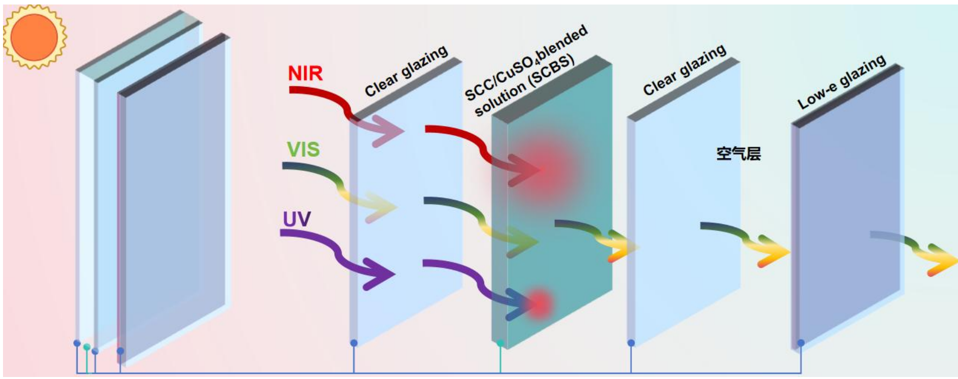

Figure 4.1 Schematic representation of the spectrally selective LFW

Figure 4.2 (a) demonstrates the selective modulation mechanism of this structure across different bands of solar radiation (UV, VIS, NIR). All window layers exhibit high transparency in the VIS spectrum, while NIR radiation is intercepted by the SCBS and converted into heat. To suppress secondary indoor heat gain caused by NIR absorption, the design introduces an air gap to block direct convective heat transfer between the second glazing layer and the indoor space, and a low-e coating to reduce radiative heat transfer.

Figure 4.2 (b) further compares the spectral transmittance performance of standard clear glazing and low-e glazing. Standard glass exhibits high transmittance (over 90%) across the full spectrum. In contrast, low-e glazing maintains high transmittance in the **VIS** range but shows significantly reduced transmittance and enhanced reflectance in the near-infrared region, thereby further minimizing solar heat gain through the window.

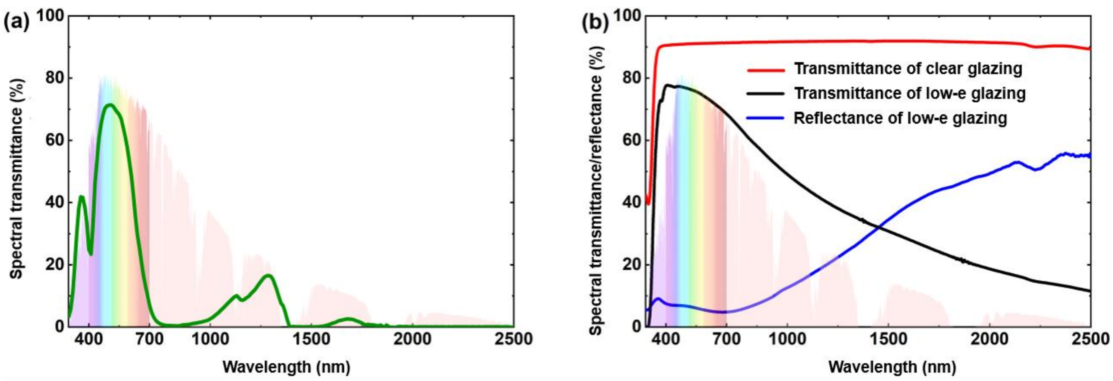

Figure 4.2 (a) Spectral transmittance of the filling fluid; and (b) Spectral transmittance of glazing layers in the in the three-layer LFW.

4.2 Model development

Figure 4.3 (a) shows the structural design of the SCBS-based LFW and Figure 4.3 (b) gives the schematic representation of the developed model. Since the solar regulation of SCBS is achieved by solar radiation absorbing, multi-layered structural design was proposed to avoid secondary solar heat gain from the fluids to indoor environment. In detail, the air gap between glazing 2 and glazing 3 increase the thermal resistance for the SCBS to conduct heat and convective heat transfer towards the indoor side, and a low-e coating was placed in glazing 3 to reject the radiative heat transfer comes from glazing 2. With the window structure shown in Figure 4.3 (a), a transient model was developed.

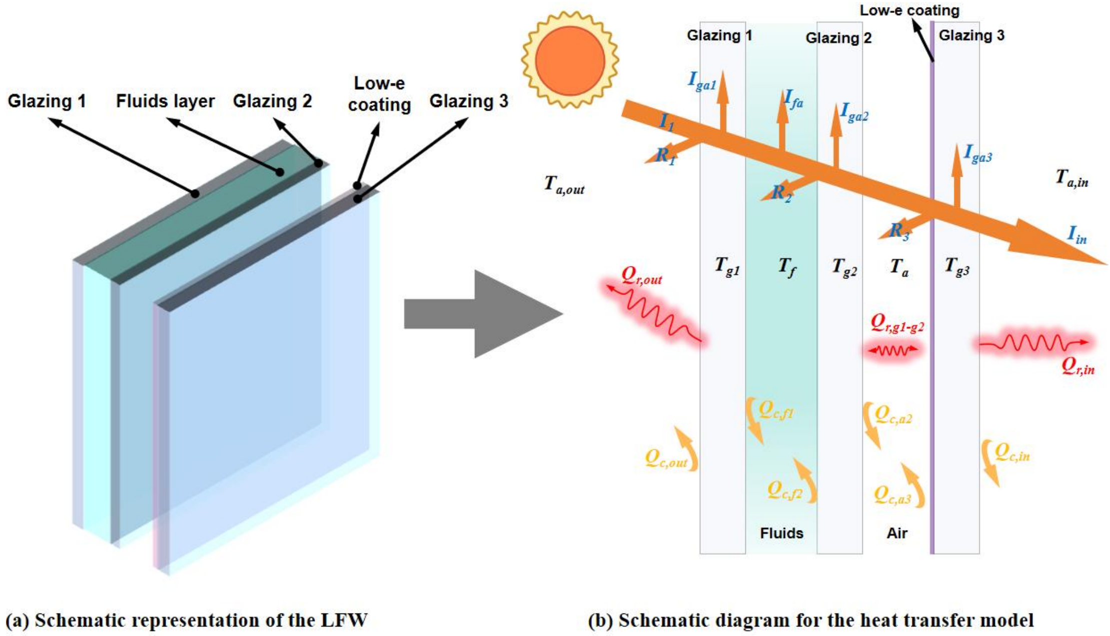

Figure 4.3 Schematic representation heat transfer models for the LFW

Detailed model descriptions are given in Section 4.2.1, and the following assumptions were made during the model development:

1) Fluids and glazings are completely opaque for the long-wave infrared;

2) The window frames are assumed to be thermally insulated;

3) The influence of chlorophyll and polysorbate-80 on the thermophysical properties

of fluids is negligible;

4) When calculating the sky conditions, fixed values are assumed for air humidity and aerosol content, which correspond to the yearly average values.

5) The window is installed on a south-facing facade.

When calculating the optical transmittance of windows, no external shading was considered.

4.2.1 Model description

(1) Optical transmittance/absorbance/reflectance

The reflectance of light at the interface between two media with different refractive indices depends on the angle of incidence and can be calculated by:

$$R_s = \left[\frac{n_1 \cdot \cos(\theta_1) - n_2 \cos(\theta_2)}{n_1 \cdot \cos(\theta_1) + n_2 \cos(\theta_2)} \right]^2 \tag{4-1}$$

$$R_p = \left[\frac{n_2 \cdot \cos(\theta_1) - n_1 \cos(\theta_2)}{n_2 \cdot \cos(\theta_1) + n_1 \cos(\theta_2)} \right]^2 \tag{4-2}$$

$$\frac{\sin(\theta_1)}{\sin(\theta_2)} = \frac{n_1}{n_2} \tag{4-3}$$

$$\rho(\theta) = \frac{1}{2} \cdot \left[R_s(\theta) + R_p(\theta) \right] \tag{4-4}$$

where n_1 and n_2 are the refractive index of air and glazing respectively;

θ_1 and θ_2 are the incidence and refraction angles of direct solar radiation.

Window receives beam radiation and diffuse radiation from sunlight. The following equations give the calculation of solar incident angel of south-facing facade.

$$\theta = \arccos\left[\cos(A_z)\times\cos(h_s)\right] \tag{4-5}$$

$$h_s = \arcsin\left[\sin(\delta)\cdot\sin(\phi)+\cos(\delta)\cdot\cos(\phi)\cdot\cos(H)\right] \tag{4-6}$$

$$A_z = \arccos\left\{\left[\sin(\delta)\cdot\cos(\phi)-\cos(\delta)\cdot\sin(\phi)\cdot\cos(H)\right]/\cos(h_s)\right\} \tag{4-7}$$

$$\delta = 23.44\times\sin\left[\frac{360}{365}\cdot\left(\frac{n}{24}+284\right)\right] \tag{4-8}$$

$$H = 15\times(T_{local}+\frac{l_{standard}-l_{local}}{15}-12) \tag{4-9}$$

where θ (°) is the incident angle of solar radiation on south-facing facade;

$\boldsymbol{h_s}$ (°) is the solar altitude;

$\boldsymbol{A_z}$ (°) is the solar azimuth;

$\boldsymbol{\phi}$ (°) is the solar latitude;

$\boldsymbol{\delta}$ (°) is the solar declination;

$\boldsymbol{n}$ (dimensionless) is the $\boldsymbol{n^{th}}$ hour in a year;

$\boldsymbol{H}$ (°) is the hour angle;

$\boldsymbol{T_{local}}$ (hour) is the local standard time displayed by a clock;

$\boldsymbol{l_{standard}}$ and $\boldsymbol{l_{local}}$ (°) are the longitude of the standard meridian of the time zone and the local longitude.

The diffuse radiation is assumed to be vertically incident into indoor environment. The incident angle of direct solar radiation depends on the solar altitude, and the interfacial reflectance between air-to-glazing or glazing-to-air can be calculated by:

$$\rho_{g-a}(\theta) = \frac{1}{2}\left[\left(\frac{n_a\cos(\theta_a)-n_g\cos(\theta_g)}{n_a\cos(\theta_a)+n_g\cos(\theta_g)}\right)^2+\left(\frac{n_a\cos(\theta_g)-n_g\cos(\theta_a)}{n_g\cos(\theta_a)+n_a\cos(\theta_g)}\right)^2\right] \tag{4-10}$$

where $\boldsymbol{n_a}$ and $\boldsymbol{n_g}$ (dimensionless) are the refractive index of air and glazing;

$\boldsymbol{\theta_a}$ and $\boldsymbol{\theta_g}$ (rad) are the incident and refraction angles of direct solar radiation.

Similarly, the interfacial reflectance between fluids-to-glazing or glazing-to-fluids can be calculated by:

$$\rho_{g-f}(\theta)=\frac{1}{2}\left[\left(\frac{n_f\cos\left(\theta_f\right)-n_g\cos\left(\theta_g\right)}{n_f\cos\left(\theta_f\right)+n_g\cos\left(\theta_g\right)}\right)^2+\left(\frac{n_f\cos\left(\theta_g\right)-n_g\cos\left(\theta_f\right)}{n_g\cos\left(\theta_f\right)+n_f\cos\left(\theta_g\right)}\right)^2\right] \quad (4\text{-}11)$$

where $\boldsymbol{n_f}$ (dimensionless) is the refractive index of filling fluid;

$\boldsymbol{\theta_f}$ (rad) is the incident angles of solar radiation in the filling fluid.

The absorbance of fluids and glazings can by calculated using the following equation:

$$A_{f(g)}(\lambda)=1-e^{-K_{abs,f(g)}(\lambda)\cdot\ S} \quad (4\text{-}12)$$

where $\boldsymbol{K_{abs,f(g)}}$ (dimensionless) is the absorbing coefficient of fluids (glazings);

$\boldsymbol{S}$ (m) is the optical path length.

For clear glazing 1, the transmittance ($\boldsymbol{T_{g1}}$), reflectance ($\boldsymbol{R_{g1}}$) and absorbance ($\boldsymbol{A_{g1}}$) at different incident angle can be calculated by:

$$T_{g,1}(\lambda)=1-A_{g1}(\lambda)-R_{g1}(\lambda) \quad (4\text{-}13)$$

$$\begin{aligned}R_{g,1}&=\rho_{a-g}+(1-\rho_{a-g})^2(1-A_g)^2\rho_{f-g}\sum_{i=1}^{\infty}\left[(1-A_g)^2\rho_{a-g}\rho_{f-g}\ \right]^i\\&=\rho_{a-g}+\frac{(1-\rho_{a-g})^2(1-A_g)^2\rho_{f-g}}{1-(1-A_g)^2\rho_{a-g}\rho_{f-g}}\end{aligned} \quad (4\text{-}14)$$

$$A_{g1}(\lambda)=\frac{A_g(\lambda)(1-\rho_{a,g})+A_g(\lambda)(1-\rho_{a,g})[1-A_g(\lambda)]\rho_{f,g}}{1-[1-A_g(\lambda)]^2\rho_{a,g}\rho_{f,g}} \quad (4\text{-}15)$$

For clear glazing 2, the transmittance ($\boldsymbol{T_{g1}}$), reflectance ($\boldsymbol{R_{g1}}$) and absorbance ($\boldsymbol{A_{g1}}$) at different incident angle can be calculated by:

$$T_{g,2}(\lambda)=1-A_{g2}(\lambda)-R_{g2}(\lambda) \quad (4\text{-}16)$$

$$R_{g2} = \rho_{f-g} + \frac{(1-\rho_{f-g})^2(1-A_g)^2\rho_{a-g}}{1-(1-A_g)^2\rho_{a-g}\rho_{f-g}} \tag{4-17}$$

$$A_{g2}(\lambda) = \frac{A_g(\lambda)(1-\rho_{f,g}) + A_g(\lambda)(1-\rho_{f,g})[1-A_g(\lambda)]\rho_{a,g}}{1-[1-A_g(\lambda)]^2\rho_{a,g}\rho_{f,g}} \tag{4-18}$$

For low-e glazing 3, since the low-e glazing shows uniform transmittance in the visible light band, the refractive index in the visible band is considered to be a fixed value of $\boldsymbol{n}_{\textbf{low-e,vis}}$. On the other hand, although the spectral transmittance of the low-e glazing in the NIR band is nonuniform, the low-e glazing receives negligible amount of NIR radiation because of the absorption by fluids layer. Thus, to simplify the calculation, the refractive index in the *NIR* of low-e layer is considered to be a fixed value equal to the average mean value. Then the transmittance, reflectance and absorbance of the low-e glazing is calculated by:

$$T_{g,3}(\lambda) = 1 - A_{g3}(\lambda) - R_{g3}(\lambda) \tag{4-19}$$

$$R_{g3} = \rho_{a-e} + \frac{(1-\rho_{a-e})^2(1-A_e)^2\rho_{a-g}}{1-(1-A_e)^2\rho_{a-g}\rho_{a-e}} \tag{4-20}$$

$$A_{g3}(\lambda) = \frac{A_e(\lambda)(1-\rho_{a-e}) + A_e(\lambda)(1-\rho_{a-e})[1-A_e(\lambda)]\rho_{a-g}}{1-[1-A_e(\lambda)]^2\rho_{a-e}\rho_{a-g}} \tag{4-21}$$

(2) Solar radiation

In this study, the solar radiation of the typical year file for Hong Kong was adapted, and it was obtained from the official websites of Energyplus. The solar absorbance and transmittance are determined by the spectral power distribution, and the solar spectral power distribution is determined by the SMART model. Detailed calculations are depicted in **Refs. [196, 197]**.

$$I(\lambda) = \Phi(\lambda)\cdot T_R(\lambda)\cdot T_O(\lambda)\cdot T_N(\lambda)\cdot T_G(\lambda)\cdot T_W(\lambda)\cdot T_A(\lambda) \tag{4-22}$$

where **Φ(*λ*)** [W/(m^2·nm)] is the solar irradiation spectrum outside the atmosphere;

T_R (dimensionless) is the spectral transmittance after Rayleigh scattering;

T_O (dimensionless) is the transmittance after the O_2 absorption;

T_N (dimensionless) is the transmittance after the N_2 absorption;

T_G (dimensionless) is the transmittance after the O_2 absorption;

T_W (dimensionless) is the transmittance after the water vapor absorption;

T_A (dimensionless) is the transmittance after the Aerosol extinction;

Figure 4.4 illustrates the spectral power distribution of solar radiation under clear-sky conditions, including direct radiation (**Figure 4.4 a**) and diffuse radiation (**Figure 4.4 b**). The direct solar radiation exhibits the highest intensity in the visible region, with multiple absorption bands in the ultraviolet and infrared regions caused by atmospheric components such as oxygen and water vapor. In contrast, diffuse radiation, influenced by Rayleigh scattering and aerosols, shows a smoother spectral curve, with a higher proportion of shortwave components and relatively weak infrared radiation. However, under non-clear weather conditions, the spectral distribution of diffuse solar radiation differs significantly from that shown in **Figure 4.4 b**.

Due to the uniform scattering of sunlight by cloud layers, the diffuse spectrum more closely resembles the direct solar spectrum. Therefore, in the model calculations presented in this study, the spectral power differences between direct and diffuse radiation are not distinguished. Instead, the total solar spectral power distribution is used to represent both components, as shown in **Figure 4.5**.

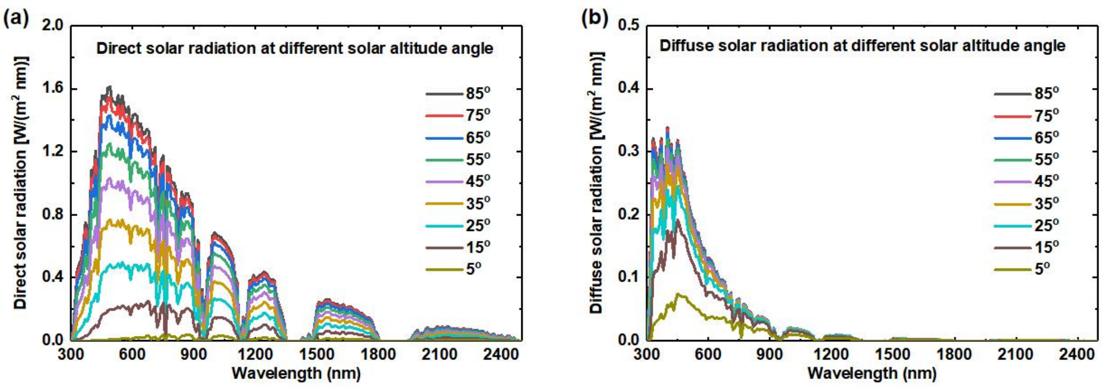

Figure 4.4 Spectral power distribution of (a) direct and (b) diffuse solar radiation

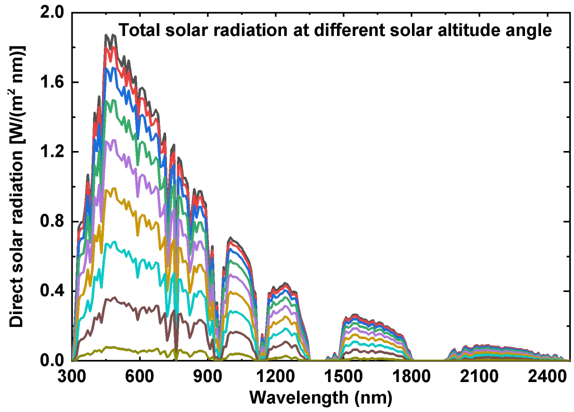

Figure 4.5 Spectral power distribution of total solar radiation

Then the solar radiation received by the building facade facing south can be calculated by:

$$I_1(\lambda) = I(\lambda) \cdot \cos(\theta) / \sin(H) \tag{4-23}$$

For glazing 1, the total amount of direct solar radiation, which compromises of the incident radiation in the front face and the reflected radiation in the back face, can be calculated by:

$$\Phi_{g1}(\lambda) = \Phi(\lambda) + R_{g2-g3} \cdot (1-A_f)^2 \cdot \frac{T_{g1} \cdot \Phi(\lambda)}{1-(1-A_f)^2 \cdot R_{g1} \cdot R_{g2-g3}} \tag{4-24}$$

$$R_{g2-g3} = R_{g2} + \frac{T_{g2}{}^2 \cdot R_{g3}}{1-R_{g2} \cdot R_{g3}} \tag{4-25}$$

For fluids layer, the total of radiation energy received can be calculated by:

$$\Phi_f(\lambda) = R_{g2-g3} \cdot (1-A_f) \cdot \frac{T_{g1} \cdot \Phi(\lambda)}{1-(1-A_f)^2 \cdot R_{g1} \cdot R_{g2-g3}} + \frac{T_{g1} \cdot \Phi(\lambda)}{1-(1-A_f)^2 \cdot R_{g1} \cdot R_{g2-g3}} \tag{4-26}$$

For glazing 2, the total amount of radiation received can be calculated by:

$$\Phi_{g2}(\lambda)=\frac{T_{g1}\cdot\ \Phi(\lambda)\cdot\ (1-A_f)}{1-(1-A_f)^2\cdot\ R_{g1}\cdot\ R_{g2-g3}}+R_{g3}\cdot\ \Phi_{g3}(\lambda) \tag{4-27}$$

For glazing 3, the total amount of direct radiation arriving the front face can be calculated by:

$$\Phi_{g3}(\lambda)=\frac{T_{g1-g2}\cdot\ \Phi(\lambda)}{1-R_{g1-g2}\cdot\ R_{g3}} \tag{4-28}$$

where $\boldsymbol{R_{g1\text{-}g2}}$ is the total reflectance of glazing 1, the fluids layer and glazing 2:

$$R_{g1-g2}=R_{g1}+\frac{T_{g1}^2\cdot\ (1-A_f)^2\cdot\ R_{g2}}{1-(1-A_f)^2\cdot\ R_{g1}\cdot\ R_{g2}} \tag{4-29}$$

(3) Heat transfer equations

For glazing 1: the temperature changes of each time step can be calculated by:

$$\begin{aligned} m_g c_g\frac{dT_{g1}}{dt} &= A_{g1}\cdot\Phi_{g1}-\frac{1}{\dfrac{1}{h_{c,g-a1}}+\dfrac{\sigma_g}{2\lambda_g}}(T_{g1}-T_{a,out}) \\ &\quad -\frac{1}{\dfrac{1}{h_{c,g-f}}+\dfrac{\sigma_g}{2\lambda_g}}(T_{g1}-T_f)-Q_{r,out} \end{aligned} \tag{4-30}$$

where $\boldsymbol{\sigma_g}$ (m) represents the glazing's thickness;

$\boldsymbol{\lambda_g}$ [W/(m·K)] represents the thermal conductivity;

$\boldsymbol{T_{g1}}$ (°C) represents the temeperature of glazing 1;

$\boldsymbol{T_{a,out}}$ (°C) represents the ambient air temperature;

$\boldsymbol{m_g}$ (kg) is the mass of glazing;

$\boldsymbol{c_g}$ [J/(kg·K)] is the specific heat capacity of glazing.

The air-to-glazing convective heat transfer coefficient is determined by the wind speed, and can be estimated by:

$$h_{c,g-a1} = \begin{cases} 2.8 + 3 \cdot v_a, \ if\, v_a < 5m/s \\ 6.15 \cdot v_a^{0.8}, \ if\, v_a > 5m/s \end{cases} \tag{4-31}$$

where $\boldsymbol{v}_{\mathbf{a}}$ (m/s) represents the air velocity.

The fluids-to-glazing convective heat transfer coefficient can be estimated by:

$$h_{c,f-ga1} = \frac{Nu_f \cdot \lambda_f}{\sigma_f} \tag{4-32}$$

$$\begin{cases} N_{u,g-f} = 1 & Ra \le 10^3 \\ N_{u,g-f} = 0.22(\frac{\Pr}{0.2+\Pr} Ra)^{0.28} (\frac{H}{\delta_g})^{-0.25} & Ra > 10^3, \ 1 < \frac{H}{\delta_g} < 10 \\ N_{u,g-f} = 0.42 Ra^{0.25} \Pr^{0.012} (\frac{H}{\delta_g})^{-0.3} & Ra > 10^3, \ \frac{H}{\delta_g} > 10 \end{cases} \tag{4-33}$$

The radiative energy loss from outer glazing (glazing 1) to outer space is determined by:

$$Q_{r,out} = \alpha \cdot \varepsilon_g \cdot \delta (T_{g1}^4 - T_{sky}^4) \tag{4-34}$$

where $\boldsymbol{T}_{sky}$ (°C) represents the sky temperature.

For fluids layer: the temperature changes of each time step can be calculated by:

$$m_f c_f \frac{dT_f}{dt} = A_f \Phi_f + \frac{1}{\frac{1}{h_{c,g-f}} + \frac{\sigma_g}{2\lambda_g}} (T_{g1} + T_{g2} - 2 \cdot T_f) \tag{4-35}$$

For glazing 2: the temperature changes of each time step can be calculated by:

$$m_g c_g \frac{dT_{g2}}{dt} = A_{g2}\Phi_{g2} - \frac{1}{\frac{1}{h_{c,g-a}} + \frac{\sigma_g}{2\lambda_g}}(T_{g2} - T_{g3}) - \frac{1}{\frac{1}{h_{c,g-f}} + \frac{\sigma_g}{2\lambda_g}}(T_{g2} - T_f) - Q_{r,g2-g3} \tag{4-36}$$

$$h_{c,ga} = \frac{\sigma_a}{Nu_a \cdot \lambda_a} \tag{4-37}$$

where $\boldsymbol{Nu_a}$ can be evaluated by:

$$Nu_a = \begin{cases} 1, & if \;\; Gr_\sigma \le 2000 \\ 0.197 \cdot (Gr_\sigma \cdot \Pr)^{1/3}(\frac{\sigma}{H})^{1/9} & if \;\; 6000 < Gr_\sigma \cdot \Pr < 1.1 \times 10^7; 11 < \frac{H}{\sigma} < 42 \\ 0.073 \cdot (Gr_\sigma \cdot \Pr)^{1/3}(\frac{\sigma}{H})^{1/9} & if \;\; 2 \times 10^5 < Gr_\sigma \cdot \Pr < 1.1 \times 10^7; 11 \le \frac{H}{\sigma} \le 42 \end{cases} \tag{4-38}$$

The radiative energy loss from the clear glazing (glazing 2) to the low-e glazing (glazing 3) can be expressed by:

$$Q_{r,g2-3} = \frac{1}{\frac{1}{\varepsilon_g} + \frac{1}{\varepsilon_e} - 1}\delta(T_{g2}^4 - T_{g3}^4) \tag{4-39}$$

For glazing 3: the temperature changes of each time step can be calculated by:

$$m_g c_g \frac{dT_{g3}}{dt} = A_{g3}\Phi_{g3} + Q_{r,g2-g3} + \frac{1}{h_{c,a} + \frac{\sigma_g}{2\lambda_g}}(T_{g2} - T_{g3}) - Q_{r,in} \tag{4-40}$$

4.2.2 Computational method

According to the model developed in **Section 4.2.1**, the MATLAB code was generated to calculate the annual performance of the LFW, using the meteorological date reported by Energyplus. The data used in this study are linearly interpolated with a time step of 1 s, and **Figure 4.6** shows the general flow chart of the calculation process.

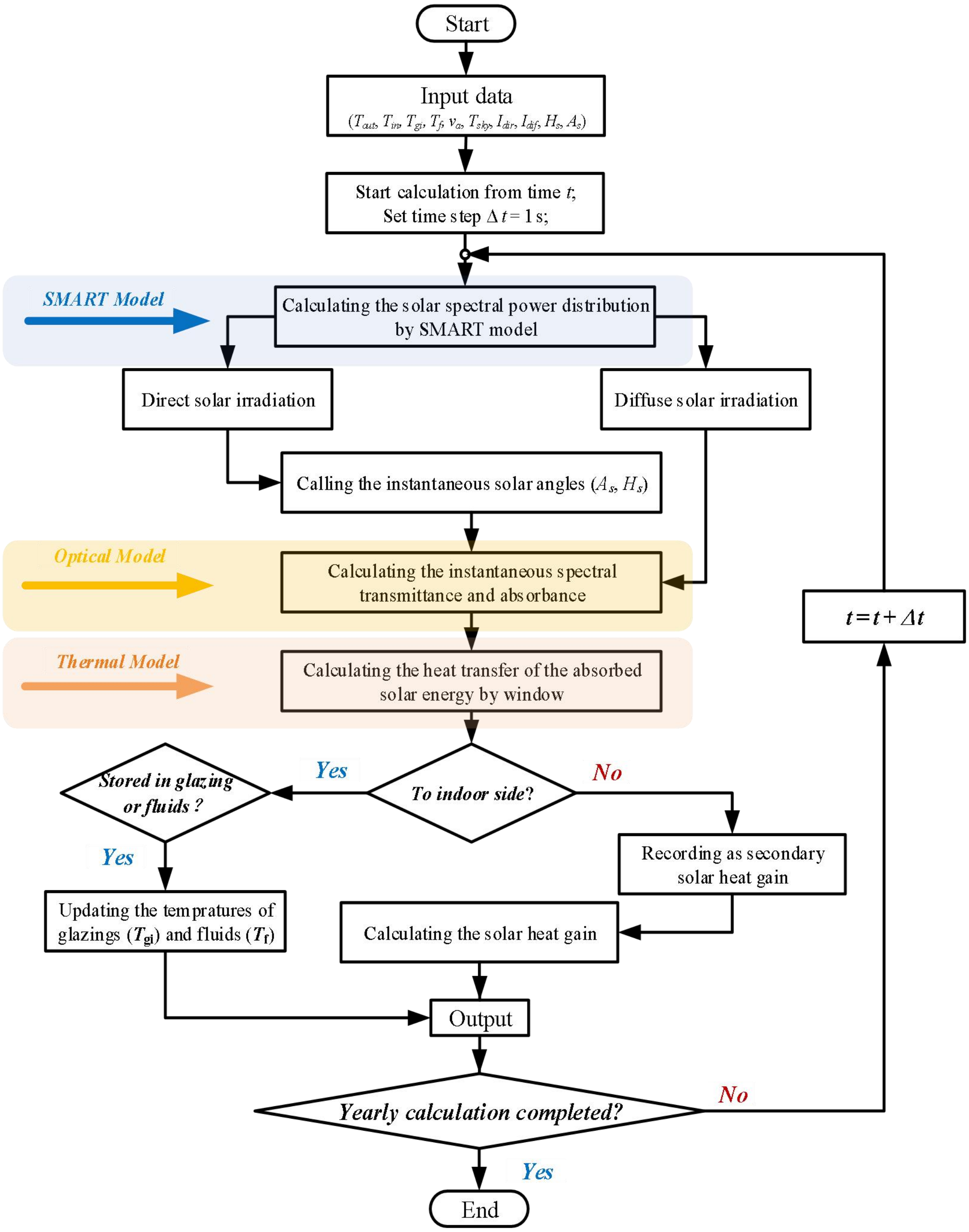

Figure 4.6 Flow chart for calculating the annual performance of the LFW

4.2.3 Experimental validation of the developed model

To demonstrate the accuracy of the developed model, experiments were carried out on a scaled chamber. The layout of the sensors in the experiments is given in **Figure 4.7 (a)**, and **Figure 4.7 (b)** shows the photo of the experimental rig. In the experimental chamber, the double pane liquid flow window with 3 mm-thick SCBS was installed in the south face, with dimensions of 20 cm (width) × 20 cm (height). During the test, the ambient air temperature, outdoor illuminance level, indoor air temperature, indoor illuminance and the inner/outer surface temperature of the glazings were recorded. **Figure 4.7 (c)** and **(d)** present the comparison on the surface temperatures of the inner and outer glazing pane. **Table 4-1** gives the detailed parameter setting of the model. As shown, the calculated data agreed well with the experimental data, showing an average temperature deviation of 0.31 °C for the outer pane and 0.02 °C for the inner pane. This result indicates that the developed model can accurately predict the optical and thermal performance of liquid-filled windows.

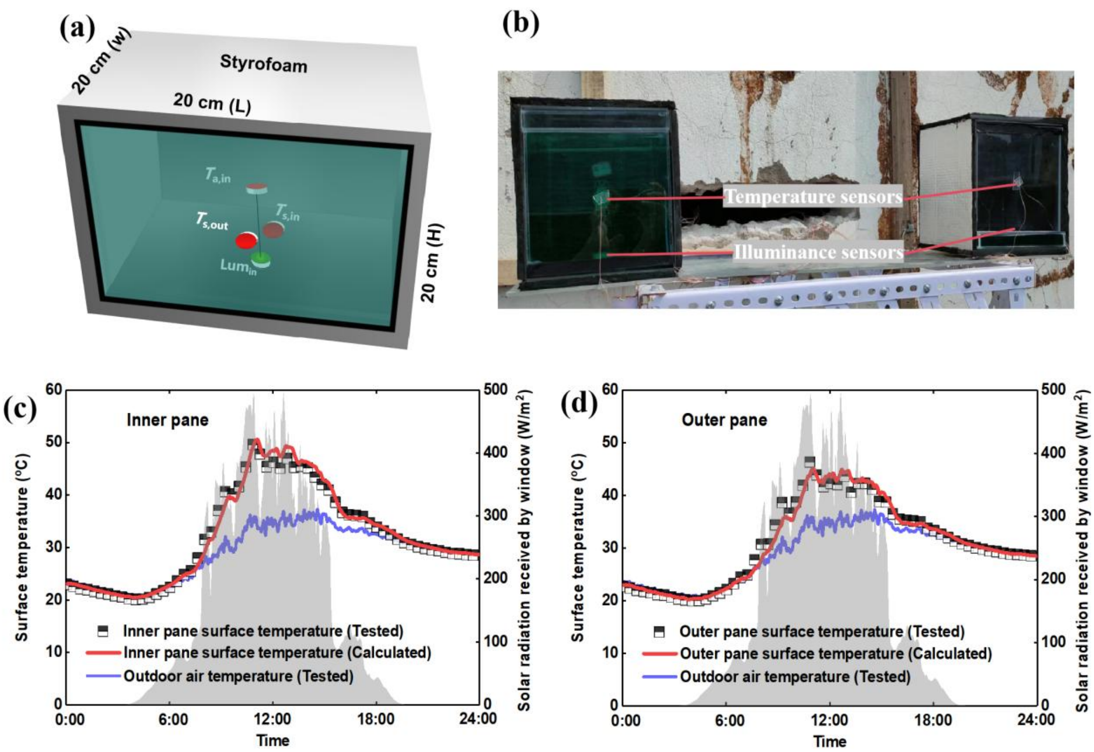

Figure 4.7 (a) Schematic of the layout of the experimental chamber; (b) photos of the experimental rig; (c) comparisons of the inner and outer pane surface temperatures of the tested window with SCBS**.**

Table 4-1 Parameter settings of the simulation.

Components	Parameters	Values
Glazing	Refractive index ($\boldsymbol{n_g}$)	1.51
	IR emissivity ($\boldsymbol{\varepsilon_g}$)	0.84
	Density ($\boldsymbol{\rho_g}$)	2.5×10^3 kg/m^3
	Length × height × thickness	4 mm × 200 mm × 200 mm
	Specific heat capacity ($\boldsymbol{c_g}$)	800 J/(kg·K)
Air gap	Thickness ($\boldsymbol{d_a}$)	12 mm
Filling fluids	Material	0.1wt%SCC/10wt%$CuSO_4$
	Thickness ($\boldsymbol{d_f}$)	3 mm
	Refractive index ($\boldsymbol{n_f}$)	1.32

4.3. Results and discussion

Hong Kong is a typical city with hot and humid climate conditions, where windows with low SHGC can contribute to the energy-saving for most of the year. In this study, the energy-saving performance of the SCBS-based LFW with the 3 mm-thick 0.1%SCC/10%$CuSO_4$ solution in Hong Kong was investigated numerically. The hourly weather data of the typical year of Hong Kong was obtained from the official websites of Energyplus, and the weather data was divided linearly with a time-step of 1 second. To showcase the energy-saving capabilities of the SCBS-based LFW, a triple layered clear window was used as the baseline for comparison. In **Section 4.1** the daylighting performances were discussed, and **Section 4.2** gives energy-related performances analysis.

4.3.1 Daylighting performance

Good daylighting performance is the primary concern of building windows. The 3 mm-thick 0.1%SCC/10%$CuSO_4$ solution filled double-layered window could have a good luminous transmittance above 56% in vertical incidence conditions. But when considering the increase of optical path length in the **SCBS** and the Fresnel reflection caused by the obliquely incidence of light **[198]**, the luminous transmittance of the

LFW may be further decreased, which would negatively affect the indoor luminous gain. To investigate whether the SCBS-based LFW is feasible in building daylighting, the indoor total luminous gain, which compromises solar direct luminous gain and diffuse luminous gain, was calculated. Figure 4.8 shows the calculated results on the design days (Jan 21 for winter and Jul 21 for summer). As seen, the highest luminous level appears at about 13:00 on the winter design day and 12:00 on the summer design day. For the 1 m^2 SCBS-based LFW, the highest indoor luminous gains are about 30324 lum and 16783 lum for winter and summer design days respectively, which reduces the total luminous gain by 41.5% and 53.3% when compared with the values of triple layered clear window (51834 lum and 35961 lum). In comparison to a previous study conducted by the present authors [190], it can be found that the luminous attenuation caused by SCBS is smaller than that of the ATO nanofluids, demonstrating that SCBS has advantages in daylighting over traditional ATO materials.

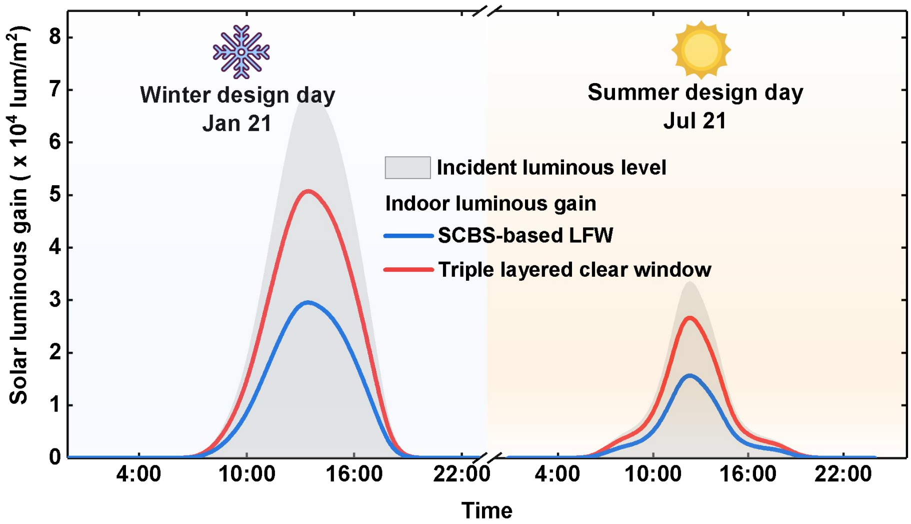

Figure 4.8 Indoor luminous gain for the SCBS-based LFW and triple layered ordinary window on the design days in Hong Kong

According to related standards for windows' transmittance, a higher luminous transmittance level than 40% must be achieved for buildings with large window area [199]. The calculated luminous transmittance shows an acceptable level of about 46.7% on the winter design day and 42.7% on the summer day. Figure 4.9 further lists the monthly average luminous transmittance of the SCBS-based LFW and the triple-layered clear window respectively. These values fluctuate in different months because the ratio of direct to diffuse solar radiation and the solar altitude are dynamic in different months, which would further lead to constantly changing solar reflectance and solar absorption of the window. However, results show that the SCBS-based LFW can ensure a feasible daylighting level with luminous transmittance higher than 0.4 for all the 12 months.

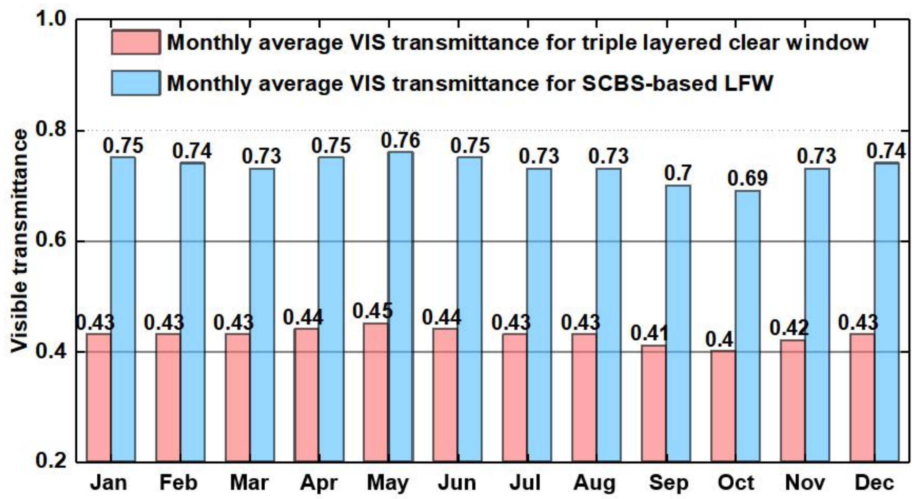

Figure 4.9 Monthly average luminous transmittance of the **SCBS**-based **LFW** and triple-layered clear window

4.3.2 Energy-saving performance

Figure 4.10 compares the temperature of SCBS liquid, the inner and outer surface temperatures of the LFW and the triple-layered clear window on the design days. The highest temperature of the SCBS in winter could be about 46.4 °C, which is higher than the highest point of the summer design day (43.6 °C). This is attributed to the greater solar altitude angle in winter that can enable the vertical south surface to receive a higher level of solar flux than summer days. The surface temperatures of the LFW and the clear window show a similar fluctuation law to the temperature of outdoor temperature. The peaks appear at the same time but with obvious differences in values. At nighttime, the outer surface temperatures for the LFW and clear window are lower than the outdoor air temperature, mainly because that the high emissivity of outer glazing pane would passively emit long-wave thermal energy to outer space. The LFW results in a higher inner surface temperature than the clear window, which indicates that the LFW would cause a higher level of secondary heat transfer to indoor environment. On the winter design day, the LFW's inner surface temperature could be about 5.1 °C higher, but it still remains lower than 26 °C. This feature ensures that the secondary heat transfer near the window does not have any detrimental effects on the thermal comfort [34].

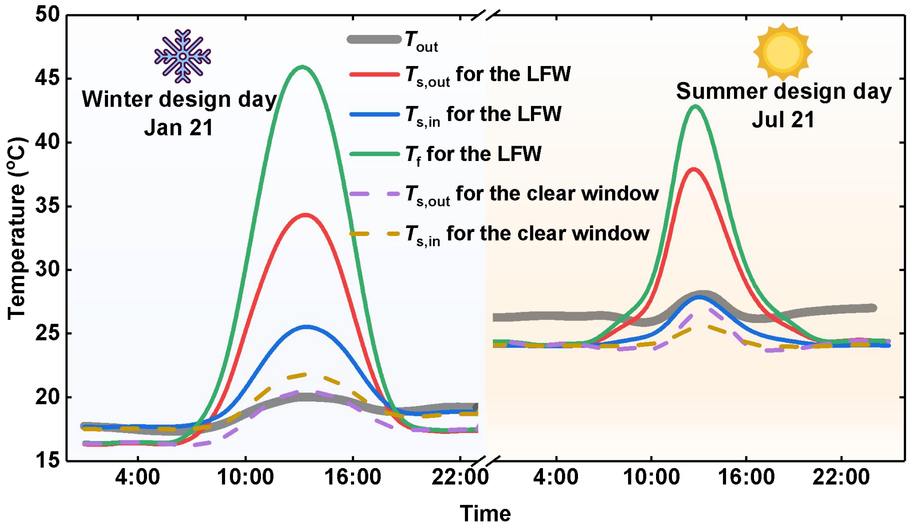

Figure 4.10 Indoor luminous gain for the SCBS-based LFW and triple layered clear window on the design days in Hong Kong

Figure 4.11 (a) and (b) depict the solar heat gains of the SCBS-based LFW and clear window on the winter and summer design days (Jan 21 and Jul. 21). On the winter design day, the highest value of the total solar heat gains appears at around 12:00, which is 147.6 W/m^2 for the LFW and 455.8 W/m^2 for the clear window. On the summer design day, the value for the LFW and clear window are 84.0 W/m^2 and 251.9 W/m^2 respectively, which indicate that the LFW positively reduces the space cooling load in Hong Kong. On the other hand, the highest value of the secondary heat transfer rate from the LFW's inner pane to indoor environment is about 24.9 W/m^2 and 17.1 W/m^2 for the winter and summer design days respectively. These values are smaller than the threshold that would cause uniform building environments to decrease human thermal comfort [200].

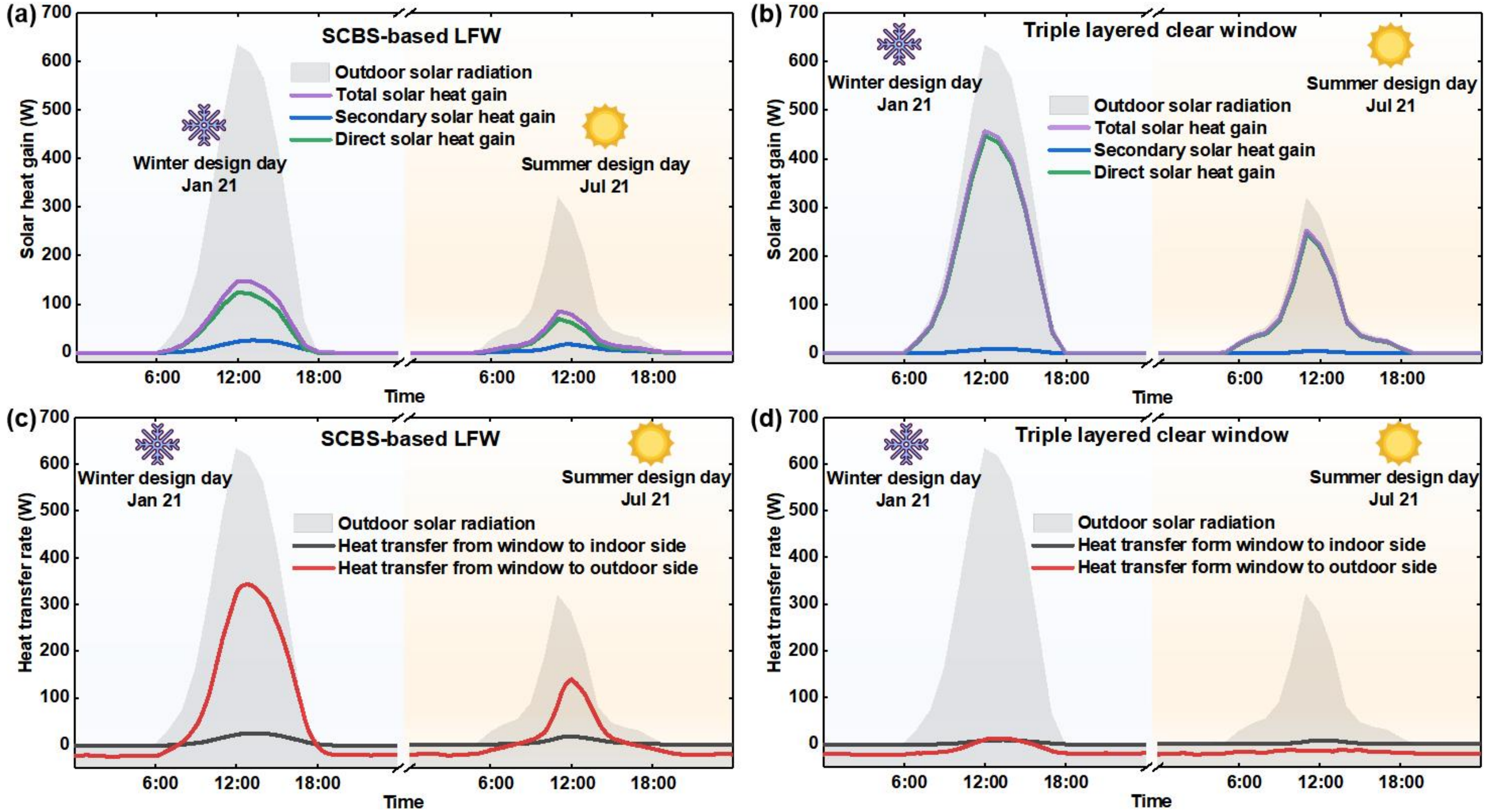

Figure 4.11 **(a)** Indoor solar gain of the SCBS-based LFW; **(b)** the clear window; **(c)** heat transfer from window to indoor and outdoor environments for the SCBS-based LFW; and **(d)** heat transfer from window to indoor and outdoor environments for the triple layered clear window.

Figure 4.11 (c) and **(d)** compare the heat transfer rate between windows to indoor and outdoor environment for the SCBS-based LFW and the clear window respectively. As shown in **Figure 7**, since the air gap between the mid glazing and inner glazing insulates the convection and conduction heat transfer, and the low-e coating in the inner glazing rejects the long-wave radiative heat transfer, most of the absorbed solar energy by the LFW would be dissipated to the outdoor environment. As shown in **Figure 4.11 (c)**, during noon time, the heat transfer from the LFW to the outdoor environment is about 342 W/m^2 for at around 13:00 on the winter design day, at the same time, the heat transfer rate from the LFW to the indoor side is only about 24.6 W/m^2. In the evening time, due to passive radiative energy loss from the outer glazing pane to the outdoor space, the temperature of the outer glazing is lower than ambient environment temperature, thus the heat transfer rate is minus in value.

Figure 4.12 shows the average indoor solar heat gain of each month, including both the direct beam and diffuse solar heat gain of the LFW and clear window. The solar heat gains of the LFW in Hong Kong fluctuate between 62.2 MJ/(m^2·month) to 94.0 MJ/(m^2·month), while the values of the triple-layered clear window are in the range of 181 MJ/m^2 to 267 MJ/m^2. The annual solar heat gains are about 912.7 MJ/m^2 for the LFW and 2630.5 MJ/m^2 for the triple-layered clear window, demonstrating that the LFW design can effectively reduce the indoor solar heat gain by about 65% (1717.8 MJ/m^2) in Hong Kong.

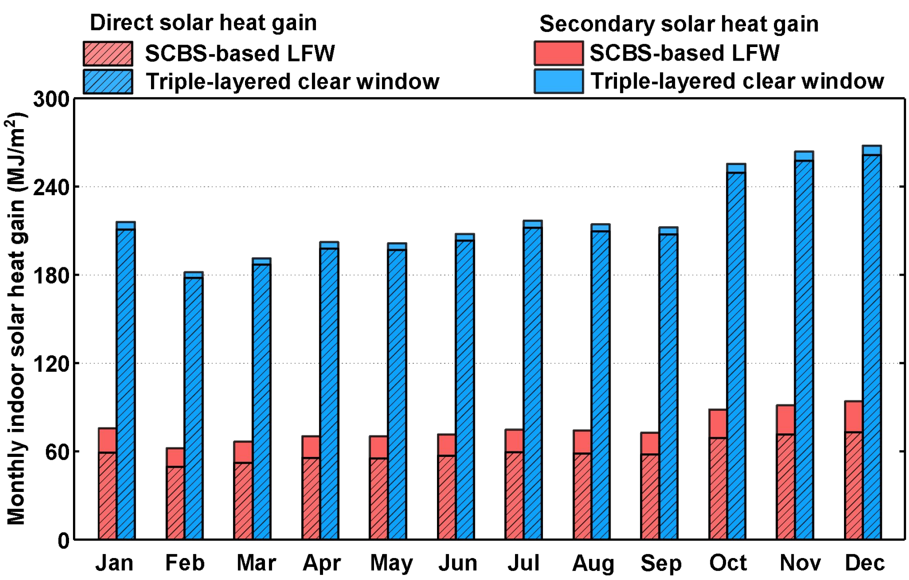

Figure 4.12 Monthly average solar heat gain of the **LFW** and clear window

On the other hand, due to the radiation transmittance/reflectance behaviors changing with incident angle-dependent, the SHGC value is dynamic in different seasons. As compared in **Figure 4.13**, from January to December, the SHGC fluctuates between 0.68 to 0.74 for the clear window, and between 0.24 to 0.26 for the LFW. The results also show that the annual average SHGC value of the LFW is about 0.25, which is more promising than the state-of-the-art low-e windows [12, 201] and other heat absorbing windows [36, 38].

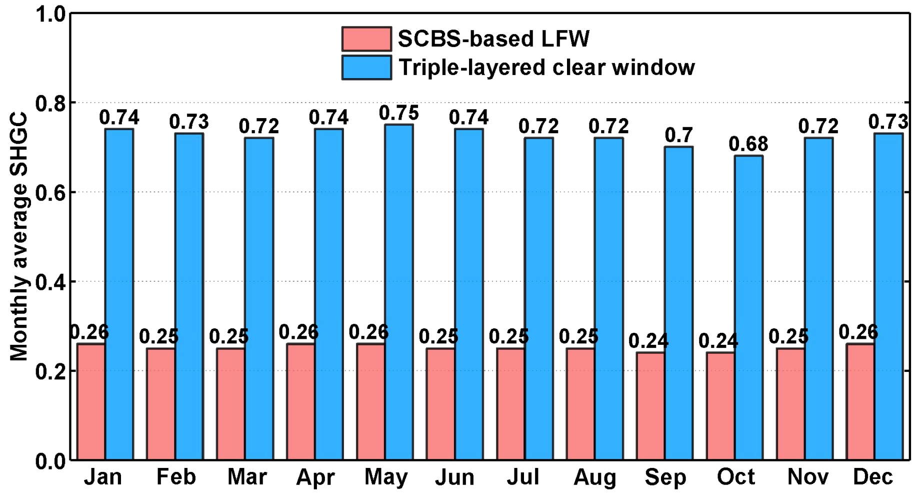

Figure 4.13 Monthly average SHGC of the SCBS-based LFW and triple-layered clear window

4.4 Summary

Liquid filled windows have been designed and investigated in the past decade because they combine the advantages of sound damping, thermal energy storage and solar NIR shielding together, which can be highly energy-efficient for buildings. In this chapter, a novel triple-layered LFW was designed with the spectrally selective solution. After that, a transient model that considering the constantly changing solar angels and dynamic solar spectral power distribution was developed to investigate the energy-saving behavior of the LFW in Hong Kong. The results demonstrated that the triple-layered LFW can ensure the monthly average photopic luminous transmittance to be higher than 40% and the monthly average SHGC values be lower than 0.26 in all the 12 months of the typical year of Hong Kong. The convective heat transfer rate from the triple-layered LFW to indoor environment is smaller than 25 W/m^2 in the design days in Hong Kong, which can effectively avoid the overheating of the near-window zones. Compared with triple-layered clear window, the triple-layered LFW cut down the indoor solar heat gain by 65%, and the 1 m^2-area triple-layered LFW can reduces the indoor solar radiation energy by 1717.8 MJ in the typical meteorological year of Hong Kong.

Chapter 5 A novel thermo-responsive smart window with spectral regulation of the biomass-derived materials

In **Chapter 4**, the static spectrally selective LFW was demonstrated to be effective in hot regions. However, its application in cold climates may lead to increased heating loads during winter. To enable adaptability in both hot and cold regions, this chapter presents a novel thermo-responsive smart window, leveraging the temperature dependent solubility of ammonia in water. This innovative design aims to achieve precise solar spectral regulation, throughout both summer and winter seasons. It integrates the spectrally selective SEBS material prepared in **Chapter 3** to modulate the solar spectrum effectively, and can achieve transmittance switching according to temperature changes. This chapter thoroughly analyzed the optical and thermal response characteristics of the smart window, evaluated its spectral modulation performance, and compared it against other commercially available thermochromic smart window technologies, to highlight the advancements of the newly developed system. Subsequently, experimental studies conducted in Harbin assess its impact on the indoor light and thermal environment of buildings. Furthermore, energy consumption simulations across various cities and climate zones were performed to validate its energy-saving potential in diverse regional contexts.

5.1 Structural design of a new ammonia pressure powered smart (apps) window

To enable the window to change its transmittance in response to ambient temperature variations, a visible and near-infrared dual band tunable thermal-responsive smart window, i.e., the APPs window (Ammonia Pressure Powered smart window) is developed and presented in this chapter. **Figure 5.1 (a)** depicts the schematic representation of the APPs window. It consists of two pieces of transparent clear glazing placed parallel at a 2 mm gap. The hollow space between the two glazing samples is connected to a cylinder, where some aqueous ammonia is stored in the left segment, and spectral splitting fluids in the right segment of the cylinder, respectively. The aqueous ammonia and spectral splitting fluids are separated by a polyethylene piston. As shown in **Figure 5.1 (a)**, in heated condition, the aqueous ammonia would be supersaturated, which allow the ammonia to push the piston rightward, extruding the spectral splitting fluids into the gap between the two glazing samples, as a result, the APPs window would change from the transparent state to an opaque state. While if the temperature drops, the solubility of ammonia would increase, and the dissolution of ammonia would suck the piston back. As the spectral splitting fluids flow back to the cylinder, the window would return to the transparent state.

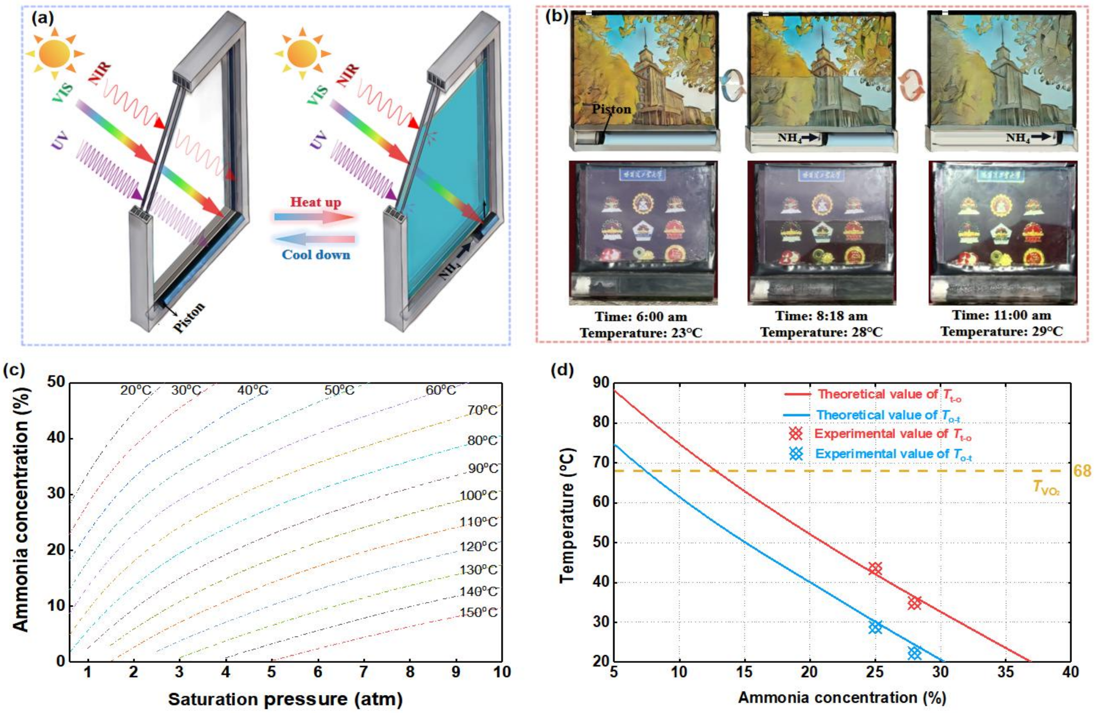

Figure 5.1 (a) Working principle of the APPs window; (b) Photos of the APPs window at different stages of a day; (c) the temperature-pressure-concentration correlation of aqueous ammonia; (d) the transition temperature of the smart window.

Figure 5.1 (b) shows the change of an APPs window sample on a sunny day in Harbin (July 28). The window initially resembled a double-glazing window in the morning, while at 9:48 the spectral splitting fluids fill the space between the two panes, and finally the window is fully filled by the spectral splitting fluids, with a switching time of about 3 minutes. It should be noted that to prevent the leakage of ammonia, the piston must be tightly attached to the inner surface of the cylinder. Normally, for ordinary pistons that can seal the 2 cm-diameter cylinders at room temperature, the maximum static friction force between piston and cylinder is about 2.0 N. To further ensure the sealing at high temperature, a larger sized piston was used in the APPs window, which must overcome a friction force about 7.8 N to push or suck the piston. To create a pressure of 7.8N, the ammonia segment pressure must be higher than 1.25 atm or lower than 0.75 atm. **Figure 5.1 (c)** shows the correlation between the saturation temperature, pressure and concentration of ammonia. **Figure 5.1 (d)** compares the transition temperatures from transparent state to opaque state ($CT_{t\text{-}o}$) and opaque state to transparent state ($CT_{o\text{-}t}$). It is clear that $CT_{t\text{-}o}$ is about 11～13℃ higher than the $CT_{o\text{-}t}$. Increased ammonia concentration would dramatically decrease the transition temperature. As long as the ammonia concentration exceeds 12.8%, the APPs window would have a more efficient transition temperature than traditional VO_2–based smart windows (at 68℃). Using the industrial concentrated ammonia solution (25% to 28%), the APPs window can achieve a transparent to opaque switching at about 35 to 42℃, and an opaque to transparent switching at about 24 to 30℃, which is considered to be an ideal property for building applications.

Ideal spectral splitting fluids for APPs windows are supposed to have broadband spectral shielding ability and good visible transmittance. Cu^{2+} exists as the octahedral structure in $CuSO_4$ solution, which causes an absorption peak at 820 nm due to the electron transition between t_{2g}-e_g. SCC can filter the blue and red visible light while retaining high transparency in the green or yellow light band. **Figure 5.2 (a)** and **Figure 5.2 (b)** exhibit the chemical structure and absorption features of $CuSO_4$ and SCC aqueous solutions. Theoretically, the $CuSO_4$ and SCC blended solution which combines the absorption features of Cu^{2+}, SCC and water together, can achieve the broadband absorption of visible light and near infrared band whilst maintain highly transparency in the green light band (500 nm to 600 nm), is ideal material for the APPs window application.

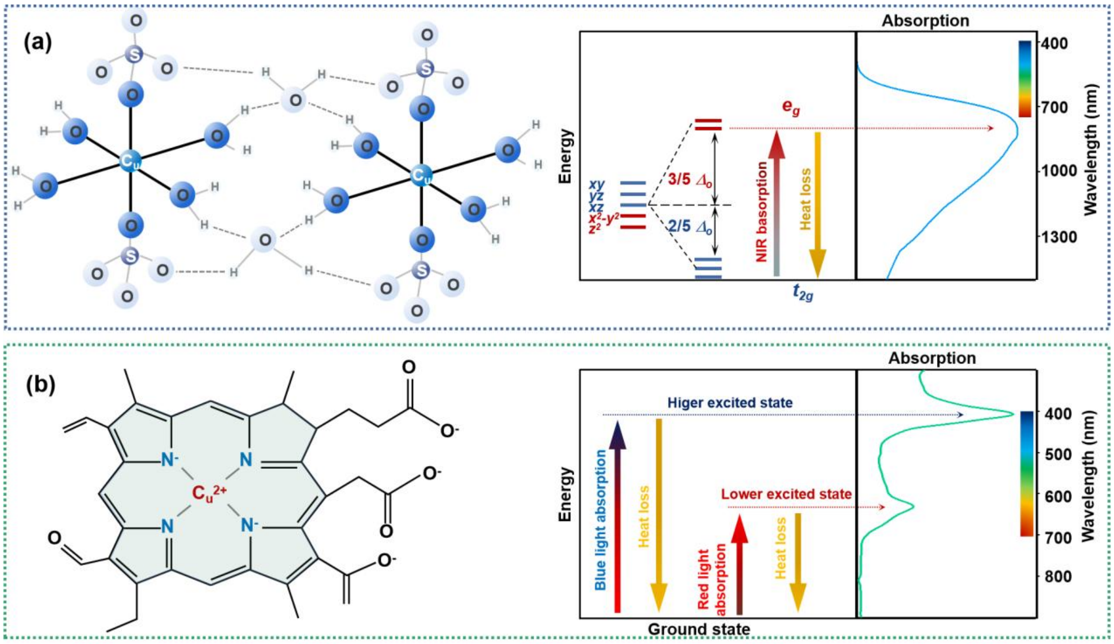

Figure 5.2 (a) Chemical structure and absorption feature of Cu^{2+} aqueous solution; **(b)** chemical structure and absorption feature of SCC aqueous solution.

5.2 Physical properties of the APPs window

5.2.1 Cyclic test of the APPs window

The prepared solutions were used in the APPs window, and the cycling test of the APPs window were shown in **Figure 5.3**, which demonstrates that the friction force between the piston and cylinder is fairly constant after hundreds of cycles. In this section, the optical properties and energy saving behaviors of the APPs window were discussed.

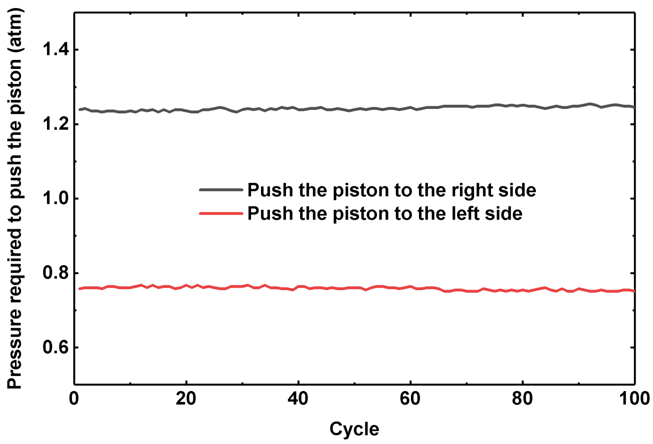

Figure 5.3 Cyclic test for the APPs window.

5.2.2 Optical properties of the APPs window

Figure 5.4 shows the optical photos of the APPs window. At cold state, the APPs window performs similarly to a normal double-glazing window, with highly visible transmittance ($\boldsymbol{T}_{\mathbf{lum}}$ = 84%, **Table 5-1**). At hot state, as the spectral splitting fluids flow into the gap between two glazing, the transparency of the APPs window decreases and exhibit colors ($CuSO_4$ solution shows slight blue color, SCC solution shows green and blended $CuSO_4$/SCC solution shows dark green).

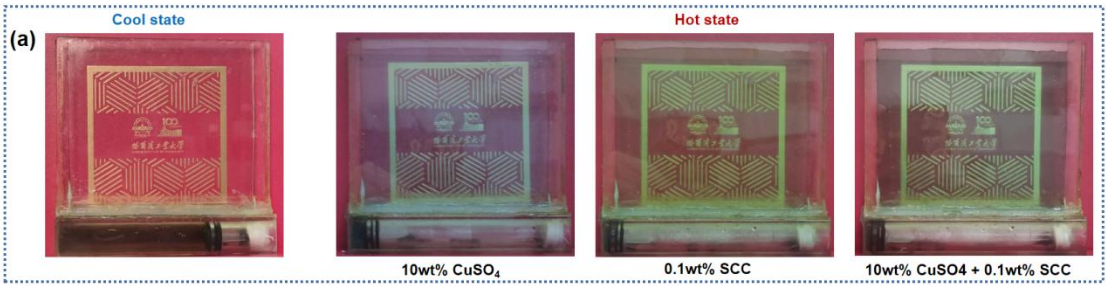

Figure 5.4 Photos of the smart window at cool state (left) and at hot state (right), with $CuSO_4$, SCC, and blended $CuSO_4$/SCC aqueous solution, respectively

The transparency and color features of the APPs window agreed well with the spectral transmittance exhibited in **Figure 5.5**. In room temperature, the APPs window exhibits high transmittance (about 84%) among the whole solar spectrum (300 to 2500 nm). While in a hot state, several absorption behaviors appear in the solar spectrum. Cu^{2+} in water would absorb the NIR, as shown in **Figure 5.5 (a)**, the manifest extinction peak at 820 nm is caused by the ***d-d*** transition of Cu^{2+}. It is also noticeable that obvious light extinctions appear in the *NIR* band with greater wavelength than 1800, mainly attributed to the light absorption of water molecules vibration. The increased $CuSO_4$ concentration (**Figure 5.5 d**) or increased fluids thickness (**Figure 5.5 a**) decreases the spectral transmittance in the NIR band dramatically, which agreed well with the Lambert-Beer law. As shown in **Figure 5.5 (a)**, 20% $CuSO_4$ solution with a thickness of 5 mm can filter nearly all the NIR.

SCC in the APPs windows works as the spectral filter of VIS band (the blue light and red light). SCC aqueous solution, as shown in **Figure 5.5 (b)** and **Figure 5.5 (d)**, arose two absorption peaks at 410 nm (blue light) and 650 nm (red light), corresponding to the electron transitions between the ground state and two different excited states. By combining the absorption features of Cu^{2+}, SCC and water molecules together, the blended aqueous solution enabled radiation regulation across the whole solar spectra (UV, VIS and NIR). As shown in **Figure 5.5 (c)**, with 10 mm thickness, the blended SCC/$CuSO_4$ solutions perfectly shield the solar radiation, and maintains the moderate transmittance in the ideal VIS band (450 nm to 650 nm), as a result, the light to solar heat gain (LSG) can reach to 2.9 (**Table 5-1**), which is much higher than even the most advanced Low-e glazing or plasma-nanomaterials based heat absorbing glazing.

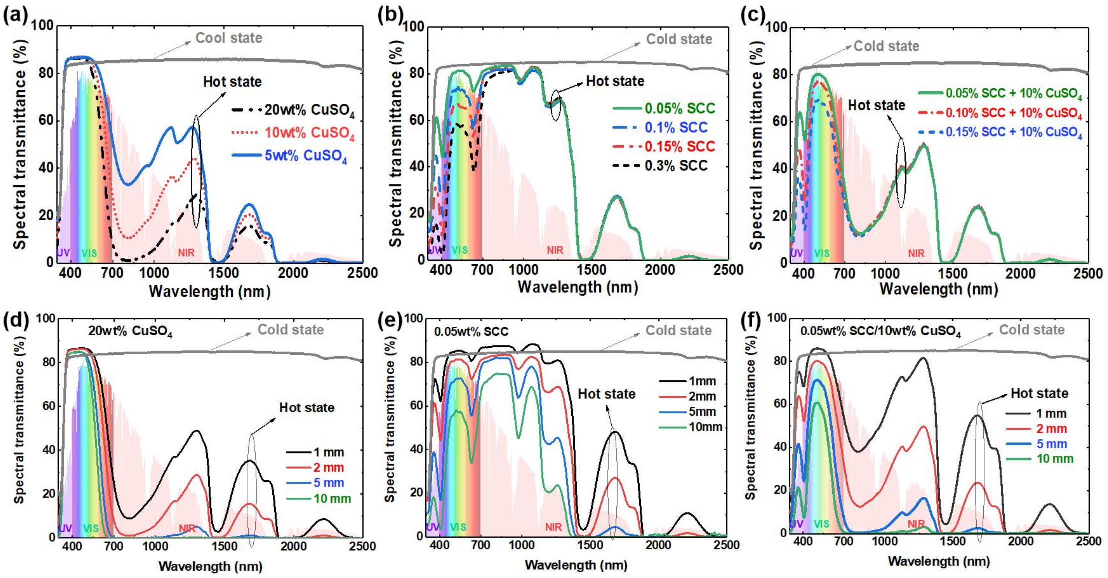

Figure 5.5 Spectral transmittance of the smart window at cool state and hot state with different thicknesses: **(a)** $CuSO_4$ solution; **(b)** SCC solution and **(c)** $CuSO_4$/SCC blended solution. Spectral transmittance of the smart window at cool state and hot state with different concentrations: **(d)** $CuSO_4$ solution; **(e)** SCC solution and **(f)** $CuSO_4$/SCC blended solution.

Figure 5.6 (a) and **(b)** compare the APPs window by the solar transmittance and melanopic transmittance at different levels of luminous transmittance. In addition to good luminous and solar modulation ability, enough melanopic transmittance (around 480 nm) is of vital importance for feasible photo-biological effects, which is an inevitable technically difficult point for traditional VO_2-based smart windows [36]. When the APPs window is in cold state, the luminous transmittance, solar radiation transmittance and melanopic transmittance are all about 84% (**Table 5-1**). While in hot state, the $CuSO_4$ solution ensures a good NIR modulation ability, and the SCC solution has a good modulation ability in the VIS band and the melanopic transmittance. The blended solution, which combines the absorption features of $CuSO_4$ and SCC together, has superior modulation ability in solar transmittance, luminous transmittance and melanopic transmittance simultaneously. Interestingly, it is also noticed from **Figure 5.6 (b)** (**Table 5-1**) that the blended solution has a M/P of around 0.84, which is similar to the solar radiation, indicating that it ensured a good photo-biological performance that is similar to the natural lighting.

Figure 5.6 (c) compares the Color Rendering Index (CRI) of the APPs window with the ones of different spectral splitting fluids. CRI is a vital parameter to assess the quality of the gamut relative for light. A rational CRI for residential buildings should be above 80. As listed in **Figure 5.6 (c)**, all the studied cases with 2 mm thickness spectral splitting fluids can ensure a higher CRI than 80. While from **Table 5-1**, it can be further inferred that with the same solar modulation, the blended solution can ensure a higher CRI than the single use of CuSO4 or SCC solution. By comprehensively considering the solar modulation ability, luminous modulation ability, photo-biological effects, and the color rending performance (**Figure 5.6 d**), it can be concluded that the blended solution is the most promising solution among the presented cases.

Table 5-1 Detailed optical properties of the APPs window in cool and hot state, with different spectral splitting fluids

Materials	**Thickness**	**Materials**	T_{lum} (%)	T_{sol} (%)	ΔT_{sol} (%)	T_{mel} (%)	***FOM***	***M/P***	***CRI***	**Color coordinates**		
										x	***y***	***z***
Bleached	——	**Air**	0.835	0.837	——	0.834	1	0.84	99	0.33	0.34	0.32
Colored	2 mm	20% $CuSO_4$	74.6	36.5	47.0	85.5	2.05	0.97	83	0.29	0.34	0.37
		10% $CuSO_4$	80.7	46.2	37.3	86.7	1.75	0.90	92	0.31	0.34	0.35
		5% $CuSO_4$	84.0	57.7	25.8	86.8	1.46	0.87	97	0.32	0.34	0.33
		0.30% SCC	54.6	54.1	29.4	50.9	1.01	0.78	85	0.34	0.40	0.26
		0.15% SCC	64.6	60.2	23.3	61.5	1.07	0.80	91	0.34	0.38	0.28
		0.10% SCC	70.7	63.1	20.4	69.1	1.12	0.82	92	0.33	0.37	0.30
		0.05% SCC	79.9	69.2	14.3	78.5	1.15	0.82	96	0.33	0.36	0.31
		0.15% SCC/10% $CuSO_4$	63.4	35.3	48.2	64.5	1.80	0.86	85	0.32	0.37	0.31
		0.1% SCC/10% $CuSO_4$	71.3	39.8	43.7	73.3	1.79	0.87	87	0.32	0.37	0.32
		0.05% SCC/10% $CuSO_4$	75.3	43.4	40.1	78.2	1.74	0.87	91	0.32	0.35	0.33
	1 mm	20% $CuSO_4$	79.8	46.4	37.1	86.1	1.72	0.91	91	0.31	0.34	0.35
	5 mm		61.4	27.8	55.7	82.5	2.21	1.13	66	0.25	0.33	0.42
	10 mm		49.9	24.5	59.0	80.5	2.03	1.35	53	0.21	0.31	0.48
	1 mm	0.05% SCC	84.5	76.6	6.9	83.5	1.10	0.83	98	0.33	0.35	0.31
	5 mm		69.8	58.5	25.0	67.0	1.19	0.81	91	0.34	0.38	0.29
	10 mm		53.3	45.0	38.5	50.5	1.18	0.80	82	0.33	0.40	0.27
	1 mm	0.05% SCC/10% $CuSO_4$	83.3	62.1	21.4	84.6	1.34	0.86	96	0.33	0.35	0.32
	5 mm		62.0	25.4	58.1	67.2	2.45	0.91	80	0.30	0.37	0.33
	10 mm		47.4	16.4	67.1	54.8	2.90	0.97	64	0.28	0.38	0.34

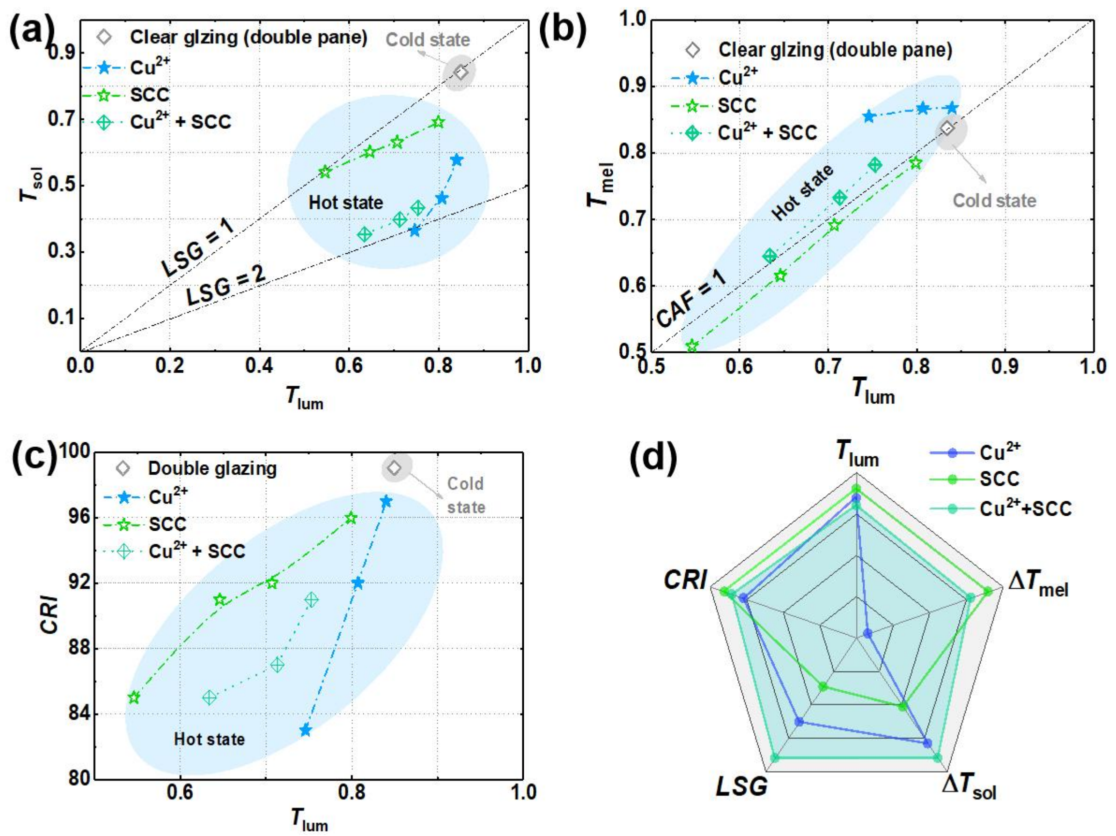

Figure 5.6 (a) Comparison on the solar radiation transmittance for the smart window in cool and hot states; **(b)** comparison on the "non-visual" transmittance for the smart window in cool and hot states; **(c)** comparison on the color rendering index (CRI) for the smart window in cool and hot states; **(d)** performance summary and comparison for the APPs window with different kinds of spectral splitting fluids.

The optical regulation mechanism of APPs windows is completely different from the spectral regulation mechanisms of existing VO_2 and hydrogel windows. The APPs window resembles a normal double layered clear glazing window in cold state, and it can switch to an opaque state at a flexible transparency transition temperature ranging from 20°C to 80°C (determined by the ammonia concentration). In addition, with the spectral absorption of Cu^{2+} and Sodium copper chlorophyllin (SCC) solution, the APPs window is deemed to have no impact on the haze rate of windows (< 1%), meanwhile, the APPs windows could achieve a solar modulation of 40% to 70% whilst maintaining a luminous transmittance above 50% in the hot state (**Table 5-2**). These features make the APPs window more appealing for building applications than their counterparts, i.e., VO_2-based window and hydrogel-based window, as compared in **Figure 5.7 (b)**, **(c)**, and **(d)**.

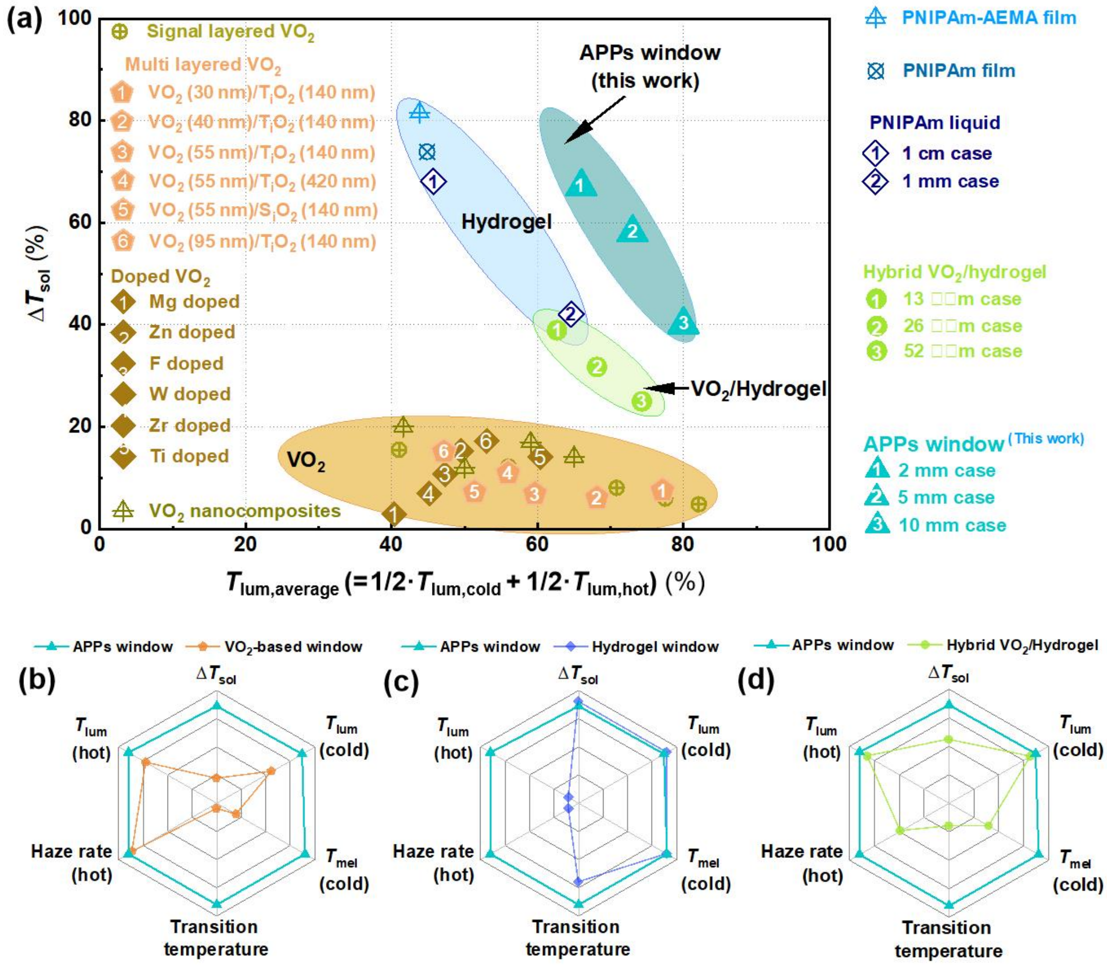

Figure 5.7 (a) Summary of the solar modulation ability (**ΔT_{sol}**) and the average luminous transmittance (**$T_{lum,\ avergae} = 1/2\ T_{lum(cold)} + 1/2\ T_{lum(hot)}$**) of some typical thermal-responsive smart windows (detailed data are recorded in **Table 5-2**), **(b), (c), (d)** Performance summary and comparison for APPs window and the existing thermal-responsive smart windows (VO_2-based window, hydrogel window and hybrid VO_2/hydrogel window).

Table 5-2 Performance summary of current thermo-responsive smart windows

Categories	Material		T_{lum} (%)		ΔT_{sol} (%)	Refs.
			Bleached	Opaque		
VO_2-based smart windows	Signal layer VO_2		49	54	7.04	Zhang et al. [139]
			78	77	5.9	Wang et al. [138]
			42.6	39.7	15.5	Xiang et al. [136]
			56.4	55.6	12.2	Xiang et al. [136]
			82.1		4.8	Wang et al. [138]
	Multi-layered VO_2	VO_2(30nm)/TiO_2(140nm)	49.5	44.8	15.1	Chen et al. [146]
		VO_2(40nm)/TiO_2(140nm)	61.5	57.7	6.9	
		VO_2(55nm)/TiO_2(140nm)	50.6	52.1	7.2	
		VO_2(55nm)/TiO_2(420nm)	58	53.9	10.9	
		VO_2(55nm)/SiO_2(140nm)	70.1	66.2	6.1	
		VO_2(95nm)/TiO_2(140nm)	78.1	76.1	7.5	
	Mg doped VO_2		40.6	40.03	2.9	Raptis et al. [140]
	Zn doped VO_2		47.2	51.92	12.1	Kang et al. [141]
	F doped VO_2		48.7	45.9	10.7	Dai et al. [142]
	W doped VO_2		44.6	45.7	6.9	Hu et al. [143]
	Zr doped VO_2		60.4		14	Shen et al. [144]
	Ti doped VO_2		53		17.2	Chen et al. [145]
	VO_2-based nanocomposites		63.7	54.4	12	Liu et al. [148]
			43.3	39.9	14.1	Liu et al. [148]
			～50	～50	17	Zhao et al. [147]
			～70	～60	20	Zhao et al. [149]
Hydrogel-based smart window			89.1	0.6	73.9	Zhou et al. [153]
			87.2	0.5	81.6	Li et al. [202]
			90.2	39	42.1	Zhang et al. [203]
			90.9	1.26	68.1	Zhang et al. [203]
H^+/Li^+ doped hydrogel (electric-/thermo-dual-responsive)	H^+ doped hydrogel	thermochrom	78.5	22.3	42.4	Pattathil et al. [204]
		thermo-/electro-chrom	78.5	4	57.2	
	Li^+ doped hydrogel	thermochrom	75.9	12	46.5	
		thermo-/electro-chrom	75.9	4.1	54.9	
VO_2/hydrogel hybrid products		13 μm	86.8	61.8	25	Zhou et al. [205]
		26 μm	84	52.3	31.7	
		52 μm	82.1	43.2	38.9	
APPs window	**10% $CuSO_4$ and 0.15% SCC**	**2 mm**	**83.7**	**75.3**	**40.1**	**this work**
		5 mm	**83.7**	**62.0**	**58.1**	
		10 mm	**83.7**	**47.4**	**67.1**	

5.3 Experimental demonstration of the APPs window

As discussed above, the APPs smart window has excellent solar regulation ability, high luminous transmittance, as well as a rational melanopic transmittance in both cool and hot states, which make it a promising candidate for building applications. To further demonstrate the practicality of the APPs window, outdoor experiments in Harbin were carried out on two consecutive days: a sunny (2022.08.06) and a rainy day (2022.08.07) respectively. **Figure 5.8** shows the outdoor solar radiation level and outdoor illuminance level in these two days, and **Figure 5.9** shows the outdoor air temperature during the testing days.

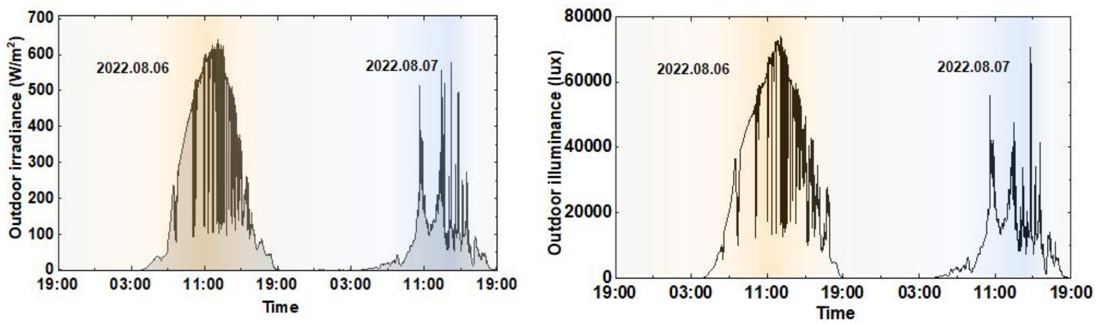

Figure 5.8 Outdoor (a) solar radiation intensity, (b) illuminance level in 2022.08.06 and 2022.08.07.

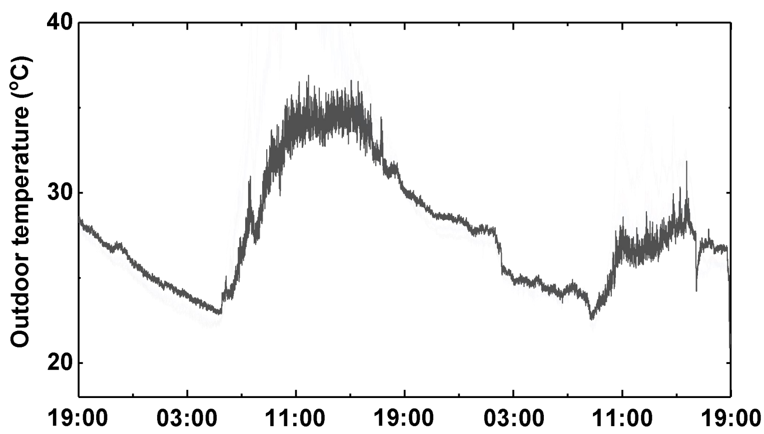

Figure 5.9 Ambient air temperature of Harbin in 2022.08.06 and 2022.08.07.

In the outdoor experiments, two hot chambers, with the same dimension of 20 cm × 20 cm × 30 cm were employed, one equipped with the APPs window, and another the normal double-glazing window, both two windows faced south; **Figure 5.10 (a)** shows the schematic of a hot chamber. The ammonia concentration in the APPs window was 28%, which enabled the APPs window to achieve transparent-to-opaque switching at 36°C, and opaque-to-transparent switching at 24°C. The blended aqueous solution, with a SCC concentration of 0.05% and $CuSO_4$ concentration of 10% were applied. In the experiments, the air temperature inside the chambers, the surface temperature of the windows, and the illuminance at the central floor of the chambers were recorded for analysis. **Figure 5.10 (b)** shows photos of the two hot chambers at hot and cool states, respectively. In the sunny day (August 6), the APPs window operated in the hot state from 8:45 to 16:34, and it remained cool states for the rest of time.

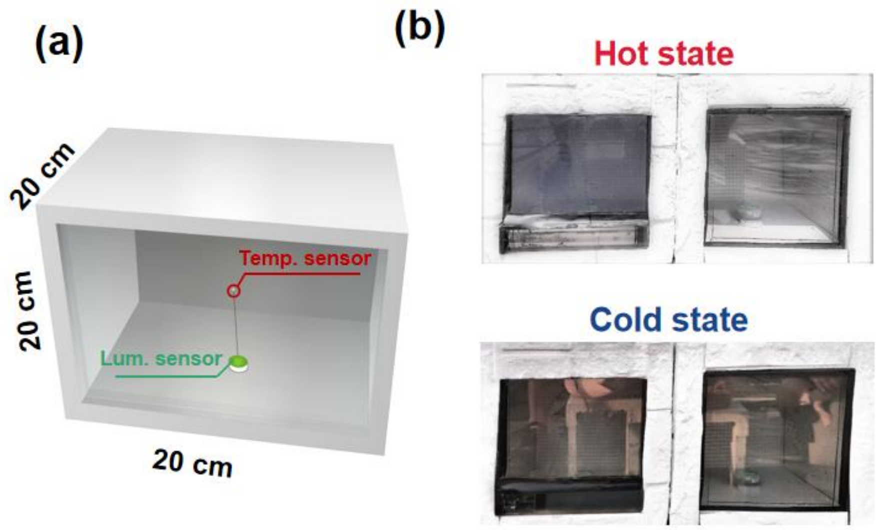

Figure 5.10 (a) Scheme of the experimental hot chamber; **(b)** Photos of the hot chambers equipped with APPs window (left) and equipped with double glazing (right), at hot state and at cool state respectively.

Figure 5.11 compares the experimental results of the air temperature inside the two chambers. In the sunny day, the hot chamber with the normal double glazing shows a maximum temperature of 56.1°C at 11:18, at the same time, the air temperature of the chamber with APPs window was just 51.8°C, about 4.3°C lower than that of normal double-glazing window. In the rainy day (August 7), the APPs window operated in the cool state for all day, as a result, there was no remarkable temperature difference between the two experimental chambers.

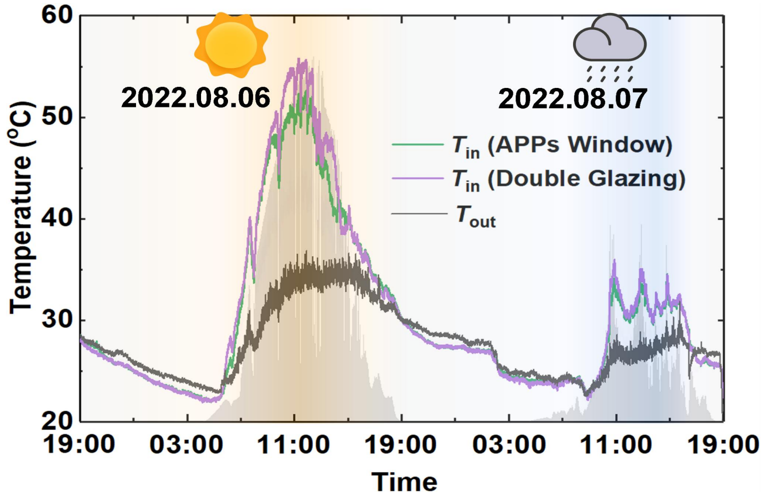

Figure 5.11 The chambers' inside temperature and outdoor temperature change during the two tested days

Figure 5.12 shows the surface temperature of the double-glazing window and the APPs window in the experimental days. There is no significant difference in the surface temperature between the two types of windows. This is mainly because the APPs window can rapidly dissipate heat through outdoor convective heat transfer. This also demonstrates that the APPs window does not cause significant secondary solar heat gain.

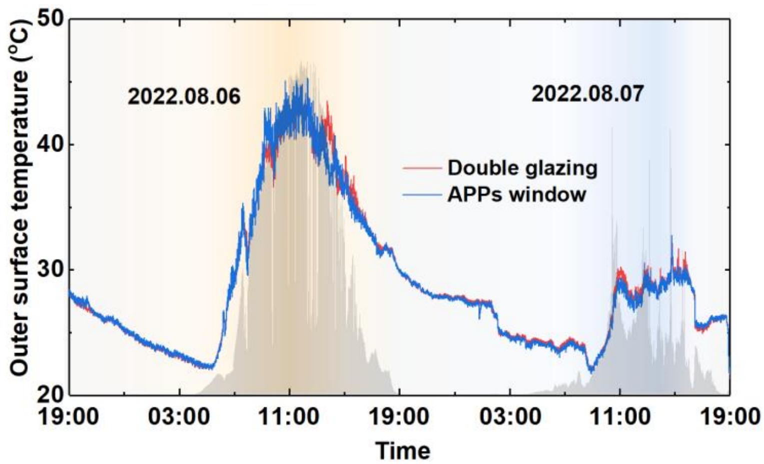

Figure 5.12 Surface temperature of the double-glazing window and the APPs window in 2022.08.06 and 2022.08.07.

Figure 5.13 compares the inside illuminance levels of the two chambers. In the sunny day, the normal double-glazing window showed the highest illuminance level of 41350 lux at 10:10, which is higher than the threshold of glare. Meanwhile, the APPs window reduced the illuminance level from 41350 lux to 17075 lux, which can remarkably reduce the glare hazard. For effective daylighting, the useful daylight illuminance (UDI) defined as that the illuminance for work plane between 100 lux to 2000 lux is the desirable daylight level ($U_{100\text{-}2000}$). As recorded in these two days, the hours of the illuminance level between 100 to 2000 lux of the two tested chambers has little difference (735 minutes for normal APPs window, and 751 minutes for double glazing window), demonstrating that the APPs window would not reduce the daylighting performance.

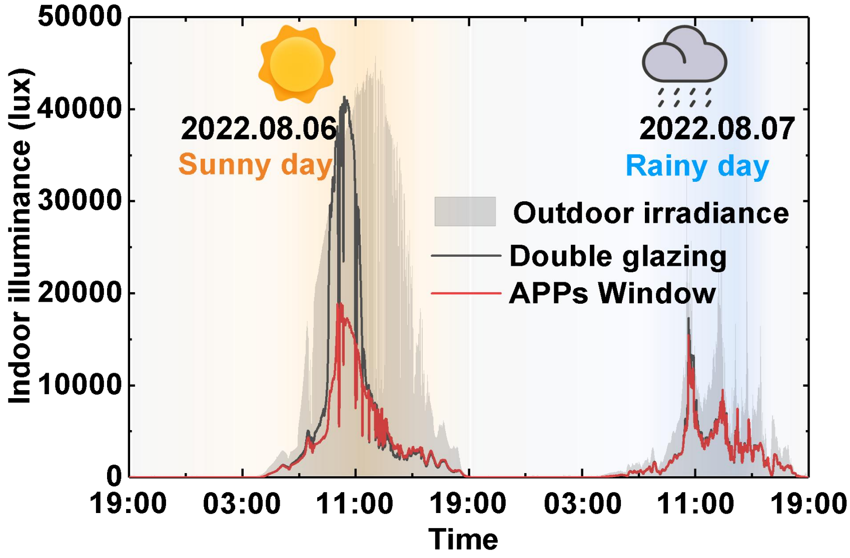

Figure 5.13 Tested illuminance in the tested sites of the APPs window and double-glazing window

As discussed in Chapter 3, the $CuSO_4$ and SCC blended solution has a M/P of natural daylight, which ensures a balance in melanopic light and photopic light, meaning that the APPs window is supposed to have a good photo-biological effect. To evaluate the photo-biological effects of the APPs window, the spectral power distribution (SPD) of solar radiation was calculated by the SMART model, as shown in **Figure 5.14**. According to the SPD of solar spectrum, the hourly circadian light (CLA) of the two tested chambers can be calculated, as shown in **Figure 5.15**. In the whole day, there was no remarkable difference in the CS value between the APPs window and normal double-glazing window, although the CLA for the normal double-glazing window is about two times higher than the APPs window at 10:00 to 11:00, demonstrating that the APPs window would not spoil the photo-biological effects of day light.

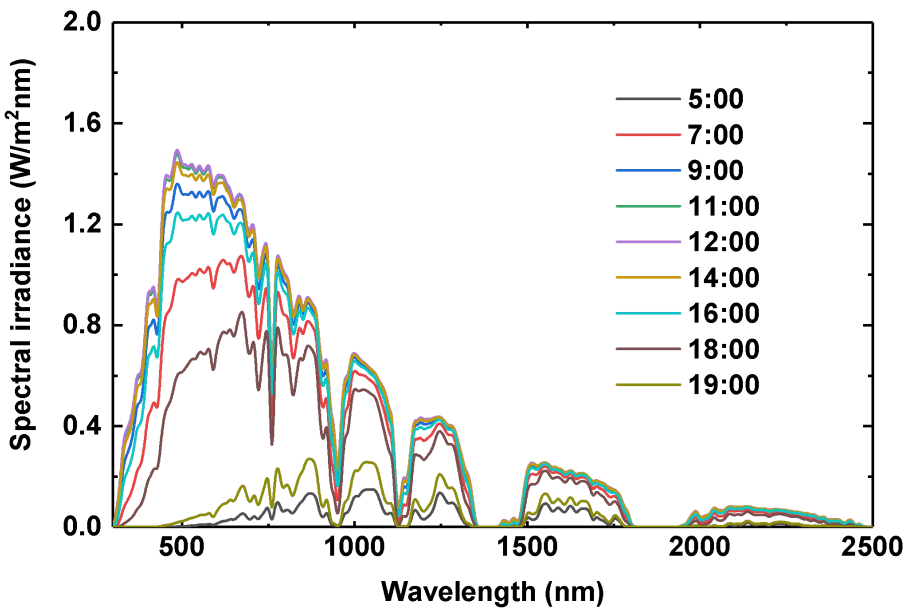

Figure 5.14 Spectral power distribution of natural light in 2022.08.06

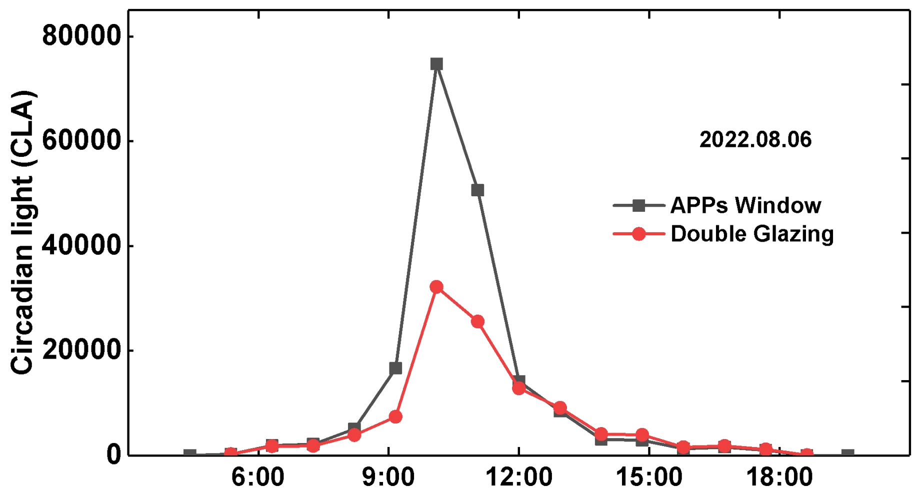

Figure 5.15 The hourly CLA value in the boxes with APPs window and normal Double-glazing window in 2022.08.06.

Then, the photo-biological effect can be evaluated by the circadian stimulus (CS), which reflects the amount of melatonin inhibition of the human circadian system after a one-hour exposure. In the early part of the day, a higher CS value than 0.3 is desirable for stimulating the circadian system and is related to better sleep quality and improved behavior and mood. Figure 5.16 compares both the daylight of APPs window and normal double-glazing window by the hourly ***CS*** value in the sunny day.

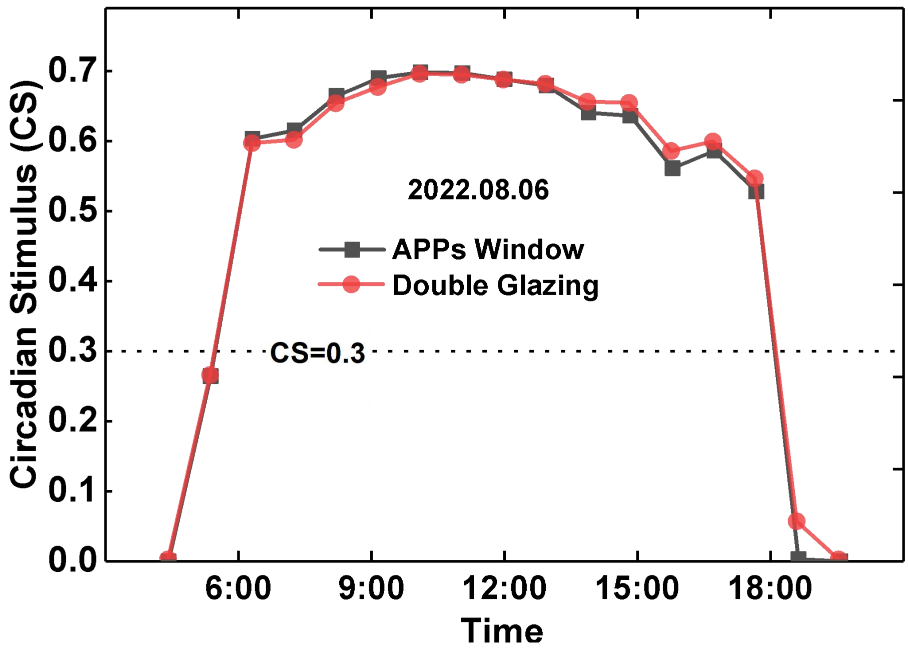

Figure 5.16 Estimated **CS** value in the sunny day (2022.08.06)

5.4 Energy-saving performance evaluation of the APPs window

To further clarify the energy-saving of APPs window, a simulation was carried out based on an office building, detailed model as given in **Figure 5.17**. The simulation considered an inner room of a building, which has dimensions of 6 m × 4.5 m × 3 m, and it is equipped with three windows in the south facade, with the dimension of 1.8 m × 1.5 m. The simulation was carried out for three cities, those of Singapore, Hong Kong and Harbin which represent three different types of climatic conditions: tropical, subtropical and temperate, respectively. The ammonia concentration of 28%, a blended aqueous solution with a SCC concentration of 0.1% and $CuSO_4$ concentration of 10%, was applied in the APPs window.

In the simulation work, a double-glazing window, with an air gap of 2 mm, was employed as the baseline for comparison. On top of that, the energy-saving performance of the APPs window was compared with one of the double layered low-e window (low-e glazing + normal clear glazing). The related settings for windows in the simulation work are given in **Table 5-3**.

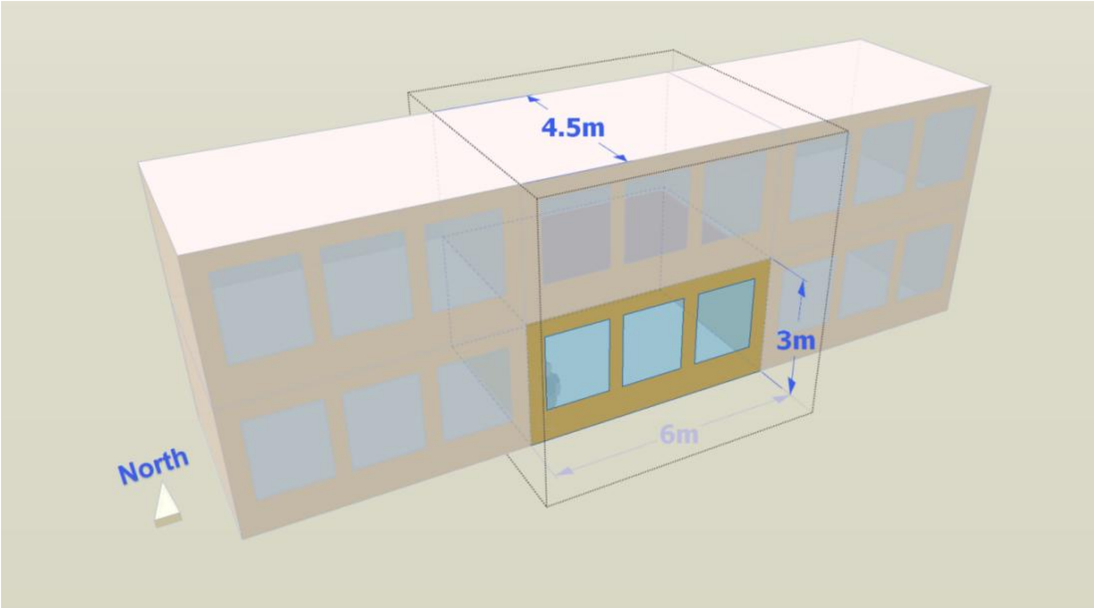

Figure 5.17 The hourly CLA value in the boxes with APPs window and normal Double-glazing window in 2022.08.06.

Table 5-3 Parameters of the clear glazing, low-e glazing, and APPs window.

Windows	Thickness	T_{sol}	R_{sol}	Front side emissivity	Back side emissivity	Thermal Conductivity
Clear glazing	3 mm	91.8%	7%	0.84	0.84	0.94 W/mK
Low-e glazing	3 mm	59.9%	17.1%	0.15	0.84	0.94 W/mK
APPs window (hot state)	7 mm	39.8%	8%	0.84	0.84	0.82 W/mK

Notes: (1) Double glazing in the simulation work is made of two clear glazing with air gap of 2 mm;
(2) Double layered low-e glazing is made of a low-e glazing and a clear glazing, with air gap of 2mm;
(3) APPs window in cold state has the same parameters of double glazing.

Figure 5.18 (a) to **(c)** shows the monthly space cooling energy consumption simulation results. It is clear that the normal double-glazing window would lead to the highest value of monthly space cooling energy consumption. Both double layered low-e glazing and the APPs window have good energy-saving performance. In Singapore, APPs window shows the lowest space cooling load for all year. In Hong Kong and Harbin, the double layered low-e window shows better energy saving performance than APPs window in cold seasons, which is attributed to the fact that the APPs window is not triggered to opaque state for adequate time. As shown in **Figure 5.18 (d)**, the APPs window works in the hot state for above 600 hours in

Singapore for each month, while in Hong Kong and Harbin, the values from October to May are no more than 300 hours. **Figure 5.18 (e)** further clarified the annual energy saving of the APPs window and double layered low-e window, with the baseline of normal double-glazing window. It should be noted that in Harbin, where the APPs window works in hot state for just about 900 hours a year, the energy-saving of APPs window is still greater than the one of double layered low-e glazing windows. This result demonstrates that the APPs window is superior to double layered low-e glazing windows in various climatic conditions. On the other hand, although the operating hours of APPs window in hot state in Singapore is much greater than those in Hong Kong, APPs window has similar annual cooling energy-saving potential in these two cities (43 MJ/m^2 for Singapore and 41 MJ/m^2 for Hong Kong), mainly because of the solar altitude angle difference between these two cities.

5.5 Summary

In this chapter, a novel thermal-responsive smart window (the APPs window) with high solar modulation ability, excellent luminous transmittance and feasible transition temperature was designed and fabricated. Compared with the counterparts, the APPs window has excellent luminous transmittance at both room temperature (84%) and hot conditions (above 50%). Furthermore, the APPs window has outstanding solar modulation ability of 40% to 70%, flexible transition temperature ranging from 20 to 80°C, good melanopic light transmittance of 70% and high CRI above 80 in hot state. In the outdoor chamber test, the APPs smart window reduced the indoor air temperature by 4.3°C in a sunny day (compared with the normal glass), meanwhile, it ensured a good daylighting quality for the whole day time, both in "photopic visual effects" and "melanopic non-visual effects". Moreover, simulation work conducted in three cities with different weather conditions and demonstrates that the APPs windows shows superior energy-saving potential than traditional double layered low-e glazing windows in both cold and hot regions, with an annual energy-saving of 43.5 MJ/m^2, 41.0 MJ/m^2 and 17.6 MJ/m^2 in Singapore, Hong Kong and Harbin, respectively.

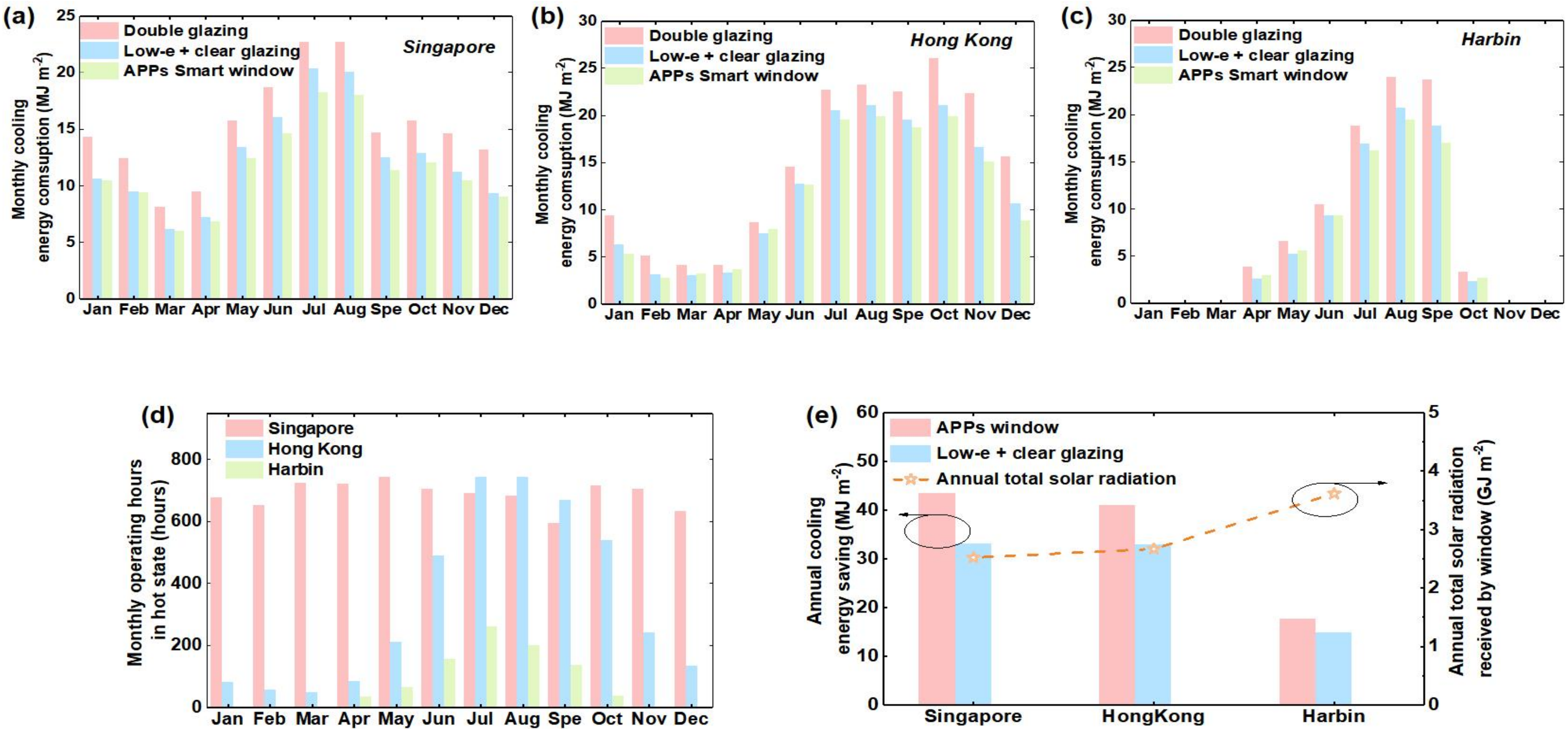

Figure 5.18 The simulated monthly space cooling energy consumption for Singapore **(a)**, Hong Kong **(b)**, and Harbin **(c)**; **(d)** monthly operating hours of the APPs window in hot state; and **(e)** the annual cooling energy-saving in the three cities.

Chapter 6 A novel actively tunable bi-static window with spectral regulation of the biomass-derived material

The APPs window proposed in **Chapter 4** can spontaneously adjust its optical properties in response to outdoor temperature, representing a passive regulation strategy. In contrast, this chapter introduces an actively tunable spectral-selective window technology, by proposing a flip-induced bi-static window, based on the structural design of flip windows. Flip windows have already been commercially adopted in daily life. For instance, the windows on the platform of the Hung Hom MTR Station in Hong Kong are 180° rotatable (**Figure 6.1b**). The original intention behind the flip window design was to facilitate glazing cleaning. In this chapter, the flip window concept is further advanced by incorporating tunable optical properties, resulting in the development of a flip-induced bi-static window. This chapter provides a detailed description of the mechanical design of the bi-static window. Subsequently, this chapter thoroughly investigates the physical properties of the proposed window, focusing on its spectral regulation capability and the switching mechanism between the two modes. Outdoor experiments were then conducted to compare the energy-saving and daylighting performance of the bi-static window in both modes. Finally, energy-saving simulations for typical cities in different climate zones were conducted to reveals the energy-saving potential of the bi-static window across various climate regions.

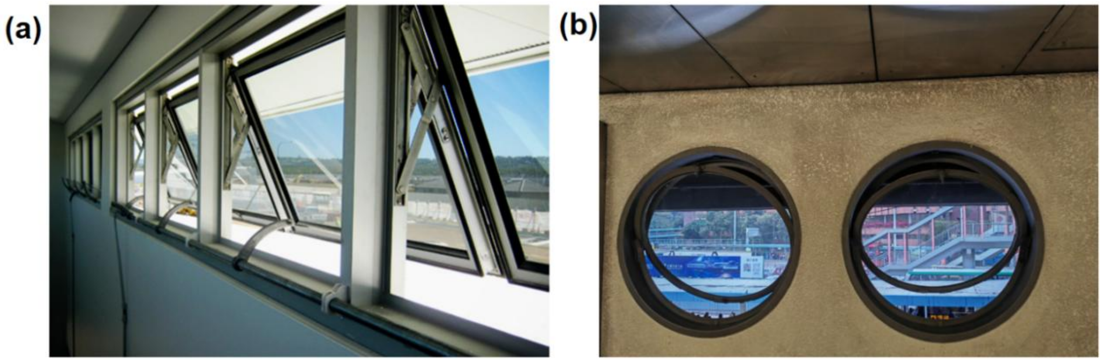

Figure 6.1 (a) Flipping windows applied in an office building; (b) Flipping windows at Hung Hom MTR Station, Hong Kong

6.1 Material and structural design of a new rotatable bi-static (RB) window

6.1.1 Ideal windows

The ideal optical properties for window is clearly seasonal. As shown in **Figure 6.2 (a)**, in cold seasons, an ideal window should be fully transparent across the entire solar spectrum, to maximize the solar heat gain through window structure in buildings. Conversely, in hot seasons, windows are supposed to minimize the indoor solar heat gain, and maintain high VIS transparency for efficient daylight. To adapt to hot seasons, the spectrally selective designs that block the solar NIR and prioritize maximum transparency in the green VIS light band (as depicted in **Figure 6.2 a**), is considered to be the optimal solution. As results, such optical properties will provide windows with a light green color (**Figure 6.2 b**). Since this spectrum configuration selectively blocks some of the red and blue VIS with low luminous efficiency, it can ensure a ultra-high light to solar heat gain (LSG) surpassing the state-of-the-art spectrally selective materials. In addition to high LSG, the natural green color has been proven to be visually soothing for the human eye, and it is also associated with various healthy photo-biological benefits for dwellers **[206, 207]**.

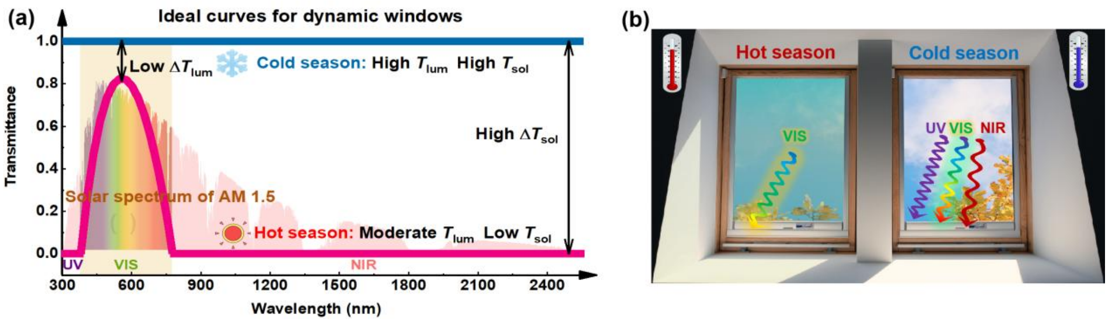

Figure 6.2 (a) Ideal transmittance curves for dynamic windows in hot and cold seasons; **(b)** schematic representation of the ideal windows for hot and cold seasons

6.1.2 Structural design of the RB window

In this study, a rotatable bi-static (RB) window was proposed to achieve optical switching between two ideal optical states. Specifically, the RB window employs the optical absorbing behaviors of filling fluids. The SCC/$CuSO_4$ blended solution (SCBS) was utilized to work as a spectrally selective fluids (SSF), to match the ideal window in hot season. To further match the ideal optical properties in cold season, a counter fluid to the SSF, i.e., the liquid paraffin (LP), was employed to create high transparency across the whole solar spectrum. The structural design of the RB window is shown in **Figure 6.3**. The switching between these two fluids is enabled by the unique 180-degree rotatable structural design, as seen from **Figure 6.3 (a)**. The SSF and LP have different densities (**Figure 6.4**). In bleached state, the liquid tank is positioned at the bottom of the window, the gravity causes the SSF to sink into the liquid tank, while the LP rises to occupy the hollow gap. This configuration yields a highly transparent window, allowing for maximum solar heat gain. Conversely, in hot conditions, the liquid tank is relocated to the top position through 180-degree rotation, causing the LP to float into the tank while the SSF sinks into the hollow gap. As a result, the window exhibits the optical properties of the SSF, characterized by high luminous transmittance and low solar heat gain.

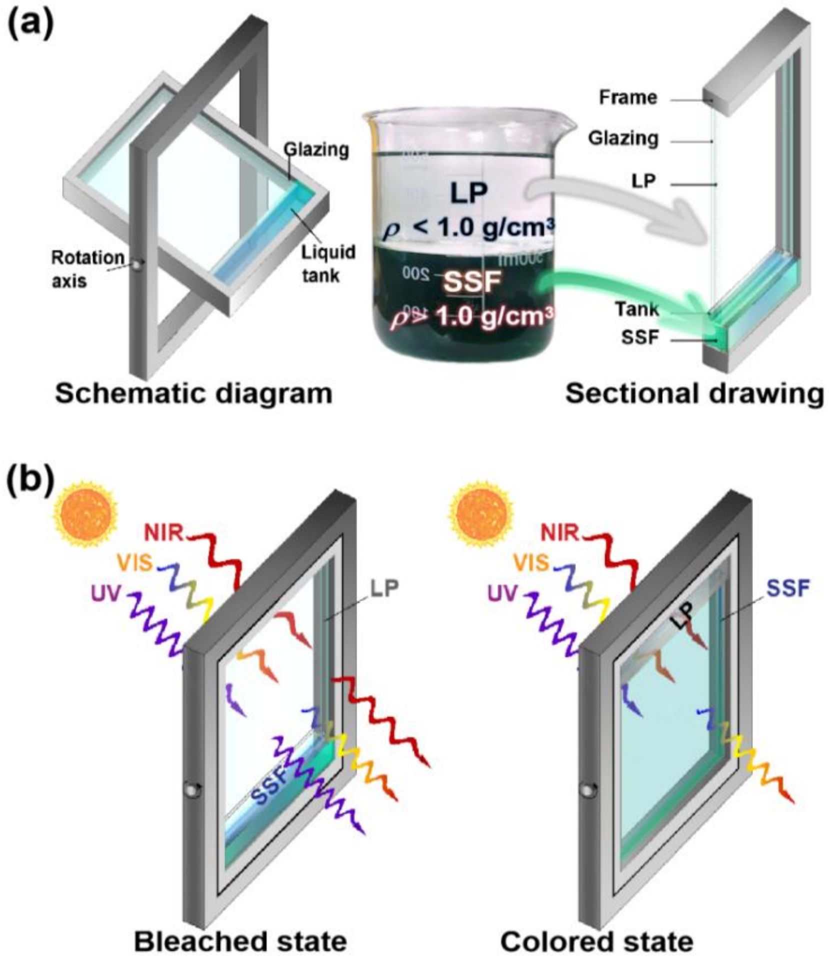

Figure 6.3 (a) Schematic representation of the RB window; **(b)** working principle of the RB window.

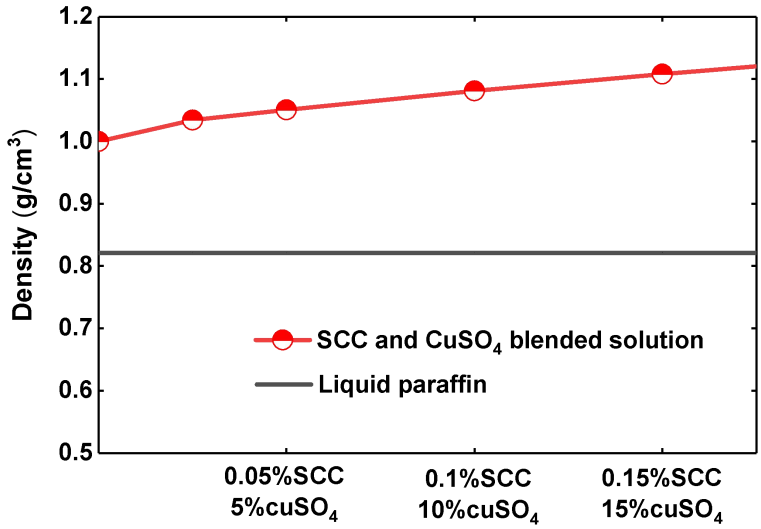

Figure 6.4 Comparisons of the density of the **LP** and **SEBS**.

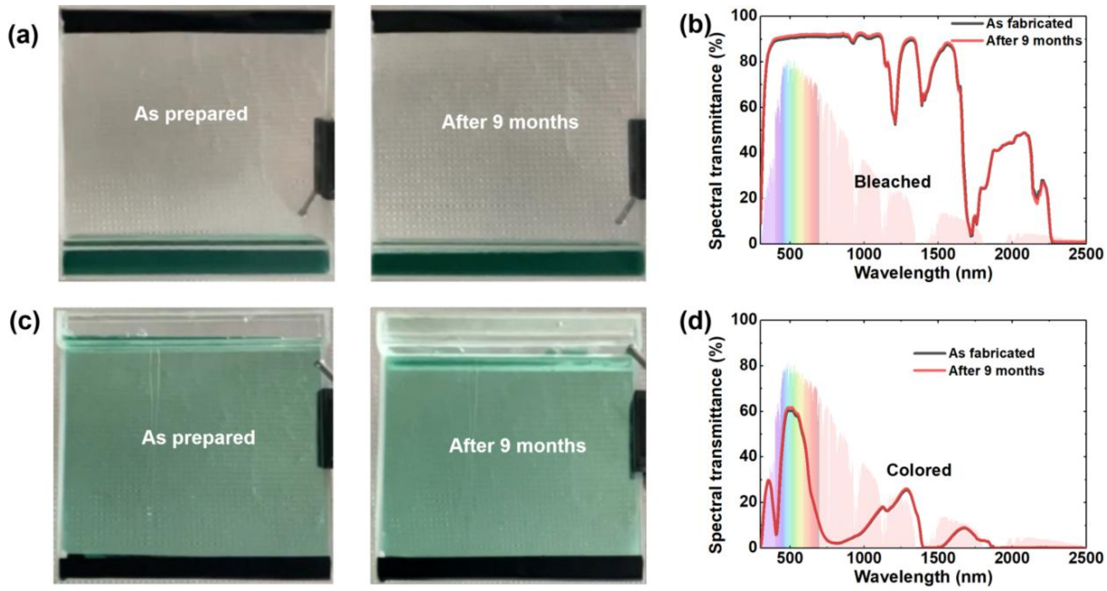

Figure 6.5 (a) Optical photos of the bleached RB window with different aging time; (b) spectral transmittance of the bleached RB window with different aging time; (c) optical photos of the colored RB window with different aging time; and (d) spectral transmittance of the colored RB window with different aging time.

Based on the above flipping mechanical structure design, reversible switching between different light transmission modes of the window can be achieved. The switching process is simple, reliably responsive, and does not rely on electricity or complex control systems, offering excellent tunability and sustainability. Figure 6.4 presents the weathering test results of the RB window structure. After a prolonged outdoor exposure test lasting up to nine months, the window maintained stable structural characteristics and continued to enable reversible switching of the liquid within the window interlayer. No significant leakage, miscibility, or performance degradation was observed. These results fully demonstrate the long-term stability and reliability of the flipping-induced dual-mode chromogenic window during operation.

6.2 Physical properties of the RB window

6.2.1 Optical properties

The LP and SSF exhibit high optical contrast (**Figure 6.6 a**), as the LP possesses excellent transparency across the solar spectrum, while the SSF displays a distinct spectral selectivity. **Figure 6.6 (b)** gives the optical photographs of a 3 mm-thick, 20 × 20 mm^2 RB window sample, with the 0.1%SC/10%$CuSO_4$ hybrid solution. The sample offers transparency in both of these two states. In bleached state, the sample shows high transparency and color neutralization. In colored state, the color closely aligns with the ideal windows for hot seasons, with a high transparency and light green color.

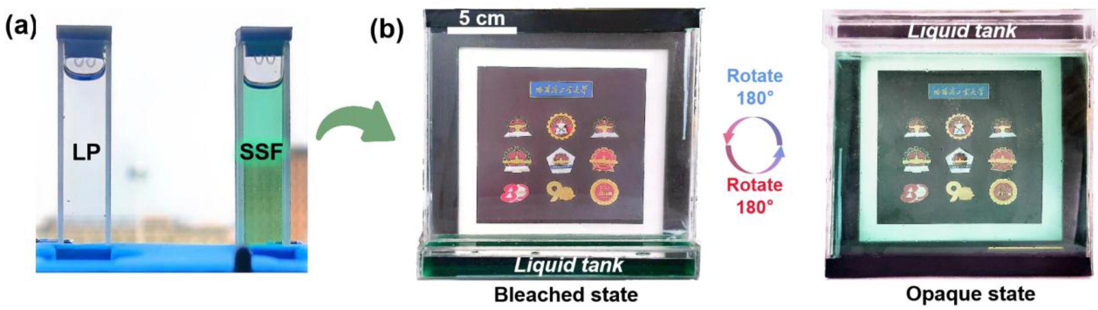

Figure 6.6 (a) The optical photo of the two optical fluids; **(b)** optical photos of the RB window in bleached and colored states

Figure 6.7 compares the spectral transmittance of the RB window using a 0.1%SCC /10% $CuSO_4$ blended solution as the SSF, under different thicknesses of the filling fluids. In the bleached state, the window exhibits excellent transmittance across the entire visible spectrum, with an overall visible light transmittance of approximately 91%. This value is higher than that of both the APPs smart window introduced in Chapter 5 and that of conventional double-glazed windows in their bleached state.

The enhanced transmittance of the RB window in bleached state is primarily attributed to the LP fluid, which has an extinction coefficient near zero in the visible region and a refractive index higher than that of air. As a result, the interfacial reflectance at the glazing–LP interface is significantly lower than that at the glazing–air interface, thereby reducing the overall reflectance of the window and increasing its transmittance.

Due to the overtone vibrations of C–H bonds, the LP fluid shows some absorption in the near-infrared region beyond 2200 nm. However, in the bleached state, the solar transmittance of the window remains above 85%. In the colored state, when the thicknesses of filling fluids are 3 mm, 5 mm, and 10 mm, the solar transmittance decreases by approximately 60.6%, 67.6%, and 74.6%, respectively, indicating a solar heat modulation capability greater than 60%. Furthermore, the window maintains a reasonable visible light transmittance in the colored state without any haze, demonstrating that the RB window possesses significant advantages over other types of smart windows.

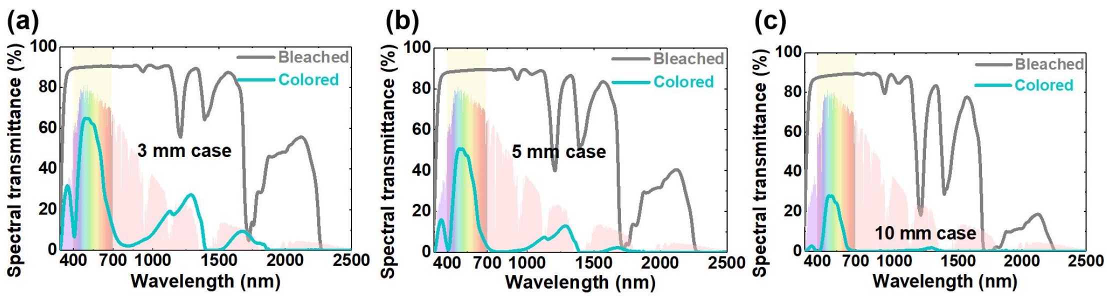

Figure 6.7 Spectral transmittance of (a) 3 mm-thick, (b) 5 mm-thick and (c) 10 mm-thick **RB** windows at bleached and colored states

To further optical the optimal design parameters for the RB window, this chapter systematically tests and analyzes the optical transmittance of the window under different filling fluids thicknesses and various concentrations of the SCBS. Key optical performance indicators were calculated, including visible light transmittance (T_{lum}), solar transmittance (T_{sol}), solar modulation ability (ΔT_{sol}), melanopic transmittance (T_{mel}), circadian efficacy ratio (M/P), color rendering index (CRI), and CIE color coordinates. Detailed data are presented in **Table 6-1**.

Figure 6.8 (a) compares the $\boldsymbol{\Delta T_{sol}}$, $\boldsymbol{T_{lum}}$, and CRI of the RB windows in the colored state, under different SSF compositions and different thicknesses of filling fluids. The results indicate that appropriately increasing the thickness of filling fluids and SSF concentration can enhance solar modulation ability; however, this also leads to a reduction in visible transmittance and CRI. Therefore, a trade-off must be made between solar heat regulation and natural daylight quality during performance optimization. Based on the analysis in **Figure 6.8 (a)**, the SSF composition of 0.1% SCC/10% $CuSO_4$ is recommended, as it offers a well-balanced performance. Using a higher concentration of SSF further reduces the CRI and visible light transmittance in the colored state, which may negatively affect daylighting in architectural applications. Moreover, increasing the interlayer thickness further would increase the volume of the reservoir, which is unfavorable for the aesthetic design of the window.

Specifically, the RB window using 0.1%SCC/10% $CuSO_4$ achieves a ΔT_{sol}, up to 60.6%, with visible transmittance of 90% in the bleached state and 56.2% in the colored state. Additionally, the CRI remains above 80 in the colored state, meeting the requirements for most building daylighting and visual comfort standards. Furthermore, under this SSF configuration, the non-visual light transmittance is close to the visible light transmittance, and the M/P ratio is close to that of natural daylight (0.84), indicating that the window in its colored state can provide a photo-biological effects similar to natural light. This further demonstrates its potential for application in creating healthy building environments.

Table 6-2 summarizes the reported optical performance parameters of representative smart window materials, including thermochromic VO_2, WO_3, and hydrogel-based smart window technologies.

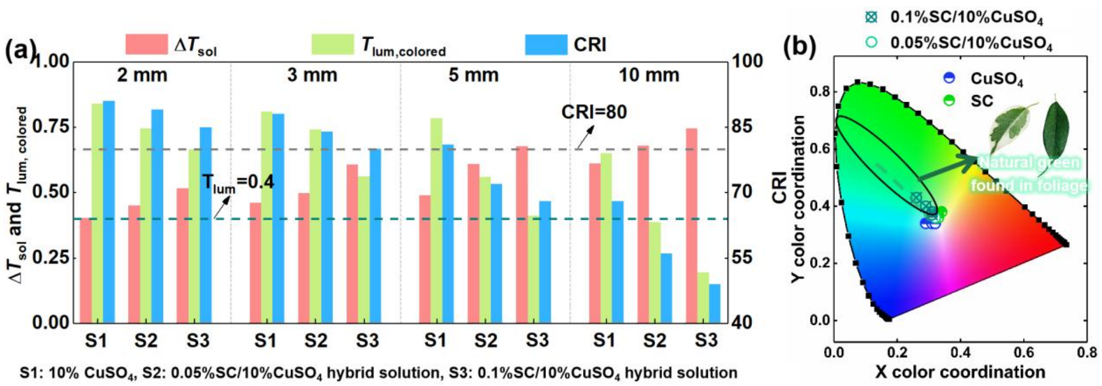

Figure 6.8 (a) performance of the RB windows with different thicknesses and different SSF; (b) chromaticity diagram of the RB window with different kinds of **SSF**.

Table 6-1 Optical properties of the APPs window in cool and hot state, with different spectral splitting fluids

Thickness	**Concentration**	T_{lum} **(%)**		T_{sol} **(%)**		ΔT_{sol}	T_{mel} **(%)**		***LSG***	***M/P***	***CRI***	CIE color coordinates	
		Bleached	**Colored**	**Bleached**	**Colored**	**(%)**	**Bleached**	**Colored**	**(colored)**	**(colored)**	**(colored)**	***x***	***y***
2 mm	20% $CuSO_4$	90.2	74.6	86.2	36.5	47.0	89.8	85.5	1.86	0.97	83	0.29	0.34
	10% $CuSO_4$	90.2	80.7	86.2	46.2	37.3	89.8	86.7	1.73	0.90	92	0.31	0.34
	5% $CuSO_4$	90.2	84.0	86.2	57.7	25.8	89.8	86.8	1.54	0.87	97	0.32	0.34
	0.15% SC	90.2	64.6	86.2	60.2	23.3	89.8	61.5	1.15	0.80	91	0.34	0.38
	0.10% SC	90.2	70.7	86.2	63.1	20.4	89.8	69.1	1.21	0.82	92	0.33	0.37
	0.05% SC	90.2	79.9	86.2	69.2	14.3	89.8	78.5	1.28	0.91	96	0.33	0.36
	10% $CuSO_4$	90.2	84	86.2	45.9	40.3	89.8	90.1	1.80	0.97	91	0.31	0.34
	0.05% SC/10% $CuSO_4$	90.2	74.5	86.2	41.1	45.1	89.8	74.3	1.72	0.84	89	0.32	0.36
	0.1% SC/10% $CuSO_4$	90.2	66.4	86.2	34.5	51.7	89.8	63.4	1.71	0.81	85	0.31	0.37
3 mm	10% $CuSO_4$	90.4	81	85.3	39.3	46	90	90.4	1.93	0.94	88	0.3	0.34
	0.05% SC/10% $CuSO_4$	90.4	74.1	85.3	35.6	49.7	90	73.6	1.87	0.83	84	0.31	0.37
	0.1% SC/10% $CuSO_4$	90.4	56.2	85.3	24.7	60.6	90	54.1	1.75	0.81	80	0.31	0.38
5 mm	10% $CuSO_4$	89.7	78.4	82.7	33.7	49	89.6	89.4	2.05	1.00	81	0.28	0.34
	0.05% SC/10% $CuSO_4$	89.7	55.9	82.7	21.9	60.8	89.6	55	1.85	0.83	72	0.30	0.38
	0.1% SC/10% $CuSO_4$	89.7	41	82.7	15.1	67.6	89.6	39.3	1.60	0.81	68	0.29	0.40
10 mm	10% $CuSO_4$	89.4	65.1	80.6	29.5	61.1	88.7	88.8	1.84	1.15	68	0.25	0.33
	0.05% SC/10% $CuSO_4$	89.4	38.6	80.6	12.6	68	88.7	37.2	1.61	0.81	56	0.27	0.41
	0.1% SC/10% $CuSO_4$	89.4	19.4	80.6	6.0	74.6	88.7	19	1.00	0.82	49	0.26	0.43

Table 6-2 Categories, materials, luminous transmittance and solar modulation ability of the thermochromic (TC) and electrochromic (EC) smart windows

Categories	*TC* materials (*EC* materials)		T_{lum} (%) Bleached	Opaque	ΔT_{sol} (%)	Refs
VO_2-based windows	Signal layer VO_2		78	77	5.9	Wang *et al.* 2015 [138]
			42.6	39.7	15.5	Xiang *et al.* 2022 [152]
			56.4	55.6	12.2	
	Multi-layered VO_2	Si-Al/VO_2	46.3	41.4	18.9	Liu *et al.* 2018 [208]
		TEOS/VO_2	52.7	48.7	16.4	
		VO_2(55nm)/TiO_2(140nm)	50.6	52.1	7.2	Chen *et al.* 2011 [146]
		VO_2(55nm)/TiO_2(420nm)	58	53.9	10.9	
		VO_2(90nm)/SiO_2(85nm)	70.1	66.2	11.6	Liu *et al.* 2020 [209]
	Zn doped VO_2		47.2	51.92	12.1	Kang *et al.* 2021 [141]
	Si doped VO_2		54.7		13.9	Zou *et al.* 2021 [210]
	Zr doped VO_2		60.4		14	Shen *et al.* 2014 [144]
	Ti doped VO_2		53		17.2	Chen *et al.* 2013 [144]
	VO_2-based nanocomposites		52.9	37.3	25.7	Zhao *et al.* 2023 [211]
			63.7	54.4	12	Liu *et al.* 2014 [148]
			43.3	39.9	14.1	
			～50	～50	17	Zhao *et al.* 2020 [147]
			～70	～60	20	Zhao *et al.* 2020 [149]

Hydrogel-based window			89.1	0.6	73.9	Zhou *et al.* 2013 **[153]**
			91.8	73.7	73.7	Zhang *et al.* 2022 **[212]**
			87.2	0.5	81.6	Li *et al.* 2019 **[202]**
			90.2	39	42.1	Zhou *et al.* 2020 **[20]**
			90.9	1.26	68.1	
VO_2/hydrogel hybrid products			86.8	61.8	25	Zhou *et al.* 2015 **[205]**
			82.1	43.2	38.9	
EC window	WO_{3-x} nanoflowers		69.7	41.7	43.6	Huang *et al.* 2023 **[213]**
	WO_x-based plasmochromic		79		70	Cots *et al.* 2021 **[214]**
	Ta-doped TiO_2 nanocrystals		93.4	4.3	80	Cao *et al.* 2019 **[156]**
	WO_{3-x}-NbO_x nanocomposite		93	22	78	Kin *et al.* 2015 **[215]**
EC/TC dual-responsive windows	H^+ doped hydrogel-WO_3	thermochromic	78.5	22.3	42.4	Zhang *et al.* 2023 **[203]**
		electrochromic	78.5	16.3	49.3	
		thermo-/electro- dual-chromic	78.5	4	57.2	
	Li^+ doped hydrogel-WO_3	thermochromic	75.9	12	46.5	
		electrochromic	75.9	22.1	44.3	
		thermo-/electro- dual-chromic	75.9	4.1	54.9	
PC	Cu-W-PC		91	18	73	Meng *et al.* 2023 **[216]**
***RB* window**	SCBS	2 mm	90.2	66.4	51.7	**this work**
		3 mm	90.4	56.2	60.6	
		5 mm	89.7	41.0	67.6	
		10 mm	89.4	19.4	74.6	

Figures 6.9 (a) and **(b)** illustrate the distribution of visible transmittance and solar modulation ability for high-haze scattering-type and haze-free type smart windows, respectively. **Figure 6.9 (c)** provides a comprehensive evaluation of various smart window systems across multiple dimensions, including visible transmittance, non-visual effects, haze, and solar heat regulation ability.

Smart windows based on light-scattering behavior demonstrate significantly higher solar modulation performance compared to haze-free systems. However, such scattering behavior renders the window opaque in its colored state, with visible light transmittance approaching zero and accompanied by high haze levels. High haze optical properties conflict with architectural design standards, limiting their practical application.

In **Figure 6.9 (b)**, the RB window proposed in this study exhibits exceptionally high solar modulation ability under non-scattering conditions, with a ΔT_{sol} ranging from 60.6% to 74.6%, far exceeding other haze-free smart window systems. Meanwhile, the visible transmittance exceeds 90% in the bleached state and remains above 50% in the colored state, significantly outperforming most conventional thermochromic (VO_2) and electrochromic (WO_3) smart windows.

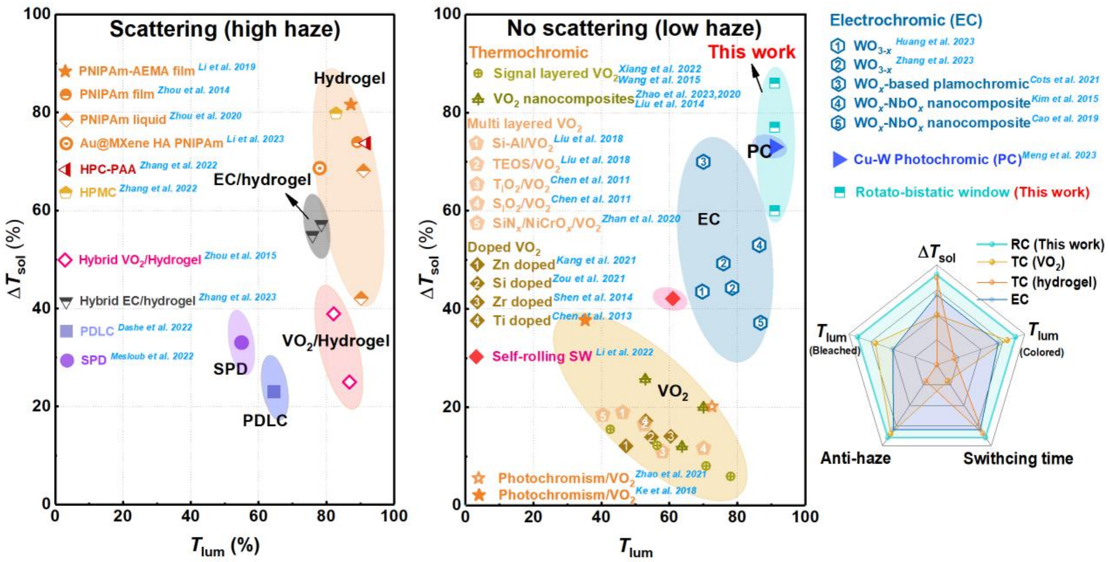

Figure 6.9 (a) comparison of smart windows with scattering-based solar regulation; (b) comparison of smart windows with no scattering behavior; (c) radar plot comparing the performance parameters of various types of smart windows

Furthermore, **Figure 6.9 (c)** highlights the comprehensive advantages of the RB window in terms of solar heat regulation, visible transmittance, response speed, and photo-biological effects. Compared to electrochromic windows that require external power input, the proposed smart window features rapid structural response and energy-free operation. Compared with thermochromic materials such as VO_2, it offers higher visible light transmittance, better solar heat regulation, and improved photo-biological effects. In contrast to hydrogel-based smart windows, it achieves higher visible transmittance in the colored state and remains haze-free, making it more suitable for architectural applications.

6.2.2 Fluid dynamics behaviors

The RB window achieves optical switching through the gravity-based flow of SSF and LP. The density difference between SSF and LP causes these two fluids to separate, forming distinct layers. In the fluids switching process, the photos of a 20 cm × 20 cm RB window sample at different stages were captured, and presented in **Figure 6.10**, and **Figure 6.11** further shows the variation in the visible transmittance of the top and bottom points. The results indicate that it takes approximately 10 seconds for SSF to flow from the top to the bottom position in the coloring process, while the bleaching process takes around 7 seconds.

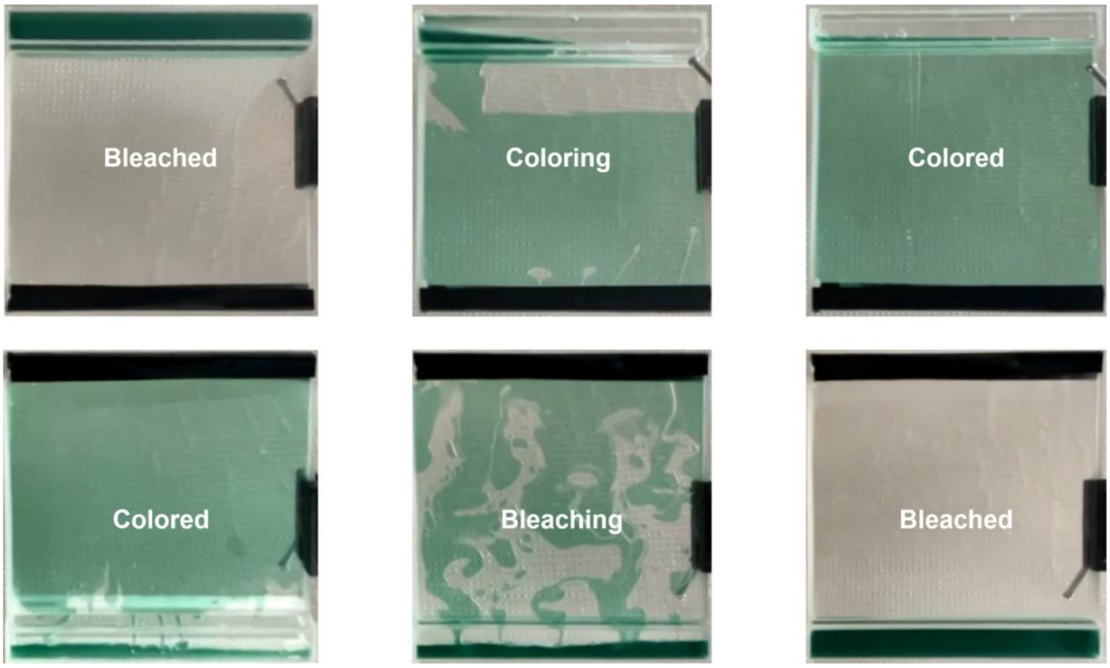

Figure 6.10 Optical photos of the switching process

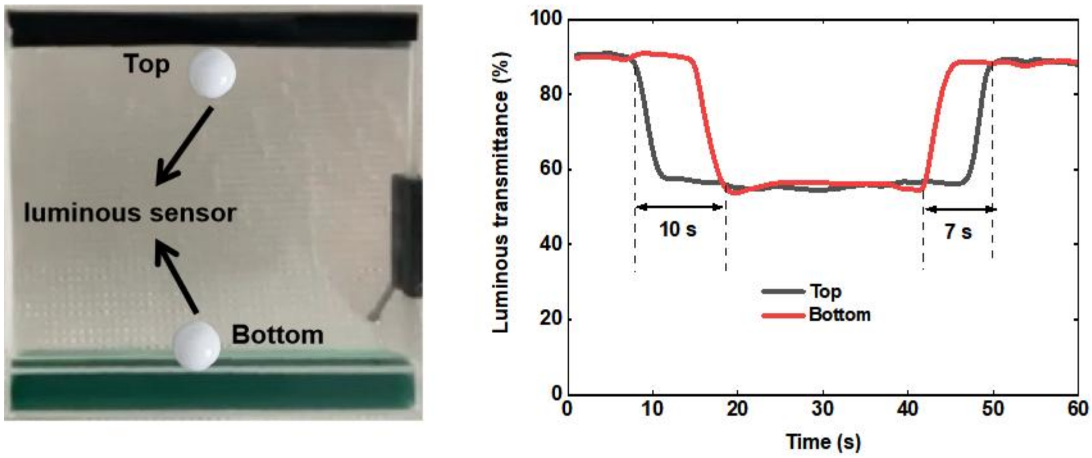

Figure 6.11 Transparency change of specific points on the **RB** window sample

To explore more details in fluid diffusion and mixing processes, CFD simulation was conducted based on the volume of fluid (VOF) model. The simulation considered key factors such as gravity, interfacial tension between fluids, and viscosity differences. The viscosities of LP and SSF at different temperatures were measured using a rotational viscometer, and the results are shown in **Figure 6.12**. Overall, the viscosities of all three liquids decrease with increasing temperature. LP consistently exhibits significantly higher viscosity than SSF and water across all tested temperatures, with the difference being particularly pronounced at lower temperatures. At 4 °C, the viscosity of LP reaches 27.6×10^{-3} Pa·s, while those of SSF and water are only 1.79×10^{-3} Pa·s and 1.57×10^{-3} Pa·s, respectively.

SSF shows slightly higher viscosity than water over the entire temperature range, but the values are relatively close, indicating that SSF possesses good fluidity. In contrast, the high viscosity of LP may result in greater flow resistance, potentially affecting the switching speed of the system. The viscosity of LP is highly sensitive to temperature, suggesting that the switching behavior of the RB window will vary significantly under different thermal conditions. **Figure 6.13** shows the visual results of the simulation, which indicates that the coloring process for the 20 cm × 20 cm RB window sample takes approximately 20 seconds, while the bleaching process takes around 16 seconds.

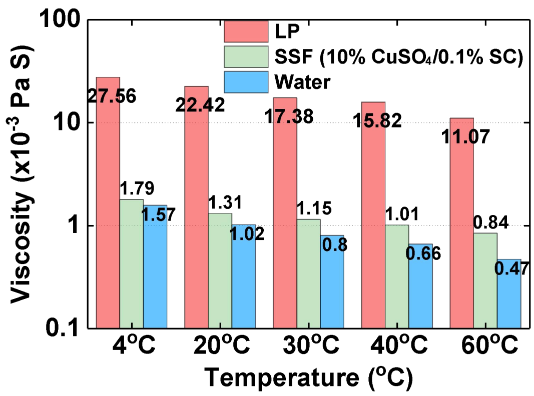

Figure 6.12 Comparisons of the viscosity between **LP** and **SSF** at different temperature

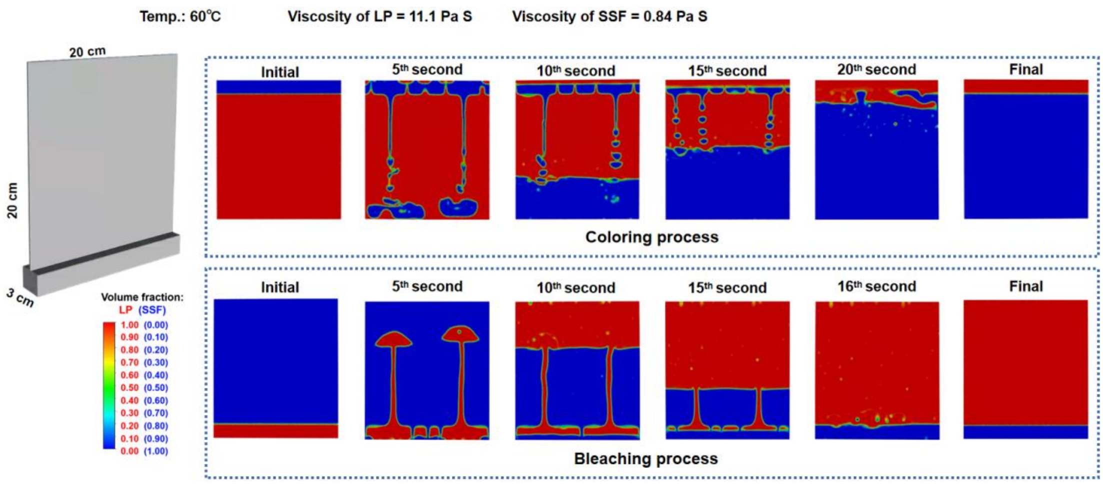

Figure 6.13 **CFD** simulation of the coloring and bleaching process of the RB window sample

To clarify the transparency-switching for the real scaled RB window, the CFD simulation was conducted in a RB window with dimensions of 150 cm (length) × 180 cm (height). **Figure 6.14** shows the bleaching process at a temperature of 20℃. The temperature of fluid will affect its viscosity and thereby affect the transparency switching process. Further, **Figure 6.15** shows the simulated transparency switching time of the RB windows, for both the coloring process and the bleaching process. A smaller window size and higher temperature results in a faster transparency switching. For the real-scaled RB window (150 cm × 180 cm) at temperature of 20 to 60℃, the coloring process requires 91 to 141 seconds, while the time consumption for bleaching process are smaller than 1 minute. This result indicates that the RB window can achieve faster transparency switching than most of the EC windows.

Figure 6.16 displays the results of the cyclic test conducted on the 20 cm × 20 cm RB window sample at room temperature (around 24°C). The visible transmittance of the RB window remains fairly constant in both the bleached and colored states, even after 1000 cycles, demonstrating the cyclic stability of the RB window during extended use. Considering its excellent solar modulation ability, long-term stability, durability in optical performance, high visible transmittance, flexible transparency switching, and easy cleaning features, the RB window proves highly attractive for residential applications.

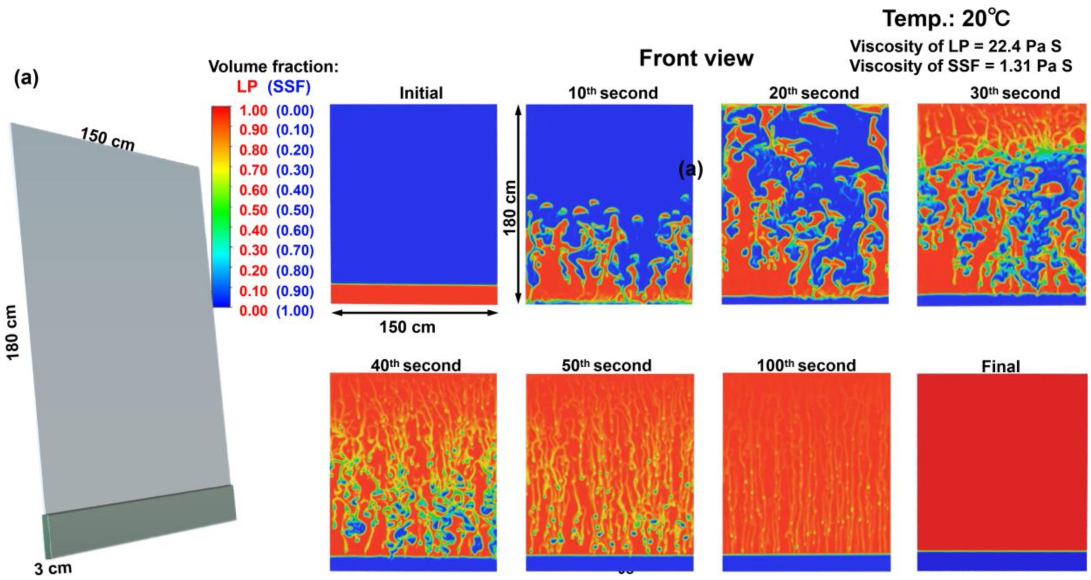

Figure 6.14 (a) CFD simulation results of the fluids switching process for a RB window with dimensions of 150 cm (length) × 180 cm (height)

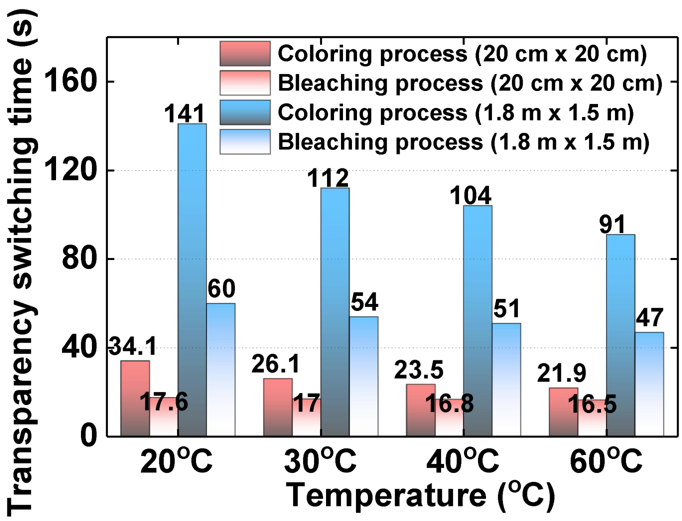

Figure 6.15 Transparency-switching time at different temperature conditions of the

real scaled RB window

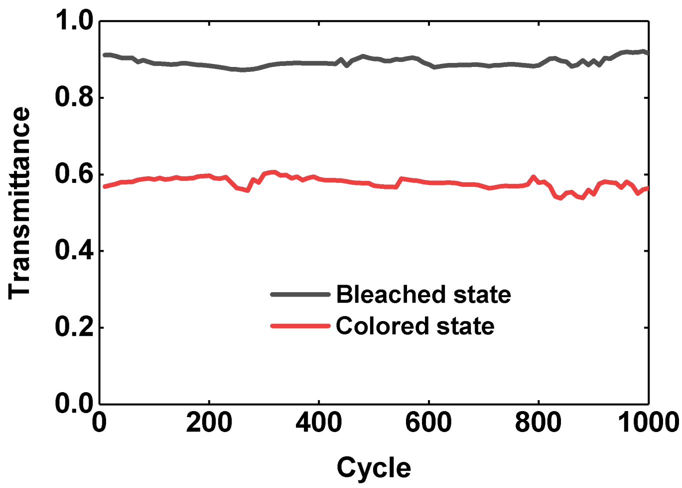

Figure 6.16 Cyclic test of the RB window

6.3 Experimental demonstration of the RB window

To further demonstrate the energy-saving performance of the RB window, continuous outdoor experimental tests were conducted on two summer days in Harbin, specifically on June 19 (sunny day) and June 20 (rainy day), 2023 respectively. The experimental chambers have a dimension of 20 cm × 20 cm × 20 cm, with south surfaces installing the RB windows. The other surfaces of the chambers were spliced with 5 mm-thick PMMA plates and wrapped with 1 cm-thick polyethylene foam (**Figure 5a**). In Chamber 1, the RB window was in the colored state, while in Chamber 2, the RB window remained in bleached state (**Figure 5b**) throughout the experiments.

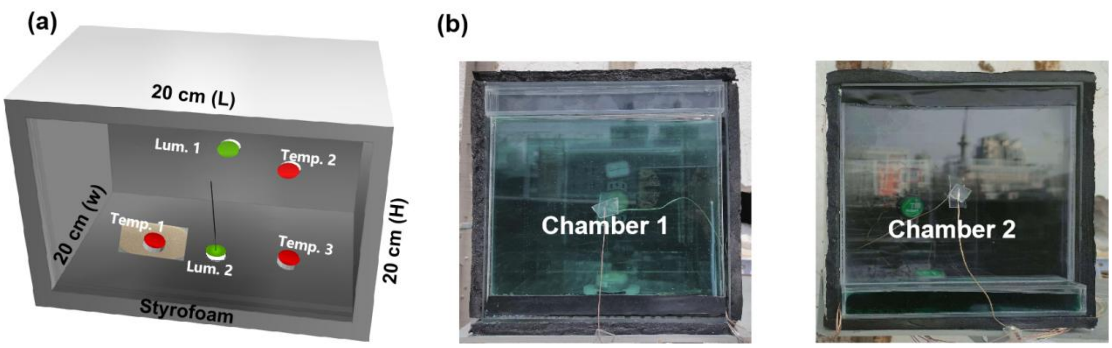

Figure 6.17 (a) Layout of sensors placement in the chamber; (b) experimental chambers with RB window in colored (left) and bleached states (right)

During the tests, two artificial skins were placed on the floor of the chambers, mimicking the solar absorption features of human skin (**Figure 6.18**). Temperature and luminous sensors were strategically placed to continuously record data for further analysis.

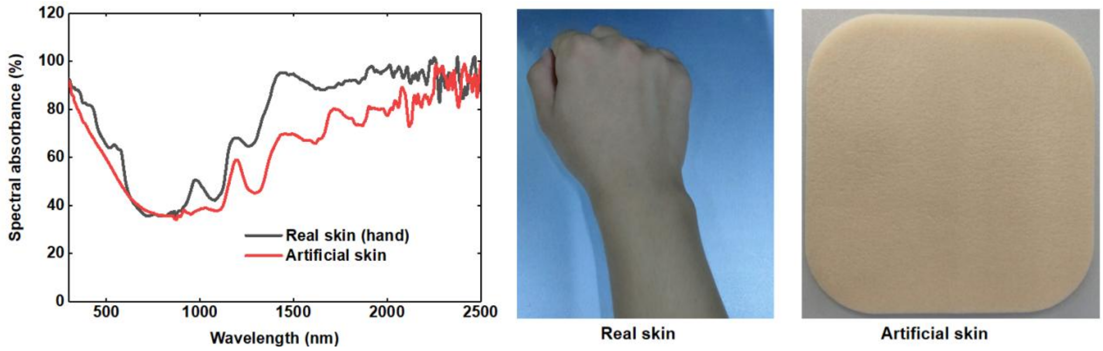

Figure 6.18 Comparison of the spectral absorption of the Real skin and Artificial skin

The outdoor solar radiation levels of the two experimental days were recorded (**Figure 6.19**). On the sunny day (19/06/2023), the maximum temperature of the inner glazing in Chamber 1 was about 4.52°C higher than Chamber 2, at the same time, the difference for the outer glazing was 5.64°C (**Figure 6.20**), indicating a secondary heat transfer caused by the solar absorption of window.

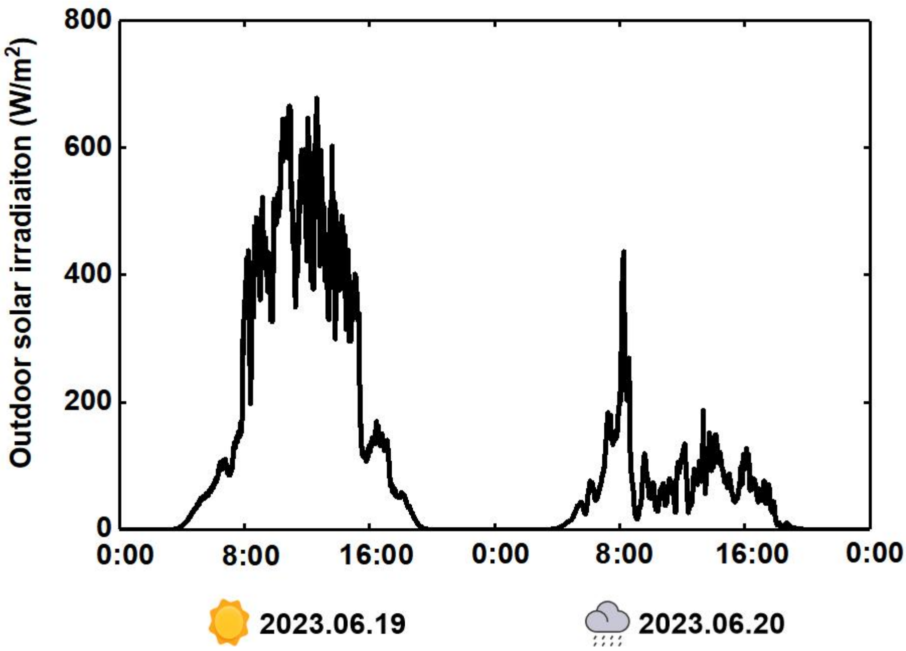

Figure 6.19 Outdoor solar irradiance of June 19 and June 20, 2023

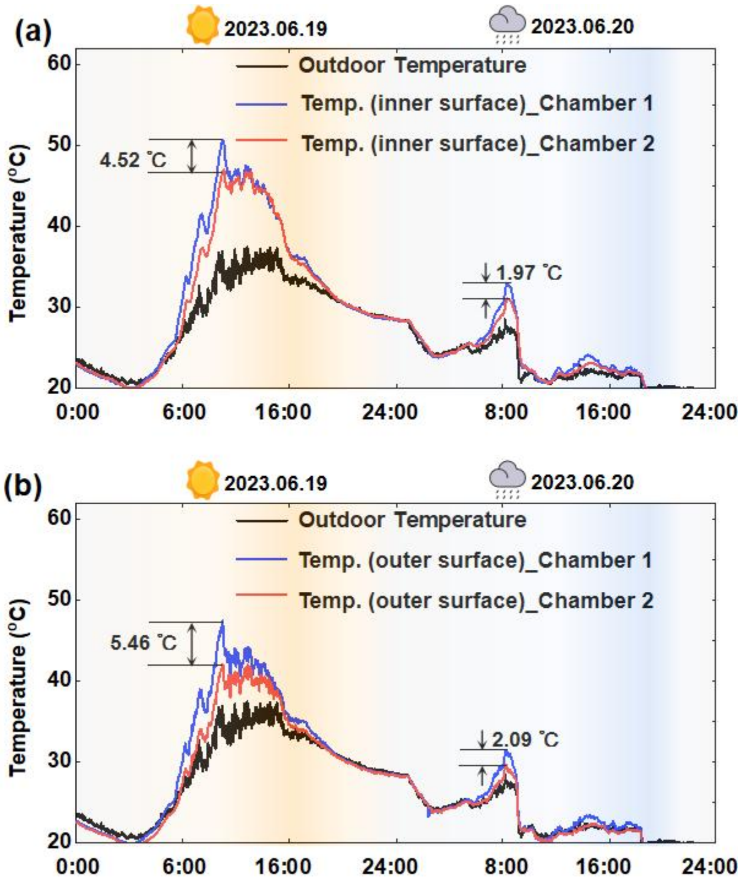

Figure 6.20 Comparisons of the surface temperature of the RB windows in Chamber 1 and Chamber 2

Although it receives the secondary heat transfer from the inner glazing, the measured temperatures inside Chamber 1 were still lower than those of Chamber 2 (**Figure 6.21**), and on the sunny day saw a more significant difference. On 19 June, Chamber 1 saw the highest maximum temperatures of 50.79℃, 50.64℃, and 49.09℃ for the chamber floor, artificial skin, and indoor air respectively, and these figures were about 11.08℃, 5.92℃ and 3.62℃ higher in Chamber 2, demonstrating RB window's ability in regulating indoor solar heat gain.

Figure 6.22 (a) shows the inside daylight at the floor of the chambers. On Jun 19, the floor of Chamber 2 showcased the highest illuminance level of 13158 lux at 12:01 PM. In contrast, the illuminance level on the floor of Chamber 1 was 9154 lux at the same time. The useful daylight illuminance (UDI) recommends a desirable illuminance level between 100 lux to 2000 lux ($U_{100\text{-}2000}$), for effective daylighting in the work plane. As recorded on these two days (**Figure 6.22 b**), both Chamber 1 and Chamber 2 maintained a similar duration of indoor illuminance above 100 lux, on both sunny days and rainy days. However, Chamber 1, with the RB window installed, achieved a longer duration within the $U_{100-2000}$. This is because the biomass dye in the RB window can effectively reduce glare. Comparing the data in **Figure 6.22 b**, Chamber 1 has a duration of approximately 349 minutes within the $U_{100-2000}$ on the sunny day, and 658 minutes on the rainy day. On the other hand, the duration for Chamber 2 are 263 and 507 minutes for the sunny day and rainy day, respectively. These results demonstrate that the RB window has the ability to create a more comfortable and suitable daylight environment, by mitigating glare and providing a more rational distribution of illuminance levels.

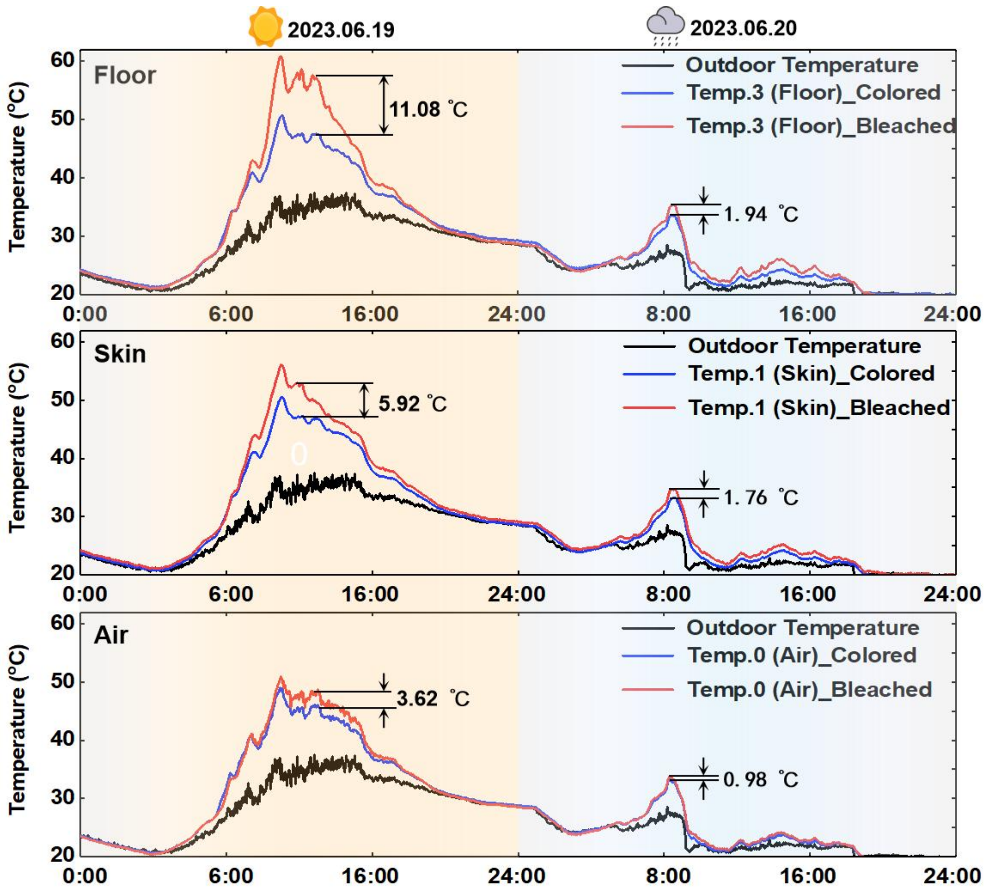

Figure 6.21 Comparisons of the temperatures of the chambers' floor (above), artificial skin (middle) and indoor air (below).

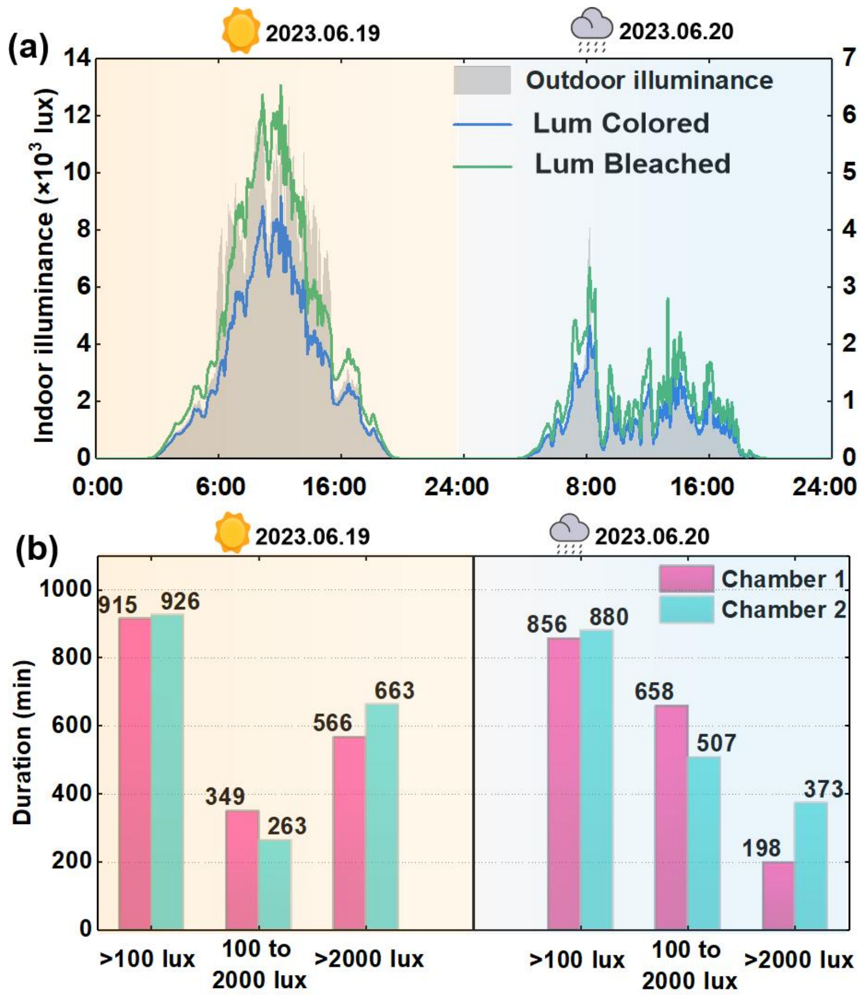

Figure 6.22 Comparisons of the indoor illuminance **(a)** and **(b)** **UDI**$_{100\text{-}2000}$.

6.4 Energy-saving simulation of the RB window

To assess the energy-saving of RB windows, simulations were conducted, considering an inner room of an office building, with dimensions of 6 m × 4.5 m × 3 m (**Figure 6.23 a**). The room installed three windows facing south, and each window has the same dimensions of 1.8 m (length) × 1.5 m (height). The weather data collected in four cities different climatic conditions **[217]**, i.e. Harbin, Hong Kong, and Singapore was used in the simulations. RB window with 3 mm-gap and 0.1%SC/10%$CuSO_4$ SSF was chosen as the object for simulation. The RB window was scheduled to be in colored state when there was a need for space cooling, and the solar radiation received by the window exceeded 200 W/m^2. Otherwise, the windows remained in their bleached state (**Figure 6.26 b**). For comparison, the same building models equipped with ordinary double-pane low-emissivity (low-e) glazing windows and double-pane clear windows were also simulated. Details regarding the window parameters used in the simulations can be found in **Table 6-3**.

Figure 6.23 (c) to **(f)** show the monthly energy consumption for building space cooling. Both RB window and double-pane low-e window could reduce space cooling energy consumption, compared to normal double-pane clear windows. In the annual round, the RB window demonstrates a higher energy-saving performance than the double-pane low-e window (**Figure 6.24**). **Figure 6.23 (g)** compares the monthly space heating consumption of different window types in Harbin. Low-e window would passively reflect the solar radiation energy, negatively increasing the space heating load in cold seasons. While, the RB window can keep a high SHGC value in cold seasons by switching into the bleached state, which is positive for buildings to reduce the space heating energy consumption. In comparison to normal double layered clear window, the RB window can achieve an annual energy-saving of 147 MJ/m^2, 69 MJ/m^2, 183 MJ/m^2, 146 MJ/m^2, in Harbin, Chengdu, Hong Kong and Singapore, respectively, while this figure for the static low-e window are 65.2 MJ/m^2, 60.5 MJ/m^2, 134 MJ/m^2, 134 MJ/m^2 respectively (**Figure 6.23** and **Figure 6.23 h**). These findings highlight the advantages of utilizing RB windows, in both hot and cold climatic zones, as it effectively addresses both space cooling and space heating requirements.

Table 6-3 Parameters of the clear glazing, low-e glazing, and RB window used in the simulation.

	Double layered clear window	Double layered Low-e window	RB window in bleached state	RB window in colored state
U-factor	1.361	1.224	1.404	1.435
SHGC	0.817	0.627	0.821	0.312

Notes: (1) Double glazing in the simulation work is made of two clear glazing with air gap of 13 mm; (2) Double layered low-e glazing is made of a low-e glazing and a clear glazing, with air gap of 13mm.

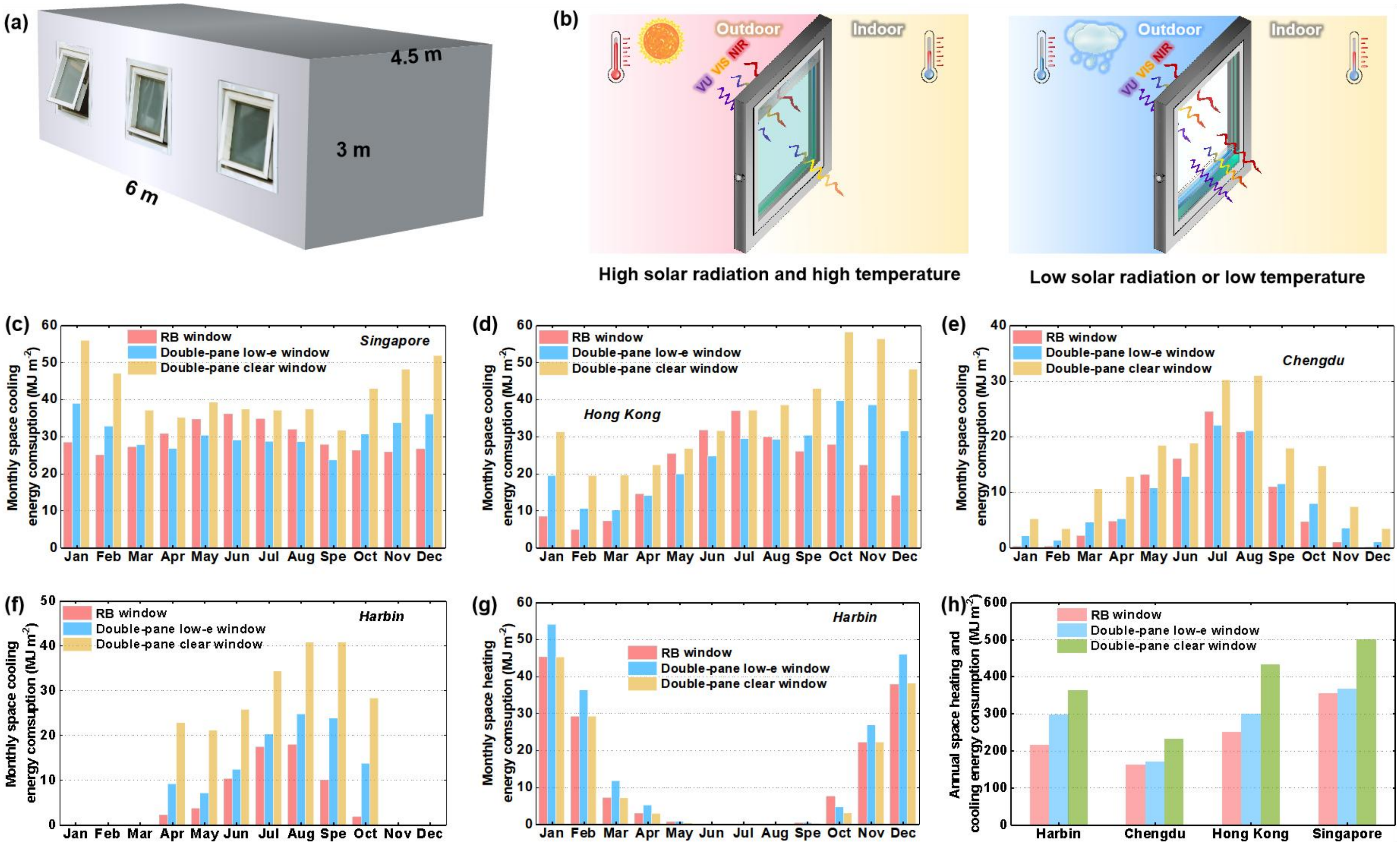

Figure 6.23 (a) Building model used in the simulation, (b) the working principles for the RB window; **(c) - (f)** monthly space cooling energy consumption in different cities; **(g)** monthly space heating energy consumption in Harbin; and **(h)** the annual space cooling and heating energy consumption in these four cities

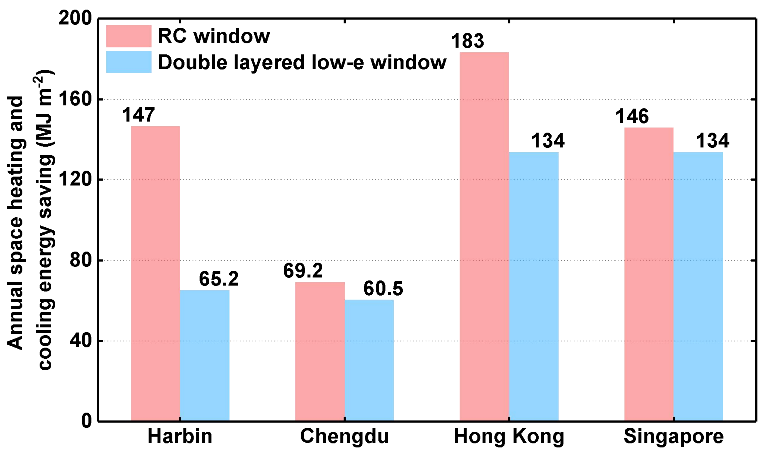

Figure 6.24 Annual space heating and cooling energy-saving of the RB window and double-layered low-e window in different cities.

6.5 Summary

In this chapter, a RB window was designed for solar regulatio. Compared with the traditional TC and EC windows, the RB window showcases significant energy-related advantages. In detail, the RB window presents superior solar modulation ability, surpassing 60%. It also exhibits high luminous transmittances in both bleached (90%) and colored states (56%). In addition, the window has high UV stability, excellent weathering assessment, low haze level (< 1%), rapid transparency switching, feasible color rendering index (CRI > 80), and rational photo-biological. In the experimental demonstration of the RB window, the results indicate that the chamber with RB window could reduce its' inner surface temperature by about 11.2℃ on a sunny day, and it ensures a more rational indoor luminous level by effectively reducing the glare. In addition, simulations conducted in four cities demonstrated the feasibility of the RB window to both hot and cold regions, which can reduce the building space heating and cooling energy consumption of about 30% to 40%.

Chapter 7 Broadband spectrally tunable window via the biomass-derived material and a Janus structure

The spectrally selective window technologies developed in this study are designed to selectively absorb solar radiation. However, once the glazing absorbs solar radiation, its surface temperature rises, and it subsequently transfers heat to the indoor environment via convection and long-wave infrared radiation, leading to the "secondary solar heat gain". Regulating the long-wave radiative characteristics of spectrally selective window surfaces is a promising strategy to avoid "secondary solar heat gain" caused by radiative heat transfer. Traditional low-e technologies achieve a reduction in thermal radiation transmission by depositing low-e coatings on glazing surfaces. These low-e coatings are primarily designed for traditional building glazing, to prevent external thermal radiation from entering indoor space. However, for spectrally selective solar-absorbing window developed in this thesis, the glazing surface temperature is typically higher than the outdoor ambient temperature. Applying a low-e coating on the exterior surface of such glazing may hinder its ability to dissipate heat to the surrounding environment, and it also hindered the radiative sky cooling behavior of the window.

For building thermal regulation, utilizing the atmospheric window (8 to 13 μm) to radiate heat into outer space is an effective passive radiative cooling approach. In summer, the heat absorbing window should integrate a high-emissivity coating on its exterior side to enhance radiative sky cooling, while a low-e coating on the interior side to suppress secondary solar heat gain. In winter, a low-emissivity on the exterior surface is desired to minimize radiative heat loss to the outdoor environment and outer space. To address these seasonal requirements on thermal regulation, this study proposes a Janus structure based on polydimethylsiloxane (PDMS) and silver nanowires (AgNWs). By integrating this Janus structure with the bi-static window developed in Chapter 5, the window can achieve optical-thermal dual regulation through its optical absorbing and reflecting behaviors. This chapter will detail the material composition and structural design of the Janus bi-static (JB) window, construct its optical model, and conduct experimental validation to systematically assess its energy saving behaviros.

7.1 Material and structural design of the Janus bi-static (JB) window

7.1.1 Ideal windows for optical-thermal dual regulation

Figure 7.1 illustrates the ideal spectral properties that windows should have in winter and summer.

(1) **Ideal window for hot season:** The ideal window in hot season is expected to maintain an appropriate visible transmittance to meet daylighting needs, but block NIR to reduce solar heat gain. In addition, the window's outer surface is supposed to have a high emissivity to enhance radiative sky cooling performance. Meanwhile, the inner surface should have a low emissivity to minimize secondary solar heat gain caused by internal radiation.

(2) **Ideal window for cold season:** The ideal window for cold season is expected to maintain high transmittance across the entire solar spectrum, to allow more solar transmission, thereby enhancing indoor lighting and heat gain. At the same time, it is desirable for the outer surface of the window to have a low an emissivity, to prevent tadiative heat transfer from the building to the outside surroundings, and to reduce the sky radiative cooling acting on the window.

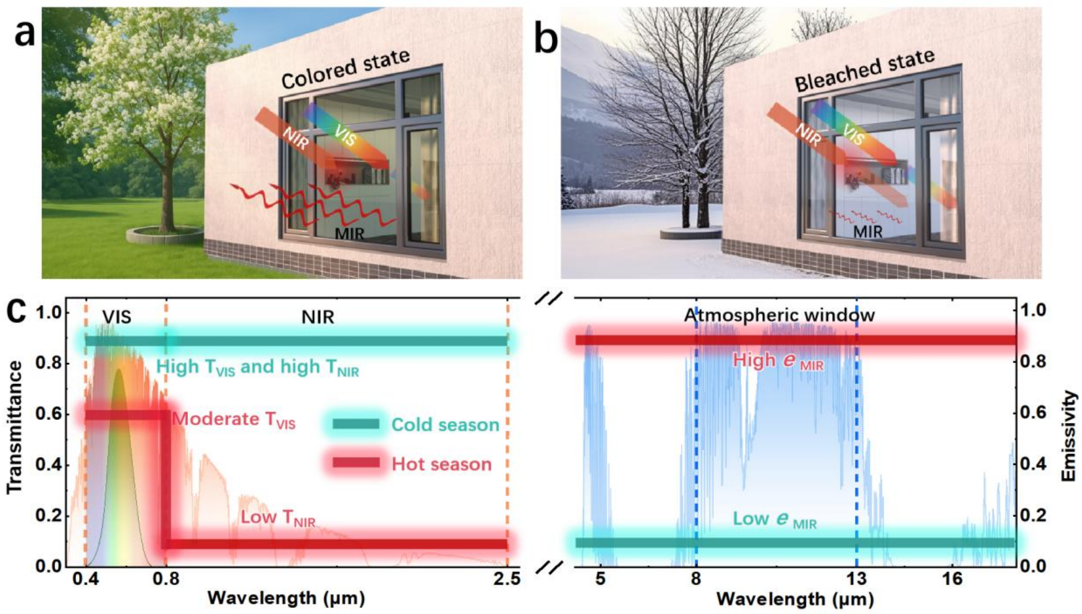

Figure 7.1 Diagrams illustrating the ideal solar and radiative heat transfer properties of windows in different seasons. **(a)** Hot season: windows reflect solar radiation and

minimize heat gain; (**b)** Cold season: windows transmit solar radiation and retain indoor heat; **(c)** Ideal seasonal variations in optical transmittance and thermal emissivity

7.1.2 Material and structural design to match the ideal window

To match the ideal optical properties displayed in **Figure 7.1**, this chapter utilizes the RB window structure proposed in Chapter 6 to achieve solar regulation. Building upon the RB window, a Janus structure based on PDMS (a material with high infrared emissivity) and AgNW (silver nanowires, a material with low infrared emissivity) was further integrated on two surfaces of the window, forming a JB (Janus bistatic) window to realize asymmetric infrared emissivity regulation. **Figure 7.2** shows the schematic structure of this JB window.

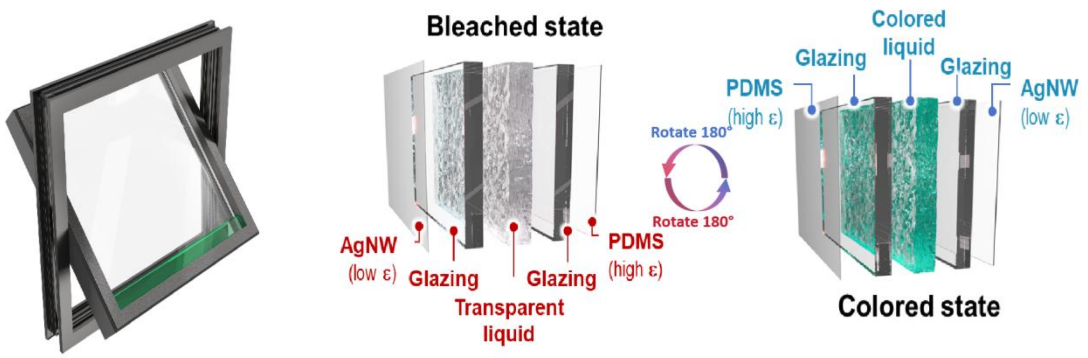

Figure 7.2 Schematic diagram of the JB window design

The spectral regulation principle of the JB window is illustrated in **Figure 7.3**. Through a reversible 180° flipping mechanism, it enables switching between two distinctly different working states: the bleached state and the colored state.

In the bleached state, liquid paraffin (LP) fills the interlayer between glazing panes. The window is highly transparent to both the visible and most of the NIR band. LP has the molecular formula C_nH_{2n+2}. The C–H bond exhibits stretching vibrations that absorb around 1.7 μm in the NIR (first overtone, 2*v*), with weaker absorption around 1.3 μm due to the second overtone (3*v*), and combination vibrations (stretching and bending) absorbing NIR energy between 2.3 to 2.5 μm (*v*). Aside from these, LP is nearly transparent across the solar spectrum. Additionally, the outer surface of the JB window is coated with AgNWs. Due to their electrical conductivity and high free electron density, they strongly reflect infrared radiation, thereby exhibiting low infrared emissivity. In this state, the window is highly transparent to the solar spectrum and has low emissivity within the atmospheric window (8 to 13 μm). This promotes solar heat gain while preventing passive radiative cooling loss through the window.

In the colored state, the JB window is filled with the SSF introduced in Chapter 3. The spectral selectivity of this fluid has been thoroughly discussed in previous chapters. With porphyrin ring in chlorophyll absorbs red and blue light, copper ions absorb short-wave NIR, and water molecules absorb the remaining infrared radiation, the SSF remains highly transparent to green light, while blocking almost all of the NIR. In the colored state, the PDMS coating faces outward and the AgNW coating faces inward. This design enhances the emissivity toward the outdoor side, while maintaining low emissivity toward the indoor side. It facilitates the dissipation of absorbed heat toward the sky and outdoors, while avoiding secondary solar heat gain from the window.

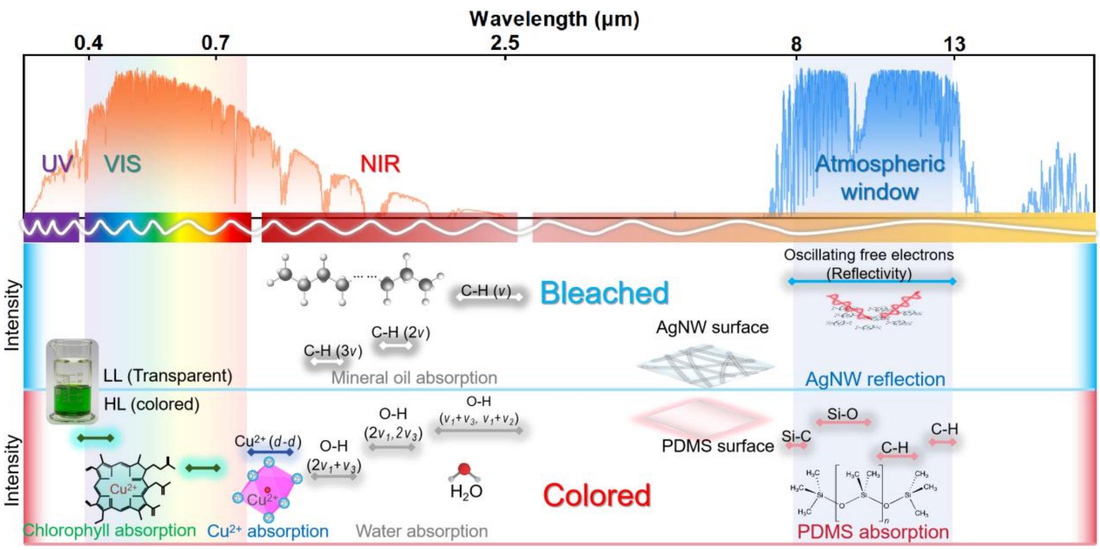

Figure 7.3 Spectral regulation mechanism of the Janus dual-mode window

7.2 Optical simulation of the Janus structure

The optical properties of the Janus dual-mode window primarily focus on optical transmission/absorption/reflection characteristics in the solar spectrum, and emissivity characteristics in the mid-infrared range. The functional materials LP and SSF, used in the solar spectrum range, have been described and analyzed in detail in Chapter 3. This chapter focuses on analyzing the emissivity characteristics of the Janus structure.

7.2.1 Infrared emissivity calculation of PDMS layer

The infrared emissivity of the PDMS film is affected by its thickness. With a specific thickness, the film becomes completely opaque to infrared radiation, and its emissivity is then determined by the interfacial reflection at the material's surface. The absorption (emissivity) and reflectance of the material can be calculated by its intrinsic refractive index (***n***) and extinction coefficient (***k***). In this study, the optical constants of PDMS reported by Zhang et al. **[218]** (see **Figure 7.4**) were collected and used, to calculate the reflectance and absorption (emissivity) of PDMS.

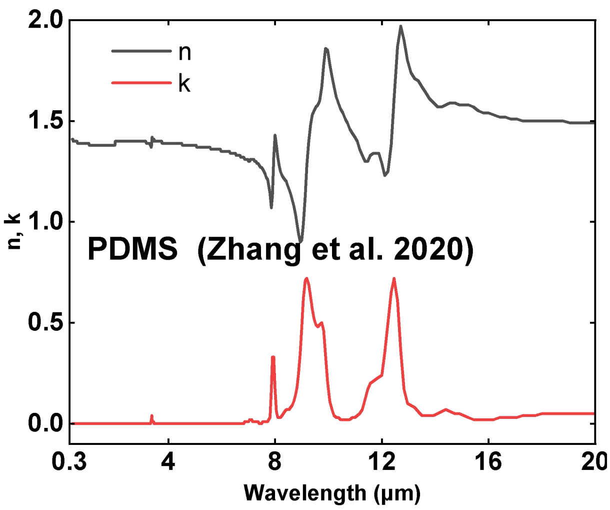

Figure 7.4 Optical constants of PDMS

For the emit direction normal to the PDMS surface, the interfacial reflectance between PDMS and air can be calculated using **Equation (7-1)**, and the emissivity can be calculated using **Equation (7-2)**.

$$\rho_{a-PDMS,\perp} = \frac{(n_{PDMS} - n_a)^2 + (k_{PDMS} - k_a)^2}{(n_{PDMS} + n_a)^2 + (k_{PDMS} - k_a)^2} \tag{7-1}$$

$$\varepsilon_{PDMS} = [1 - \rho_{a-PDMS}(\theta)] \cdot \left[1 - \exp\left(-\frac{4\pi k \sigma_{PDMS}}{\lambda}\right)\right] \tag{7-2}$$

where $\rho_{a\text{-}PDMS}$ (dimensionless) is the reflectance at the air-to-PDMS interface; σ_{PDMS} (μm) is the thickness of PDMS layer.

With tilted incident angle, the interfacial reflectance can be calculated by:

$$R_s = \left| \frac{(n_{PDMS} - i \cdot k_{PDMS}) \cdot \cos(\theta_{PDMS}) - n_a \cos(\theta)}{(n_{PDMS} - i \cdot k_{PDMS}) \cdot \cos(\theta_{PDMS}) + n_a \cos(\theta)} \right|^2 \quad (7\text{-}3)$$

$$R_p = \left| \frac{(n_{PDMS} - i \cdot k_{PDMS}) \cdot \cos(\theta) - n_a \cos(\theta_{PDMS})}{(n_{PDMS} - i \cdot k_{PDMS}) \cdot \cos(\theta) + n_a \cos(\theta_{PDMS})} \right|^2 \quad (7\text{-}4)$$

$$\frac{\sin(\theta_{PDMS})}{\sin(\theta)} = \frac{n_a}{n_{PDMS} + i \cdot k_{PDMS}} \quad (7\text{-}5)$$

$$\rho_{a-PDMS}(\theta) = \frac{1}{2} \cdot \left[R_s(\theta) + R_p(\theta) \right] \quad (7\text{-}6)$$

To verify the accuracy of the emissivity calculation, a comparison was conducted between the calculated values and the tested emissivity of a 10 mm-thick PDMS sample. In this study, the PDMS layer was created by mixing the main agent and curing agent at a 10:1 ratio. **Figure 7.5** depicts this comparison between the tested emissivity of PDMS and the calculated value. The results reveal a strong agreement between the two datasets, affirming the model's ability to accurately predict the emissivity of PDMS.

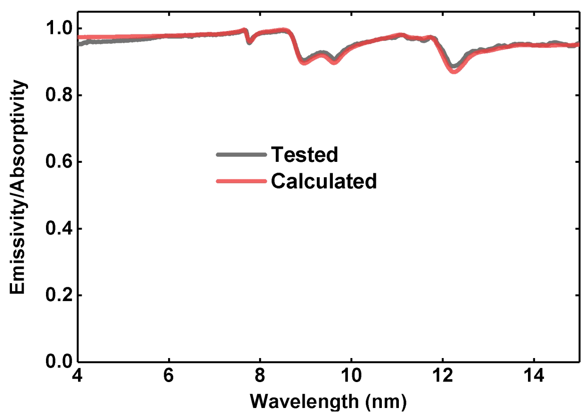

Figure 7.5 Comparison between the tested emissivity and calculated data for PDMS

To determine the optimal thickness of PDMS layer, the optical characteristics of

PDMS at different thicknesses were examined. Figure 7.6 shows the solar transmittance and emissivity for PDMS layers with thicknesses varying from 50 μm to 10 mm. With the thickness of PDMS layer increases from 200 to 300 μm, the emissivity in the atmospheric window (8 to 13 μm) is almost unchanged. Considering that the glazing substrate of the PDMS is opaque for MIR, a 100 μm-thick PDMS is recommended to achieve the minimal MIR reflectance.

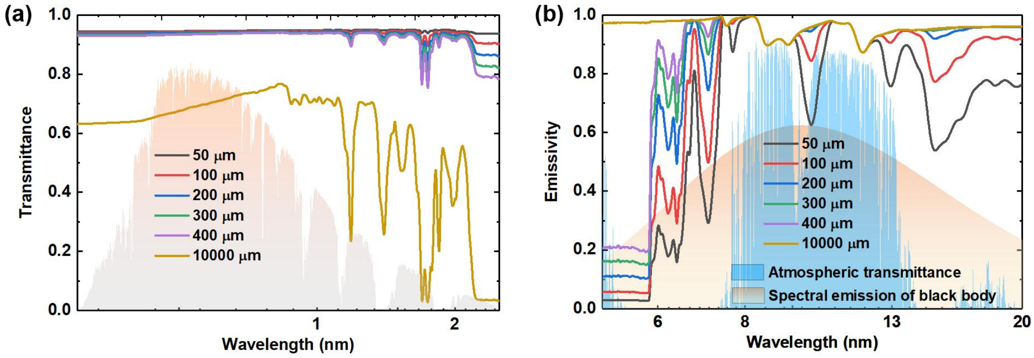

Figure 7.6 Optical properties of PDMS at different thicknesses: (a) solar spectral transmittance, (b) MIR emissivity.

It is important to note that the emissivity of PDMS is affected by interfacial Fresnel reflection, decreasing as the emission angle increases. Figure 7.7 (b) shows the angularly averaged emissivity of a 200 μm-thick PDMS on vertical surface within the atmospheric window (8 to 13 μm). The emissivity is highest in the horizontal (normal) direction, reaching approximately 0.94. As the emission angle deviates from the normal direction, the emissivity gradually decreases, eventually dropping to zero in the vertical direction.

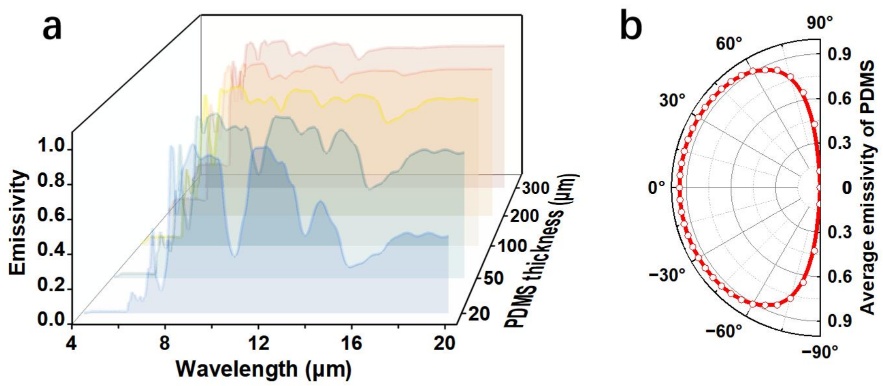

Figure 7.7 MIR emissivity of PDMS: (a) emissivity for various thicknesses and (b) average emissivity over 8-13 μm at different angles.

7.2.2 Infrared emissivity calculation of AgNW layer

In the Janus structure, a low-e AgNW/PET film is designed as a counter side to the PDMS layer. The optical properties of AgNW networks on polyethylene terephthalate (PET) substrates were modeled using the Electromagnetic Waves, Frequency Domain (ewfd) interface in COMSOL Multi-physics. A reduced-order periodic unit cell approach was implemented to efficiently simulate the randomly oriented nanowire network while maintaining computational tractability. Each unit cell consisted of two intersecting nanowires forming a parallelogram configuration, with the intersection angle varied parametrically from 0° to 90° to represent the statistical distribution of nanowire orientations observed in experimental samples.

Considering the propagation characteristics of plane waves in a periodic structure, periodic boundary conditions are applied to the edges of the air layer, PET layer, and PML (Perfectly Matched Layer), a virtual matching layer used in simulations. During the simulation process, the intrinsic optical constants of Ag and PET are taken from the data reported by Arkadiusz et al. **[219]** and Zhang et al.**[218]**, as shown in **Figure 7.8**.

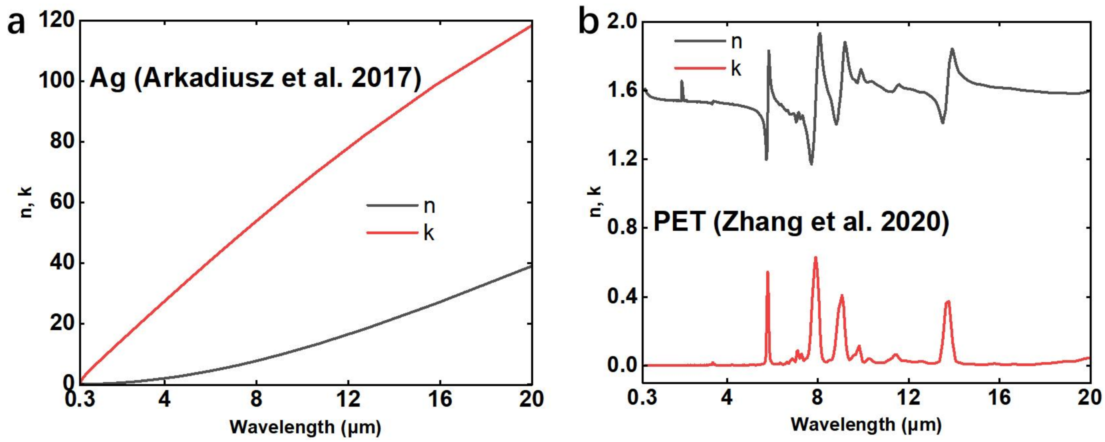

Figure 7.8 Optical constants of (a) Ag **[219]** and (b) PET **[218]**

where w (m) and ξ (rad) are the geometrical parameters shown in **Figure 7.9**.

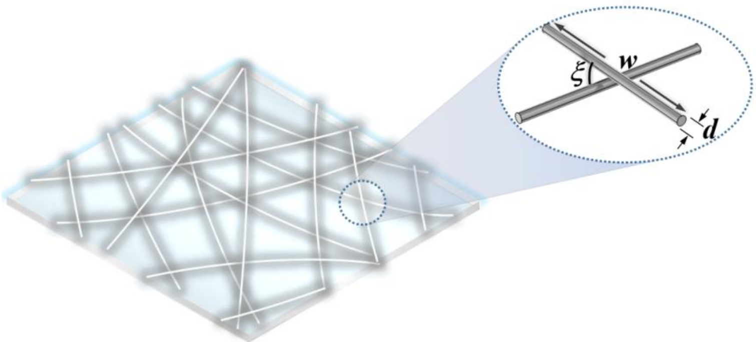

Figure 7.9 Schematic diagram of the AgNW/PET structure

To reveal the electromagnetic properties of AgNWs, the electric field distribution at a height equal to the AgNW diameter (d) above the PET film surface was simulated. The electric field distribution for a unit cell with different intersection angles (ξ), under incident light with a wavelength of 10 μm, is shown in **Figure 7.10**. The results indicate that the smaller ξ leads to a stronger electric field. This is primarily because smaller spacing between nanowires enhances near-field radiation effects, thereby strengthening the optical absorption of the nanowires. **Figure 7.11** presents the simulated infrared emissivity of the AgNW/PET film at different ξ angles. As ξ increases, the emissivity shows an overall decreasing trend. In practical application scenarios, the AgNWs are randomly cross arranged on PET film, thus the emissivity of the AgNW/PET film can be calculated by calculated by the area-weighted average of unit cells from various orientations.

$$\varepsilon = \frac{\int_0^{\pi/2} \varepsilon(\xi) w^2 \sin(\xi)\ d\xi}{\int_0^{\pi/2} w^2 \sin(\xi)\ d\xi} \tag{7-7}$$

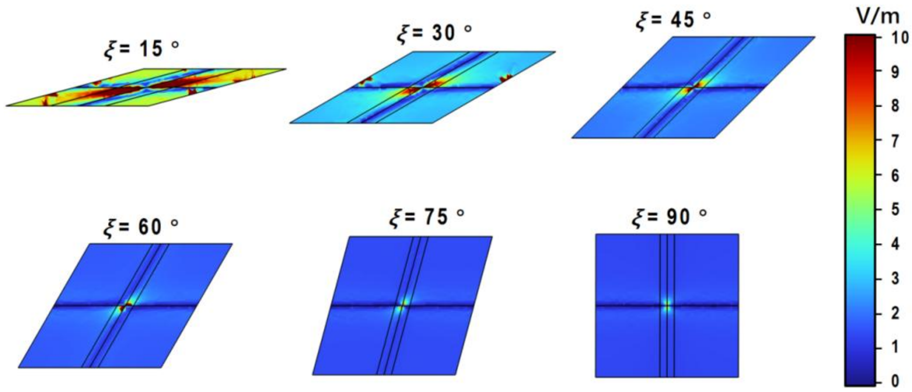

Figure 7.10 Electric field distribution of the AgNW/PET film at the height of ***d***

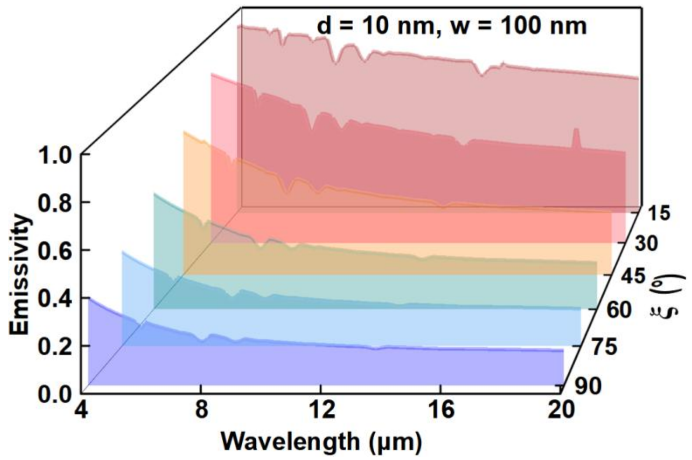

Figure 7.11 Emissivity of AgNW/PET surface with different *ξ* angles

Figure 7.12 (a) presents the infrared emissivity of the AgNW/PET film with a fixed AgNW diameter of 20 nm, under various inter-nanowire spacings (***w***). **Figure 7.12(b)** illustrates the emissivity when the spacing ***w*** is fixed at 200 nm, while the AgNW diameter varies from 10 nm to 50 nm. The results show that decreasing the spacing between nanowires or increasing their diameter leads to a notable increase in emissivity. This trend can be attributed to the enhanced near field coupling and increased surface coverage, which improve the material's ability to absorb and emit infrared radiation. These findings demonstrate that the infrared emissivity of AgNW/PET films can be tuned by controlling the filling factor of the AgNWs, either by adjusting the nanowire density. Such tunability offers crucial clues for designing AgNWs with feasible parameters.

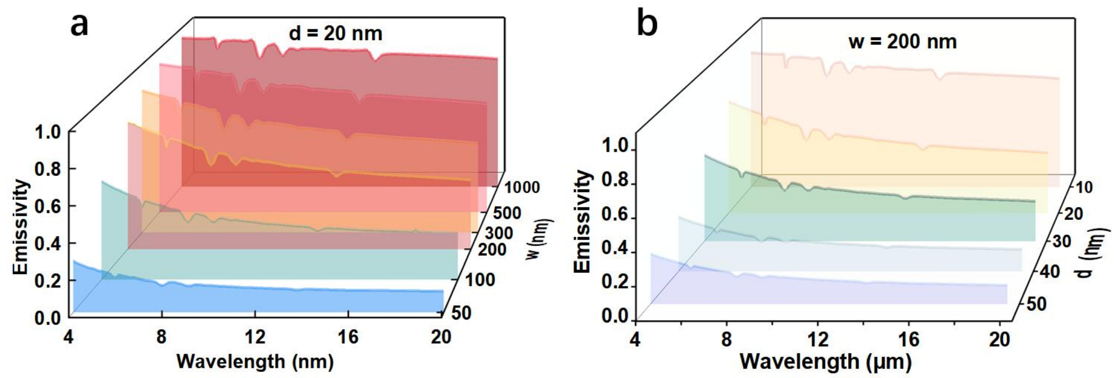

Figure 7.12 Emissivity of AgNW/PET films as a function of (a) silver nanowire diameter and (b) the distance between two parallel nanowires.

The AgNW/PET film with the AgNW diameter of 20 nm, and spacing (***w***) of 100 nm was identified in this study to balance the low MIR emissivity and high solar transparency. **Figure 7.13 (a)** shows the simulated infrared emissivity of the AgNW/PET film with the AgNW diameter of 20 nm, and spacing (***w***) of 100 nm, at various emission angles (0° representing the normal direction). The emissivity gradually decreases as the emission angle increases from 15° to 88°. **Figure 7.13 (b)** further presents the directional average emissivity (8 to 13 μm) within the atmospheric window. The results again demonstrate that the emissivity of the AgNW/PET surface decreases as the emission angle increases, especially beyond 45°, where a noticeable drop in emissivity is observed.

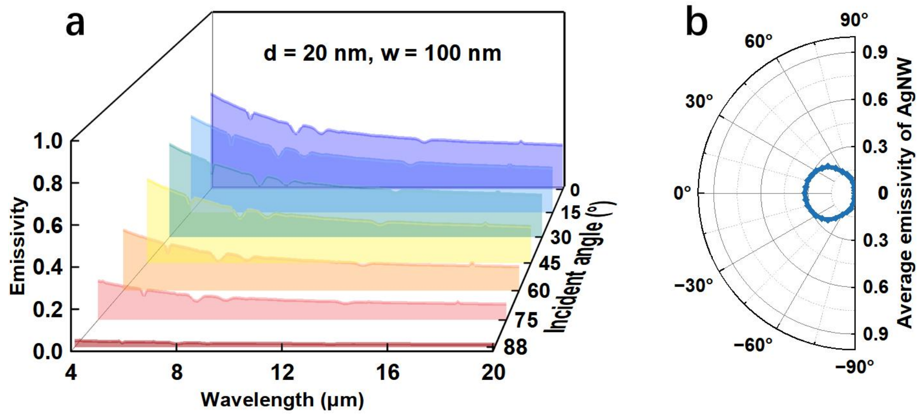

Figure 7.13 MIR emissivity of the AgNW/PET film with diameter of 20 nm, and spacing (***w***) of 100 nm: (a) spectral emissivity at different angles and (b) average emissivity within the atmospheric window (8-13 μm)

7.3 Physical properties of the JB window

7.3.1 Fabrication of the JB window sample

Based on the simulation results, the design parameters of the Janus structure can be identified. With the thickness of PDMS layer being 100 μm, and the AgNW diameter being around 10 nm and the spacing being around 100 nm. In the Janus structure, the PDMS layer was prepared by mixing PDMS prepolymer and curing agent in a 10:1 weight ratio. The resulting mixture was blade-coated onto the outer surface of the RB window, and subsequently cured in an oven at 80°C for 30 minutes to form a solid PDMS film. The commercially available AgNW/PET film, with sheet resistances of

7.5 Ω was selected to approximate the AgNW configuration with a diameter of approximately 10 nm and an inter-wire spacing of around 100 nm. This film was seamlessly attached to the inner surface of the RB window. By incorporating this Janus structure onto the RB window, a JB window was fabricated.

Figure 7.14 (a) shows the photo of the scaled-down model (20 cm × 20 cm) of the JB window. The prototype consists of two 3 mm-thick glass panes, sandwiching a 3 mm-thick fluid-filled interlayer. To distinguish the different sides of the Janus structure, infrared images were captured of each surface using an infrared camera. **Figure 7.14 (b)** displays infrared images of the Janus window in its colored and bleached states, with the left image representing the colored state and the right image the bleached state. Although the surface temperature of both states is identical, the infrared images show significant contrast, clearly demonstrating the difference in infrared emissivity between these two surfaces. **Figure 7.14 (c)** presents an Atomic Force Microscopy (AFM) image of the PDMS-coated surface, while **Figure 7.14 (d)** shows a Scanning Electron Microscopy (SEM) image of the AgNW/PET surface. These micro- and nano-structural characterizations provide further insight into the surface morphology and material quality on both sides of the Janus window.

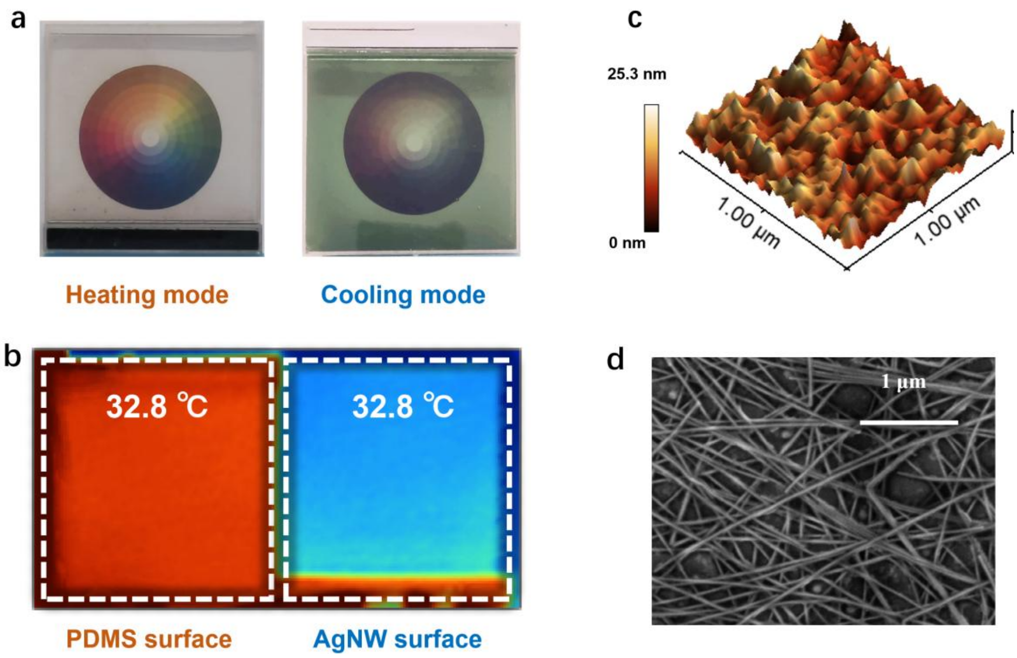

Figure 7.14 Characterization of the Janus bimodal window: (a) Schematic of the JB window; (b) infrared images in colored (left) and bleached (right) states; (c) AFM image of the PDMS surface; (d) SEM image of the AgNW/PET film surface.

7.3.2 Optical properties of the JB window

Figure 7.15 presents the measured spectral transmittance and the MIR emissivity of the JB window. As shown in **Figure 7.15 (a)**, the colored state exhibits low transmittance in the NIR region, effectively blocking solar radiation through the SCBS. Simultaneously, as illustrated in **Figure 7.15 (b)**, it demonstrates a high emissivity close to 1 in the mid-infrared range, particularly within the 8 to 13 μm atmospheric window. This high emissivity facilitates the dissipation of indoor heat to the external environment via thermal radiation, enabling passive cooling.

In contrast, the bleached state shows high transmittance in the visible spectrum, as well as the NIR band, which is beneficial for daylighting and enhancing solar heat gain. Meanwhile, its low emissivity in the MIR range helps suppress the outward radiation of indoor heat, thereby improving thermal insulation performance of the window and avoiding the radiative sky cooling behaviors of the window. This dual-mode optical and thermal properties demonstrate the potential of the JB window for dynamic climate-adaptive building applications.

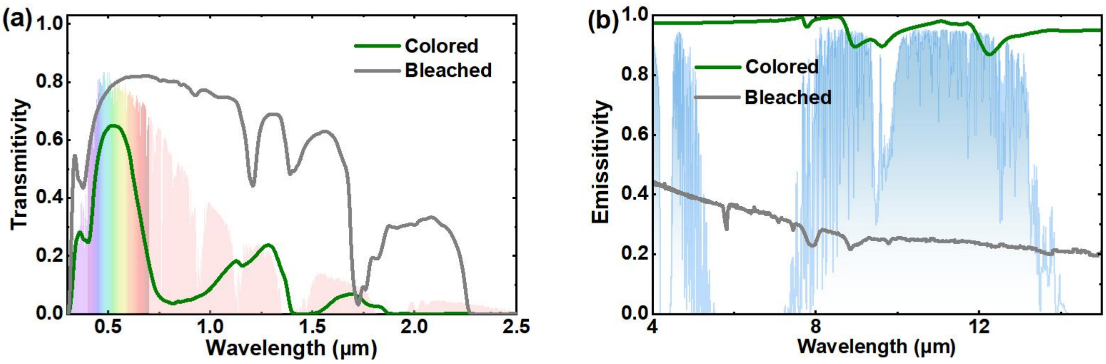

Figure 7.15 (a) spectral transmittance of the JB window in solar spectrum; and (b) MIR emissivity the JB window

To demonstrate the superior performance of the JB widow, this study evaluated its optical properties under various AgNW densities and different SCBS compositions. These performance metrics were then compared with those of recently reported state-of-the-art broadband tunable smart window technologies. **Table 7-1** provides a comprehensive summary of the optical and thermal performance indicators of the JB window alongside those of existing advanced smart window counterparts.

In this study, when employing a SSF composed of 0.1% SCC and 10% $CuSO_4$, combined with a 7.5 Ω AgNW/PET film, the JB widow exhibits a visible transmittance in the bleached state ($\boldsymbol{T_{lum,bleached}}$) of 0.81, and a transmittance in the colored state ($\boldsymbol{T_{lum,colored}}$) of 0.49. Under these conditions, the solar modulation ability ($\boldsymbol{\Delta T_{sol}}$) reaches 0.51, while the emissivity modulation ability in the atmospheric window range ($\boldsymbol{\Delta\varepsilon}$) reaches 0.70. Alternatively, when using an SSF composed of 0.05% SCC and 10% $CuSO_4$ with the same 7.5 Ω AgNW/PET film, the $\boldsymbol{T_{lum,colored}}$ increases to 0.62, with a corresponding $\boldsymbol{\Delta T_{sol}}$ of 0.44 and $\boldsymbol{\Delta\varepsilon}$ remaining at 0.70. Furthermore, when the AgNW/PET film with a sheet resistance of 10 Ω is used in combination with the 0.05% SCC/10% $CuSO_4$ **SSF**, the $\boldsymbol{T_{lum,bleached}}$ improves to 0.87, while the $\boldsymbol{T_{lum,colored}}$ is 0.65, and the $\boldsymbol{\Delta T_{sol}}$ reaches 0.49. In this case, the $\boldsymbol{\Delta\varepsilon}$ is slightly reduced to 0.58, but still remains within a highly effective range for thermal regulation.

Taken together, these results demonstrate that the JB window developed in this study offers a unique combination of high-performance features, including high visible transmittance in the bleached state, moderate visible transmittance in the colored state, strong solar modulation, outstanding MIR emissivity modulation, and haze-free optical clarity. These advantages position the proposed JB window as a superior alternative to other tunable smart windows. **Figure 7.16** provides a comparative analysis of the solar heat gain modulation ($\boldsymbol{\Delta T_{sol}}$) and MIR emissivity modulation ($\boldsymbol{\Delta\varepsilon}$) of the JB window, against various state-of-the-art smart window technologies. The results clearly indicate that the JB outperforms existing materials and structures in both solar and thermal regulation capabilities, highlighting its potential for advanced energy-efficient building applications.

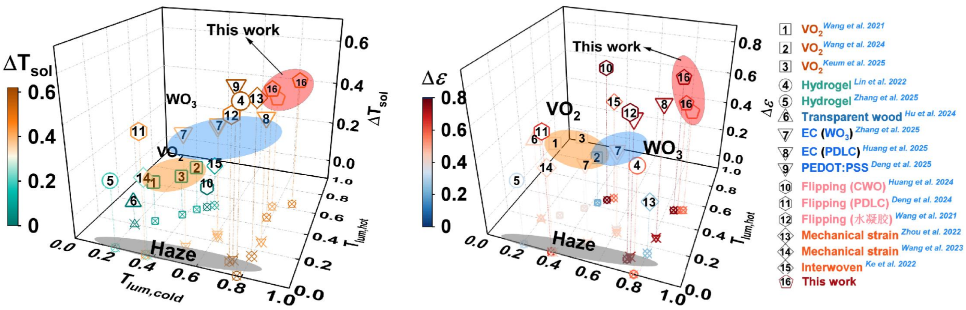

Figure 7.16 Comparison between the (a) $\boldsymbol{\Delta T_{sol}}$ and (b) $\boldsymbol{\Delta\varepsilon}$ between the JB window and recently reported, state-of-the-art smart windows

Table 7-1 Optical parameters of the JB window and its counterparts

Categories	Scattering or not?	T_{lum}		T_{sol}		T_{sol}	ε		$\Delta\varepsilon$	Refs
		Cold	**Hot**	**Cold**	**Hot**		**Cold**	**Hot**		
VO_2	No	0.28	0.26	—	—	0.09	0.21	0.61	0.4	Wang et al. 2021 [220]
W-doped VO_2	No	0.43	0.43	0.51	0.40	0.11	0.71	0.94	0.23	Wang et al. 2024 [221]
VO_2	No	0.38	0.36	0.38	0.29	0.09	0.3	0.7	0.40	Keum et al. 2025 [222]
WO_3	No	0.50	0.12	0.39	0.08	0.39	0.4	0.82	0.42	Zhang et al. 2024 [223]
	No	0.60	0.26	0.57	0.19	0.38	0.42	0.82	0.4	
	No	0.61	0.24	0.58	0.18	0.4	0.37	0.82	0.45	
Electrically controlled device	No	0.85	0.85	—	—	≈0	0.49	0.9	0.41	Jia et al. 2023 [224]
Liquid filled EC device	No	0.81	0.27	0.69	0.25	0.44	0.19	0.93	0.74	Huang et al. 2025 [225]
ITO/PEDOT:PSS	No	≈0.73	≈0.1	≈0.7	≈0.1	0.6	0.2	0.94	0.74	Deng et al. 2025 [226]
Reconfigurable interwoven surface	No	0.5	0.5	0.45	0.55	0.1	0.36	0.93	0.57	Ke et al. 2022 [227]
Flipping structure	No	0.47	0.47	≈0.25	≈0.25	0	0.13	0.94	0.81	Huang et al. 2024 [228]
Flipping PDLC	Yes	0.36	haze	0.43	0	0.42	0.3	0.95	0.65	Deng et al. 2024 [229]
Flipping structure with hydrogel	Yes	0.72	0.08 haze	0.57	0.07	0.50	0.1	0.9 (PE)	0.8	Wang et al. 2021 [152]
Hydrogel and AgNW	Yes	0.78	haze	0.66	0.07	0.58	0.35	0.92	0.57	Lin et al. 2022 [230]
VO_2 and hydrogel	Yes	0.21	haze	0.20	0	0.2	0.35	0.69	0.33	Zhang et al. 2025 [231]
Mechanical strain	Yes	≈0.8	≈0.15	0.8	0.25	0.55	0.59	0.84	0.25	Zhou et al. 2022 [232]
Mechanical strain	Yes	0.37	haze	—	—	0.24	0.45	0.9	0.45	Wang et al. 2023 [233]
Transparent wood	Yes	0.20	0.2	0.22	0.21	0.01	0.19	0.63	0.44	Hu et al. 2024 [234]
JB window	No	0.81	0.49	0.71	0.20	0.51	0.24	0.94	0.7	This work
	No	0.81	0.62	0.69	0.27	0.44	0.24	0.94	0.7	
	No	0.87	0.65	0.79	0.30	0.49	0.36	0.94	0.58	

7.4 Experimental demonstration of the JB window

To evaluate the energy-saving performance of the JB window, a seven-day continuous outdoor field experiment was conducted in Hong Kong, from May 5 to May 11, 2025. During the period, comprehensive meteorological data, including Global Horizontal Irradiance (GHI), Diffuse Horizontal Irradiance (DHI), ambient air temperature, and wind speed, were continuously recorded by a nearby weather station. The week-long experiment encompassed a range of typical weather conditions, such as sunny, cloudy, overcast, and rainy days, thereby ensuring the robustness of the results under realistic environmental variability (see **Figure 7.17**).

The experimental setup involved two thermally insulated chambers, each with dimensions of 30 cm × 30 cm × 30 cm. On the south-facing side of Chamber 1, a 20 cm × 20 cm JB window was installed, with a 7.5 Ω silver nanowire coating as the low-emissivity layer, and 0.1% SCC/10$CuSO_4$ as the SSF. In contrast, Chamber 2 was fitted with a conventional low-e glazing window, with the same size and orientation. Apart from the window, all other surfaces of the test chambers were constructed using 5 mm thick PMMA (polymethyl methacrylate) sheets, externally insulated with 1 cm thick polyethylene foam to minimize thermal losses (see **Figure7.18 b**). To emulate the thermal absorption characteristics of actual indoor environments, the interior of each chamber was lined with artificial skin simulant material, whose spectral absorptivity characteristics are detailed in **Figure 6.18** of this study. A dense array of sensors was deployed at strategically selected locations within each test chamber, to monitor both thermal and optical parameters. Thermocouples were installed at four key positions: the center of the air volume, the floor surface, the artificial skin surface, and the inner surface of the glazing. Additionally, an illuminance sensor was embedded at the center of the floor to monitor indoor light in real time. All sensors were configured for continuous data acquisition throughout the experimental period, and their configurations are illustrated in **Figure 7.18 (a)**.

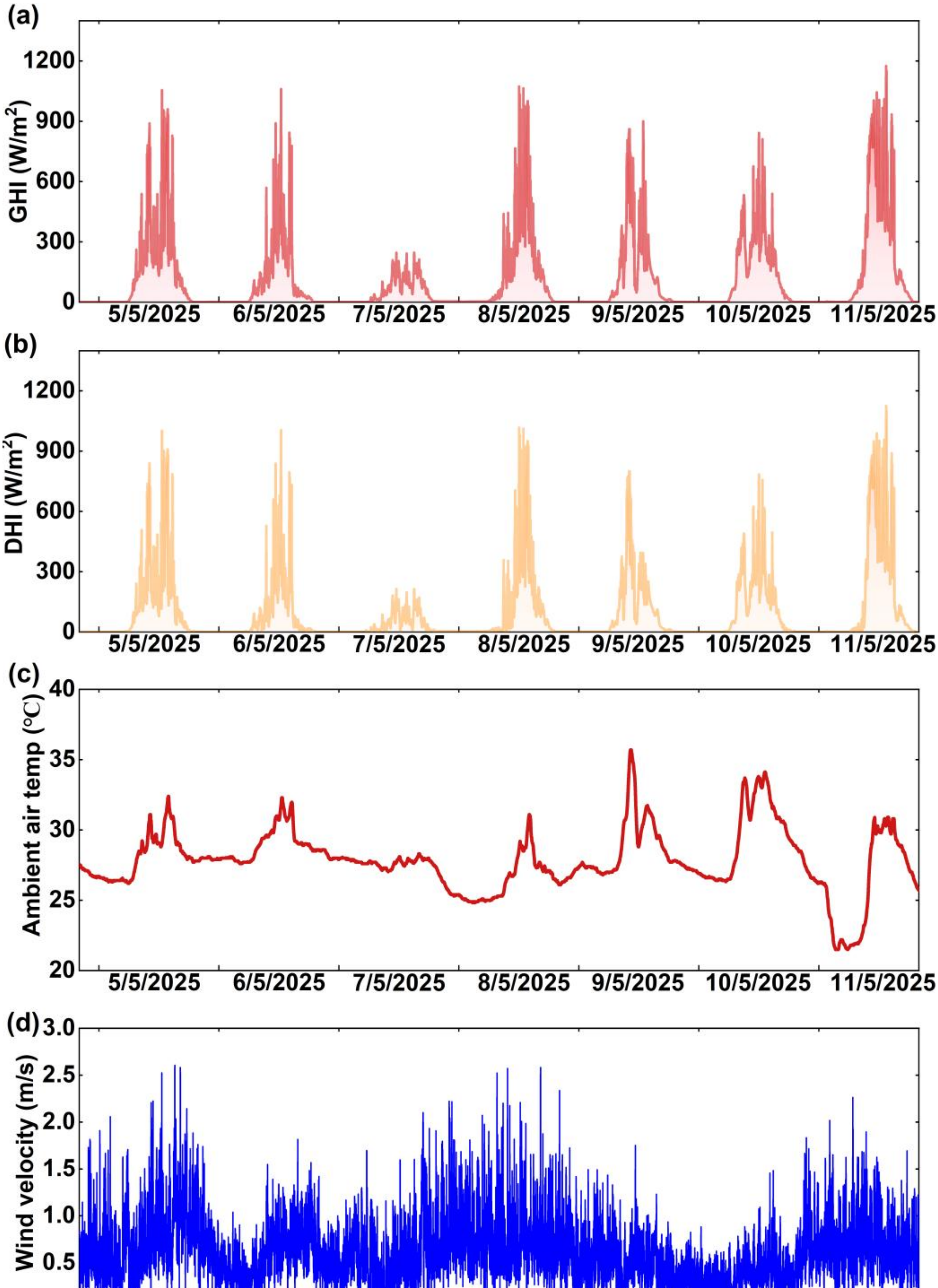

Figure 7.17 Environmental conditions during the experimental period: **(a)** Global horizontal solar irradiance; **(b)** direct horizontal solar irradiance; **(c)** outdoor air temperature; **(d)** outdoor wind speed during the experimental period.

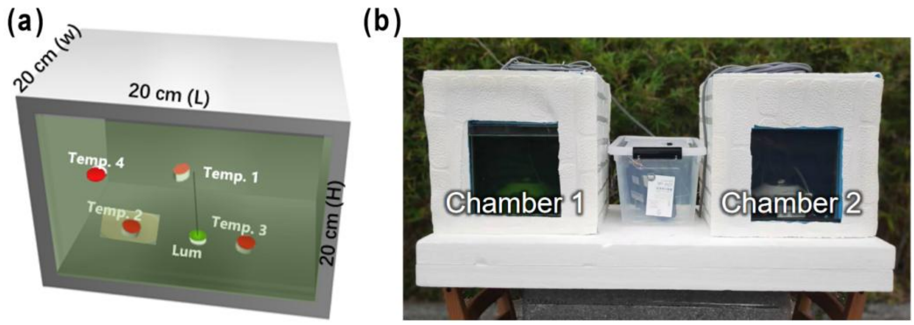

Figure 7.18 Experimental chamber setup and sensor layout: (a) Schematic diagram of sensor layout in the experimental chamber; (b) photos of the experimental chambers

Figure 7.19 presents the temporal variations of indoor illuminance in both chambers. During most daylight hours, both boxes recorded illuminance levels exceeding 2000 lux, which can potentially cause discomfort due to glare. On average, the chamber equipped with the JB window exhibited approximately 40% lower indoor illuminance levels. This demonstrates the effectiveness of the colored (solar control) mode of the Janus window in attenuating natural daylight transmittance, thereby contributing to visual comfort by reducing glare.

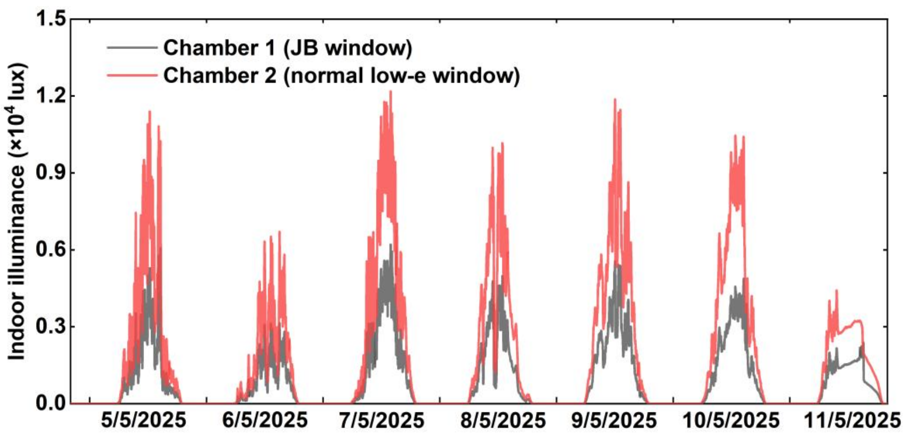

Figure 7.19 Comparison of indoor illuminance between two chambers

Figure 7.20 provides a comparative analysis of several thermal performance metrics, including indoor air temperature, artificial skin surface temperature (proxy for human skin exposure), floor surface temperature, and inner glazing surface temperature. Compared to the low-e glazing window, the JB window reduced indoor air temperature by up to 7.3°C, skin surface temperature by up to 9.0°C, floor surface temperature by up to 10.3°C, inner window surface temperature by up to 9.3°C. These results provide evidence that the JB window significantly enhances thermal comfort, and has a high potential to reduce cooling loads in summertime, outperforming traditional low-e glazing in building energy saving.

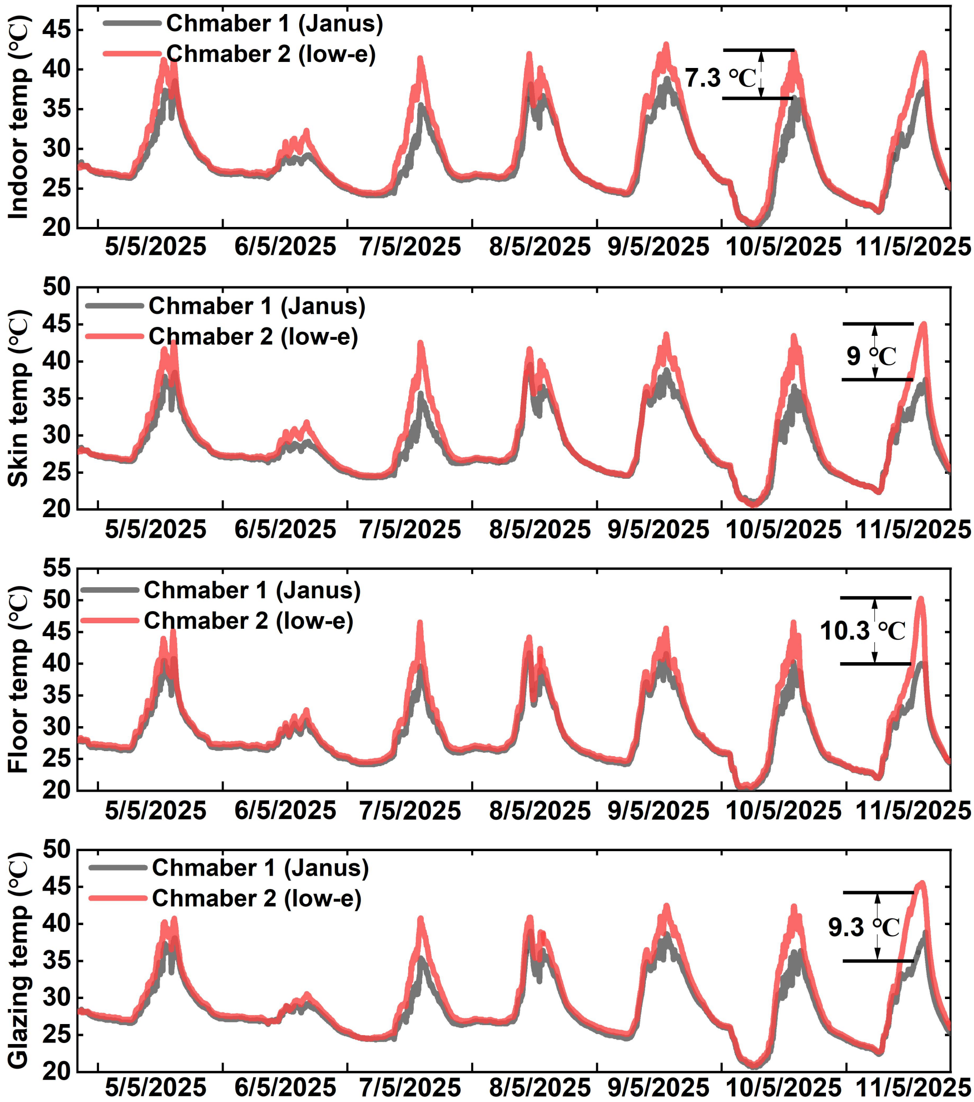

Figure 7.20 Comparison of temperatures at different locations of the two chambers

7.5 Energy-saving simulation of the JB window

To validate and quantify the energy-saving potential of the JB window across different climate zones, this study conducted a comprehensive simulation based through developing an optical transmission model and transient heat transfer model specific for the JB window.

7.5.1 Model development

(1) Optical transmission/absorption model

In the optical modeling of the JB window, it is essential to comprehensively account for both multi-layer absorption and multi-interface reflection phenomena. The JB window consists of six distinct optical media arranged in sequence: "PDMS-glazing-filling fluids (SCBS or LP)-glazing-PET-AgNW". Due to the similar refractive indices of PET film and glazing (both approximately 1.5), the interfacial reflection between PET and glazing can be considered negligible. Therefore, the PET film can be excluded from the optical model of the JB window in the simulation. Then the JB window can be considered as five optical media arranged in sequence: "PDMS-glazing-filling fluids (SCBS or LP)-glazing-AgNW".

The optical transmission model incorporates the spectral absorption and reflection of each of the five media. Each layer's absorption and reflection coefficient is wavelength-dependent, and contributes to the overall attenuation of solar radiation. In these five media, the interfacial Fresnel reflections at five key optical boundaries include: Air-PDMS interface, PDMS-Glazing interface, Glazing-Fluid interface, Fluid-Glazing interface, Glazing-Fluid interface and Glazing-AgNW-Air interface.

The interfacial reflectance of Air-PDMS interface, PDMS-Glazing interface, Glazing-Fluid interface, Fluid-Glazing interface, Glazing-Fluid interface can be calculated by the model developed in **Chapter 4**:

$$\rho_{a-PDMS}(\theta)=\frac{1}{2}\left(\frac{n_a\cos(\theta_a)-n_{PDMS}\cos(\theta_{PDMS})}{n_a\cos(\theta_a)+n_{PDMS}\cos(\theta_{PDMS})}\right)^2+\frac{1}{2}\left(\frac{n_a\cos(\theta_{PDMS})-n_{PDMS}\cos(\theta_a)}{n_{PDMS}\cos(\theta_a)+n_a\cos(\theta_{PDMS})}\right)^2 \quad (7\text{-}8)$$

$$\rho_{PDMS-g}(\theta)=\frac{1}{2}\left(\frac{n_g\cos(\theta_g)-n_{PDMS}\cos(\theta_{PDMS})}{n_g\cos(\theta_g)+n_{PDMS}\cos(\theta_{PDMS})}\right)^2+\frac{1}{2}\left(\frac{n_g\cos(\theta_{PDMS})-n_{PDMS}\cos(\theta_g)}{n_{PDMS}\cos(\theta_g)+n_g\cos(\theta_{PDMS})}\right)^2 \quad (7\text{-}9)$$

$$\rho_{f-g}(\theta)=\rho_{g-f}(\theta)=\frac{1}{2}\left(\frac{n_g\cos(\theta_g)-n_f\cos(\theta_f)}{n_g\cos(\theta_g)+n_f\cos(\theta_f)}\right)^2+\frac{1}{2}\left(\frac{n_g\cos(\theta_f)-n_f\cos(\theta_g)}{n_f\cos(\theta_g)+n_g\cos(\theta_f)}\right)^2 \quad (7\text{-}10)$$

and the reflectance of Glazing-AgNW-Air interface will be calculated by the CPMSOL software.

For the PDMS layer:

When radiation incident from the air-PDMS interface, the reflectance can be calculated by:

$$R_{PDMS} = \rho_{a-PDMS} + \frac{(1-\rho_{a-PDMS})^2 \cdot \varepsilon_{PDMS}^2 \cdot \rho_{PDMS-g}}{1-\varepsilon_{PDMS}^2 \cdot \rho_{a-PDMS} \cdot \rho_{PDMS-g}} \tag{7-11}$$

When radiation incident from the glazing-PDMS interface, the reflectance can be calculated by:

$$R_{PDMS}^{'} = \rho_{PDMS-g} + \frac{(1-\rho_{PDMS-g})^2 \cdot \varepsilon_{PDMS}^2 \cdot \rho_{a-PDMS}}{1-\varepsilon_{PDMS}^2 \cdot \rho_{a-PDMS} \cdot \rho_{PDMS-g}} \tag{7-12}$$

$$\varepsilon_{PDMS}(\theta) = \exp\left(-\frac{4\pi \cdot k_{PDMS} \cdot s_{PDMS}}{\cos\theta_{PDMS}}\right) \tag{7-13}$$

The transmittance of the PDMS layer can be calculated by:

$$T_{PDMS} = \frac{\left[1-\rho_{a-PDMS}\right] \cdot \left[1-\rho_{PDMS-g}\right] \cdot \varepsilon_{PDMS}}{1-\varepsilon_{PDMS}^2 \cdot \rho_{a-PDMS} \cdot \rho_{PDMS-g}} \tag{7-14}$$

For the PDMS-glazing unit:

The transmittance can be calculated by:

$$T_{PDMS,g} = \frac{T_{PDMS} \cdot \varepsilon_g \left(1-\rho_{g-f}\right)}{1-\varepsilon_g^2 \cdot R_{PDMS}^{'} \cdot \rho_{g-f}} \tag{7-15}$$

$$\varepsilon_g(\theta) = \exp\left(-\frac{4\pi \cdot k_g \cdot s_g}{\cos\theta_g}\right) \tag{7-16}$$

When radiation incident from the air-PDMS interface, the reflectance of the PDMS-glazing unit can be calculated by:

$$R_{PDMS,g} = \frac{T_{PDMS}^2 \cdot \varepsilon_g^2 \cdot \rho_{g-f}}{1-\varepsilon_g^2 \cdot R_{PDMS}^{'} \cdot \rho_{g-f}} + R_{PDMS} \tag{7-17}$$

When radiation incident from the glazing-fluid interface, the reflectance can be calculated by:

$$R'_{PDMS,g} = \rho_{g-f} + \frac{(1-\rho_{g-f})^2 \cdot \varepsilon_g^2 \cdot R'_{PDMS}}{1-\varepsilon_g^2 \cdot R'_{PDMS} \cdot \rho_{g-f}} \tag{7-18}$$

For the PDMS-glazing-fluid unit:

The transmittance can be calculated by:

$$T_{PDMS,g,f} = \frac{T_{PDMS,g} \cdot \varepsilon_f \cdot \left(1-\rho_{g-f}\right)}{1-\varepsilon_f^2 \cdot R'_{PDMS,g} \cdot \rho_{g-f}} \tag{7-19}$$

$$\varepsilon_f(\theta) = \exp\left(-\frac{4\pi \cdot k_f \cdot s_f}{\cos\theta_f}\right) \tag{7-20}$$

When radiation incident from the air-PDMS interface, the reflectance of the PDMS-glazing-fluid unit can be calculated by:

$$R_{PDMS,g,f} = R_{PDMS,g} + \frac{T_{PDMS,g}^2 \cdot \varepsilon_f^2 \cdot \rho_{g-f}}{1-\varepsilon_f^2 \cdot R'_{PDMS,g} \cdot \rho_{g-f}} \tag{7-21}$$

When radiation incident from the glazing-fluid interface, the reflectance can be calculated by:

$$R'_{PDMS,g} = \rho_{g-f} + \frac{(1-\rho_{g-f})^2 \cdot \varepsilon_g^2 \cdot R'_{PDMS,g}}{1-\varepsilon_f^2 \cdot R'_{PDMS,g} \cdot \rho_{g-f}} \tag{7-22}$$

For the JB window:

The transmittance can be calculated by:

$$T_{JB} = \frac{T_{PDMS,g,f}\varepsilon_{AgNW}\left(1-\rho_{AgNW}\right)}{1-\varepsilon_{AgNW}^2 R'_{PDMS,g,f}\rho_{AgNW}} \tag{7-23}$$

When radiation incident from the air-PDMS interface, the reflectance can be calculated by:

$$R_{JB} = R_{PDMS,g,f} + \frac{T_{PDMS,g,f}^{2} \cdot \varepsilon_{f}^{2} \cdot \rho_{AgNW}}{1 - \varepsilon_{AgNW}^{2} \cdot R_{PDMS,g,f}^{'} \cdot \rho_{AgNW}} \tag{7-24}$$

When radiation incident from the air-AgNW interface, the reflectance can be calculated by:

$$R_{JB}^{'} = \rho_{AgNW} + \frac{(1-\rho_{AgNW})^{2} \cdot \varepsilon_{g}^{2} \cdot R_{PDMS,g,f}^{'}}{1 - \varepsilon_{AgNW}^{2} \cdot R_{PDMS,g,f}^{'} \cdot \rho_{AgNW}} \tag{7-25}$$

(2) Heat transfer model

The thermal balance between the window, indoor environment and outdoor environment can be expressed by:

$$c_g \cdot m_g \cdot \frac{dT_{g1}}{dt} = A_{g1} \cdot \phi_{solar} - Q_{h,out} - Q_{rsc} - Q_{h,f1} \tag{7-26}$$

$$c_f \cdot m_f \cdot \frac{dT_f}{dt} = A_f \cdot \phi_{solar} - Q_{h,f1} - Q_{h,f2} \tag{7-27}$$

$$c_g \cdot m_g \cdot \frac{dT_{g2}}{dt} = A_{g2} \cdot \phi_{solar} - Q_{h,in} - Q_{r,in} - Q_{h,f2} \tag{7-28}$$

where c_g (J/kg·K) is the specific heat of the glazing;

c_f (J/kg·K) is the specific heat of the the fluids (SCBS or LP);

m_g (kg) is the mass of the glazing;

m_f (kg) is the mass of the fluid;

T_{g1} (°C) is the temperature of the glazing 1;

T_{g2} (°C) is the temperature of the glazing 2;

$Q_{h,out}$ (W) is the convective heat transfer to outdoor environment;

Q_{rsc} (W) is the radiative heat transfer from glazing to outdoor environment;

$Q_{c,g2}$ (W) is the conductive heat transfer from glazing to the clear glazing;

$Q_{r,g2}$ (W) is the radiative heat transfer from the glazing to the clear glazing.

The convective heat transfer can be calculated by:

$$Q_{h,out} = \frac{1}{\frac{1}{h_{out}} + \frac{\sigma_{g1}}{\lambda_{g1}}}(T_{g1} - T_{a,out}) \quad (7\text{-}29)$$

$$Q_{h,in} = \frac{1}{\frac{1}{h_{in}} + \frac{\sigma_{g2}}{2\lambda_{g2}}}(T_{g2} - T_{a,in}) \quad (7\text{-}30)$$

where σ_1 and σ_2 (m) are the thicknesses of the glazing;

λ_1 and λ_2 [W/(m·K] are the thermal conductivity the glazing;

h_{in} and h_{out} ($W \cdot m^{-2} \cdot K^{-1}$) are the convective heat transfer coefficients respectively, can be calculated by **[235, 236]**:

$$h_{in} = \begin{cases} 1.42\left|T_{g2} - T_{a,in}\right|^{1/4}, \ if\ 1.42\left|T_{g2} - T_{a,in}\right|^{1/4} > 1.31\left|T_{g2} - T_{a,in}\right|^{1/3} \\ 1.31\left|T_{g2} - T_{a,in}\right|^{1/3}, \ if\ 1.42\left|T_{g2} - T_{a,in}\right|^{1/4} < 1.31\left|T_{g2} - T_{a,in}\right|^{1/3} \end{cases} \quad (7\text{-}31)$$

$$h_{out} = 3.34 \begin{cases} 5.15v_a^{0.81}, \ if\ \omega = 0^{\circ} \\ 3.34v_a^{0.84}, \ if\ \omega = 45^{\circ} \\ 4.78v_a^{0.71}, \ if\ \omega = 90^{\circ} \\ 4.05v_a^{0.65}, \ if\ \omega = 135^{\circ} \\ 3.54v_a^{0.76}, \ if\ \omega = 180^{\circ} \end{cases} \quad (7\text{-}31)$$

The radiative heat transfer between glazing and indoor environment can be calculated by:

$$Q_{r,in} = \frac{1}{\frac{1}{\varepsilon_{g2}} + \frac{1}{\varepsilon_{in}} - 1} \cdot \delta \cdot (T_{g2}^4 - T_{a,in}^4) \quad (7\text{-}32)$$

where ε_{in} (dimensionless) is the emittance of indoor environment, being 1.0.

The net radiative sky cooling power of outdoor surface of the window can be calculated by:

$$Q_{rsc} = P_{rad,PDMS} - P_{rad,atm} \quad (7\text{-}33)$$

$$P_{rad,PDMS}(T) = 2\pi\int_0^{\pi/2} d\theta \cdot \sin\theta\cos\theta \int_0^{\infty} d\lambda \cdot \varepsilon_{PDMS}(\theta,\ \lambda) \cdot I_b(\lambda, T) \quad (7\text{-}34)$$

$$P_{rad,atm}(T) = (1-\psi) \cdot Q_{rad,clearsky}(T) + \psi \cdot Q_{rad,cloud}(T) \quad (7\text{-}35)$$

$$Q_{rad,clearsky}(T) = 2\pi\int_0^{\pi/2} d\theta \cdot \sin\theta\cos\theta\int_0^{\infty} d\lambda \cdot \varepsilon_{PDMS}(\theta,\ \lambda) \cdot \varepsilon_{atm}(\theta,\ \lambda) \cdot I_b(\lambda, T_a) \quad (7\text{-}36)$$

$$Q_{rad,cloud}(T) = \delta \cdot T_{cloud}^4 \quad (7\text{-}37)$$

$$T_{cloud} = \ln(\psi) \cdot \Delta T_{ref} + T_a \quad (7\text{-}38)$$

$$\varepsilon_{atm}(\theta, \lambda) = 1 - T_{atm}(0, \lambda) \quad (7\text{-}39)$$

$$I_b(\lambda) = \frac{2\pi hc^2}{\lambda^5\left[\exp\left(\frac{hc}{\lambda k_B T_{PDMS}}\right) - 1\right]} \quad (7\text{-}40)$$

where $\boldsymbol{T_{atm}}$ (dimensionless) represents the transmittance of atmospheric window;

$\boldsymbol{\psi}$ (dimensionless) represents cloud cover fraction;

$\boldsymbol{T_{ref}}$ (K) reference temperature difference of 10 K [237];

$\boldsymbol{I_b}$ is the blackbody emission, can be calculated by:

h (J/s) is the Planck constant, being 6.62607015 × 10^{-34} J/s.

The transmittance of atmospheric window ($\boldsymbol{T_{atm}}$) is determined by sky conditions, which can be dealt as a function of **PWV** [238-240] and altitude, as shown in **Figure 7.21**.

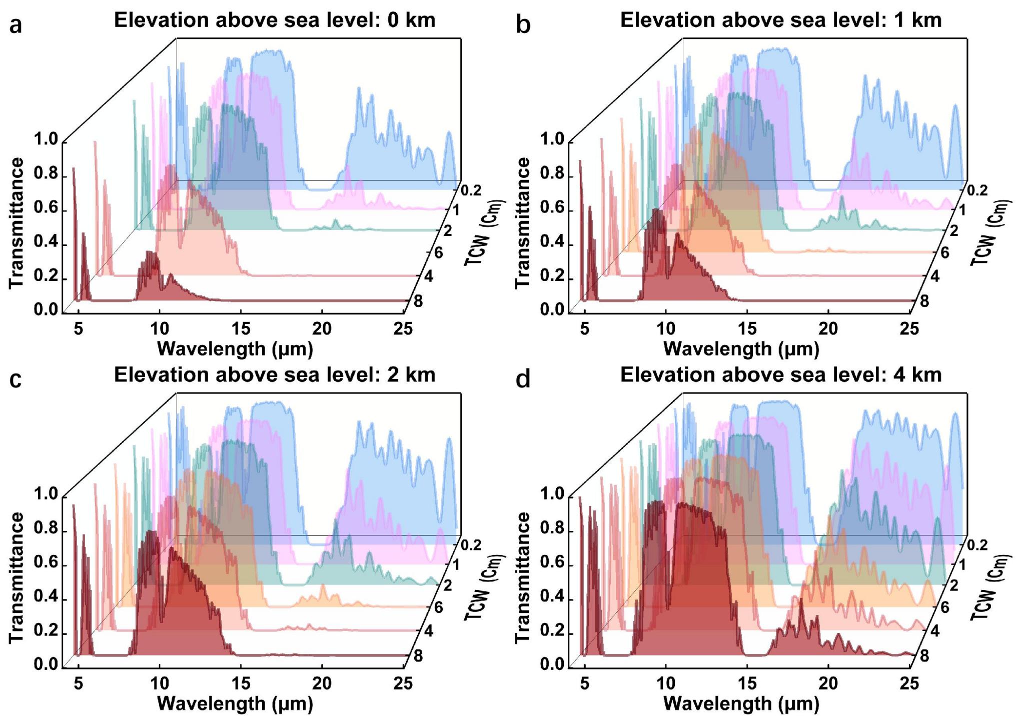

Figure 7.21 Atmospheric transmittance at different PWV and elevation: (a) 0 km, (b) 1 km (c) 2 km and (d) 4 km

The radiative sky cooling obtained from the window primarily dissipates through outdoor convective heat transfer, indoor radiative heat transfer, and indoor convective heat transfer. The indoor radiative cooling gain (**RCG**) can be evaluated by:

$$RCG(\theta) = \frac{h_{a,in} + h_{r,in}}{h_{a,out} + h_{a,in} + h_{r,in}} Q_{rsc} \tag{7-41}$$

(3) Solar heat gain

The solar heat gain is the sum up of direct solar heat gain and secondary solar heat gain, can be calculated by:

$$P_{SHG} = P_{SHG,direct} + P_{SHG,secondary} \tag{7-42}$$

$$P_{SHG,direct} = (1-\varsigma)\cdot T_{transparent}(\theta)\cdot \int_{300}^{2500} \Phi_{solar}(\lambda)\, d\lambda \tag{7-43}$$

$$P_{SHG,secondary} = h_{a,in}\cdot(T_g - T_g^{'}) + \frac{1}{\frac{1}{\varepsilon_g} + \frac{1}{\varepsilon_{in}} - 1}\cdot \delta \cdot (T_g^4 - T_g^{'4}) \tag{7-44}$$

where $\boldsymbol{T_g}$ (°C) is the glazing temperature;

$\boldsymbol{T_g'}$ (°C) is the glazing temperature calculated by considering the reflectance being 1 **[11, 59]**.

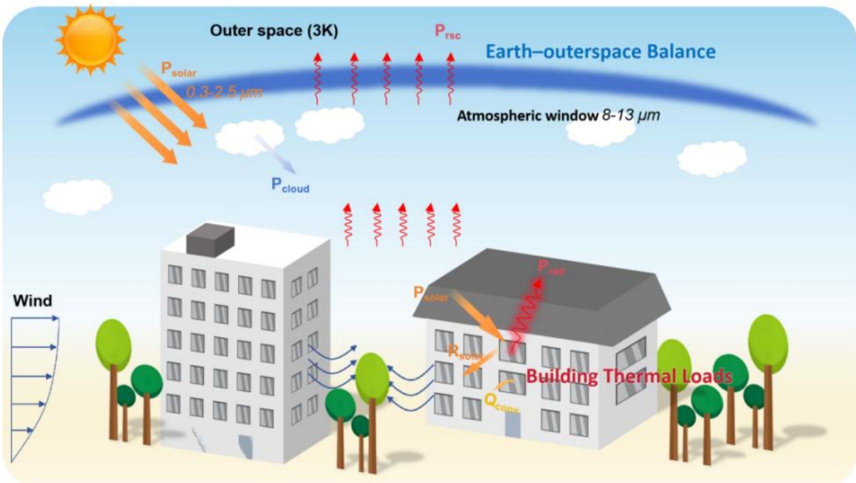

Figure 7.22 Schematic diagram of the developed model

(4) Model implementation

According to the developed model, the **MATLAB** code was generated to calculate the heat transfer behaviors of the JB window, utilizing the hourly meteorological data of 1929 sites in the world (CAMS global atmospheric composition forecasts) (**Figure 7.23**). The JB window used in the simulation incorporated a 0.1%SCC/10%$CuSO_4$ solution as the SSF, and a AgNW/PET film with a sheet resistance of 7.5 Ω serving as the low-e surface. In the simulation, the JB window operates based on the following dynamic switching logic:

1) The window enters the colored state when the outdoor air temperature exceeds 24 °C and the global horizontal irradiance (GHI) is greater than 200 W/m^2.

2) Under all other conditions, the window remains in the bleached state.

The meteorological data used in the calculation was linearly interpolated with a time step of 1 s.

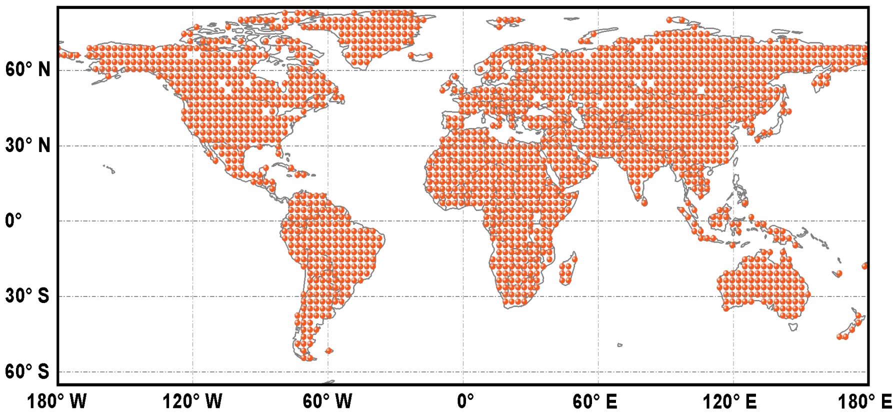

Figure 7.23 Geographical Distribution of Energy Simulation Sites

7.5.2 Simulation results

According to the ASHRAE standard **[241]**, climate zones are classified based on local outdoor temperature conditions using Cooling Degree Days at a base temperature of 10 °C (CDD10 °C). Globally, there are nine thermal climate zones: extremely hot zone (Zone 0), very hot zone (Zone 1), hot zone (Zone 2), warm zone (Climate Zone

3), mixed zone (Zone 4), cool zone (Zone 5), cold zone (Zone 6), very cold zone (Zone 7), subarctic/arctic zone (Zone 8). The geographical distribution of these climate zones is shown in Figure 6-21, and the outdoor meteorological parameters in different regions around the world are presented in **Figure 7.24**.

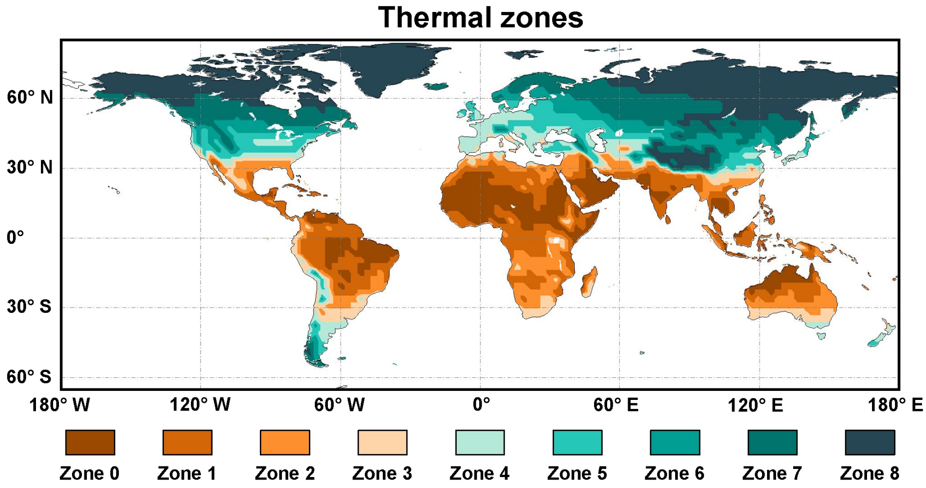

Figure 7.24 World climate zones map **[241]**

As shown in **Figure 7.25**, the simulated cumulative load reduction of the JB window, compared to conventional low-e glazing window, are presented. For the conventional low-e window, the low-e coating is applied on the interior side of the glazing. Across the majority of global regions, the Janus bimodal window demonstrates greater energy-saving potential than conventional low-e glazing windows, with particularly significant advantages in low-latitude regions. **Figure 7.26** illustrates the reduction in heating and cooling loads achieved by the Janus window relative to traditional low-e glazing across the nine global thermal climate zones. In thermal zones 0 to 7, the JB window outperforms conventional low-e glazing window, with the average annual reduction in heating and cooling load per square meter of glazing being 0.69 GJ, 0.52 GJ, 0.33 GJ, 0.13 GJ, 0.16 GJ, 0.15 GJ, 0.10 GJ, and 0.01 GJ, respectively. However, in thermal zone 8, the JB window performs worse in terms of energy savings, increasing the average annual building heating load by 0.07 GJ/m^2 compared to the traditional low-e window.

Overall, the energy-saving advantage of the JB bimodal window diminishes as climate zones become colder. In Greenland, the coldest region globally, the JB window increases the building heat load by more than 0.5 GJ/(m^2·year) compared to conventional low-e glazing, as shown in **Figure 7.25b**. The primary reason for this lies in the differences in heat exchange mechanisms between the window and indoor/outdoor air. Indoor air is typically stagnant, and heat transfer between the window and indoor air occurs mainly through natural convection and thermal radiation. Because the heat transfer coefficient for natural convection is relatively low, radiative heat transfer becomes dominant. In this context, placing the low-e coating on the interior side of the glazing significantly reduces radiative heat exchange, thereby lowering the window's U-value and reducing building heat loss. However, an exception is observed in the Qinghai–Tibet Plateau (see **Figure 7.25b**). Despite its classification as a severely cold region, the JB bimodal window reduces the building's heat load by approximately 0.5 GJ/(m^2·year) compared to conventional low-e glazing. This is due to low outdoor wind speeds high radiative cooling effects in Qinghai–Tibet Plateau.

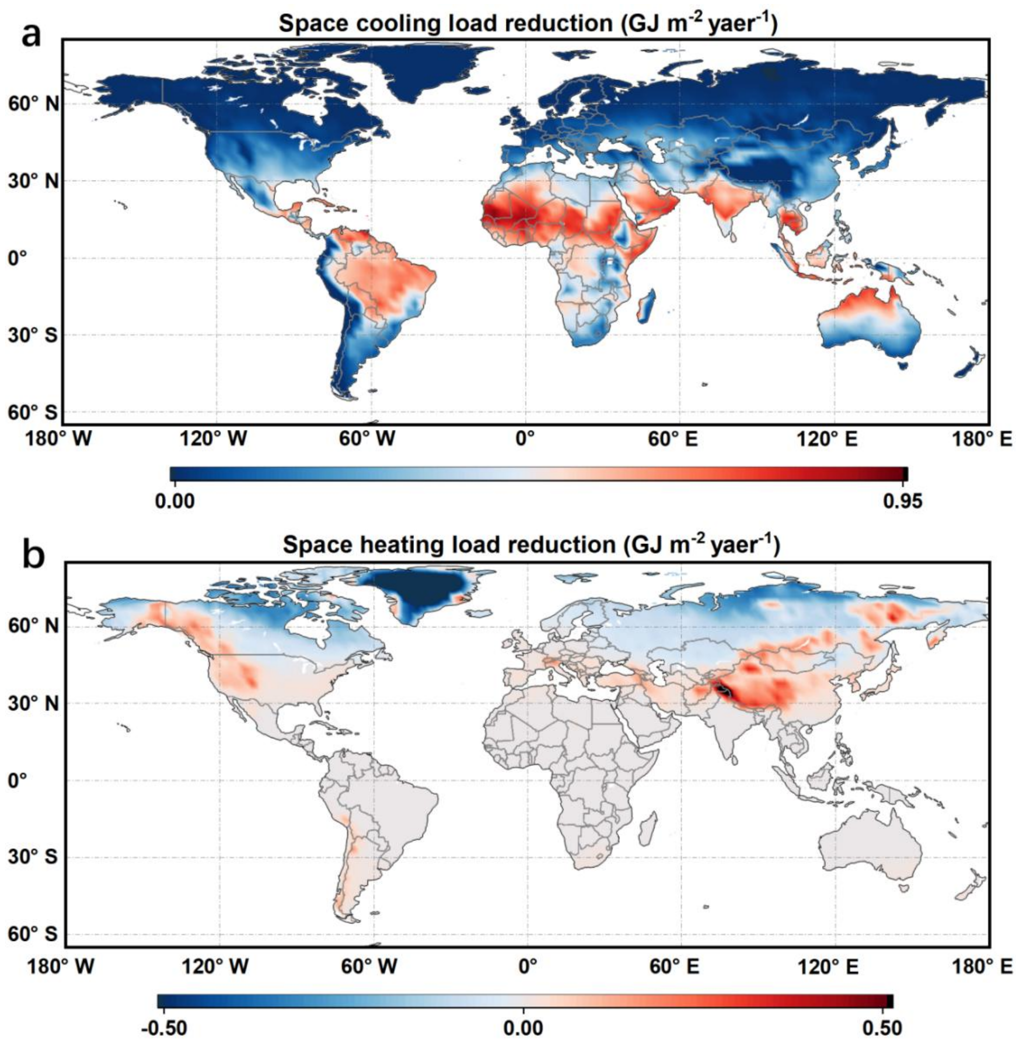

Figure 7.25 World map of the load reduction of Janus window compared to low-e glazing: (a) space cooling load reduction; (b) space heating load reduction.

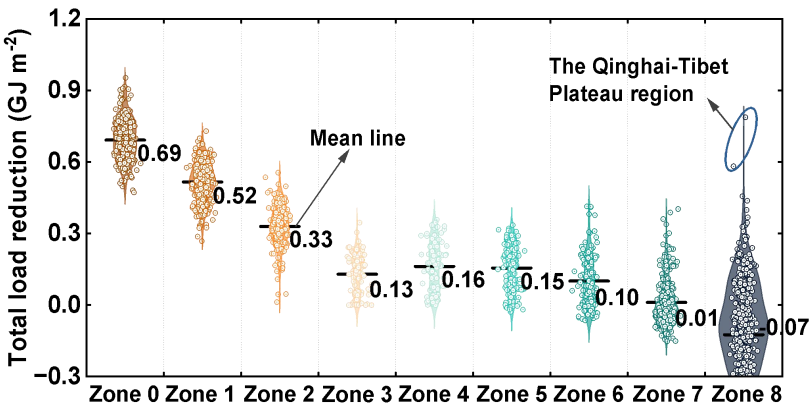

Figure 7.26 Load reduction of Janus window compared to low-e glazing in different climate zones

7.6 Summary

To mitigate the secondary radiative heat transfer into indoor spaces caused by solar absorption of spectrally selective windows, and to enhance the radiative sky cooling capability during summer, this chapter proposed and validated a VIS-NIR-MIR broadband tunable JB window. Firstly, a Janus structure based on AgNWs and PDMS was designed and fabricated, enabling asymmetric infrared emissivity regulation on the indoor and outdoor sides of the window. Material simulations and infrared characterization confirmed that PDMS possesses excellent high-emissivity properties, while AgNWs enable high reflectivity and low emissivity in the MIR range. By integrating the Janus structure with the RB window, the resulting JB window exhibits strong solar shading and radiative cooling capabilities in summer, and high visible transmittance and thermal insulation in winter, achieving dynamic broadband modulation across the solar and MIR spectra. This chapter explores the optical performance of the JB window in detail, demonstrating its significant performance advantages compared to the state-of-the-art smart window technologies. Outdoor field tests conducted in Hong Kong under hot and humid climate conditions showed that the Janus window can significantly reduce indoor temperatures, with a maximum cooling effect exceeding 10°C. Furthermore, energy consumption simulations across 1,929 global locations were performed to verify and quantify the energy-saving potential of the Janus dual-mode window across various climate zones worldwide. Results demonstrate that the JB window outperform traditional low-e window in in almost all regions with latitudes below 60°.

Chapter 8 Conclusions and recommendations for future work

Windows are widely recognized as the weakest component of the building envelope in terms of energy efficiency, accounting for significant building energy losses. Among various heat transfer modes, radiative heat transfer, including solar radiation heat gain and mid-infrared (MIR) thermal emission, contributes to over 50% of the total energy consumption associated with windows. Therefore, controlling radiative heat transfer is critical for improving the overall energy performance of buildings.

To address the dual challenge of regulating solar heat gain while preserving daylighting, spectrally selective glazing has emerged as a promising technological solution. Building upon the spectrally selective concept, the present study introduces an advanced spectral regulation strategy utilizing liquid-filled windows. These windows leverage the unique optical properties of specially designed fluids, to achieve dynamic and tunable control over the solar spectrum. Beyond solar spectral regulation, liquid-filled windows offer several inherent advantages, including sound insulation, thermal insulation, heat storage, and controllable fluid dynamics. Owing to these multifunctional characteristics, they have garnered increasing attention in the context of nearly zero-energy buildings in recent years.

In this thesis, the focus is on harnessing the spectral modulation capabilities of fluids. A range of liquid-filled windows have been designed and fabricated, including Static LFW, APPs window, RB window, and JB window. The research presented in this work is multidisciplinary in nature, integrating fluid material development, mechanical mechanism design, mathematical modeling, optical simulation, building energy simulation, and experimental validation. Through systematic investigation, the spectral regulation behaviors of these liquid-filled windows are characterized.

8.1 Conclusion

This thesis aims to provide a comprehensive understanding of how liquid-filled windows can be engineered to act as smart radiative regulators, contributing to year-round energy savings, thermal comfort, and environmental sustainability in buildings. The key conclusions of this research are summarized as follows:

(1) A novel biomass-derived spectrally selective material was developed, capable of precise light/heat decoupling across the solar spectrum. This material exhibits a high visible transmittance over 0.56, a low solar transmittance below 0.25 and a feasible CRI of 80. The FOM of the new material can reach up to 3.06, which surpasses all previously reported optical material. A novel biomass-derived spectrally selective material was developed, capable of precise light/heat decoupling across the solar spectrum. This material exhibits a high visible transmittance over 0.56, a low solar transmittance below 0.25 and a feasible CRI of 80. The FOM of the new material can reach up to 3.06, which surpasses all previously reported optical material. With excellent thermal stability and long-term performance, this novel biomass-derived spectrally selective material was holds promising for window application.

(2) Based on this biomass-derived spectrally selective material, a triple-layered LFW was designed. Its optical performance was characterized and validated under the climatic conditions of Hong Kong.

(3) A model that accounts for continuously changing solar angles and the dynamic solar spectral power distribution was developed to simulate the energy-saving performance of the LFW in Hong Kong, with a modeling error of no more than 5%. The simulation results show that the triple-layered LFW can ensure the monthly average photopic luminous transmittance to be higher than 40%, and the monthly average SHGC values be lower than 0.26 in all the 12 months of the typical year of Hong Kong. Annual simulations for a typical meteorological year in Hong Kong demonstrated that the LFW can reduce solar heat gain by 1717.8 MJ/m^2 per year, which can reduce electricity consumption by nearly 500 MJ/m^2 per year in Hong Kong, highlighting its strong energy-saving potential in subtropical climates.

(4) A passively thermo-responsive APPs window has been developed, featuring a tunable transition temperature ranging from 20 °C and 80 °C. The APPs window achieves solar modulation ability > 70%, with a visible transmittance of 84% at ambient temperature and >50% under high-temperature conditions.

(5) The APPs window shows superior energy-saving potential than traditional double layered low-e glazing windows. It can achieve an annual energy-saving of 43.5 MJ/m^2, 41.0 MJ/m^2 and 17.6 MJ/m^2 in Singapore, Hong Kong and Harbin, respectively.

(6) An actively switchable RB window was proposed, featuring a visible transmittance > 90% in the bleached state, >56% in the colored state, solar modulation ability > 60%, haze < 1%, and CRI > 80, outperforming most reported smart window technologies in both clarity and energy performance.

(7) Experimental results in Harbin during summer showed that the RB window can lower indoor floor temperatures by approximately 11 °C, and simulation results across hot and cold regions indicate that it can reduce building cooling/heating loads by 30% to 40%, demonstrating strong applicability across diverse climates.

(8) A JB window was developed by incorporating a Janus structure into the RB window. This Janus structure utilizes the emissivity contrast between AgNW/PET and PDMS, achieving an infrared emissivity difference of 0.7 between the colored state and the bleached state.

In summary, this study begins with material-level spectral management, and gradually builds a multi-scale, multifunctional intelligent window system, capable of broadband dynamic modulation of visible, near-infrared, and mid-infrared spectrum. Through a combination of optical–thermal modeling, laboratory experiments, field validation, and nationwide energy simulations, the study comprehensively demonstrates the climate-adaptive energy-saving potential of the proposed window technologies. The findings may provide theoretical insights and technological pathways for next-generation energy-efficient window systems, contributing toward the realization of carbon neutrality, and advancing the global agenda for sustainable building design.

8.2 Recommendations for future work

This thesis focuses on the application of spectrally selective absorbing technologies in transparent building envelopes. Based on the findings, the author proposes the following recommendations for future work:

(1) This study identifies interfacial reflection as a persistent challenge in achieving precise spectral regulation. Future research should explore advanced strategies to effectively control interfacial reflectance and enhance spectral selectivity. One promising approach involves the application of micro- and nano-scale surface structures to manipulate light–matter interactions at interfaces.

(2) The current work focuses on spectrally absorptive materials, which require a careful balance between visible transmission, NIR blocking, and color rendering. Future studies could consider incorporating photoluminescence materials to address these trade-offs. Photoluminescence materials offer the potential to decouple optical properties across different spectral regions, enabling more flexible and efficient spectral regulation.

(3) In building engineering, the principle of spectral regulation can be extended beyond transparent envelope systems to opaque and semi-transparent building components. This expansion could broaden the range of applications and contribute to more comprehensive energy-saving solutions in building design.

(4) Spectral regulation can be incorporated into vehicles. In vehicular environments, spectral regulation technologies should be further refined to address the specific requirements of confined cabin spaces, including optimized color rendering, and photo-biological effects that influence driver alertness and comfort. Future efforts should focus on developing targeted spectral control strategies tailored to the high melanopic sensitivity (around 490 nm) typical of driving conditions.

(5) Spectral regulation also offers promising opportunities for thermal management in photovoltaic (PV) systems. By selectively filtering out non-contributing wavelengths and enhancing transmission in power-generating spectral bands, spectral control materials can significantly improve the thermal and electrical performance of PV modules, contributing to higher efficiency and longer system lifespan.

References

[1] William N. R. Kent E. Pinkerton, *Climate Change and Global Public Health* (Respiratory Medicine). 2021.

[2] U. Nations, "Paris Agreement," 2015. [Online]. Available: http://unfccc.int/files/essential_background/convention/application/pdf/english_paris_agreement.pdf

[3] J. Wise, "COP28 decision to "transition away" from fossil fuels is hailed as milestone but loopholes are decried," ed: British Medical Journal Publishing Group, 2023.

[4] W. G. B. Council, "Bringing embodied carbon upfront," 2019. [Online]. Available: https://worldgbc.org/advancing-net-zero/embodied-carbon/

[5] J. Mayernik, O. o. E. Efficiency, and E. Renewable. *Buildings Energy Data Book*, National Renewable Energy Laboratory, 2015/06/11. [Online]. Available: https://data.openei.org/submissions/

[6] H. Son and T.-H. Song, "Heat transfer and stress distribution in the central part of vacuum glazing," *Applied Thermal Engineering,* vol. 159, p. 113926, 2019/08/01/ 2019, doi: https://doi.org/10.1016/j.applthermaleng.2019.113926.

[7] Y. Ma *et al.*, "Energy and daylighting performance of a building containing an innovative glazing window with solid-solid phase change material and silica aerogel integration," *Energy Conversion and Management,* vol. 271, p. 116341, 2022/11/01/ 2022, doi: https://doi.org/10.1016/j.enconman.2022.116341.

[8] F. Merli, E. Belloni, C. V. Fiorini, A. M. Anderson, M. K. Carroll, and C. Buratti, "End-of-life performance of hydrophilic and hydrophobic silica aerogel for window applications: Experimental characterization, lighting performance and electricity consumption simulations," *Construction and Building Materials,* vol. 479, p. 141378, 2025/06/13/ 2025, doi: https://doi.org/10.1016/j.conbuildmat.2025.141378.

[9] S. Chen, Y. Lyu, C. Li, X. Li, W. Yang, and T. Wang, "Liquid flow glazing contributes to energy-efficient buildings: A review," *Renewable and Sustainable Energy Reviews,* vol. 191, p. 114087, 2024/03/01/ 2024, doi: https://doi.org/10.1016/j.rser.2023.114087.

[10] Y. Lyu *et al.*, "Experimental study on thermal performance of finned tube water flow window," *Renewable Energy,* vol. 219, p. 119515, 2023/12/01/ 2023, doi: https://doi.org/10.1016/j.renene.2023.119515.

[11] J. Pu, C. Shen, and L. Lu, "Investigating the annual energy-saving and energy-output behaviors of a novel liquid-flow window with spectral regulation of ATO nanofluids," *Energy,* vol. 283, p. 129111, 2023/11/15/ 2023, doi: https://doi.org/10.1016/j.energy.2023.129111.

[12] B. P. Jelle, S. E. Kalnæs, and T. Gao, "Low-emissivity materials for building applications: A state-of-the-art review and future research perspectives," *Energy and Buildings,* vol. 96, pp. 329-356, 2015.

[13] J. Pu, C. Shen, J. Wang, Y. Zhang, C. Zhang, and S. A. Kalogirou, "Near-infrared absorbing glazing for energy-efficient windows: A critical review and performance assessments from the building requirements," *Nano Energy,* vol. 110, p. 108334, 2023.

[14] Q. Duan, L. Hinkle, J. Wang, E. Zhang, and A. Memari, "Condensation effects on energy performance of building window systems," *Energy Rep,* vol. 7, pp. 7345-7357, 2021.

[15] Y. Cui *et al.*, "Thermochromic VO2 for Energy-Efficient Smart Windows," *Joule,* vol. 2, no. 9, pp. 1707-1746, 2018/09/19/ 2018, doi: https://doi.org/10.1016/j.joule.2018.06.018.

[16] J. M. Li *et al.*, "Two-dimensional materials for electrochromic applications," (in English), *Energychem,* vol. 3, no. 5, p. 100060, Sep 2021, doi: ARTN 100060
10.1016/j.enchem.2021.100060.

[17] S. W. Zhao *et al.*, "Dynamic full-color tunability of high-performance smart windows utilizing absorption-emission effect," (in English), *Nano Energy,* vol. 89, p. 106297, Nov 2021, doi: ARTN 106297
10.1016/j.nanoen.2021.106297.

[18] J. Q. Wang *et al.*, "A fully self-powered, ultra-stable cholesteric smart window triggered by instantaneous mechanical stimuli," (in English), *Nano Energy,* vol. 85, p. 105976, Jul 2021, doi: ARTN 105976
10.1016/j.nanoen.2021.105976.

[19] M. Salamati, P. Mathur, G. Kamyabjou, and K. Taghizade, "Daylight performance analysis of TiO2@ W-VO2 thermochromic smart glazing in office buildings," *Building and Environment,* vol. 186, p. 107351, 2020.

[20] Y. Zhou *et al.*, "Liquid thermo-responsive smart window derived from hydrogel," *Joule,* vol. 4, no. 11, pp. 2458-2474, 2020.

[21] D. S. Kim *et al.*, "A stretchable patch of multi-color electrochromic devices for driving integrated sensors and displaying bio-signals," *Nano Energy,* vol. 113, p. 108607, 2023.

[22] G. Bräuer, "Large area glass coating," *Surface and Coatings Technology,* vol. 112, no. 1-3, pp. 358-365, 1999.

[23] L. Yunos, M. L. Jane, P. J. Murphy, and K. Zuber, "Frequency selective surface on low emissivity windows as a means of improving telecommunication signal transmission: A review," *Journal of Building Engineering,* vol. 70, p. 106416, 2023/07/01/ 2023, doi: https://doi.org/10.1016/j.jobe.2023.106416.

[24] Q. Chen *et al.*, "Rapid annealing obtained ITO films with both extremely low infrared emissivity and high visible light transmission for energy-efficient window applications," *Ceramics International,* 2024/11/20/ 2024, doi: https://doi.org/10.1016/j.ceramint.2024.11.291.

[25] W. N. S. Wan Shamsuddin, A. Roccisano, K. Zuber, P. J. Murphy, and M. Llusca Jane, "Environmentally robust Ag–Cu based low-e coatings," *Solar*

Energy Materials and Solar Cells, vol. 248, p. 112033, 2022/12/01/ 2022, doi: https://doi.org/10.1016/j.solmat.2022.112033.

[26] V. Gupta and C. Deb, "Envelope design for low-energy buildings in the tropics: A review," *Renewable and Sustainable Energy Reviews,* vol. 186, p. 113650, 2023.

[27] G. Bräuer, "Large area glass coating," *Surface and Coatings Technology,* vol. 112, no. 1, pp. 358-365, 1999/02/01/ 1999, doi: https://doi.org/10.1016/S0257-8972(98)00737-3.

[28] J. Kim, S. Baek, J. Y. Park, K. H. Kim, and J.-L. Lee, "Photonic Multilayer Structure Induced High Near-Infrared (NIR) Blockage as Energy-Saving Window," *Small,* vol. 17, no. 29, p. 2100654, 2021/07/01 2021, doi: https://doi.org/10.1002/smll.202100654.

[29] J. J. Wang and D. Shi, "Spectral selective and photothermal nano structured thin films for energy efficient windows," *Applied Energy,* vol. 208, pp. 83-96, 2017.

[30] J. Wang, S. Liu, X. Meng, W. Gao, and J. Yuan, "Application of retro-reflective materials in urban buildings: a comprehensive review," *Energy and Buildings,* vol. 247, p. 111137, 2021.

[31] T. Nagahama, T. Sato, T. Harima, and J. Shimizu, "Optical properties and field test results of spectrally-selective solar control window film that enables not increasing downward reflection," *Energy and Buildings,* vol. 157, pp. 176-183, 2017.

[32] R. Danks, J. Good, and R. Sinclair, "Assessing reflected sunlight from building facades: A literature review and proposed criteria," *Building and Environment,* vol. 103, pp. 193-202, 2016.

[33] M. Vilarigues and R. Da Silva, "The effect of Mn, Fe and Cu ions on potash-glass corrosion," *Journal of Non-Crystalline Solids,* vol. 355, no. 31-33, pp. 1630-1637, 2009.

[34] N. Wang and J. Wang, "A spectrally-resolved method for evaluating the solar effect on user thermal comfort in the near-window zone," *Building and Environment,* vol. 202, p. 108044, 2021.

[35] G. V. Kaliyannan, S. V. Palanisamy, E. Priyanka, S. Thangavel, S. Sivaraj, and R. Rathanasamy, "Investigation on sol-gel based coatings application in energy sector–A review," *Materials Today: Proceedings,* vol. 45, pp. 1138-1143, 2021.

[36] E. Zhang, Q. Duan, J. Wang, Y. Zhao, and Y. Feng, "Experimental and numerical analysis of the energy performance of building windows with solar NIR-driven plasmonic photothermal effects," *Energy Conversion and Management,* vol. 245, p. 114594, 2021.

[37] N. Luamsri, J. Wootthikanokkhan, E. Wimolmala, P. Rakkwamsuk, and W. Sangkhun, "Spectral selectivity and stability of energy-saving window films based on poly (vinyl chloride) reinforced with ATO nanoparticles," *Polymer Testing,* vol. 80, p. 106157, 2019.

[38] M. A. Jahid, J. Wang, E. Zhang, Q. Duan, and Y. Feng, "Energy savings potential of reversible photothermal windows with near infrared-selective plasmonic nanofilms," *Energy Conversion and Management,* vol. 263, p. 115705, 2022.

[39] T. Bates and R. Douglas, "Absorption bands of Cr3+ ions in solutions, crystals, and glasses," *J. Soc. Glass Technol,* vol. 43, pp. 289-307, 1959.

[40] S. Kumar, "Optical Absorption of Glasses Containing Ions with Partially Filled 3d Orbitals," *Part I, II, and III, Central Glass and Ceramics Res. Inst. Bull.(India),* vol. 6, no. 3, pp. 99-120, 1959.

[41] D. R. Smith and R. F. Cooper, "Dynamic oxidation of a Fe2+-bearing calcium–magnesium–aluminosilicate glass: the effect of molecular structure on chemical diffusion and reaction morphology," *Journal of non-crystalline solids,* vol. 278, no. 1-3, pp. 145-163, 2000.

[42] E. Meechoowas, S. Poosrisoma, P. Jampeerung, and T. Jitwatcharakomol, "The effect of heat treatment on Fe2+/Fe3+ ratio in Soda-lime silicate glass," *Key Engineering Materials,* vol. 659, pp. 194-198, 2015.

[43] G. Tranell, O. Ostrovski, and S. Jahanshahi, "The equilibrium partitioning of titanium between Ti 3+ and Ti 4+ valency states in CaO-SiO 2-TiO x slags," *Metallurgical and Materials Transactions B,* vol. 33, pp. 61-67, 2002.

[44] P. E. Gray and L. C. Klein, "High temperature visible spectroscopy of Co2+ ions in sodium phosphate glasses," *Journal of non-crystalline solids,* vol. 79, no. 1-2, pp. 75-82, 1986.

[45] C. A. Bates, "Jahn-Teller effects in paramagnetic crystals," *Physics reports,* vol. 35, no. 3, pp. 187-304, 1978.

[46] W. Johnston, "Optical spectra of the various valence states of vanadium in Na2 O. 2SiO2 glass," *Journal of the American Ceramic Society,* vol. 48, no. 12, pp. 608-611, 1965.

[47] A. Paul, "Optical and esr spectra of titanium (III) in Na 2 OB 2 O 3 and Na 2 OP 2 O 5 glasses," *Journal of Materials Science,* vol. 10, pp. 692-696, 1975.

[48] L. H. d. C. ANDRADE *et al.*, "Y. Guyot; BOULON, G.. Long fluorescence lifetime of Ti3+-Doped low Silica Calcium Aluminosilicate Glass," *Physical Review Letters,* vol. 8, p. 027402.

[49] A. Malyarevich *et al.*, "Absorption, emission and absorption saturation of Cr4+ ions in calcium aluminate glass," *Journal of non-crystalline solids,* vol. 351, no. 43-45, pp. 3551-3555, 2005.

[50] S. Singh and A. Kumar, "Molar extinction coefficients of the cupric ion in silicate glasses," *Journal of materials science,* vol. 30, pp. 2999-3004, 1995.

[51] R. L. Stewart, "Thin sheet mirror and Nd2O3 doped glass," ed: Google Patents, 2005.

[52] G. A. Pecoraro and L. J. Shelestak, "Transparent infrared absorbing glass and method of making," ed: Google Patents, 2001.

[53] B. V. J. Rao, "Heat absorbing blue soda-lime-silica glass," ed: Google Patents, 1972.

[54] L. Fu *et al.*, "Spectroscopic and laser-induced damage properties of Fe 2+-doped fluorophosphate glass, a new color-separation material," *Applied Physics B,* vol. 113, pp. 81-86, 2013.
[55] A. Lipovskii, V. Melekhin, V. Petrikov, and B. Tatarintsev, "Influence of reduction-oxidation synthesis conditions on the nature of color centers in silicate glass doped with selenium," *Glass Physics and Chemistry,* vol. 34, pp. 155-159, 2008.
[56] B. Edwin, "Heat absorbing glass," ed: Google Patents, 1934.
[57] Y. V. Volk *et al.*, "Stimulated emission of Co2+-doped glass–ceramics," *Journal of non-crystalline solids,* vol. 353, no. 24-25, pp. 2408-2414, 2007.
[58] A. Lin, B. H. Kim, D. S. Moon, Y. Chung, and W.-T. Han, "Cu2+-doped germano-silicate glass fiber with high resonant nonlinearity," *Optics Express,* vol. 15, no. 7, pp. 3665-3672, 2007.
[59] J. Pu, M. Han, L. Lu, C. Shen, and F. Wang, "Spectrally selective design and energy-saving demonstration of a novel liquid-filled window in hot and humid region," *Energy,* vol. 297, p. 131090, 2024.
[60] G. A. Pecoraro and L. J. Shelestak, "Transparent infrared absorbing glass and method of making," ed: Google Patents, 1988.
[61] O. Zandi *et al.*, "Impacts of surface depletion on the plasmonic properties of doped semiconductor nanocrystals," *Nature Materials,* vol. 17, no. 8, pp. 710-717, 2018.
[62] A. Agrawal, S. H. Cho, O. Zandi, S. Ghosh, R. W. Johns, and D. J. Milliron, "Localized surface plasmon resonance in semiconductor nanocrystals," *Chemical reviews,* vol. 118, no. 6, pp. 3121-3207, 2018.
[63] L. Wang *et al.*, "Plasmonics and enhanced magneto-optics in core− shell Co−Ag nanoparticles," *Nano letters,* vol. 11, no. 3, pp. 1237-1240, 2011.
[64] Y. Zhang *et al.*, "Surface-plasmon-driven hot electron photochemistry," *Chemical reviews,* vol. 118, no. 6, pp. 2927-2954, 2017.
[65] M. L. Brongersma, N. J. Halas, and P. Nordlander, "Plasmon-induced hot carrier science and technology," *Nature nanotechnology,* vol. 10, no. 1, pp. 25-34, 2015.
[66] B. Yang, C. Li, Z. Wang, and Q. Dai, "Thermoplasmonics in solar energy conversion: materials, nanostructured designs, and applications," *Advanced Materials,* vol. 34, no. 26, p. 2107351, 2022.
[67] S. V. Boriskina *et al.*, "Losses in plasmonics: from mitigating energy dissipation to embracing loss-enabled functionalities," *Advances in Optics and Photonics,* vol. 9, no. 4, pp. 775-827, 2017.
[68] R. H. Doremus, "Optical properties of small gold particles," *The Journal of Chemical Physics,* vol. 40, no. 8, pp. 2389-2396, 1964.
[69] R. Doremus, "Optical properties of small silver particles," *The Journal of Chemical Physics,* vol. 42, no. 1, pp. 414-417, 1965.
[70] C. Zhang, C. Shen, Q. Yang, S. Wei, and C. Sun, "Blended Ag nanofluids with optimized optical properties to regulate the performance of PV/T systems," *Solar Energy,* vol. 208, pp. 623-636, 2020.

[71] K.-S. Lee and M. A. El-Sayed, "Dependence of the enhanced optical scattering efficiency relative to that of absorption for gold metal nanorods on aspect ratio, size, end-cap shape, and medium refractive index," *The Journal of Physical Chemistry B,* vol. 109, no. 43, pp. 20331-20338, 2005.

[72] N. Félidj *et al.*, "Multipolar surface plasmon peaks on gold nanotriangles," *The Journal of chemical physics,* vol. 128, no. 9, 2008.

[73] T. Akai, K. Kadono, H. Yamanaka, T. Sakaguchi, M. Miya, and H. Wakabayashi, "Preparation of Copper-Ruby Glasses by Sputtering and Their Optical Properties," *Journal of the Ceramic Society of Japan,* vol. 101, no. 1169, pp. 105-107, 1993, doi: 10.2109/jcersj.101.105.

[74] D. Latha, S. Sampurnam, C. Arulvasu, P. Prabu, K. Govindaraju, and V. Narayanan, "Biosynthesis and characterization of gold nanoparticle from Justicia adhatoda and its catalytic activity," *Materials Today: Proceedings,* vol. 5, no. 2, pp. 8968-8972, 2018.

[75] A. Klinkova *et al.*, "Structural and optical properties of self-assembled chains of plasmonic nanocubes," *Nano letters,* vol. 14, no. 11, pp. 6314-6321, 2014.

[76] A. Lee *et al.*, "Probing dynamic generation of hot-spots in self-assembled chains of gold nanorods by surface-enhanced Raman scattering," *Journal of the American Chemical Society,* vol. 133, no. 19, pp. 7563-7570, 2011.

[77] L. O. Herrmann *et al.*, "Threading plasmonic nanoparticle strings with light," *Nature Communications,* vol. 5, no. 1, p. 4568, 2014.

[78] M. Guo, L. Gao, Y. Wei, Y. Ma, Y. Jianyong, and B. Ding, "Solar transparent radiators based on in-plane worm-like assemblies of metal nanoparticles," *Solar Energy Materials and Solar Cells,* vol. 219, p. 110796, 2021.

[79] J. Pu, C. Shen, S. Yang, C. Zhang, D. Chwieduk, and S. A. Kalogirou, "Feasibility investigation on using silver nanorods in energy saving windows for light/heat decoupling," *Energy,* vol. 245, p. 123289, 2022.

[80] C. Shen, Q. Yang, C. Zhang, S. Ma, and Y. Dong, "Optimized optical properties of Au nanorods with flow regulation to enhance the performance of direct absorption solar collectors," *Solar Energy,* vol. 218, pp. 611-620, 2021.

[81] P. N. Njoki *et al.*, "Size correlation of optical and spectroscopic properties for gold nanoparticles," *The Journal of Physical Chemistry C,* vol. 111, no. 40, pp. 14664-14669, 2007.

[82] Y.-p. Zhu, X.-k. Wang, W.-l. Guo, J.-g. Wang, and C. Wang, "Sonochemical synthesis of silver nanorods by reduction of sliver nitrate in aqueous solution," *Ultrasonics sonochemistry,* vol. 17, no. 4, pp. 675-679, 2010.

[83] H. H. Khaligh, K. Liew, Y. Han, N. M. Abukhdeir, and I. A. Goldthorpe, "Silver nanowire transparent electrodes for liquid crystal-based smart windows," *Solar Energy Materials and Solar Cells,* vol. 132, pp. 337-341, 2015.

[84] J. Liang, K. Tong, and Q. Pei, "A water-based silver-nanowire screen-print ink for the fabrication of stretchable conductors and wearable thin-film transistors," *Advanced Materials,* vol. 28, no. 28, 2016.

[85] W. Liu, C. Lu, X. Wang, R. Y. Tay, and B. K. Tay, "High-performance microsupercapacitors based on two-dimensional graphene/manganese dioxide/silver nanowire ternary hybrid film," *ACS nano,* vol. 9, no. 2, pp. 1528-1542, 2015.

[86] M. Bobinger, D. Angeli, S. Colasanti, P. La Torraca, L. Larcher, and P. Lugli, "Infrared, transient thermal, and electrical properties of silver nanowire thin films for transparent heaters and energy-efficient coatings," *physica status solidi (a),* vol. 214, no. 1, p. 1600466, 2017.

[87] S. Lin *et al.*, "Direct spray-coating of highly robust and transparent Ag nanowires for energy saving windows," *Nano Energy,* vol. 62, pp. 111-116, 2019.

[88] S. Stookey and R. Araujo, "Selective polarization of light due to absorption by small elongated silver particles in glass," *Appl. Opt.,* vol. 7, no. 5, pp. 777-779, 1968.

[89] K. Baba, J.-i. Katsu, and M. Miyagi, "Optical anisotropy of stretched gold island films: experimental results," *Optics letters,* vol. 17, no. 8, pp. 622-624, 1992.

[90] T. Seward III, "Coloration and optical anisotropy in silver-containing glasses," *Journal of Non-Crystalline Solids,* vol. 40, no. 1-3, pp. 499-513, 1980.

[91] C.-L. Li, C.-C. Cheng, S.-W. Kuo, C.-F. Huang, and J.-K. Chen, "Manipulation of ferrofluids encapsulated in sandwich structures using alternating magnetic field for high contrast in transmittance," *Microfluidics and Nanofluidics,* vol. 19, pp. 1441-1453, 2015.

[92] J. Li *et al.*, "Transmittance tunable smart window based on magnetically responsive 1D nanochains," *ACS Applied Materials & Interfaces,* vol. 12, no. 28, pp. 31637-31644, 2020.

[93] R. M. Pasquarelli, D. S. Ginley, and R. O'Hayre, "Solution processing of transparent conductors: from flask to film," *Chemical Society Reviews,* vol. 40, no. 11, pp. 5406-5441, 2011.

[94] A. Rahal, A. Benhaoua, C. Bouzidi, B. Benhaoua, and B. Gasmi, "Effect of antimony doping on the structural, optical and electrical properties of SnO2 thin films prepared by spray ultrasonic," *Superlattices and Microstructures,* vol. 76, pp. 105-114, 2014.

[95] J. Leem and J. Yu, "Physical properties of electrically conductive Sb-doped SnO2 transparent electrodes by thermal annealing dependent structural changes for photovoltaic applications," *Materials Science and Engineering: B,* vol. 176, no. 15, pp. 1207-1212, 2011.

[96] B. Shen, Y. Wang, L. Lu, and H. Yang, "Synthesis and characterization of Sb-doped SnO2 with high near-infrared shielding property for energy-efficient windows by a facile dual-titration co-precipitation method," *Ceramics International,* vol. 46, no. 11, pp. 18518-18525, 2020.

[97] J. Mazloom, F. Ghodsi, and M. Gholami, "Fiber-like stripe ATO (SnO2: Sb) nanostructured thin films grown by sol–gel method: optical, topographical and

electrical properties," *Journal of alloys and compounds,* vol. 579, pp. 384-393, 2013.

[98] M. F. Hossain, M. A. H. Shah, M. A. Islam, and M. S. Hossain, "Transparent conducting SnO2 thin films synthesized by nebulized spray pyrolysis technique: Impact of Sb doping on the different physical properties," *Materials Science in Semiconductor Processing,* vol. 121, p. 105346, 2021.

[99] S. Gürakar, T. Serin, and N. Serin, "Studies on optical properties of antimony doped SnO2 films," *Applied Surface Science,* vol. 352, pp. 16-22, 2015.

[100] X. Liu, C. Shen, and J. Wang, "Investigation on the lighting/heating performance of tubular daylighting devices (TDDs) based on nanofluids," *Energy and Buildings,* vol. 263, p. 112028, 2022.

[101] M. Gu, Q. Guo, and S. Lu, "Feasibility analysis of energy-saving potential of the underground ice rink using spectrum splitting sunshade technology," *Renewable Energy,* vol. 191, pp. 571-579, 2022.

[102] M. Kadi, A. Smaali, and R. Outemzabet, "Analysis of optical and related properties of tin oxide thin films determined by Drude-Lorentz model," *Surface and Coatings Technology,* vol. 211, pp. 45-49, 2012.

[103] J. Qu *et al.*, "Transparent thermal insulation coatings for energy efficient glass windows and curtain walls," *Energy and Buildings,* vol. 77, pp. 1-10, 2014.

[104] X. Xingyu and L. Lin, "Antimony doped tin oxide/multi-walled carbon nanotubes: highly near-infrared blocking coating used for heat conservation windows," *Energy Procedia,* vol. 105, pp. 4836-4841, 2017.

[105] B. Shen, Y. Wang, L. Lu, and H. Yang, "pH-dependent doping level and optical performance of antimony-doped tin oxide nanocrystals as nanofillers of spectrally selective coating for energy-efficient windows," *Ceramics International,* vol. 47, no. 14, pp. 20335-20340, 2021.

[106] R. Parra, D. Leinen, J. R. Ramos-Barrado, and F. Martin, "Spray-grown highly oriented antimony-doped tin dioxide transparent conducting films," *Journal of the European Ceramic Society,* vol. 40, no. 4, pp. 1361-1367, 2020.

[107] B. Shen, Y. Wang, L. Lu, and H. Yang, "Spraying fabrication of spectrally selective coating with improved near-infrared shielding performance for energy-efficient glazing," *Ceramics International,* vol. 47, no. 13, pp. 18991-18997, 2021.

[108] W. Zhang, L. Lu, and X. Xu, "Thermal and daylighting performance of glass window using a newly developed transparent heat insulated coating," *Energy Procedia,* vol. 158, pp. 1080-1085, 2019.

[109] S.-C. Kim, J.-H. Yoon, and H.-M. Lee, "Comparative experimental study on heating and cooling energy performance of spectrally selective glazing," *Solar Energy,* vol. 145, pp. 78-89, 2017.

[110] Z. Li, M. Sun, B. Dong, and J. Liu, "High infrared insulation and high visible light transmittance Sb/Yb co-doped SnO2 film prepared with sol–gel method," *Chemical Physics Letters,* vol. 787, p. 139238, 2022.

[111] Y. Yuan *et al.*, "Experimental investigation of full solar spectrum utilization based on nanofluid spectral splitter for greenhouse applications," *Energy Conversion and Management,* vol. 254, p. 115215, 2022.
[112] H. Zhang *et al.*, "Controlling the growth of hexagonal CsxWO3 nanorods by Li+-doping to further improve its near infrared shielding performance," *Solar Energy Materials and Solar Cells,* vol. 238, p. 111612, 2022.
[113] B. Shen, Y. Wang, L. Lu, and H. Yang, "Enhancing the spectral tunability of localized surface plasmon resonance and small polaron transfer in Li-doped CsxWO3 nanocrystals for energy-efficient windows," *Solar Energy,* vol. 231, pp. 228-235, 2022.
[114] G. Li, C. Guo, M. Yan, and S. Liu, "CsxWO3 nanorods: realization of full-spectrum-responsive photocatalytic activities from UV, visible to near-infrared region," *Applied Catalysis B: Environmental,* vol. 183, pp. 142-148, 2016.
[115] B. Shen, Y. Wang, L. Lu, and H. Yang, "Enhanced spectral modulation of CsxWO3 nanocrystals through anionic doping for energy-efficient glazing," *Solar Energy Materials and Solar Cells,* vol. 236, p. 111519, 2022.
[116] G. Yang *et al.*, "Alkali metal tungsten bronze-doped energy-saving glasses for near-infrared shielding applications," *Ceramics International,* vol. 47, no. 22, pp. 31122-31129, 2021.
[117] G. Yang *et al.*, "Sodium tungsten bronze (NaxWO3)-doped near-infrared-shielding bulk glasses for energy-saving applications," *Journal of Materials Science & Technology,* vol. 89, pp. 150-157, 2021.
[118] C. Guo, S. Yin, Q. Dong, and T. Sato, "Simple route to (NH 4) x WO 3 nanorods for near infrared absorption," *Nanoscale,* vol. 4, no. 11, pp. 3394-3398, 2012.
[119] Y. Yao, L. Zhang, Z. Chen, C. Cao, Y. Gao, and H. Luo, "Synthesis of CsxWO3 nanoparticles and their NIR shielding properties," *Ceramics International,* vol. 44, no. 12, pp. 13469-13475, 2018.
[120] J. Liu *et al.*, "One pot synthesis of Pt-doped CsxWO3 with improved near infrared shielding for energy-saving film applications," *Solar Energy,* vol. 178, pp. 17-24, 2019.
[121] K. Lin *et al.*, "Facile phase transfer of hydrophobic Fe 3 O 4@ Cu 2− x S nanoparticles by red blood cell membrane for MRI and phototherapy in the second near-infrared window," *Journal of Materials Chemistry B,* vol. 8, no. 6, pp. 1202-1211, 2020.
[122] Q. Tian *et al.*, "Sub-10 nm Fe3O4@ Cu2–x S core–shell nanoparticles for dual-modal imaging and photothermal therapy," *Journal of the American Chemical Society,* vol. 135, no. 23, pp. 8571-8577, 2013.
[123] M. Lyu, J. Lin, and D. Shi, "Solar desalination via multilayers of transparent photothermal Fe3O4@ Cu2–xS thin films," *Energy Technology,* vol. 9, no. 11, p. 2100590, 2021.

[124] L. Shi, Y. He, Y. Huang, and B. Jiang, "Recyclable Fe3O4@ CNT nanoparticles for high-efficiency solar vapor generation," *Energy Conversion and Management,* vol. 149, pp. 401-408, 2017.

[125] Y. Chen *et al.*, "Core-shell structured CsxWO3@ ZnO with excellent stability and high performance on near-infrared shielding," *Ceramics International,* vol. 44, no. 3, pp. 2738-2744, 2018.

[126] K. Adachi, Y. Ota, H. Tanaka, M. Okada, N. Oshimura, and A. Tofuku, "Chromatic instabilities in cesium-doped tungsten bronze nanoparticles," *Journal of Applied Physics,* vol. 114, no. 19, 2013.

[127] Y. Yao *et al.*, "Cs0. 32WO3/PMMA nanocomposite via in-situ polymerization for energy saving windows," *Solar Energy Materials and Solar Cells,* vol. 215, p. 110656, 2020.

[128] S. Zhao *et al.*, "Dynamic full-color tunability of high-performance smart windows utilizing absorption-emission effect," *Nano Energy,* vol. 89, p. 106297, 2021.

[129] E. Castellón, M. Zayat, and D. Levy, "Novel Reversible Humidity-Responsive Light Transmission Hybrid Thin-Film Material Based on a Dispersive Porous Structure with Embedded Hygroscopic and Deliquescent Substances," *Advanced Functional Materials,* vol. 28, no. 27, p. 1704717, 2018.

[130] Y. Ke *et al.*, "Adaptive thermochromic windows from active plasmonic elastomers," *Joule,* vol. 3, no. 3, pp. 858-871, 2019.

[131] Y. Ke, X. Wen, D. Zhao, R. Che, Q. Xiong, and Y. Long, "Controllable fabrication of two-dimensional patterned VO2 nanoparticle, nanodome, and nanonet arrays with tunable temperature-dependent localized surface plasmon resonance," *ACS nano,* vol. 11, no. 7, pp. 7542-7551, 2017.

[132] T. Chang *et al.*, "Facile and low-temperature fabrication of thermochromic Cr2O3/VO2 smart coatings: enhanced solar modulation ability, high luminous transmittance and UV-shielding function," *ACS applied materials & interfaces,* vol. 9, no. 31, pp. 26029-26037, 2017.

[133] H. Liu, J. Lu, and X. R. Wang, "Metamaterials based on the phase transition of VO2," *Nanotechnology,* vol. 29, no. 2, p. 024002, 2017.

[134] H. Ye *et al.*, "The demonstration and simulation of the application performance of the vanadium dioxide single glazing," *Solar Energy Materials and Solar Cells,* vol. 117, pp. 168-173, 2013/10/01/ 2013, doi: https://doi.org/10.1016/j.solmat.2013.05.061.

[135] Y. Gao *et al.*, "Nanoceramic VO2 thermochromic smart glass: A review on progress in solution processing," *Nano Energy,* vol. 1, no. 2, pp. 221-246, 2012.

[136] Z. Xiang *et al.*, "Optimized thermochromic properties for smart window application of VO2 films by wet-etching process," *Optical Materials,* vol. 128, p. 112359, 2022.

[137] Y. Cui, Y. Wang, B. Liu, H. Luo, and Y. Gao, "First-principles study on the phase transition temperature of X-doped (X= Li, Na or K) VO 2," *RSC Advances,* vol. 6, no. 69, pp. 64394-64399, 2016.

[138] N. Wang, S. Liu, X. Zeng, S. Magdassi, and Y. Long, "Mg/W-codoped vanadium dioxide thin films with enhanced visible transmittance and low phase transition temperature," *Journal of Materials Chemistry C,* vol. 3, no. 26, pp. 6771-6777, 2015.

[139] Z. Zhang *et al.*, "Thermochromic VO2 thin films: solution-based processing, improved optical properties, and lowered phase transformation temperature," *Langmuir,* vol. 26, no. 13, pp. 10738-10744, 2010.

[140] M. Panagopoulou *et al.*, "Thermochromic performance of Mg-doped VO2 thin films on functional substrates for glazing applications," *Solar energy materials and solar cells,* vol. 157, pp. 1004-1010, 2016.

[141] J. Kang, J. Liu, F. Shi, Y. Dong, and S. Jiang, "The thermochromic characteristics of Zn-doped VO2 that were prepared by the hydrothermal and post-annealing process and their polyurethane composite films," *Ceramics International,* vol. 47, no. 11, pp. 15631-15638, 2021.

[142] L. Dai *et al.*, "F-doped VO 2 nanoparticles for thermochromic energy-saving foils with modified color and enhanced solar-heat shielding ability," *Physical Chemistry Chemical Physics,* vol. 15, no. 28, pp. 11723-11729, 2013.

[143] L. Hu *et al.*, "Porous W-doped VO 2 films with simultaneously enhanced visible transparency and thermochromic properties," *Journal of Sol-Gel Science and Technology,* vol. 77, pp. 85-93, 2016.

[144] N. Shen *et al.*, "The synthesis and performance of Zr-doped and W–Zr-codoped VO 2 nanoparticles and derived flexible foils," *Journal of Materials Chemistry A,* vol. 2, no. 36, pp. 15087-15093, 2014.

[145] S. Chen *et al.*, "The visible transmittance and solar modulation ability of VO 2 flexible foils simultaneously improved by Ti doping: an optimization and first principle study," *Physical Chemistry Chemical Physics,* vol. 15, no. 40, pp. 17537-17543, 2013.

[146] Z. Chen *et al.*, "VO2-based double-layered films for smart windows: Optical design, all-solution preparation and improved properties," *Solar energy materials and solar cells,* vol. 95, no. 9, pp. 2677-2684, 2011.

[147] X. Zhao *et al.*, "Durability-enhanced vanadium dioxide thermochromic film for smart windows," *Materials Today Physics,* vol. 13, p. 100205, 2020.

[148] C. Liu, X. Cao, A. Kamyshny, J. Law, S. Magdassi, and Y. Long, "VO2/Si–Al gel nanocomposite thermochromic smart foils: Largely enhanced luminous transmittance and solar modulation," *Journal of colloid and interface science,* vol. 427, pp. 49-53, 2014.

[149] X. Zhao, S. A. Mofid, B. P. Jelle, G. Tan, X. Yin, and R. Yang, "Optically-switchable thermally-insulating VO2-aerogel hybrid film for window retrofits," *Applied Energy,* vol. 278, p. 115663, 2020.

[150] A.-L. Liu *et al.*, "The role of ipRGCs in ocular growth and myopia development," *Science Advances,* vol. 8, no. 23, p. eabm9027, 2022.

[151] D. M. Berson, F. A. Dunn, and M. Takao, "Phototransduction by retinal ganglion cells that set the circadian clock," *Science,* vol. 295, no. 5557, pp. 1070-1073, 2002.

[152] S. Wang, Y. Zhou, T. Jiang, R. Yang, G. Tan, and Y. Long, "Thermochromic smart windows with highly regulated radiative cooling and solar transmission," *Nano Energy,* vol. 89, p. 106440, 2021.
[153] Y. Zhou, Y. Cai, X. Hu, and Y. Long, "Temperature-responsive hydrogel with ultra-large solar modulation and high luminous transmission for “smart window” applications," *Journal of Materials Chemistry A,* vol. 2, no. 33, pp. 13550-13555, 2014.
[154] Q. Lei, L. Wang, H. Xie, and W. Yu, "Active-passive dual-control smart window with thermochromic synergistic fluidic glass for building energy efficiency," *Building and Environment,* vol. 222, p. 109407, 2022/08/15/ 2022, doi: https://doi.org/10.1016/j.buildenv.2022.109407.
[155] J. Wang *et al.*, "A fully self-powered, ultra-stable cholesteric smart window triggered by instantaneous mechanical stimuli," *Nano Energy,* vol. 85, p. 105976, 2021.
[156] S. Cao, S. Zhang, T. Zhang, Q. Yao, and J. Y. Lee, "A visible light-near-infrared dual-band smart window with internal energy storage," *Joule,* vol. 3, no. 4, pp. 1152-1162, 2019.
[157] A. Ghosh and T. Mallick, "Evaluation of colour properties due to switching behaviour of a PDLC glazing for adaptive building integration," *Renewable Energy,* vol. 120, pp. 126-133, 2018.
[158] A. Ghosh and B. Norton, "Optimization of PV powered SPD switchable glazing to minimise probability of loss of power supply," *Renewable Energy,* vol. 131, pp. 993-1001, 2019.
[159] Y.-S. Hsiao *et al.*, "Enhanced electrochromic performance of carbon-coated V2O5 derived from a metal–organic framework," *Applied Surface Science,* vol. 542, p. 148498, 2021.
[160] A. U. Viola, L. M. James, L. J. Schlangen, and D.-J. Dijk, "Blue-enriched white light in the workplace improves self-reported alertness, performance and sleep quality," *Scandinavian journal of work, environment & health,* pp. 297-306, 2008.
[161] A. N. French, I. G. Morgan, P. Mitchell, and K. A. Rose, "Patterns of myopigenic activities with age, gender and ethnicity in S ydney schoolchildren," *Ophthalmic and Physiological Optics,* vol. 33, no. 3, pp. 318-328, 2013.
[162] G. Hoffmann *et al.*, "Effects of variable lighting intensities and colour temperatures on sulphatoxymelatonin and subjective mood in an experimental office workplace," *Applied Ergonomics,* vol. 39, no. 6, pp. 719-728, 2008.
[163] L. J. Schlangen, L. Price, D. Sliney, and M. Spitschan, "Report on the Workshop Use and Application of the new CIE s 026/e: 2018, Metrology for ipRGC-influenced responses to light “specifying light for its eye-mediated non-visual effects in humans”," in *Proceedings of the 29th Session of the CIE*: CIE, 2019, pp. 114-118.
[164] M. Carboni, M. Carravetta, X. Zhang, and E. Stulz, "Efficient NIR light blockage with matrix embedded silver nanoprism thin films for energy saving

window coating," *Journal of Materials Chemistry C,* vol. 4, no. 8, pp. 1584-1588, 2016.
[165] J. B. Maas, J. K. Jayson, and D. A. Kleiber, "Effects of spectral differences in illumination on fatigue," *Journal of Applied Psychology,* vol. 59, no. 4, p. 524, 1974.
[166] A. N. French, R. S. Ashby, I. G. Morgan, and K. A. Rose, "Time outdoors and the prevention of myopia," *Experimental eye research,* vol. 114, pp. 58-68, 2013.
[167] F. Rao, A. Chan, and X.-F. Zhu, "The influence of LED lighting on task accuracy: time of day, gender and myopia effects," *Modern Physics Letters B,* vol. 31, no. 19-21, p. 1740019, 2017.
[168] Y. YUKANG, "GUANG ZHOU'S RURAL HOUSING: A GUIDELINES FOR SUSTAINABLE DESIGN," *Procedia of Multidisciplinary Research,* vol. 1, no. 9, pp. 10-10, 2023.
[169] F. Zhang, "Evaluation of changing the components involved in CIE color rendering index," *Optik,* vol. 219, p. 165261, 2020.
[170] C. S. McCamy, "Correlated color temperature as an explicit function of chromaticity coordinates," *Color Research & Application,* vol. 17, no. 2, pp. 142-144, 1992.
[171] C. CCUP, "Commission internationale de l'Eclairage proceedings," ed: Cambridge University Press, Cambridge, 1931.
[172] O. Sylvania, "ColorCalculator user guide," *downloaded on Jun,* vol. 3, 2014.
[173] H. L. Mahoney and T. M. Schmidt, "The cognitive impact of light: illuminating ipRGC circuit mechanisms," *Nature Reviews Neuroscience,* vol. 25, no. 3, pp. 159-175, 2024.
[174] C. Beier, Z. Zhang, M. Yurgel, and S. Hattar, "Projections of ipRGCs and conventional RGCs to retinorecipient brain nuclei," *Journal of Comparative Neurology,* vol. 529, no. 8, pp. 1863-1875, 2021.
[175] K. R. Harrison, A. P. Chervenak, S. M. Resnick, A. N. Reifler, and K. Y. Wong, "Amacrine cells forming gap junctions with intrinsically photosensitive retinal ganglion cells: ipRGC types, neuromodulator contents, and connexin isoform," *Investigative Ophthalmology & Visual Science,* vol. 62, no. 1, pp. 10-10, 2021.
[176] Z. Zhang, C. Beier, T. Weil, and S. Hattar, "The retinal ipRGC-preoptic circuit mediates the acute effect of light on sleep," *Nature communications,* vol. 12, no. 1, p. 5115, 2021.
[177] T. Sonoda, S. K. Lee, L. Birnbaumer, and T. M. Schmidt, "Melanopsin phototransduction is repurposed by ipRGC subtypes to shape the function of distinct visual circuits," *Neuron,* vol. 99, no. 4, pp. 754-767. e4, 2018.
[178] M. Figueiro, J. Brons, B. Plitnick, B. Donlan, R. Leslie, and M. S. Rea, "Measuring circadian light and its impact on adolescents," *Lighting research & technology,* vol. 43, no. 2, pp. 201-215, 2011.

[179] S. Babilon, S. Beck, and T. Q. Khanh, "A field test of a simplified method of estimating circadian stimulus," *Lighting Research & Technology,* vol. 54, no. 5, pp. 459-473, 2022.
[180] M. S. Rea, M. G. Figueiro, A. Bierman, and J. D. Bullough, "Circadian light," *Journal of circadian rhythms,* vol. 8, no. 1, p. 2, 2010.
[181] M. G. Figueiro, K. Gonzales, and D. Pedler, "Designing with circadian stimulus," *Lighting design+ application,* vol. 46, no. 10, pp. 30-34, 2016.
[182] Z. Hu, P. Zhang, Y. Huang, M. Li, and Q. Dai, "The impact of melanopic illuminance and CCT on spatial brightness perception of illuminated interiors and energy-saving implications," *Building and Environment,* vol. 223, p. 109524, 2022.
[183] S. Santimalai and T. Tayjasanant, "Visual and melanopic performance of a tropical daylight-mimicking lighting: a case study in Thailand," *International Journal of Electrical & Computer Engineering (2088-8708),* vol. 13, no. 5, 2023.
[184] S. Morimoto and T. Noguchi, "Bronze-colored infrared and ultraviolet radiation absorbing glass," ed: Google Patents, 1995.
[185] K. Johnsen and M.-C. Dubois, *Impact of coated windows on visual perception: A pilot study in scale models*. SBI forlag, 2003.
[186] J.-H. Jou *et al.*, "Efficient very-high color rendering index organic light-emitting diode," *Organic Electronics,* vol. 12, no. 5, pp. 865-868, 2011.
[187] F. M. Vossen, M. P. Aarts, and M. G. Debije, "Visual performance of red luminescent solar concentrating windows in an office environment," *Energy and Buildings,* vol. 113, pp. 123-132, 2016.
[188] J. Lin, Y. Zhao, and D. Shi, "Optical thermal insulation via the photothermal effects of Fe3O4 and Fe3O4@ Cu2-x S thin films for energy-efficient single-pane windows," *Mrs Communications,* vol. 10, no. 1, pp. 155-163, 2020.
[189] M. Sun, J. Liu, and B. Dong, "Effects of Sb doping on the structure and properties of SnO2 films," *Current Applied Physics,* vol. 20, no. 3, pp. 462-469, 2020.
[190] C. Zhang *et al.*, "Experimental study of indoor light/thermal environment with spectrally selective windows using ATO nanofluids in winter," *Energy and Buildings,* vol. 278, p. 112597, 2023.
[191] C. Shen, G. Lv, S. Wei, C. Zhang, and C. Ruan, "Investigating the performance of a novel solar lighting/heating system using spectrum-sensitive nanofluids," *Applied Energy,* vol. 270, p. 115208, 2020.
[192] C. S. Long, H.-H. Lu, D.-F. Lii, and J.-L. Huang, "Effects of annealing on near-infrared shielding properties of Cs-doped tungsten oxide thin films deposited by electron beam evaporation," *Surface and Coatings Technology,* vol. 284, pp. 75-79, 2015.
[193] F. Shi, J. Liu, X. Dong, Q. Xu, J. Luo, and H. Ma, "Hydrothermal synthesis of CsxWO3 and the effects of N2 annealing on its microstructure and heat

shielding properties," *Journal of Materials Science & Technology,* vol. 30, no. 4, pp. 342-346, 2014.

[194] J.-X. Liu *et al.*, "Microstructure and electrical–optical properties of cesium tungsten oxides synthesized by solvothermal reaction followed by ammonia annealing," *Journal of Solid State Chemistry,* vol. 183, no. 10, pp. 2456-2460, 2010.

[195] Y. Li, X. Wu, J. Li, K. Wang, and G. Zhang, "Z-scheme g-C3N4@ CsxWO3 heterostructure as smart window coating for UV isolating, Vis penetrating, NIR shielding and full spectrum photocatalytic decomposing VOCs," *Applied Catalysis B: Environmental,* vol. 229, pp. 218-226, 2018.

[196] S. Senthilarasu, E. F. Fernández, F. Almonacid, and T. K. Mallick, "Effects of spectral coupling on perovskite solar cells under diverse climatic conditions," *Solar Energy Materials and Solar Cells,* vol. 133, pp. 92-98, 2015.

[197] C. A. Gueymard, "Parameterized transmittance model for direct beam and circumsolar spectral irradiance," *Solar Energy,* vol. 71, no. 5, pp. 325-346, 2001.

[198] Y. Piffer, J. C. Jonsson, S. Güths, R. M. S. Machado, and R. Lamberts, "Development and validation of an optical model for water-based windows with clear glazing: A parametric performance assessment," *Building and Environment,* vol. 209, p. 108635, 2022.

[199] T. Hong, "A close look at the China design standard for energy efficiency of public buildings," *Energy and buildings,* vol. 41, no. 4, pp. 426-435, 2009.

[200] X. Su, O. B. Kazanci, Z. Wang, B. W. Olesen, L. Sun, and Y. Yuan, "Local thermal comfort chart for non-uniform building environments: Comparison with vehicle environments and its application," *Building and Environment,* vol. 234, p. 110162, 2023.

[201] E. Cuce and S. B. Riffat, "A state-of-the-art review on innovative glazing technologies," *Renewable and sustainable energy reviews,* vol. 41, pp. 695-714, 2015.

[202] X.-H. Li, C. Liu, S.-P. Feng, and N. X. Fang, "Broadband light management with thermochromic hydrogel microparticles for smart windows," *Joule,* vol. 3, no. 1, pp. 290-302, 2019.

[203] L. Zhang, Y. Du, F. Xia, and Y. Gao, "Two birds with one stone: A novel thermochromic cellulose hydrogel as electrolyte for fabricating electric-/thermal-dual-responsive smart windows," *Chemical Engineering Journal,* vol. 455, p. 140849, 2023.

[204] P. Pattathil, R. Giannuzzi, and M. Manca, "Self-powered NIR-selective dynamic windows based on broad tuning of the localized surface plasmon resonance in mesoporous ITO electrodes," *Nano energy,* vol. 30, pp. 242-251, 2016.

[205] Y. Zhou, Y. Cai, X. Hu, and Y. Long, "VO 2/hydrogel hybrid nanothermochromic material with ultra-high solar modulation and luminous transmission," *Journal of Materials Chemistry A,* vol. 3, no. 3, pp. 1121-1126, 2015.

[206] M. Elsadek, B. Liu, and J. Xie, "Window view and relaxation: Viewing green space from a high-rise estate improves urban dwellers' wellbeing," *Urban forestry & urban greening,* vol. 55, p. 126846, 2020.

[207] L. Kexiu, M. Elsadek, B. Liu, and E. Fujii, "Foliage colors improve relaxation and emotional status of university students from different countries," *Heliyon,* vol. 7, no. 1, 2021.

[208] C. Liu *et al.*, "Index-tunable anti-reflection coatings: Maximizing solar modulation ability for vanadium dioxide-based smart thermochromic glazing," *Journal of Alloys and Compounds,* vol. 731, pp. 1197-1207, 2018.

[209] Y. Zhan *et al.*, "Tuning thermochromic performance of VOx-based multilayer films by controlling annealing pressure," *Ceramics International,* vol. 46, no. 2, pp. 2079-2085, 2020.

[210] Z. Zou *et al.*, "Phase transition mechanism and application of silicon-doped VO2 thin films to smart windows," *Journal of Materials Science: Materials in Electronics,* vol. 32, no. 19, pp. 23825-23833, 2021.

[211] X. Zhao *et al.*, "Thermochromic composite film of VO2 nanoparticles and [(C2H5) 2NH2] 2NiBr4@ SiO2 nanospheres for smart window applications," *Chemical Engineering Journal,* vol. 460, p. 141715, 2023.

[212] L. Zhang, Y. Du, H. Xia, G. Yang, and Y. Gao, "HPC-PAA hydrogel smart windows with and without Cs0. 32WO3: High solar modulation ability and luminous transmittance," *Ceramics International,* vol. 48, no. 24, pp. 37122-37131, 2022.

[213] Y. Huang *et al.*, "Oxygen-deficient tungsten oxide nanoflowers for dynamically tunable near-infrared light transmittance of smart windows," *Nano Research,* vol. 16, no. 10, pp. 12165-12172, 2023.

[214] A. Cots, S. Dicorato, L. Giovannini, F. Favoino, and M. Manca, "Energy efficient smart plasmochromic windows: properties, manufacturing and integration in insulating glazing," *Nano Energy,* vol. 84, p. 105894, 2021.

[215] J. Kim *et al.*, "Nanocomposite architecture for rapid, spectrally-selective electrochromic modulation of solar transmittance," *Nano letters,* vol. 15, no. 8, pp. 5574-5579, 2015.

[216] W. Meng *et al.*, "Scalable photochromic film for solar heat and daylight management," *Advanced Materials,* vol. 36, no. 5, p. 2304910, 2024.

[217] F. Song *et al.*, "Meteorological data set for building thermal environment analysis of China," 2007.

[218] X. Zhang, J. Qiu, X. Li, J. Zhao, and L. Liu, "Complex refractive indices measurements of polymers in visible and near-infrared bands," *Appl. Opt.,* vol. 59, no. 8, pp. 2337-2344, 2020.

[219] A. Ciesielski, L. Skowronski, M. Trzcinski, and T. Szoplik, "Controlling the optical parameters of self-assembled silver films with wetting layers and annealing," *Applied Surface Science,* vol. 421, pp. 349-356, 2017.

[220] S. Wang, T. Jiang, Y. Meng, R. Yang, G. Tan, and Y. Long, "Scalable thermochromic smart windows with passive radiative cooling regulation,"

Science, vol. 374, no. 6574, pp. 1501-1504, 2021/12/17 2021, doi: 10.1126/science.abg0291.
[221] Z. Wang *et al.*, "Temperature-adaptive smart windows with passive transmittance and radiative cooling regulation," *Applied Energy,* vol. 369, p. 123619, 2024/09/01/ 2024, doi: https://doi.org/10.1016/j.apenergy.2024.123619.
[222] J. Keum *et al.*, "Innovative dual-band energy-efficient smart windows using VO2(M)-Based Fabry-Pérot structures for solar and radiative cooling modulation," *Materials Today Physics,* vol. 52, p. 101665, 2025/03/01/ 2025, doi: https://doi.org/10.1016/j.mtphys.2025.101665.
[223] H. Zhang *et al.*, "All-Solid-State Transparent Variable Infrared Emissivity Devices for Multi-Mode Smart Windows," *Advanced Functional Materials,* vol. 34, no. 16, p. 2307356, 2024/04/01 2024, doi: https://doi.org/10.1002/adfm.202307356.
[224] Y. Jia *et al.*, "Transparent dynamic infrared emissivity regulators," *Nature Communications,* vol. 14, no. 1, p. 5087, 2023/08/22 2023, doi: 10.1038/s41467-023-40902-w.
[225] Y. Huang *et al.*, "A novel liquid flow electrochromic smart window for all-year-round dynamic photothermal regulation," *Energy & Environmental Science,* 10.1039/D4EE05416D vol. 18, no. 4, pp. 1824-1834, 2025, doi: 10.1039/D4EE05416D.
[226] K. Feng *et al.*, "Electrically Controlled Smart Window for Seasonally Adaptive Thermal Management in Buildings," *Small,* vol. 21, no. 5, p. 2407033, 2025/02/01 2025, doi: https://doi.org/10.1002/smll.202407033.
[227] Y. Ke *et al.*, "On-Demand Solar and Thermal Radiation Management Based on Switchable Interwoven Surfaces," *ACS Energy Letters,* vol. 7, no. 5, pp. 1758-1763, 2022/05/13 2022, doi: 10.1021/acsenergylett.2c00419.
[228] J. Huang *et al.*, "A Janus Spectrally Selective Glazing Toward All-Season Energy-Efficient Windows," *Small,* vol. 21, no. 10, p. 2407204, 2025/03/01 2025, doi: https://doi.org/10.1002/smll.202407204.
[229] Y. Deng *et al.*, "Annual Energy-Saving Smart Windows with Actively Controllable Passive Radiative Cooling and Multimode Heating Regulation," *Advanced Materials,* vol. 36, no. 27, p. 2401869, 2024/07/01 2024, doi: https://doi.org/10.1002/adma.202401869.
[230] C. Lin *et al.*, "All-weather thermochromic windows for synchronous solar and thermal radiation regulation," *Science Advances,* vol. 8, no. 17, p. eabn7359, doi: 10.1126/sciadv.abn7359.
[231] R. Zhang *et al.*, "Thermochromic smart window utilizing passive radiative cooling for Self-Adaptive thermoregulation," *Chemical Engineering Journal,* vol. 471, p. 144527, 2023/09/01/ 2023, doi: https://doi.org/10.1016/j.cej.2023.144527.
[232] Z. Zhou *et al.*, "Synergistic modulation of solar and thermal radiation in dynamic energy-efficient windows," *Nano Energy,* vol. 93, p. 106865, 2022/03/01/ 2022, doi: https://doi.org/10.1016/j.nanoen.2021.106865.

[233] S. Wang *et al.*, "A solar/radiative cooling dual-regulation smart window based on shape-morphing kirigami structures," *Materials Horizons,* 10.1039/D3MH00671A vol. 10, no. 10, pp. 4243-4250, 2023, doi: 10.1039/D3MH00671A.

[234] X. Hu *et al.*, "Facile and Widely Applicable Route to Self-Adaptive Emissivity Modulation: Energy-Saving Demonstration with Transparent Wood," *Nano Letters,* vol. 24, no. 2, pp. 657-666, 2024/01/17 2024, doi: 10.1021/acs.nanolett.3c03711.

[235] A.-J. N. Khalifa, "Natural convective heat transfer coefficient – a review: I. Isolated vertical and horizontal surfaces," *Energy Conversion and Management,* vol. 42, no. 4, pp. 491-504, 2001/03/01/ 2001, doi: https://doi.org/10.1016/S0196-8904(00)00042-X.

[236] M. G. Emmel, M. O. Abadie, and N. Mendes, "New external convective heat transfer coefficient correlations for isolated low-rise buildings," *Energy and Buildings,* vol. 39, no. 3, pp. 335-342, 2007/03/01/ 2007, doi: https://doi.org/10.1016/j.enbuild.2006.08.001.

[237] A. Aili, X. Yin, and R. Yang, "Global radiative sky cooling potential adjusted for population density and cooling demand," *Atmosphere,* vol. 12, no. 11, p. 1379, 2021.

[238] Y. Zhu, H. Qian, R. Yang, and D. Zhao, "Radiative sky cooling potential maps of China based on atmospheric spectral emissivity," *Solar Energy,* vol. 218, pp. 195-210, 2021/04/01/ 2021, doi: https://doi.org/10.1016/j.solener.2021.02.050.

[239] B. Sun, L. Lu, J. Chen, T. Ma, and Y. Yuan, "Full-spectrum radiative cooling for enhanced thermal and electrical performance of bifacial solar photovoltaic modules: A nationwide quantitative analysis," *Applied Energy,* vol. 362, p. 123037, 2024/05/15/ 2024, doi: https://doi.org/10.1016/j.apenergy.2024.123037.

[240] J. Yang and J. Qiu, "A Method for Estimating Precipitable Water and Effective Water Vapor Content from Ground Humidity Parameters," *Chinese Journal of Atmospheric Sciences,* vol. 26, no. 1, pp. 9-22, 2002, doi: 10.3878/j.issn.1006-9895.2002.01.02.

[241] S. Edition *et al.*, "Energy standard for buildings except low-rise residential buildings," *ASHRAE, Atlanta, GA, USA, Tech. Rep. IP Edition,* 2010.